Karlsruher Institut für Technologie

ETP-KA/2019-14

Characterizing detector modules for the Upgrade of the Silicon Tracker of the Compact Muon Solenoid experiment

Zur Erlangung des akademischen Grades einer
DOKTORIN DER NATURWISSENSCHAFTEN (Dr. rer. nat.)

von der KIT-Fakultät für Physik des
Karlsruher Instituts für Technologie (KIT)

genehmigte

Dissertation

von

M.Sc. Nikkie Deelen
aus Veldhoven (Die Niederlande)

Tag der mündlichen Prüfung: 18.10.2019

Referent: Prof. Dr. Wim de Boer Institut für Experimentelle Teilchenphysik
Korreferent: Prof. Dr. Thomas Müller Institut für Experimentelle Teilchenphysik

Nikkie Deelen:
Characterizing detector modules for the Upgrade of the Silicon Tracker of the Compact Muon Solenoid experiment
October 2019

Acknowledgements

I would like to thank my supervisor at CERN, Dr. Stefano Mersi, for his guidance and advice during each stage of the research. I would also like to acknowledge my professors from KIT, Prof. Dr. Wim de Boer and Prof. Dr. Thomas Müller. I would also like to express my appreciation to Dr. Duccio Abbaneo, for giving me the opportunity to perform my studies in the Detector Applications section of the CMS Experiment Systems group at the Experimental Physics department at CERN. The support of Dr. Georg Auzinger, Dr. Sarah Seif El Nasr-Storey and other colleagues from CERN and KIT was greatly appreciated as well.

Finally, I wish to thank my husband Jeroen, my parents Ties and Yvonne, and my sister Emmie because they will always stand beside me.

Abstract

Since its start-up in 2008 the Large Hadron Collider has been producing proton-proton collisions with a center-of-mass energy approaching 14 TeV for high-energy physics experiments at the European Center for Nuclear research. The resulting physics events are studied by four large experiments around the 27 km collider ring one of them being the Compact Muon Solenoid detector. To boost the discovery potential of the Large Hadron Collider it will be upgraded in several phases, such that its particle interaction flux will be increased from $1 \times 10^{34}\,\mathrm{cm}^{-1}\,\mathrm{s}^{-2}$ to $5 \times 10^{34}\,\mathrm{cm}^{-1}\,\mathrm{s}^{-2}$. This is referred to as the High Luminosity Upgrade. Consequently, the four large experiments at the laboratory will be improved as well to cope with these operating conditions.

This research is focused on the characterization of prototype modules designed for the upgrade of the Compact Muon Solenoid's tracking sub-detector. It is composed of the Inner Tracker at its center that is surrounded by the Outer Tracker. The prototype modules under study consist of silicon pixel sensors and silicon strip sensors for the Inner and Outer Tracker, respectively. Prototype front-end readout chips are connected to the sensors for the initial signal processing. These are mounted on printed circuit boards that are used to supply power to, and to extract data from the readout chips. In the first part of this thesis the calibration of the threshold setting of the prototype binary front-end chips for the Outer Tracker is described. The second part covers a beam test setup that was designed, build, and tested with the aim to perform high-rate studies ($\sim$1 MHz) with the tracker prototypes. This kind of setup can be used to characterize any kind of silicon tracker module in particle beams.

Due to the technology that is used to produce the binary readout chips a 10 % difference in response and threshold calibration value is expected between chips and their individual readout channels. For this reason, a method to calibrate this threshold setting was developed. This method makes use of fluorescent, or radioactive photons of a single energy that irradiate the silicon sensors while a threshold scan is executed with the binary chip. The threshold setting corresponding to the signal in the silicon can be extracted from the scan by estimating at what value the number of particle hits per event reaches zero. A calibration curve is obtained by repeating the threshold scan with photons of different energies, and from this curve the gain of the binary front-end readout chip can be estimated.

The average calibration value found for the thus far tested readout chips, expressed as the signal induced in silicon, was $367 \pm 12\,e$ per threshold unit. Different calibration values for different chips and readout channels were measured. For the chips used in this research the differences were not greater than 10 %. A toy Monte-Carlo simulation was developed in order to study the results of the thresholds scans in further detail. This simulation included a simple model for the charge sharing between the strips of the silicon sensors.

As a preparation for high-rate beam studies with Upgrade Tracker modules that can measure particle fluxes of up to $\sim$100 MHz cm^{-2}, a new beam telescope was developed. This telescope can be used to reconstruct particle tracks that are then compared to clusters measured by a prototype module that is placed in the center of the setup. Commonly used beam telescopes have a $\sim$4600 times slower readout ($\sim$113 µs versus 25 ns) than the tracker prototypes concerned in this research. Therefore, this new setup dedicated to stress testing prototype tracker modules was build with pixel detectors with the same readout speed as the tracker prototypes. To

validate the setup it was tested in a particle beam with a prototype tracker module installed in its center.

The tracking resolution of the telescope was determined to be 7 µm in the horizontal, and 10 µm in the vertical direction. This is better than what was expected from a straight line fit that takes as the uncertainty of the hit locations measured by the telescope $100\,\mu m/\sqrt{12}$ and $150\,\mu m/\sqrt{12}$, where 100 µm is the pixel pitch in the horizontal direction and 150 µm the pixel pitch in the vertical direction. This was explained by the charge-sharing between the pixels of the telescope modules that allows for having sub-pixel precision on the location of the particle hit.

Tests with a Tracker prototype module in the the center of the new beam telescope confirmed that it is fully operational and ready for use in high-rate studies. Both the telescope and the prototype tracker module could be readout simultaneously. This was confirmed by a clear correlation between the tracks reconstructed with the telescope data, and the particle hit positions found with the new tracker module.

Contents

1. Introduction

The most powerful particle accelerator in the world is the Large Hadron Collider (LHC) were protons from two proton beams traveling in opposite directions around a 27 km long ring are accelerated to near light speed and an energy of 7 TeV before they are brought to collide with each other [1]. When these high energy protons collide enough energy is produced to form other (massive) particles. These particles resulting from the proton-proton collisions are studied with cylindrically-shaped detectors that can be up to 30 m long with a diameter of up to 25 m, and they usually weigh around a few kilo tonne. These detectors are not only able to determine the kind of particles that are produced but they also measure their energy, momentum and electrical charge. These measurements are used to study particle physics principles that could provide a better understanding of what matter is made of, or what the origin of the universe is.

There are four large detectors at the LHC. Two of the four detectors, namely A Toroidal LHC ApparatuS (ATLAS, [2]) and the Compact Muon Solenoid (CMS, [3]), were designed to study more general particle physics processes like for instance the production of the recently discovered Higgs boson particle. These detectors have a completely independent design such that the measurements from one detector can be verified with the measurements from the other detector. The other two detectors at the LHC are A Large Ion Collider Experiment (ALICE, [4]) that studies the origin of the universe based on the state of matter that is formed in these particle collisions, and the LHC beauty (LHCb, [5]) experiment that specializes in measuring the differences between matter and antimatter. Even though each of the four the detectors has a completely different design the following general concepts do apply to all of them.

The particles produced during the proton-proton collisions will fly radially outward in three-dimensional space, away from the point where two protons interacted with each other. To measure the particle collision products accurately three of the four detectors are build around the interaction point in a cylindrical shape with the beam pipes carrying the protons of the LHC running through their center. Only the LHCb detector has a different configuration but this is outside of the scope of this research. Each detector makes use of a magnet that produces a large magnetic field in the order of 4 T. This magnetic field bends charged particles in the plane perpendicular to the incoming proton beams due to the Lorentz force and it allows for measuring the momentum and charge of charged particles by determining their bending radius. Neutral particles are not affected by the magnetic field. The magnetic field aids the determination of some of the particles' properties. The actual detection of the particles is explained below.

The detection of the particles that are produced during the proton-proton collisions is based on the interactions they have with the detector materials. Most of these interactions are of an electromagnetic nature like the ionization of atoms in the detector material. Other interactions occur through the strong nuclear force of atoms. These are referred to as hadronic interactions because they are only observed when the particle interacting with the material is a hadron particle meaning it is build up of quarks like the proton for instance. Since not all of a particle's properties can be measured with one type of detector different cylindrical sub-detectors are placed inside each other. Below follows a description of the different kinds of measurements and the type of detector with which they are made.

The curved particle trajectories resulting from the magnetic field inside the detector volume are visualized with silicon sensors or tracking detectors. The tracking detectors are commonly

made with multiple layers of hundreds of very thin (100 µm to 300 µm) silicon sensors with a surface area of up to fifteen square centimeter per detector module, which in CMS adds up to a total sensor area of $\sim$200 m^2. Each silicon module is divided into microscopic pixels like in a digital camera. When a charge particle passes through the silicon it ionizes the silicon atoms. The ionization results in a charge that can be collected at the individual pixels of the silicon sensor. As the silicon modules have a microscopic grid structure the position at which a charged particle hits a tracking detector layer is very accurately known. By connecting the particle hits in the different tracking detector layers a particle track can be reconstructed that reveals the charge and momentum information of the particle that produced the track.

The energy of the particles produced during a collision is determined by measuring the energy a particle loses when it traverses material in so-called calorimeter sub-detectors. Depending on the calorimeter material and the type of particle interactions the energy loss can be in the form of for instance light or heat that is detected by the calorimeter. Only when a particle has lost all its energy inside the calorimeter volume the particle's energy can be known accurately. This means that the particle needs to be stopped or absorbed completely inside the calorimeter's volume and therefore this is referred to as a destructive kind of measurement. This means that the calorimeter sub-detectors need to be place outside of the tracking sub-detectors. The more interactions a particle has in the calorimeter material the faster it loses its energy. Subsequently, calorimeters are usually designed with very dense materials like lead or tungsten.

In general, electromagnetic interactions have a higher probability of occurring than hadronic interactions. In other words hadron particles need to pass through more detector material before they are completely absorbed and their energy is accurately known. This observation can be used for particle identification. Often particle detectors have two calorimeters one for charged particles that have electromagnetic interactions and another one for hadronic particles. Since the particles produced by the proton-proton collisions in the LHC fly radially outward of the collision point the electromagnetic calorimeter cylinder is placed inside the cylinder of the hadronic calorimeter.

Another sub-detector type that is installed in the LHC's detectors is the muon detector. Muons are charged particles that rarely interact with matter, and therefore they cannot be absorbed by the calorimeters. Due to their charge they do leave hits in the tracker detector and they can also be detected outside of the calorimeters. Consequently, muon sub-detectors are placed at the very outside of each detector. As for tracking sub-detectors they are usually based on ionization of the detector material by the muons. By combining particle trajectories measured in the tracking sub-detectors and the particle trajectories measured by the muon sub-detector muons can be identified and their momentum can be measured. With the combination of the measurements from all sub-detectors a collision event can be reconstructed that forms the basis for particle physics studies.

The CMS detector is composed of the different types of sub-detectors that are described above and it is illustrated in Figure 1.1. It shows a slice of the cross section of the cylindrically-shaped CMS detector. The tracking sub-detector which is the innermost part of the cylinder is drawn on the left and the outermost sub-detector is the muon detector on the right. Moreover, it shows the trajectories of different types of particles as they travel through the CMS detector volume. Charged particle have a curved trajectory due to the magnetic field from the cylindrical solenoid magnet which is in between the calorimeter sub-detectors and the muon sub-detectors.

To study a particle physics process with a high accuracy many proton-proton collisions are needed to produce enough occurrences or events of that process. Therefore, the proton beams in the LHC are split up in 2808 bunches of on average 1.2×10^{11} protons each. To produce the collisions two bunches, one from each of the two proton beams that travel in opposite directions around the accelerator ring, cross each other and between 20 and 40 actual proton-proton collisions take place. These bunch crossings happen every 25 ns at each of the four interaction

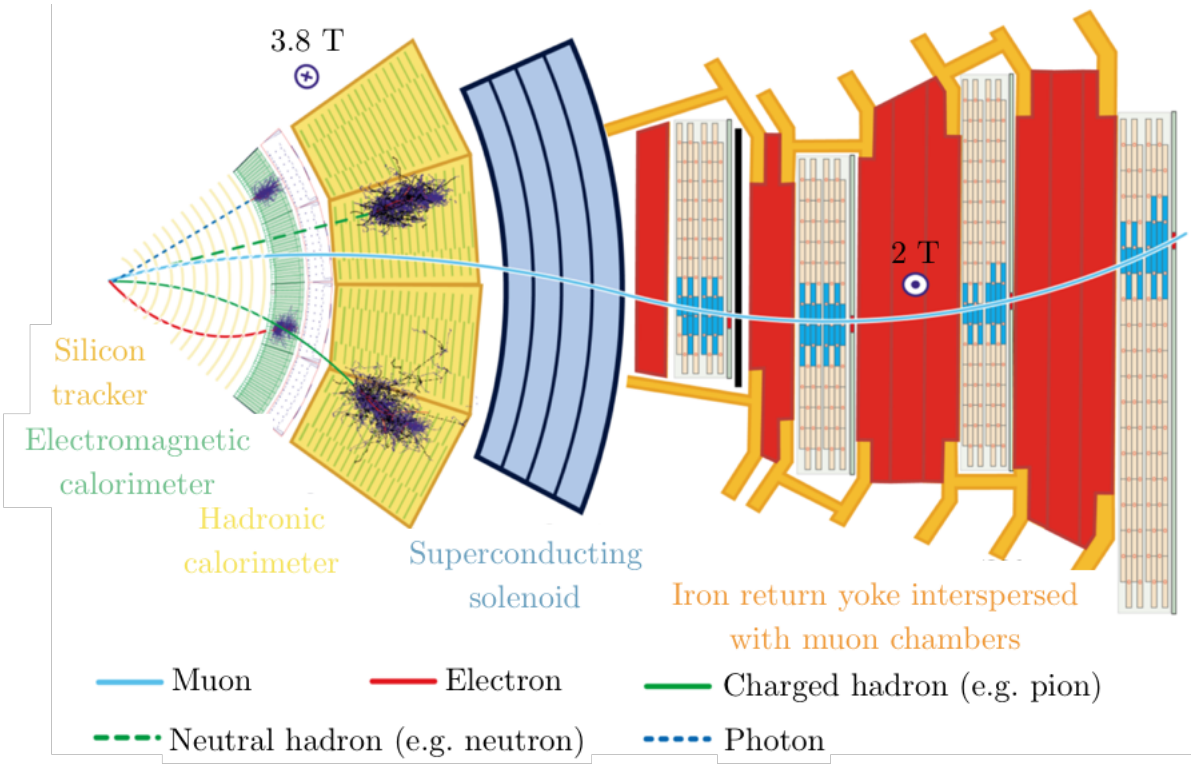

Figure 1.1. *A sixteenth part of the cross section of the CMS detector. Adapted from [6].*

points that are inside the four detectors. To increase the number of rare particle physics events produced at the LHC by proton-proton collisions and to allow for studying those rare processes with a higher accuracy an upgrade of the collider and the four detectors is ongoing [7]. The aim of the upgrade is to increase the number of particle interactions per bunch crossing from 40 to 200. To achieve this the beams in the LHC need to be more intense and more focused. The detectors that measure the results of the collisions will need to be able to detect particles faster than before and with a higher spatial precision in order to cope with the increased number of proton-proton collisions per bunch crossing.

To prepare for the upgrade of the detectors prototype sub-detectors modules are being designed and tested [8]. This research is on the characterization of prototype silicon sensor modules for the upgrade of the CMS tracker. A silicon sensor modules consist of a silicon sensor and readout electronics. The signals produced in the silicon sensors are processed by readout electronics in the form of chips that have one readout channel per silicon sensor pixel. Each readout channel is directly, electrically connected to the silicon pixel it is associated to. When a charged particle traverses the silicon sensor it induces a charge in one, or sometimes more than one silicon pixel. To force the charge to be collected at the readout channels of the readout chips an electric field is applied to the sensor. For the upgrade of the CMS tracker it was chosen to use binary readout chips. The binary readout chip outputs a logical 1 if the signal is above the voltage of an integrated comparator. This variable voltage of the comparator is called the threshold voltage.

Silicon sensor detector modules can be characterized by exposing them to a particle source for instance from a radioactive material or a particle beam while monitoring their response. These particle sources can be used to study for instance calibration procedures for the prototype modules since the type of particles from the source is known as well as the particles' energy. Having well-known calibration procedures is vital for the operation of the silicon modules in the

CMS tracking sub-detector as it allows for the monitoring of their condition. Due to the large amount of particles that traverse the silicon tracker resulting from the millions of proton-proton collisions in the LHC every second the silicon crystalline material slowly deteriorates. This can be compensated for by choosing the right operating conditions based on the calibration results.

The type of calibration that was studied during this research can be used to determine the sensitivity, or gain of the silicon tracker module. The gain is the relation between the energy of a particle that traverses the silicon sensor, and the amount of charge that is collected at the readout channels of the binary chip because of the ionization that the particle causes in the silicon. The gain of the binary readout chip can be determined from the response of the tracker prototype module to photons with different monochromatic energies as a function of the threshold voltage. A linear calibration curve can be obtained when plotting the photon energy versus the threshold that the photon energy corresponds to. The slope of this curve is equal to the gain of the prototype.

The gain calibration is described in Chapter 2. The goal of this study was to find a gain calibration procedure that can be easily repeated in a laboratory environment for many modules. This is needed because most of the thousands of silicon tracker modules needed to construct the silicon tracker detector for upgrade of CMS will have to be calibrated in the lab first. A variation between the calibration values of different readout chip and readout channels of 10 % is expected due to the technology with which the readout electronics of the silicon tracker modules are produced.

The other part of the research was focused on testing the CMS silicon tracker prototypes in particle beams. Most studies where tracker prototypes are placed in a particle beam aim at estimating how efficient the prototype can detect a particle in realistic operating conditions like high particle fluxes in the order of $100\,\mathrm{MHz\,cm^{-2}}$. Therefore, a reference measurement is needed which is usually provided by well-known silicon sensor tracking detectors placed in the same particle beam. The prototype silicon tracker module is placed in line with the reference silicon tracker modules such that particle trajectories reconstructed from particle hits measured by the reference modules can be compared to hits on the prototype module.

The collection of reference silicon tracker modules is referred to as a beam telescope and it is usually available in a test facility that provides the particle beam. Most of these commonly available beam telescope are however not capable of handling particle fluxes higher than $0.1\,\mathrm{MHz\,cm^{-2}}$. This makes them unsuitable for testing the CMS silicon tracker prototypes to the extend of their design limits, and thus the aim of the second part of the research was designing and testing a new beam telescope capable of dealing with particle fluxes up to $100\,\mathrm{MHz\,cm^{-2}}$. The design, construction, commissioning and testing of this telescope is described in Chapter 3.

The LHC, CMS, the CMS Tracker detector and the upgrade of the CMS Tracker detector are explained in more detail in the following sections of this introductory chapter. As was already mentioned above, the research methodologies and results of the two different parts are described in the next two chapters. Finally the conclusions of this research are summarized in Chapter 4.

1.1. The LHC and its pre-accelerator complex

In the LHC protons are accelerated in a 27 km ring to near light speed and 7 TeV [1]. However before these particles are send to the LHC smaller linear and circular accelerators pre-existing to the LHC boost their energy to 450 GeV. All these accelerators together form the accelerator complex of the European Organization for Nuclear Research (CERN), of which the majority is schematically drawn in Figure 1.2. The large circular structure represents the LHC and the

locations of the four detectors at LHC are indicated with labels. The smaller circular structures attached to the LHC are the pre-accelerators. The protons are derived from helium and then they are first accelerated by the Linear Accelerator 4 (Linac 4, [9]). Then they go to the Booster and from there to the Proton Synchrotron (PS, [10]) before their final pre-acceleration in the Super Proton Synchrotron (SPS, [11, 12]).

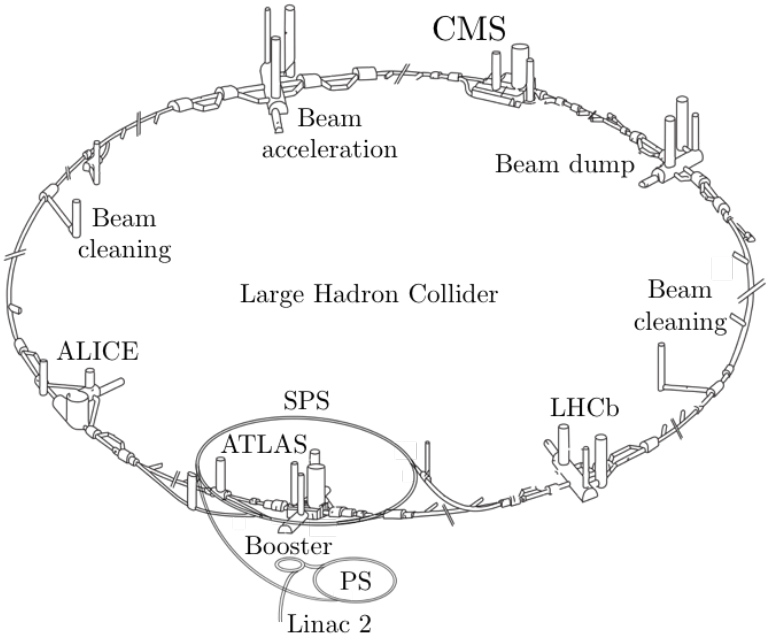

Figure 1.2. *A Schematic drawing of CERN's accelerator complex and the four big experiments. Adapted from [13].*

The pre-accelerators are not only used to prepare the protons and lead ions for injection into the LHC, they also provide particle beams for experiments that are not linked to the LHC directly. In addition they provide beams for CERN's beam test facilities which comprises two big experimental halls for beam tests at CERN. The East Area receives beam from the PS and the North Area get particles from the SPS. Both arenas are divided in several different experimental areas where particle physics measurements can be executed. In Chapter 3 results are discussed from tests in the H6 line of the SPS beam, which is tuned for tracker detector experiments.

The LHC was designed to be operated at a particle interaction flux, or luminosity of $1 \times 10^{34}\,\mathrm{cm}^{-1}\,\mathrm{s}^{-2}$ [1, 7]. By optimizing operating parameters of the LHC, for instance by reducing the beam diameters, double the design luminosity and the number of proton-proton collisions per bunch crossing or pile-up was obtained in the year 2017 [14]. Since interesting physics events are rare, it would take ten years after 2020 to reduce the statistical uncertainty on LHC measurements by half, at this luminosity [15]. Therefore, it was decided to upgrade the machine and consequently the experiments to allow for running at a luminosity of $5 \times 10^{34}\,\mathrm{cm}^{-1}\,\mathrm{s}^{-2}$ in order to uphold the scientific progress at CERN. This is referred to as the High Luminosity Upgrade of the LHC (HL-LHC).

The four big experiments at CERN are ALICE [4], ATLAS [2], CMS [3]) and the LHCb [5]. ATLAS and CMS are both referred to as general-purpose detectors; they are intended to study a wide-range of particle physics phenomena. They were developed completely separately such that the results of one of the experiments can be validated with the findings of the other and vice versa. LHCb is dedicated to CP-violation measurements and ALICE is aimed at

understanding the properties of Quark-Gluon plasma. The CMS detector will be described in more detail in the next section before going deeper into silicon trackers, the CMS Tracker and the High Luminosity Upgrade of the CMS Silicon Tracker.

1.2. The Compact Muon Solenoid

Except for the muon chambers, all sub-detectors of CMS fit inside the 5.9 m diameter bore of a superconducting solenoid magnet [3]. This makes CMS relatively compact at a height of 15 m, length of 21 m and total mass of 12.5×10^3 kg. The cylindrical or barrel-shaped detector shown in Figure 1.3 was designed to reconstruct muons at a very high accuracy as one of the main decay channels of the Higgs boson is via two Z-particles that decay further into four muons. The di-muon mass resolution of CMS is better than 1 % at 100 GeV [16]. This is compatible to the Higss mass of $m_{\text{Higgs}} = (125.7 \pm 0.4)$ GeV [17, p. 33].

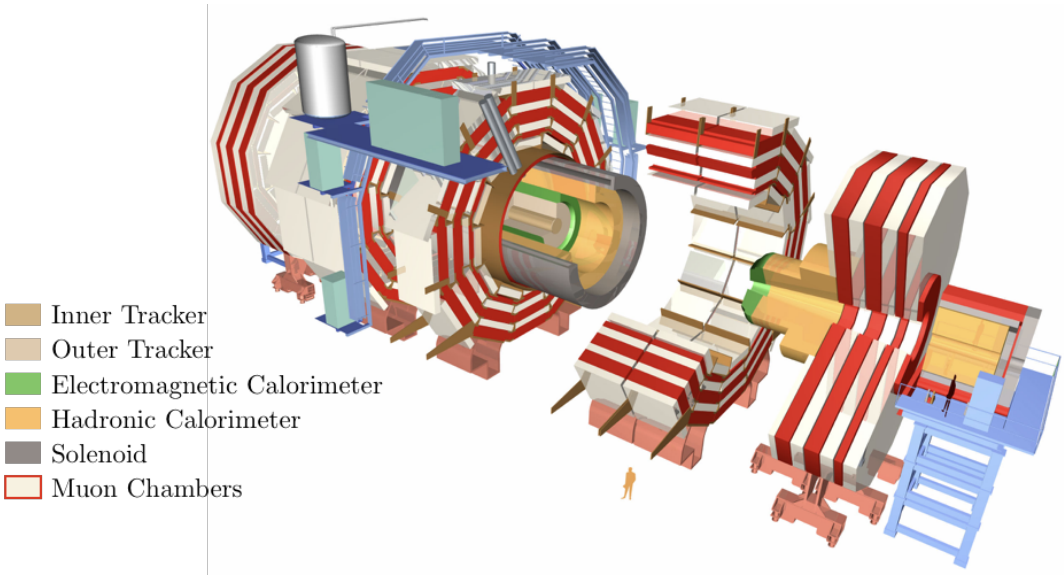

Figure 1.3. *A schematic view of the CMS experiment and its sub-detectors [18].*

When looking at CMS from the center of the detector to the outside the following sub-detectors are observed: the Pixel Tracker and the Strip Tracker [19, 20], the Electromagnetic Calorimeter (ECAL, [21]), the Hadronic Calorimeter (HCAL, [22]), the Solenoid magnet [23] and finally the Muon chambers [24] that are alternated with the iron yoke (red). On either end of the barrel end-cap disks are placed that also have ECAL, HCAL and muon sub-detector to cover most space where the particles produced by the proton-proton collisions will fly through. The CMS layout is typical for barrel-shaped High Energy Physics (HEP) experiments.

Both the CMS Pixel and the Strip Tracker consist of silicon sensor detectors. The Pixel Tracker has 768 modules spread over 4 barrel layers and two end-cap disks with 672 pixel modules, all width 250 µm thick sensors. Each module has $100 \times 150\,\mu\text{m}^2$ pixels. With this pixel size, and taking the Lorentz angle of 23° account, the intrinsic resolution of the Pixel Tracker is between 10 µm and 15 µm. The Strip detector is is designed with 320 µm silicon sensors of which the strip pitch varies between 60 µm and 270 µm with a strip length between 7 cm and 12.5 cm depending on the layer a module is in. The total silicon sensor surface of both the pixel and the strip detector amounts to 200 m^2 making it the largest silicon tracker ever build.

The High-Luminosity upgrade of CMS is executed in two phases. As part of the Phase-1 Upgrade a new Phase-1 Pixel Detector was commissioned in CMS in the first half of 2017. Both the Phase-1 Pixel Detector and the current Strip Tracker are discussed in more detail in the next section but first silicon sensor technology is explained. During Phase-2 or the CMS High-Luminosity Upgrade both the Inner Tracker and the Outer Tracker will be upgraded. These upgrades are discussed in Section 1.6.

1.3. Silicon sensor detectors

The properties of the semi-conductor silicon are summarized in Table 1.1 [25]. The working principle of silicon sensor detectors is based on the bulk properties of pure silicon, in which atomic energy levels can no longer be observed. Instead there are two energy levels for all electrons in the silicon volume, namely the valence and the conduction band. When electrons are exited from the valence to the conduction band, the electrons and their corresponding holes can move freely through the silicon.

Table 1.1.
Properties of silicon [25].

Parameter	**Symbol**	**Unit**	**Value**
Atomic number	Z		14
Density	ρ	$\mathrm{g\,cm^{-2}}$	2.328
Band gap energy	E_{gap}	eV	1.124
Electron mobility	μ_{e}	$\mathrm{cm^2\,V^{-1}\,s^{-1}}$	1350
Hole mobility	μ_{h}	$\mathrm{cm^2\,V^{-1}\,s^{-1}}$	450
Maximum electric field	E_{max}	$\mathrm{V\,\mu m^{-1}}$	30

By introducing impurities or doping to the silicon, the band gap between the valence and conduction band can be reduced. This makes it easier for silicon atoms to become ionized. When ionizing radiation traverses an average silicon sensor, it generates around $\sim 2 \times 10^4$ extra free charge carriers in the silicon volume. However, without cooling the silicon to cryogenic temperatures, this signal can not be detected as an average silicon sensor already has roughly $\sim 1 \times 10^9$ free charge carriers as a result of spontaneous excitations.

This kind of cooling is unpractical at a large scale as in the case of the CMS detector. Instead, layers of silicon with different dopant materials are used to create a space charge region that is free of charge carriers, called a pn-junction. This is demonstrated Figure 1.4; the positive side (p) has acceptor doping like boron and the negative side (n) has donor doping like phosphorus. Donor atoms add extra electrons to the silicon and acceptor atoms add extra holes. The electric field at the junction is shown in Figure 1.4 too, which causes for the absence of free charge carriers in the space charge region. The space charge region needs to be increased such that the charge carriers resulting from ionization can be detected, and thus an external bias voltage is applied. The resulting depleted region's width w is computed by

$$w = \sqrt{2\epsilon\rho\mu V_{\mathrm{bias}}} \tag{1.1}$$

where ϵ is the dielectric constant of silicon, ρ its density, μ the mobility of the free charge carriers and V_{bias} the bias voltage applied to the silicon. The bias voltage at full depletion V_{FD}, of a sensor with thickness D is given by

$$V_{\mathrm{FD}} = \frac{D^2}{2\epsilon\mu\rho} \tag{1.2}$$

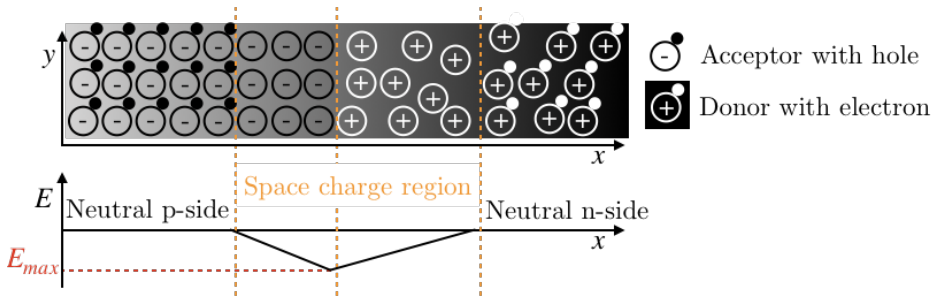

Figure 1.4. *An illustration of the silicon PN-junction.*

By placing n-doped silicon implants in a p-doped silicon bulk volume, a detector is created with pixels/strips of which the pitch is defined by the distance between the implants, as shown in Figure 1.5. When an ionizing particle pass through the sensor, the resulting free charge carriers travel in opposite directions due to the electric field in the silicon as a result of the bias voltage. In Figure 1.4 the electrons travel towards the strips, inducing a current on the aluminum strips that are capacitively coupled to the n^+ implants. A readout chip of which its readout channels connect directly to the aluminum is used to process the signals from individual strips.

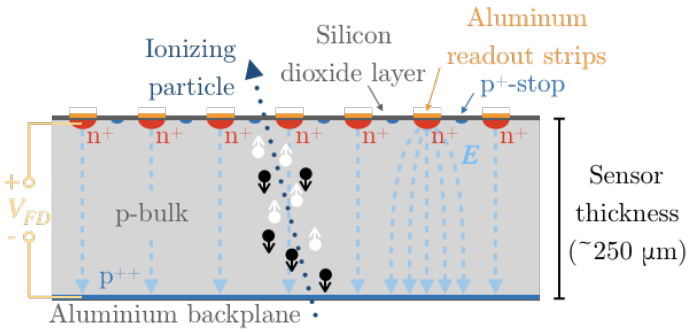

Figure 1.5. *An illustration of a silicon sensor, with electrons in white and holes in black, traveling in opposite directions.*

A silicon dioxide layer on the implant side is used to prevent the silicon from reacting. An aluminum back plane on the back connects to the bias voltage. The pixels connect to the bias voltage through a bias ring around active sensor area. Depending on the application, other doping schemes can be used like n-in-p^+, p^{++}-in-n, and so on. Based on this design choice, the sensors have to be either forward or reversed biased to increase the depletion zone, where forward bias refers to the p-side being connected to the positive terminal of the voltage supply.

Noise from statistical fluctuations of electrons and holes in the silicon is mainly caused by leakage current (shot noise), bias resistance (parallel thermal noise), pixel resistance (serial thermal noise) and noise from the load capacitance.

1.4. The current Silicon Strip Tracker

Figure 1.6 shows a schematic view of the Silicon Strip Tracker (SST) module and its readout. The grey silicon strip sensor is wire-bonded to Analog Pipeline Voltage mode chips (APVs), the front-end readout chips of the detector. They are bump-bonded to a hybrid circuit board that also houses Phase Locked Loop (PPL) chips to decode the trigger and clock, and APV Multiplexer chips to multiplex the data of all APVs in a module before it is shipped to the

back-end electronics. The Detector Control Unit (DCU) chip on the hybrid can monitor slowly varying analog signals, like the temperature of the module.

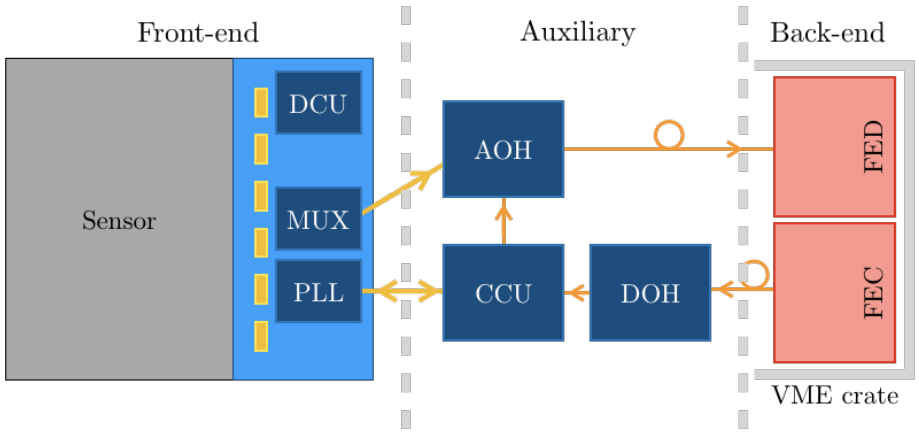

Figure 1.6. *Schematic overview of the CMS Silicon Strip Tracker DAQ [19]. The yellow squares on the blue hybrid represent the APV chips. Yellow arrows represent flat ribbon cables, providing electrical connections. Orange arrows represent optical fibers.*

The APV is designed to have 128 analog inputs. All 128 channels have a pre-amplifier and shaper stage. The shaper's output is designed to be sampled at 40 MHz, which is the LHC clock frequency. At each clock cycle, its output is stored in a 160 clock cycle-long buffer that matches the Level-1 trigger latency of 3.2 µs. This pipeline buffer is readout upon the Level-1 Accept signal (L1A, [26]) which comes from the CMS trigger.

The SST back-end has a Front-end Driver (FED) and a Front-end Controller (FEC) for readout and control, which are both Versa Module Europe (VME) bus cards [27]. The FED receives the data via the Analog Optical Hybrid (AOH, [28]). The FEC sends control signals over the Digital Optical Hybrid (DOH, [28]) which sends it to the Communication and Control Units (CCUs, [29]). These control I^2C busses used to send configuration signals to the SST front-end. Both optical hybrids are used to convert electrical signals into optical ones, or vice versa.

A photograph of a fully assembled SST module on an aluminum support plate is presented in Figure 1.7. The kapton flat ribbon cable coming from the hybrid leads the analog signals from the APVs to the AOHs, it guides the signals between the PLLs and the DOHs and provides the low voltage power to the hybrid. The kapton frame around the sensor provides bias voltage and back-plane insulation to the sensor.

1.5. The current Inner Tracker: Phase-1

The Phase-1 Inner Tracker (IT) is not only discussed here as a reference to compare the Phase-2 Inner Tracker to, but also because Inner Tracker Barrel Pixel (BPix) modules are used in the new CMS telescope, which is described in Chapter 3. The Forward Pixel modules (FPix) that are in the forward region of CMS, are not discussed here. However, they are very similar to BPix modules [31].

A BPix module is composed of a silicon pixel sensor with $100 \times 150\,\mu m^2$ pixels, on which ROCs are bump-bonded [32]. A High Density Interconnect (HDI) is mounted on top of the sensor and a thin carbon fiber plate glued to the ROCs is used as a module base that can be connected to a cooling frame. The HDI houses the Token Bit Manager (TBM) that distributes the clock and trigger to the ROCs, controls the readout of all ROCs in a module and adds a

Figure 1.7. *A CMS Silicon Strip Tracker module and its hybrid (green). A row of six APV25 chips can be seen wire-bonded to the strips [30].*

header and trailer to their data [33]. Furthermore, it sends the control signals coming from the back-end to the front-end chips.

The analog signal from the 300 µm thick n^+-type pixels, that are surrounded by p^+-type stops rings, is processed by the readout chips. Each pair of columns in a ROC, forms a double column that is controlled by a circuit on the column periphery. Each Pixel Unit Cell (PUC) in a double column is bump-bonded to a pixel in the silicon sensor.

The PUCs are connected by two local bus lines: the Column OR and the data transfer line. A PUC contains two functional blocks: the analogue and the readout block. The analogue part amplifies the signal from the silicon pixel and if it is above a tunable threshold, the Column OR notifies the periphery that in turn registers the time stamp of the event. At that moment it sends a token signal past the double column which initiates the transfer of pixel address and signal by the readout block. Both are stored in a local buffer until the L1A arrives. Next, the time stamp, pixel address and analog signal are send directly to the Pixel Front-end Driver (PIX-FED, [34]) which is connected to the DAQ PC via the Front-End Readout Optical Link (FEROL, [35])

The token that is send from double column to double column, comes from the TBM. Upon receiving the L1A signal, it passes the token to the ROCs and sends a header on the data link to the PIX-FED. Then it sends the data from the readout chips, one after another. When the token bit (successfully) returns after it has passed all ROCs, it finally sends the readout trailer. In the Phase-1 Pixel case, the FED is a Micro Telecommunications Computing Architecture (µTCA, [36]) card, with readout firmware on its FPGA.

The full readout chain of the Phase-1 Inner Tracker is drawn schematically in Figure 1.8. A portcard with auxiliary electronics, sits in between the back-end and the modules. It houses a Pixel Opto-Hybrid (POH) to converts the electrical signals from the modules to optical signals that the PIX-FED receives. The portcard additionally connects to a pixel DOH that converts the optical control signals from the PIX-FEC to electrical signals that are send to the TBM. The PIX-FEC is of µTCA type as well. Another µTCA type card in the pixel readout is the Tracker-FEC (TK-FEC, [37]) that controls the CCU and DC-DC converters, just like in the Silicon Strip Tracker, see Section 1.4.

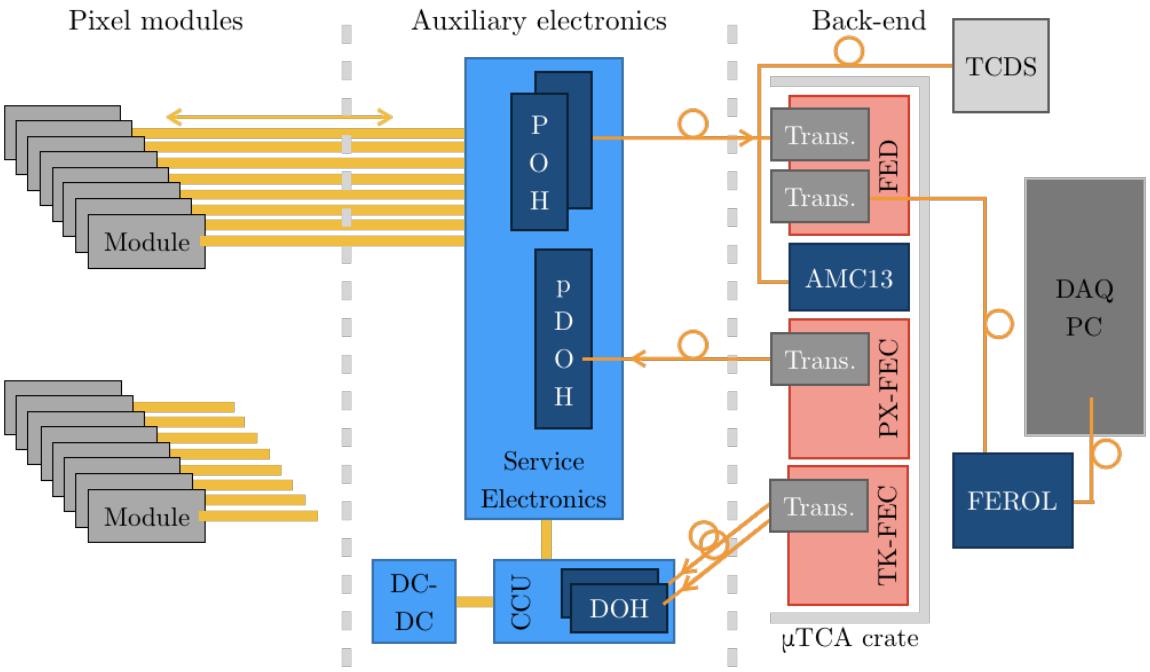

Figure 1.8. *Schematic overview of the CMS Phase-1 Inner Tracker DAQ [31]. Yellow lines represent twisted pair cables, providing electrical connections. Orange arrows represent optical fibers.*

The Advanced Mezzanine Card 13 (AMC13) in the μTCA crate distributes the clock and trigger signals over the crate's back-plane to the back-end cards [38]. These arrive at the AMC13 via the Timing and Control Distribution System (TCDS) that is connected to the LHC clock [39, 40].

A photograph of a fully assembled BPix module is given in Figure 1.9. In the Inner Tracker the yellow flat ribbon cable is replaced by a long twisted pair cable. The small green-colored chip in the center of the module is the TBM.

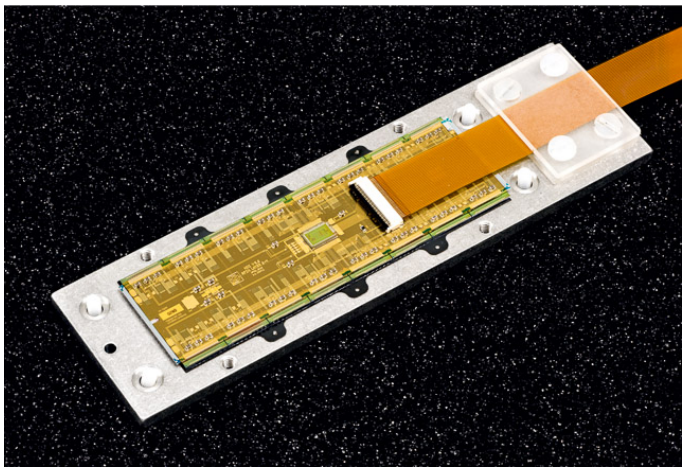

Figure 1.9. *A Barrel Pixel module. Photo courtesy of T. Kuhlmann from DESY-ZE.*

1.6. The high luminosity upgrade of the CMS Tracker

The following explains the upgrades of the CMS Tracker that will be implemented during High Luminosity Upgrade of the CMS Tracker to prepare it for the increased particle flux [8]. First, the Tracker needs to be radiation tolerant enough to be fully efficient up to the HL-LHC target integrated luminosity of $3000\,\mathrm{fb}^{-1}$. In the case of the Outer Tracker, it will be designed to withstand the high fluence of up to $1 \times 10^{15}\,\mathrm{n_{eq}\,cm^{-2}}$ which it will experience in its inner layers. The Inner Tracker will be kept accessible, just like in the present Tracker. This will allow for replacing damaged modules during extended technical stops of the HL-LHC.

Furthermore the granularity of the tracker needs to be increased to cope with the HL-LHC design conditions, such as the pile-up of 200 per bunch crossing. This ensures that the channel occupancy stays below 1 % and thus the current tracking efficiency will be maintained after the upgrades. For both the Inner and the Outer tracker the pixel and strip pitch will be reduced to accomplish this. Additionally, both the tracking performance and the energy measurement of the calorimeters will be enhanced by reducing the material budget of the Phase-2 CMS Tracker, which, in some areas of the Phase-2 Tracker, will be half of the material budget of the present Tracker.

To manage the high pile-up conditions, some pattern recognition needs to be implemented in the tracker which will ease reconstruction of events by the High Level Trigger, as it can be used for event selection at the Level-1 trigger stage. Additionally, the tracking acceptance will be extended to $|\eta| = 4$.

To underline the differences between the present Tracker System and the Phase-2 Tracker system both are shown in Figures 1.10 and 1.11. For both the current and the Phase-2 Tracker system a cross section is shown in the figure. The horizontal axis of the figures is parallel to axes of the incoming proton beams and the vertical axis is parallel to the radius of the CMS barrel. In Figures 1.10 and 1.11 the blue and the red lines represent the current Silicon Strip Tracker that is currently installed in CMS and the Phase-2 Outer Tracker after the upgrade. The green and yellow lines represent the currently installed Phase-1 Inner Tracker and the Phase-2 Inner Tracker after the upgrade. Each of the colored lines represents a silicon sensor tracker module.

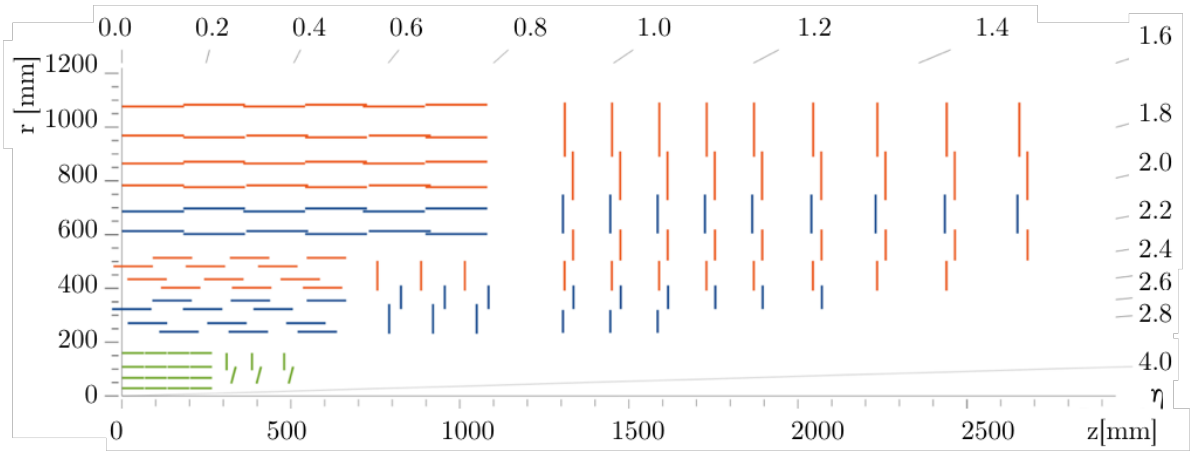

Figure 1.10. *A quarter of the cross-section of the current CMS Tracker system [8].*

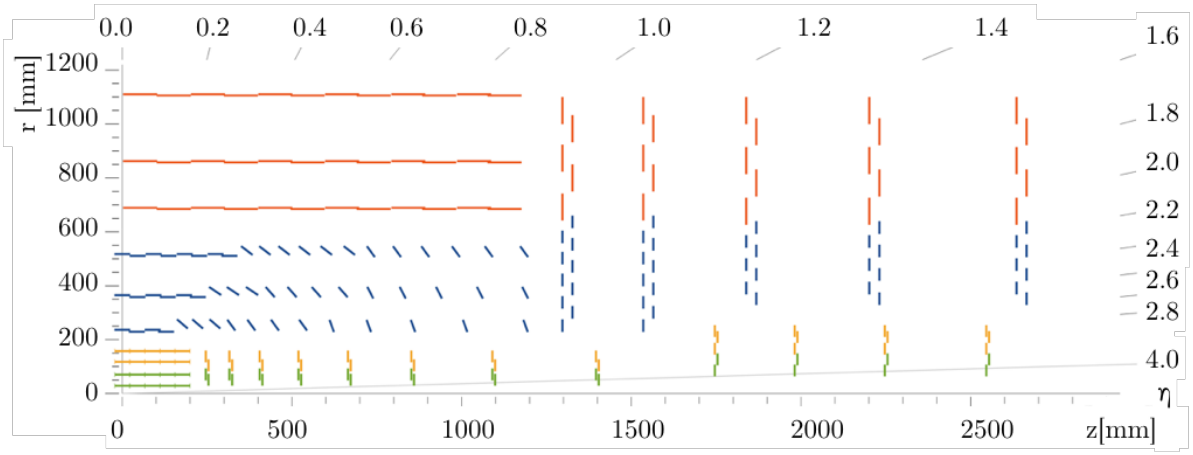

Figure 1.11. *A quarter of the cross-section of the CMS Phase-2 Tracker system [8].*

Table 1.2.
A summary of the properties of the current and the CMS Phase-2 Tracker system [3, 8, 31].

Property	**Symbol**	**Unit**	**Phase-1 IT**	**Phase-2 IT**	**SST**	**Phase-2 OT**
Trigger rate	R_{trig}	kHz	100	750	100	750
Cooling power	P_{cool}	kW	15	50	68	100
Sensor type			n^+-in-n	n-in-p	p-on-n	n-in-p
No. modules	N_{mod}		1140	4352	8632	13 296
Module size	A_{mod}	cm^2	1.6×6.5	1.6×6.5	6×12 or 9×10	5×10 or 10×10
Pitch	p	μm^2	100×150	50×50 or 25×100	60 to 270	90
Strip length	l_{strip}	cm			7 to 12.5	5

1.6.1. Phase-2 Inner Tracker

The baseline of the Phase-2 Inner Tracker modules are 100 µm to 150 µm thick sensors with pixels of either $25 \times 100\,\mu\text{m}^2$ or $50 \times 50\,\mu\text{m}^2$ (compared to $100 \times 150\,\mu\text{m}^2$ in Phase-1). They are radiation tolerant enough to deal with HL-LHC conditions.

The new IT ROCs are currently being designed by teams of both ATLAS and CMS, under the CERN Research and Development project number 53 (RD53). It will have a $2500\,\mu\text{m}^2$ cell size, based on 65 nm CMOS technology.

An overview of the Phase-2 IT DAQ is given in Figure 1.12. The modules on the left connect to service electronics. A Low-power Gigabit Transceiver (Lp-GBT) in combination with a Versatile Transceiver Plus (VTRx), form the interface between the electrical and optical signals that go from the front-end to the back-end and the other way around. The back-end is based on the Advanced Telecommunications Architecture (ATCA) [41]. A Detector Trigger Control board (DTC) both receives the data and controls the readout. It receives trigger and clock via the back plane from the Detector Timing Hub (DTH), similar to the AMC13 in Phase-1. It is connected to a new version of the TCDS system, which is referred to here as TCDS2.

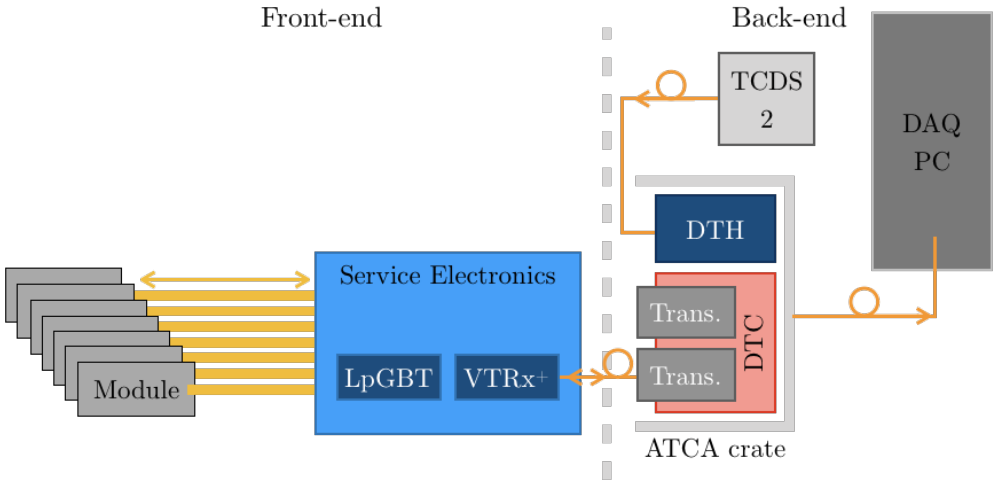

Figure 1.12. *Schematic overview of the CMS Phase-2 Inner Tracker DAQ [8]. Yellow lines represent twisted pair electrical links. The orange arrows represent optical fibers.*

1.6.2. Phase-2 Outer Tracker

For the Outer Tracker Phase-2 Upgrade, two types of modules have been designed: the Strip-Strip (2S) and macroPixel-Strip (PS) modules of pitch $100 \times 1467\,\mu m^2$. The PS modules are designed to go in the inner layers of the Phase-2 Outer Tracker and the 2S modules are designed for its outside layers. This research is aimed at 2S modules and therefore these will be described below.

An illustration of a 2S module is shown in Figure 1.13. Both 2S and PS modules have two sensors on top of each other with a gap of a few millimeter in between. Both sensors are n-in-p, forward biased silicon sensors. In the 2S case they have 5 cm long strips with a 90 µm pitch.

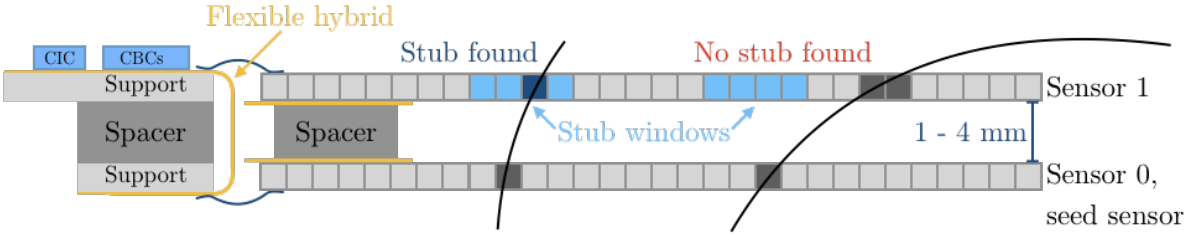

Figure 1.13. *Illustration of a 2S module, seen from the side. Two lines representing particle trajectories demonstrate the stub finding logic.*

The readout channels of the front-end readout chips of a 2S module are wire-bonded two both sensors: the even number channels to the bottom sensor (Sensor 0) and the odd number channels to the top sensor, Sensor 1. These front-end CMS Binary Chips (CBCs), which design is based on 130 nm CMOS technology, have a total 254 channels that process the analog input from the strips. The CBC output is binary: based on a tunable threshold it decides whether a particle was detected or not.

Additionally, CBCs use the information from both sensors to find so-called stubs, illustrated in Figure 1.13 too. Depending on a particle's bending radius in the magnetic field of CMS, it will hit a different strip number in the bottom sensor and in the top sensor. This information can be used to select on high transverse momentum particles (>2 GeV), that are likely to be a result from rare-physics events. The smaller the bending radius of the particle, and thus the

closer the hits in the top and bottom sensor are together, the higher the transverse momentum. This form of pattern recognition can be included in the trigger of CMS, improving the event selection at an early stage. To compensate for the RΦ-position of a strip in the detector, there is the possibility to offset the stub finding window for each strip as well as the stub window size at each position.

An overview of the OT DAQ is given in Figure 1.14. A full-size 2S sensor is $10 \times 10\,\mathrm{cm}^2$ large, with 5 cm long strips in each half. A total of sixteen CBCs are used to read the module out, eight on either side of the module. They output a digital bit-stream with hit and stub information to the Concentrator Integrated Circuit chips (CICs) on the front-end hybrids, that multiplex the data from all eight CBCs on one side. The binary output allows for a reduced material budget in the detector volume as the number of cables for data and powering the modules is reduced, compared to when analogue information would have to be shipped out. Both the CBCs and the CICs are bump-bonded on the front-end hybrids.

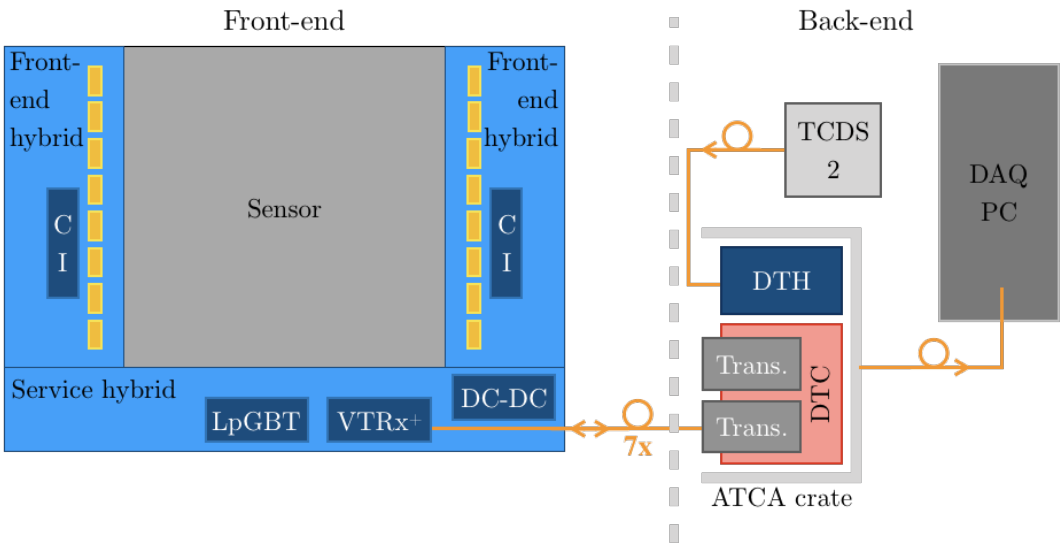

Figure 1.14. *Schematic overview of the CMS Phase-2 Outer Tracker DAQ [8]. The orange arrows represent optical links.*

Analogous to the Phase-2 IT, a LpGBT VTRx combination on the service hybrid of a module, converts the electrical signals to optical signals, before they are send to the back-end. DC-DC converters on the same service hybrid are used to provide power to the front-end chips. The Phase-2 OT back-end hardware is the same as the Phase-2 IT back-end hardware, as well as the core of the DTCs firmware. Dedicated firmware blocks handle for instance the CIC control and data acquisition, and other Outer Tracker specific needs.

In Chapter 2, two prototype versions of the CBC, incorporated in prototype 2S modules are investigated, namely CBC version 2 and version 3. Therefore, the CBC2 and CBC3 chips are described in more detail in the next two sections, as well as the prototype modules that were used for the studies presented here.

CBC2

Figure 1.15 gives a schematic view of the CBC2 front-end logic. The analog signal from the strip that is wire-bonded to a readout channel is first amplified and shaped by the pre-amplifier. At the time of its design, both n-in-p and p-in-n sensors were still candidates for 2S modules.

To accommodate signals from both sensor types, switches with the labels e^- and e^+ are used in the CBC2, to process either negative or positive pulses.

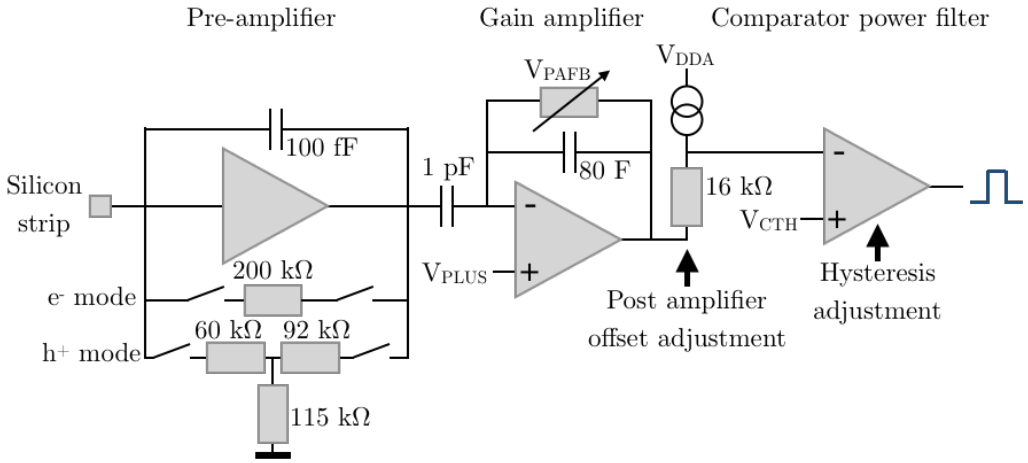

Figure 1.15. *The analog front end of a CBC2 chip [42]. The silicon strip is schematically drawn on the left in the form of a square. The output is binary because of the discriminator at the end of the front-end process and is fed into the Hit Detect Logic, seen in Figure 1.16.*

After the pre-amplifier, the signal is further amplified by the gain amplifier before it is processed by a comparator with variable threshold. If the signal surpasses the threshold, a binary "one" is outputted and send to the Hit Detect Logic (HDL), see Figure 1.16. A programmable post amplifier offset adjustment is used to compensate for differences in gain between different channels. The tuning of all these offsets in the CBC, is referred to as offset tuning or trimming.

The CBC2 HDL is used to synchronize the binary output to the clock, which is designed to be the 40 MHz LHC clock frequency. There are two HDL modes in CBC2; one simply synchronizes the output to the clock. The other outputs a pulse of one clock cycle length, when the rising edge of the comparator output is detected. In Figure 1.16 the front-end output is drawn at the top of the scheme. Each vertical dotted line represents the rising edge of the clock. The second vertical, digital pattern in the drawing represents the line that is used to enable or disable the Hit Detect Logic. The third pattern is for the selection of the detection mode. If it is high, the output will be synchronized and if it is low, a one clock cycle long pulse is send out at the time the rising edge of the clock passes.

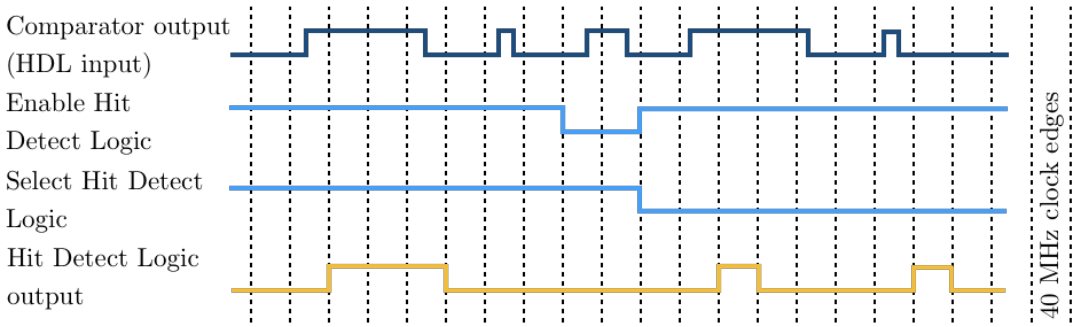

Figure 1.16. *Examples of how the CBC2 chip processes an input signal (front-end output, Figure 1.15), shown at the top. The produced output at the bottom, depends on the Hit Detect Logic setting, given by the middle two lines. Drawn after [42].*

Then there is stub finding logic on the chip which is not discussed in detail here. It features the definition of the seed layer and a selectable stub finding window size in the other layer. In addition, the stub finding window can be offset to compensate for the RΦ-position of the detector in the CMS Outer Tracker. For more information, the stub finding logic of the CBC2 is explained in detail in [42, p. 13-17].

The hit and stub logic information are stored in a pipeline buffer of 256 clock cycles deep, until the L1A signal is received by the CBC2. Then the data corresponding to the trigger latency that is selected by the user, is send to the back-end firmware. Two pointers are used for the trigger latency; a write pointer at the buffer stage of the event, and the trigger pointer which is set when the L1A is received. The trigger latency is defined in the CBC2 as the difference between the write and trigger pointer.

An image of a prototype CBC2 mini module is given in Figure 1.17. On the left side, silicon baby-sensors are seen on their aluminum support. They are 254 strips wide, or 2.3 cm, and 5 cm long. These sensors in this particular module are n-in-p type and thus have to be forward biased. Therefore the CBC2s in this module are operated in electron mode.

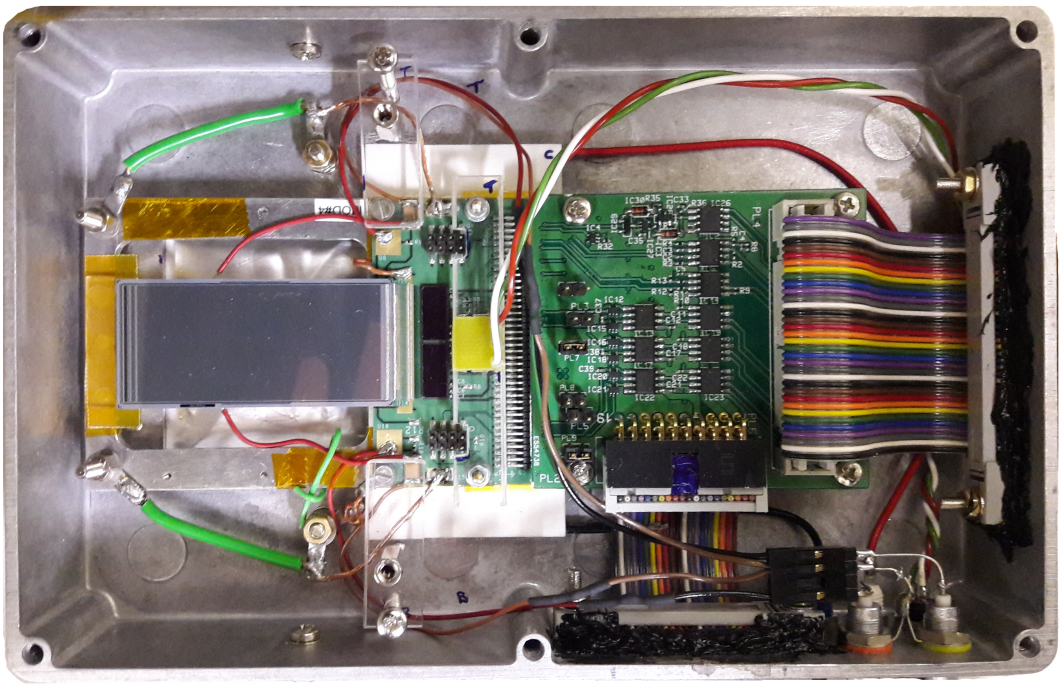

Figure 1.17. *A CBC2 mini module prototype.*

The CBC2s are bump-bonded on the green CBC2 hybrid in the center of the image. The two black squares on hybrid are the CBC2 chips. The hybrid slots into the interconnect card which houses two connectors for the low voltage power and data cables. The bias voltage comes in on the red and yellow LEMO connectors at the bottom right corner of the module. It links directly to the sensors. The aluminum box surrounding the module can be closed by an aluminum lit. The box has windows on both sides, below and above the sensors, that are covered with aluminum foil to shield the module from environmental light.

At high occupancy, the CBC2 starts to behave unexpected. This is caused by the post-amplification feedback bias [43]. The V_{plus} was used as current, and mirror current source which was causing the CBC2 to not output all hits at high occupancy. For the CBC2, this is referred to as common-mode noise. In CBC3, which is described in the next section, there are two bias sources: V_{plus} for bias current and V_{plus2} for mirror bias current.

CBC3

The CBC3 is a newer CBC prototype chip following the CBC2. It can only process signals from n-in-p type sensors, which have become the baseline of the 2S module design. Therefore the electron/hole switches have been removed from the front-end logic, which is given in Figure 1.18. It is almost the same as the CBC2 front-end logic. In addition to the second V_{plus} setting, a low pass filter was added for the V_{DDA} power, to reduce the common-mode noise.

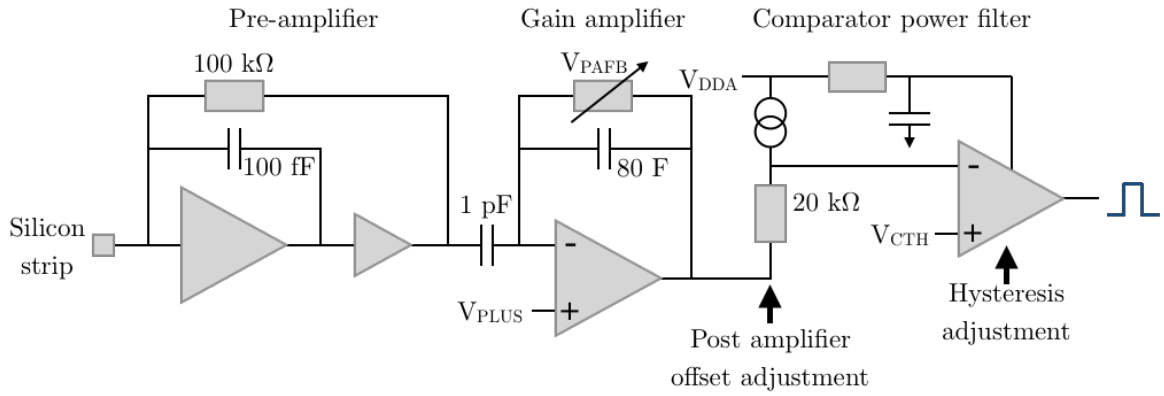

Figure 1.18. *The analog front end of a CBC3 chip [44]. The binary output is send to the HDL of the CBC3. CBC3 can only be operated in electron mode.*

The HDL of the CBC3 is illustrated in Figure 1.19. The top digital pattern shows an example front-end logic output. The two HDL settings from the CBC2 have been maintained, and in addition the logial OR of the two has been added. These are shown on the three digital patterns in the middle. A additional Highly-Ionizing Particle mode has been added as well. With this setting one force the HDL output back to zero, if it has been high for a certain amount of clock cycles. For obvious reasons, this setting can only applied for the sampled and OR HDL settings.

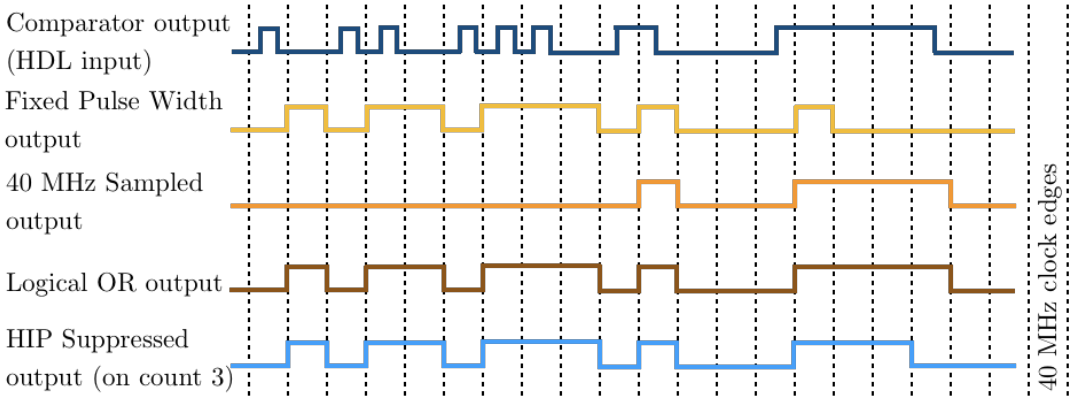

Figure 1.19. *Examples of how the CBC3 chip processes an input signal (front-end logic output, Figure 1.18, shown on top) depending on the Hit Detect Logic setting [44].*

The stub logic of the CBC3 is very similar to the CBC2 stub logic. In CBC3 information on the bending radius of the particle's track that created a stub is encoded in the data as well. In addition, clusters in a stub with a size of two or four strips are used to give cluster position information of half-strip resolution. The same is applied to the stub finding window and the window offset. More details are given in [44, p. 22-26] [45].

A CBC3 mini module prototype is shown in Figure 1.20. The n-in-p silicon baby-sensors are supported on an aluminum frame, similar to the CBC2 mini module in Figure 1.17. On the right side the dark-grey hybrid is visible with the two CBC3 chips bump-bonded on top of it. An interconnect card for low voltage power and data links is not connected to the hybrid on this photo. The high voltage bias is supplied over the yellow and black wires visible in the picture.

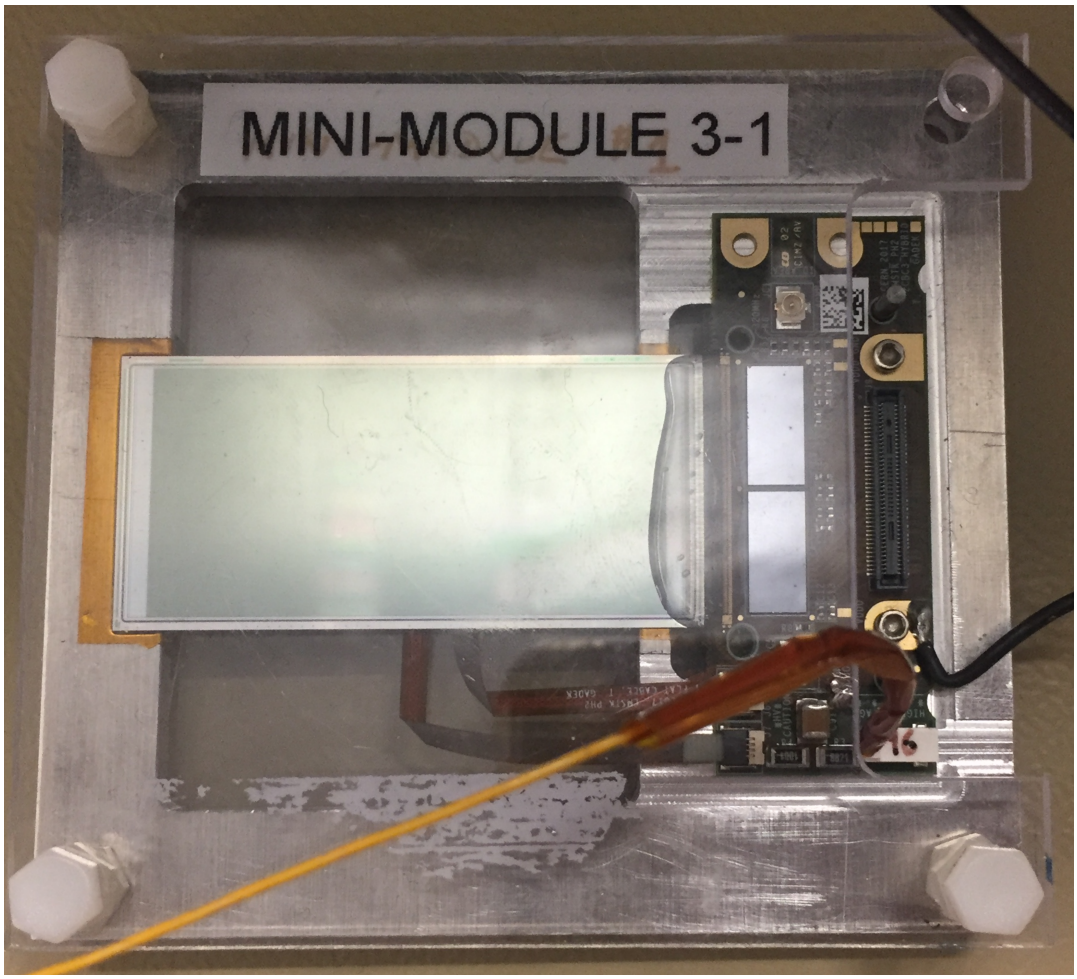

Figure 1.20. *A CBC3 mini module prototype.*

2. Laboratory Measurements

This chapter, describes a study on testing methods for the calibration of the V_{Cth} setting of the CBCs, the readout chips of the CMS Phase-2 Outer Tracker modules. The aim is to find a calibration method that can be repeated easily and fast in a laboratory environment, during the production phase. This is study was performed during the prototyping phase of the CMS Phase-2 Outer Tracker modules; in order to better understand the characteristics of the modules, laboratory tests were executed. Most of the studies discussed here were carried out with a CBC2 mini module. At the end of the chapter, the CBC3 case is discussed, before a conclusion is drawn in Section 2.9.

2.1. Introducing the CBC threshold unit calibration

During the operation of the future CMS Phase-2 Outer Tracker, the threshold at which a CBC should detect a hit, will be calibrated regularly. This can be accomplished quickly by using a calibration pulse. This pulse of known height is generated on the CBC itself and fed directly into the pre-amplifier of the front-end logic, see Figure 1.15. By sending calibration pulses with different pulse heights while monitoring the output of the CBC the gain of the front-end can be determined. For an unirradiated CBC2 this is around $45\,\mathrm{mV\,fC^{-1}}$ [46].

The CBC calibration pulse is generated by a capacitor on the chip, but because of the 130 nm CMOS technology the capacitance of this capacitor can only be reproduced within 10 %. Like so, before this pulse can be used to calibrate the CBC threshold it needs to be characterized. The 130 nm CMOS technology affects all circuit elements, and therefore both strip-to-strip and chip-to-chip variations in response, threshold *et cetera* are expected.

The output of the CBC2 is given in V_{Cth} units, which is the DAC setting of the threshold voltage of the comparator. The actual threshold voltage of the CBC2 is roughly linear with V_{Cth}, as can be seen in Figure 2.1. According to its design specifications, $1\,V_{Cth}$ unit corresponds to $\sim$2.5 mV [42]. Given the CBC2 front-end gain and the electron charge, a V_{Cth} unit is around

$$\begin{aligned} 1\,\mathrm{fC} &= 45\,\mathrm{mV}\,, \\ 1\,\mathrm{fC} &= 6242\,e\,, \\ 1\,V_{Cth} &= 2.5\,\mathrm{mV} = 0.055\,\mathrm{fC} \approx 343\,e\,. \end{aligned} \tag{2.1}$$

This can be confirmed by measuring well-defined signals with a CBC2 module. To produce one free electron-hole pair in silicon at room temperature, 3.67 eV is required [17, p. 479]. With that information, the signal expressed in number of electrons, can be related to the output of the CBC2 in V_{Cth}. Finding the amount of signal that a V_{Cth} unit corresponds to for a given CBC, is the main topic of this chapter. From here on, this will be referred to as the V_{Cth} calibration.

The main goal is to develop a technique that can be easily repeated for many modules in a laboratory, so that during the production phase, most CMS Phase-2 Outer Tracker Modules can be calibrated. Fluorescent X-ray emmission of metals can be used, because it has a very narrow energy distribution and it is easily produced [48]. In our setup, fluorescent light is obtained by exiting a target of pure metal with primary X-rays of sufficient energy, obtained with a cathode tube. The secondary fluorescent X-rays of interest, are those deriving from the

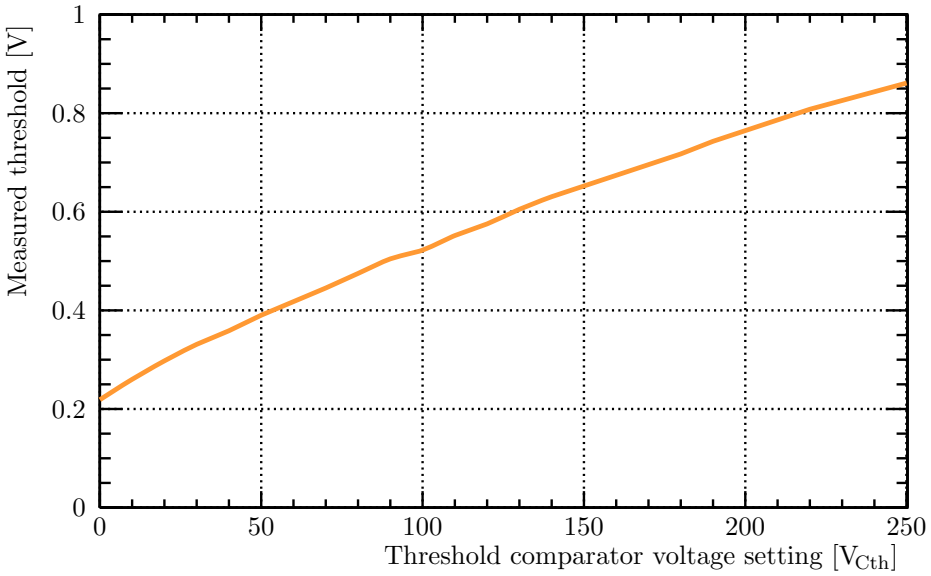

Figure 2.1. *Measured threshold comparator voltage in* mV *versus the threshold comparator voltage setting in* V_{Cth}*, of a CBC2 chip [47].*

L-to-K shell transition, the Kα line. By choosing a few different materials, it is possible to measure the calibration curve.

Measuring photons is complicated because they can not be triggered on by an external trigger detector. It is common practice to trigger on particles with scintillating materials and a Photomultiplier (PM) [49] before or after they hit the silicon. A PM converts the light signal from the scintillating material into an electrical signal. If the photon interacts with a material it will be fully absorbed, thereby making it impossible to trigger on it.

This is resolved by the use of the internal trigger of the firmware with which the CBC2 mini module is read out. Every 100 µs a trigger is send to the CBCs, forcing them to transmit their data. Since the exact arrival time of the photons in not known, this triggering happens randomly with respect to arrival of the incoming particles. As a trigger defines an event, most of the events will therefore not contain any hits. To compensate for the random triggering, millions of events need to be taken to gather enough statistics, as number of hits N_H, is the occupancy multiplied by the number of events N_E obtained, and in this case the occupancy is in the order of 1×10^{-5}.

A constant source of Kα photons can be established when illuminating a pure material with X-rays from commercial cathode tubes. In this case, a Phywe XR 4.0 Expert Unit is used, which is displayed in Figure 2.2. On the left side, the wolfram X-ray tube is sitting in a protective enclosure. It has a nominal operating voltage of 35 kV at 1.0 mA. An aperture in the enclosure allows for the primary X-rays to travel to the experimental chamber of the unit, which is displayed in Figure 2.3. A collimator can be placed inside this aperture to select the photons that travel straight ahead. However, the inner diameter of the aperture is 2 mm^2, so photons leaving the X-ray enclosure at an angle less than $\sim 3^\circ$ will not be stopped by the collimator.

Inside the box, a metal foil is mounted on a block, at 45° with respect to the incoming photons from the X-ray source. This is visible slightly to the left of the center Figure 2.3. Therefore the Kα photons are produced at a 90° angle with respect to the incoming photons

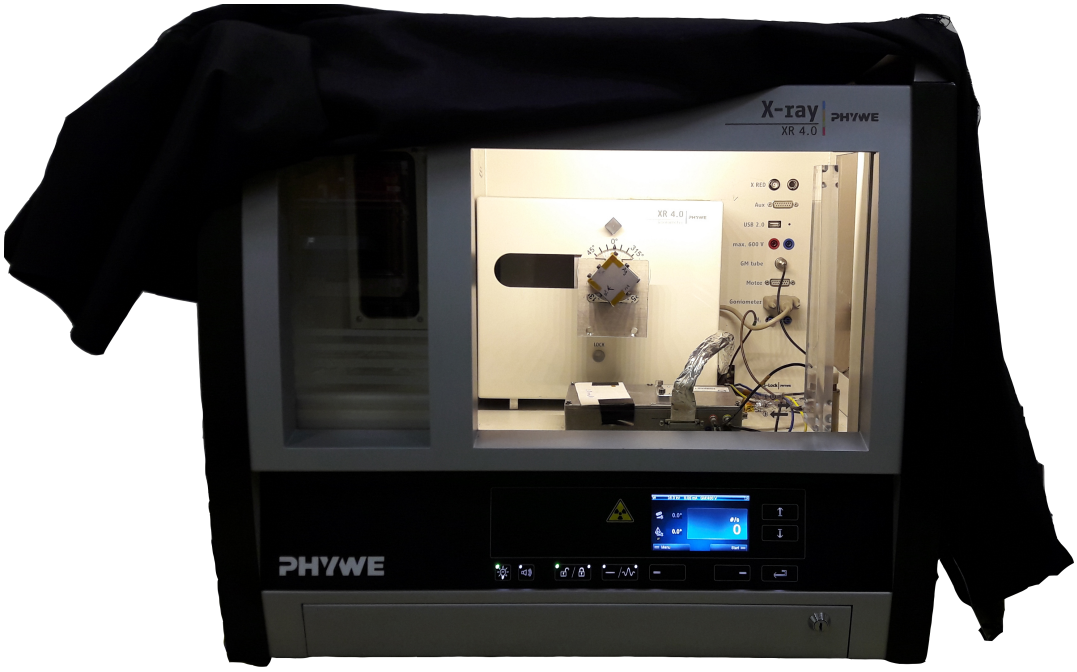

Figure 2.2. *The Phywe XR 4.0 Expert Unit with X-ray light source used for the threshold calibrations.*

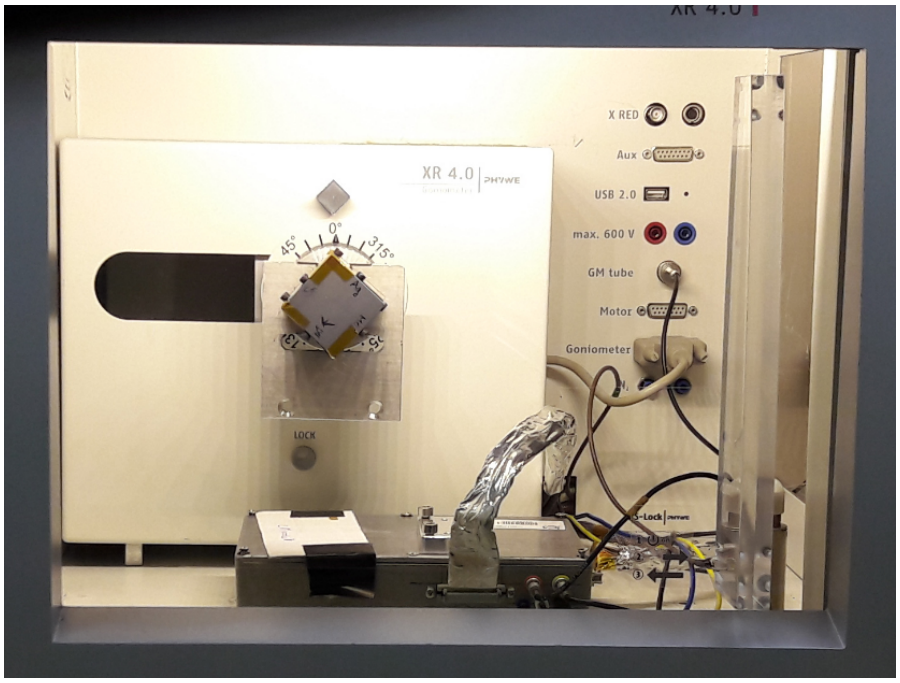

Figure 2.3. *The experimental chamber of the Phywe XR 4.0 Expert Unit unit.*

from the tube. A CBC2 mini module is placed on the bottom of the experimental chamber, such that its sensors, one on top of the other, are illuminated by the resulting Kαs.

For the V_{Cth} calibration, four different metals were selected to generate the Kα photons; zinc, molybdenum, silver and tin. Each metal delivers Kα photons of different energy as summarized in Table 2.1. These low energy photons with $E_\gamma < 100\,\text{keV}$, lose their energy through the photo-electric effect [17, p. 452-455]. The photon rates in the table are a result of past experience with the same system. They were measured during the qualification of CMS Pixel modules [50].

Table 2.1.
Properties of metal foils used to calibrate a CBC2 mini module.

Metal	**Symbol**	**Photon flux [50]** Φ_{photon} kHz cm^{-2}	**Photon energy [51]** E_{photon} keV	**Attenuation factor [52]** μ cm^2 g^{-1}	**Signal in silicon** S ke
Zinc	Zn	130	8.64	54.83	2.40
Molybdenum	Mo	100	17.48	7.425	4.86
Silver	Ag	45	22.16	3.807	6.16
Tin	Sn	20	25.27	2.866	7.02

Due to the binary output of the CBC chip, a range of V_{Cth} units has to be scanned in order to find the threshold setting that relates to the input signal, see Section 2.3.2. When scanning the threshold, it is as if an integration over the signal and the noise is performed. When looking at the number of clusters per even the expected result is therefore a double S-curve shape.

When going from low to high threshold first the noise dominates. This manifests itself as the first plateau of the number of clusters per event graph. Once the threshold is above the noise level, the signal takes over and a second plateau is detected. The scan is continued and a threshold is found from which point forward the signal is not detected anymore; the cluster rate is zero. That threshold matches the signal which can be expressed in number of electrons that are equal to that V_{Cth}. Depending on whether there is charge sharing between the strips of the silicon sensors or not, this will either be a gradual (charge sharing) or a sharp transition (no charge sharing). This is described in Section 2.3.5.

The results of the threshold scans with all four metals were plotted in a graph, where the number of electrons corresponding to a signal is shown versus the threshold in V_{Cth}; a linear relation was found. This is because the signal is proportional to the energy deposited in the sensor, by a factor 3.67 [17, p. 479]. By fitting a line to the points in the graph the number of electrons per V_{Cth} was obtained, which is the V_{Cth} calibration value that is sought after. This is the subject of Section 2.3.6. Since the CBC2 mini module used for the measurements in this chapter has only two CBCs, data from threshold measurements with a full-size CBC2 module (16 chips) were investigated, which is described in Section 2.3.7.

To study the calibration results in more depth, a simple toy Monte-Carlo simulation was used which is presented in Section 2.4. Then, in addition to the Kα photons, another particle source which easy to handle in a laboratory, was tested to explore its potential for V_{Cth} calibrations, namely an $^{241}_{95}$Am source. $^{241}_{95}$Am emits gamma radiation with an energy of 60 keV. First, the simulation is used to predict the results from the threshold scans. Based on the simulation that showed that the $^{241}_{95}$Am signal can be detected by the mini module at $75\,V_{Cth}$, a threshold scan was completed with the CBC2 mini module while it was being exposed to the photons from an $^{241}_{95}$Am source. With the results of this measurement the toy Monte-Carlo model was further developed, Section 2.5.4.

A comparison between the two calibration signals follows in Section 2.6, before the same calibration is discussed in light of the CBC3 chip (Section 2.7). The conclusions from these laboratory tests are written down in Section 2.9.

2.1.1. The CBC2 mini module

The module used during these tests is a 2CBC2 mini module, module number 4 produced at CERN. A picture of this module is given in Figure 1.17 on Page 17.

Before use, the CBC's offset settings for individual channels must be tuned, which is referred to as trimming, see Section 1.6.2. Protocols exist in the Ph2_ACF middleware framework, that tune the offsets to assure that each channel has the same response to the same signal [42]. Afterwards, an S-curve measurement is carried out to determine the noise and the pedestal. Because the noise of the mini module is a result of many different independent processes, it can be approximated by a Gaussian distribution of which the cumulative distribution is an error function. By scanning the threshold, and computing the amount of clusters per event, an integration over the noise is obtained and the resulting graph has an S-shape. The pedestal and noise are defined as the turn-over point and the width of the curve respectively. They are retrieved from the scan by fitting an error function and extracting the parameters.

The measured results for the pedestal and noise per CBC2 are shown in Figures 2.4a and 2.4b. Shown are the distributions for all channels connected to the respective CBCs. The offsets are properly tuned because the pedestal distribution peaks around $120\,\mathrm{V_{Cth}}$ and the noise between $2\,\mathrm{V_{Cth}}$ and $3\,\mathrm{V_{Cth}}$.

The mini module is designed to work at a clock frequency of 40 MHz. With the particle rates given in Table 2.1 an estimation can be made, of how many events need to be taken to measure roughly 100 photons in each strip.

Taking the dimensions of the strips of $5\,\mathrm{cm} \times 90\,\mu\mathrm{m}$ into account, with the tin metal foil in the primary X-ray beam the particle rate $R_{\mathrm{sn,strip}}$ in a strip is

$$\begin{aligned} R_{\mathrm{sn,strip}} &= \Phi_{\mathrm{sn}} \cdot A_{\mathrm{strip}} \\ &= 20\,\mathrm{kHz\,cm^{-2}} \cdot (5\,\mathrm{cm} \times 90\,\mu\mathrm{m}) = 0.9\,\mathrm{kHz} \end{aligned} \tag{2.2}$$

where A_{strip} is the area of the strip and Φ_{sn} the tin fluorescent photon flux. Therefore the probability $P_{\mathrm{sn,strip}}$ of detecting a hit, given the system's clock frequency f_{clock}, is

$$\begin{aligned} P_{\mathrm{sn,strip}} &= \frac{R_{\mathrm{sn,strip}}}{f_{\mathrm{clock}}} \\ &= \frac{0.9\,\mathrm{kHz}}{40\,\mathrm{MHz}} = 2.25 \times 10^{-5} \end{aligned} \tag{2.3}$$

Then the time t_{100} it takes to measure a hundred photons in a strip at a trigger frequency ν of 10 kHz, is given by

$$t_{100} = 100 \cdot \frac{1}{\nu} \cdot \frac{1}{P_{sn,strip}} \tag{2.4}$$

$$\begin{aligned} &= 100 \cdot \frac{1}{10\,\mathrm{kHz}} \cdot \frac{1}{2.25 \times 10^{-5}} \\ &= 4 \times 10^{2}\,\mathrm{s} \end{aligned} \tag{2.5}$$

Using the same equations for the other metals, it is computed that each step in a threshold scan with fluorescent photons takes 2×10^2 s, 8×10^1 s and 7×10^1 s for silver, molybdenum and zinc respectively.

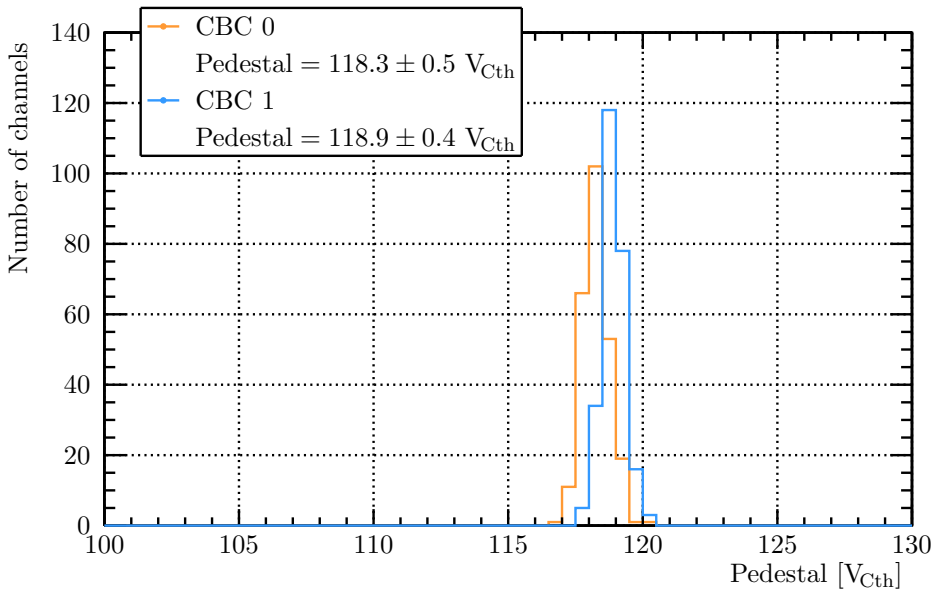

(a) *Pedestal.*

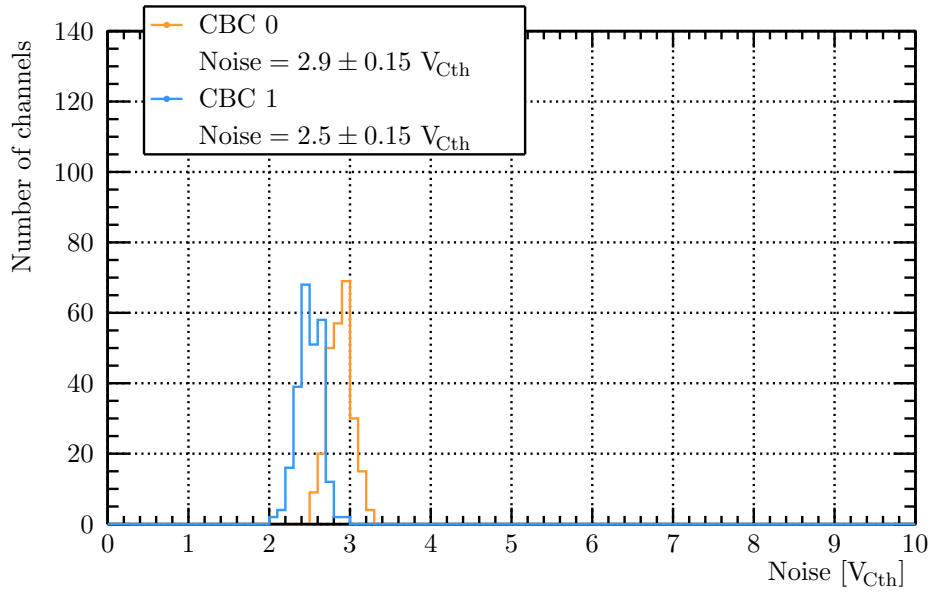

(b) *Noise.*

Figure 2.4. *Pedestal and noise distributions in* V_{Cth}*, for each of the two CBC2s in the mini module.*

2.2. Noise and background scans with X-ray source

The first two threshold scans with the CBC2 mini module are reference measurements of the noise and the background. The noise was measured when the X-ray source was turned off. The background was measured with the source turned on, but without a metal foil installed in the primary X-ray beam.

The noise scan is plotted in Figure 2.5, where number of clusters per event is given versus the threshold comparator voltage setting in V_{Cth}. Each color represents a combination of one

of the sensors with one of the two CBCs. It is important to note that high V_{Cth} values result in a low threshold, because the signal coming from the strips is a negative pulse.

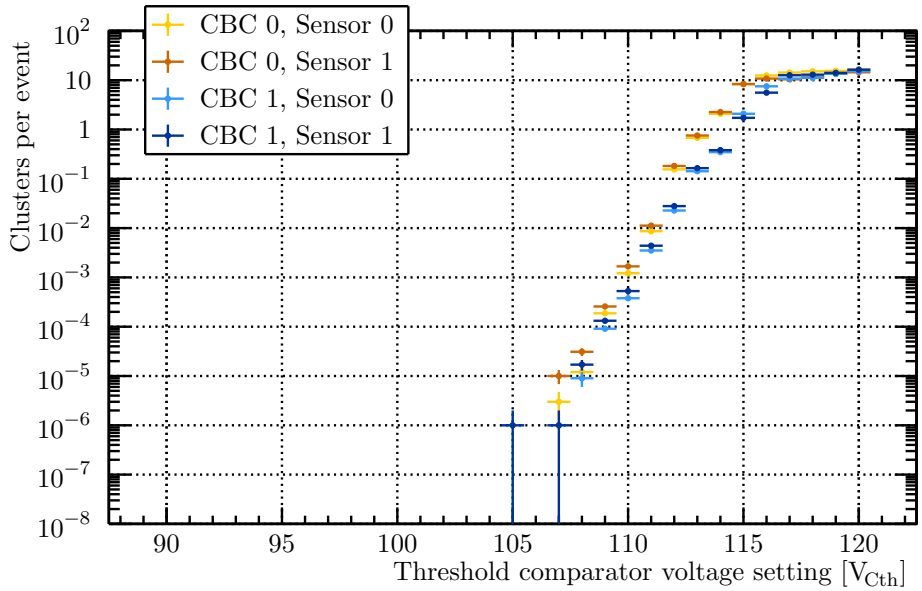

Figure 2.5. *Measured number of clusters per event versus threshold for a V_{Cth} scan with a CBC2 mini module without a signal present.*

This noise threshold scan is analogous to the S-curve measurement presented in Section 2.1.1. In Figure 2.5 however, the S-curve shape with a pedestal of $\sim$118 V_{Cth} is not clearly visible. Instead, an early plateau around 115 V_{Cth} is observed. This is a result of the CBC2 not being designed for high occupancy data; when the occupancy approaches 20 % the CBC2 starts to behave unpredictably due to cross-talk between its channels. It happens in the noise region between 115 V_{Cth} and 120 V_{Cth}, where the threshold is low. This is circumvented in the Ph2_ACF framework by measuring the S-curves in groups of eight readout channels at a time, so that there can never be more that eight hits per event.

In Figures 2.6 and 2.7 threshold scans with background X-rays are shown, with and without the collimator installed in the aperture of the Phywe XR 4.0 Expert Unit unit respectively. Since there is no metal foil installed, these are primary X-rays that are produced by the cathode tube, they are not Kα photons. The necessity of the collimator is clearly demonstrated here, as the primary X-ray number of clusters per event goes up to a level comparable to the fluorescent photon rate, when it is not installed. Consequently, for the threshold scans with the metal foil in place the collimator was used. The background in Figure 2.6 will be subtracted from the signal in Section 2.3.4.

2.3. Results of the threshold scans

In this section the threshold scans with Kα signals are analyzed and it is explained how the V_{Cth} calibration curve was obtained.

2.3.1. Sensor illumination

In Section 2.2 the threshold scan measurements are split in groups of CBC-sensor combinations. In order to verify that individual channels do not have to be treated separately, the uniformity

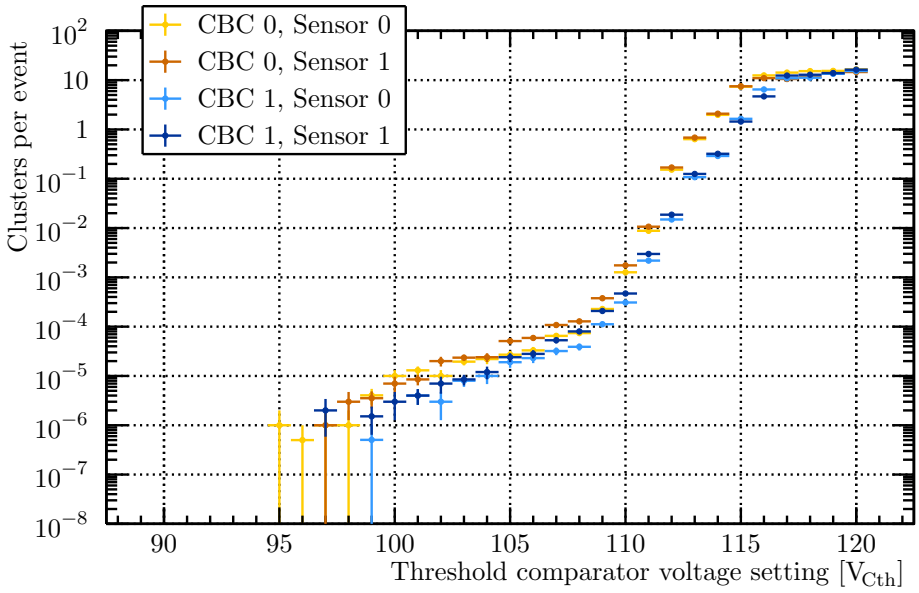

Figure 2.6. *Measured number of clusters per event versus threshold for a* V_{Cth} *scan with a CBC2 mini module that was exposed to background X-rays, with collimator.*

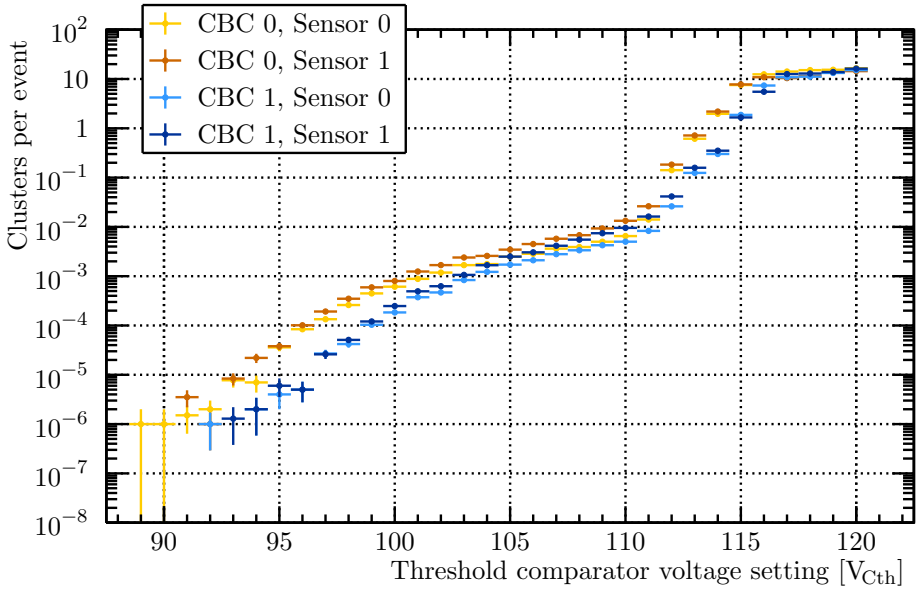

Figure 2.7. *Measured number of clusters per event versus threshold for a* V_{Cth} *scan with a CBC2 mini module that was exposed to background X-rays, without collimator.*

of the sensor illumination by the Kα photons was examined. Figure 2.8 gives the total hit count of one run in the threshold scan with tin Kαs, at 110 V_{Cth}. The yellow curve is for Sensor 0, the blue curve for Sensor 1. The first 127 strips of both sensors are wire-bonded to CBC 0 and the others to CBC 1.

Figure 2.8 shows that the sensor was uniformly illuminated by Kαs, and thus the channels in a CBC-sensor group can all be treated together. This was further cross-checked by computing the signal threshold for each individual channel, see Section 2.3.8. There is a difference in the amount of hits that was detected by the two different CBCs. Because there is a sharp edge in Figure 2.8 between CBC 0 and CBC 1, this is not due to a different particle hit rate, but rather to a different chip response caused by the 130 nm technology. The difference in hit count between the sensors is due to the attenuation factor of X-rays in silicon. More on that follows in Section 2.3.2.

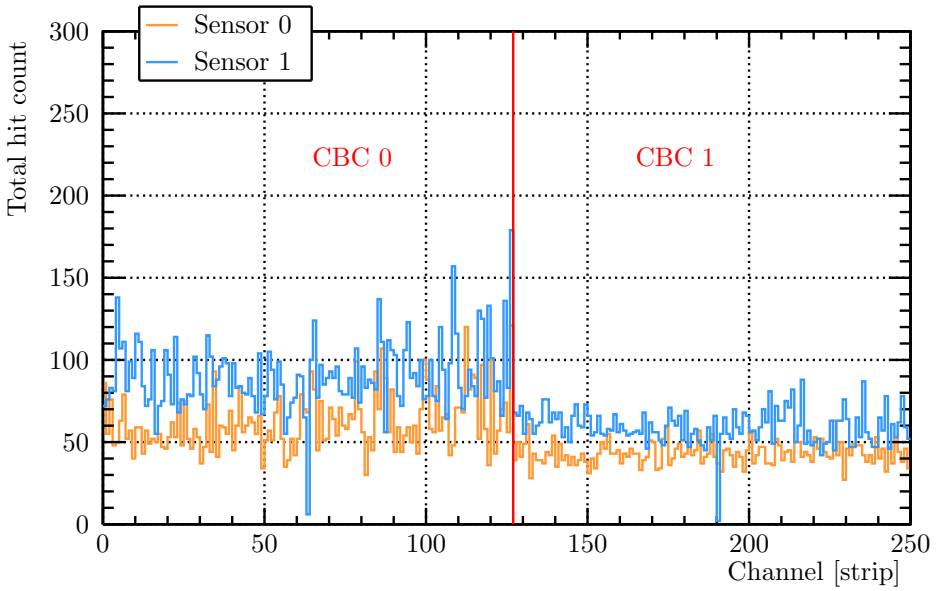

Figure 2.8. *Total hit count per strip in the CBC2 mini module at* 110 V_{Cth}*, while it was being illuminated by fluorescent radiation from a tin foil, irradiated by X-rays.*

2.3.2. number of clusters per event versus threshold

Figures 2.9 to 2.12 present the threshold scans with the four different metals zinc, molybdenum, silver and tin. As for the noise and background scans, the colors indicate which CBC-sensor combination is concerned.

Between 120 V_{Cth} and 110 V_{Cth} the noise of the module overshadows the signal, and compares to Figure 2.5. From 110 V_{Cth} downward, the signal takes over, corresponding to the second plateau in the curves. The signal can be distinguished from the background by comparing measurements done without target, shown in Figure 2.6. When the threshold continues to go up, with decreasing V_{Cth}, the number of clusters per event gradually goes down. If there would be no charge sharing between the strips of the module, the number of clusters per event would abruptly drop to zero when the threshold passes the signal energy. As a result it can be concluded that the strips of the sensors do share charge as expected. This effect was also modeled in a dedicated simulation presented in Section 2.4.

The scans are shown from low to high Kα photon energy, see Table 2.1. When looking at the V_{Cth} axes, the higher the signal energy, the lower the V_{Cth} unit at which the number of clusters

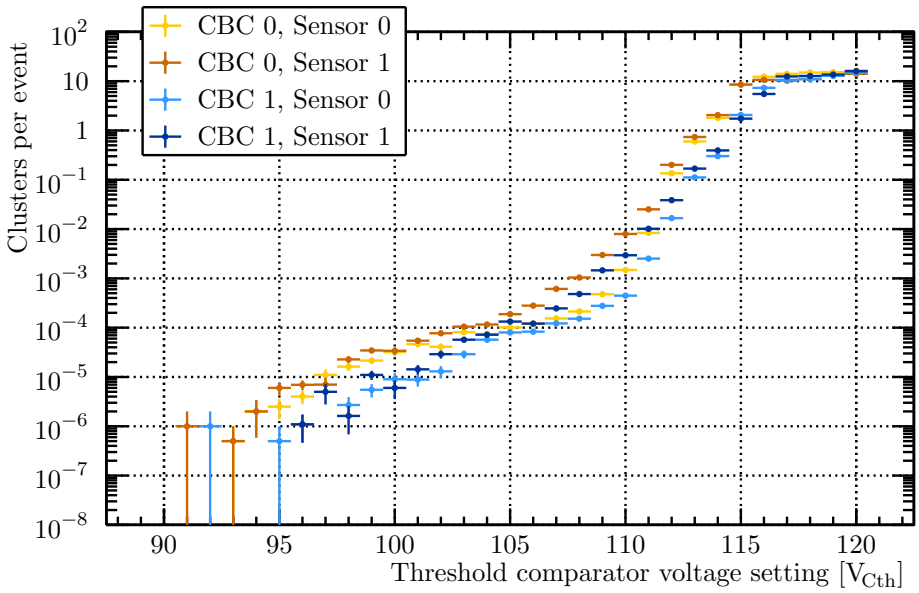

Figure 2.9. *Measured number of clusters per event versus threshold for a* V_{Cth} *scan with a CBC2 mini module, that was exposed to fluorescent radiation from a zinc foil being irradiated by the primary X-rays.*

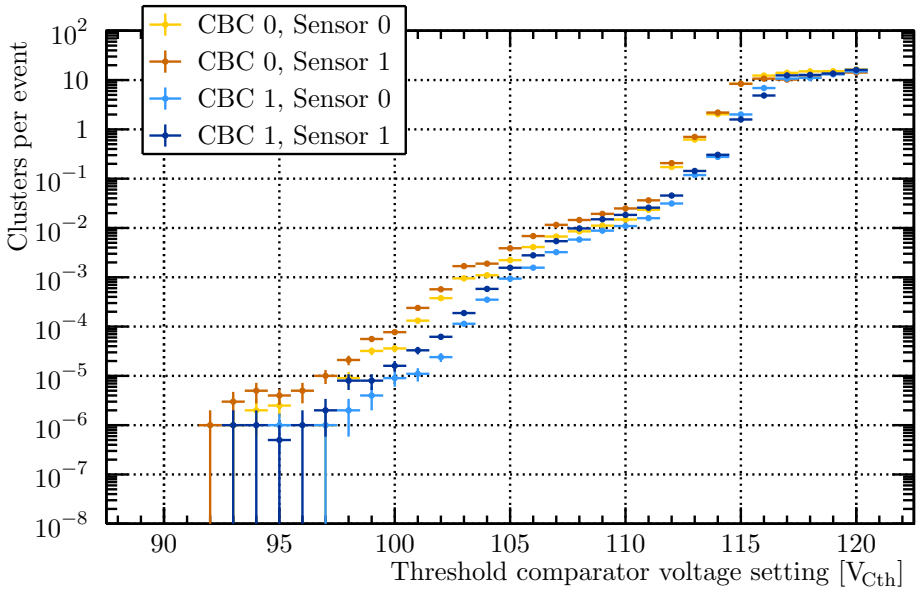

Figure 2.10. *Measured number of clusters per event versus threshold for a* V_{Cth} *scan with a CBC2 mini module, that was exposed to fluorescent radiation from a molybdenum foil being irradiated by the primary X-rays.*

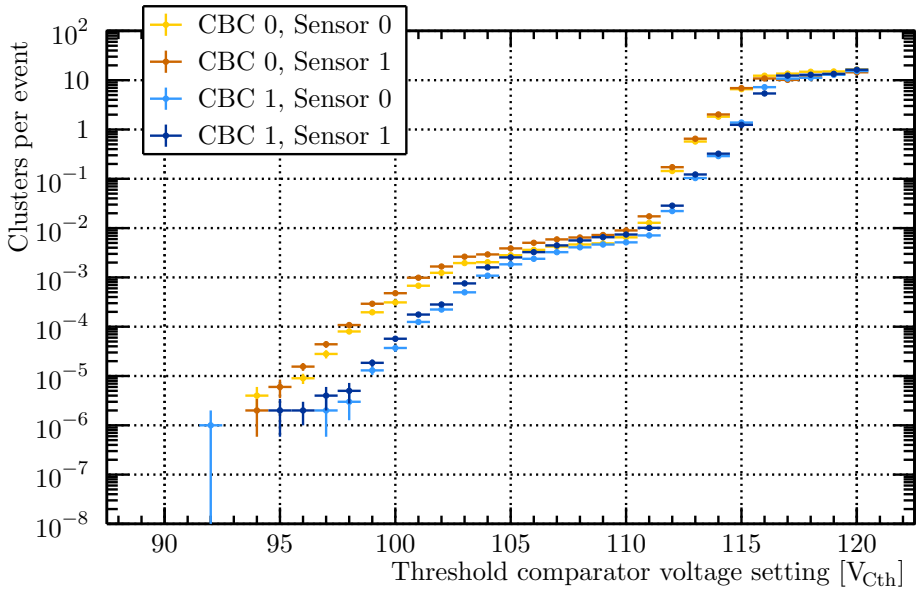

Figure 2.11. *Measured number of clusters per event versus threshold for a* V_{Cth} *scan with a CBC2 mini module, that was exposed to fluorescent radiation from a silver foil being irradiated by the primary X-rays.*

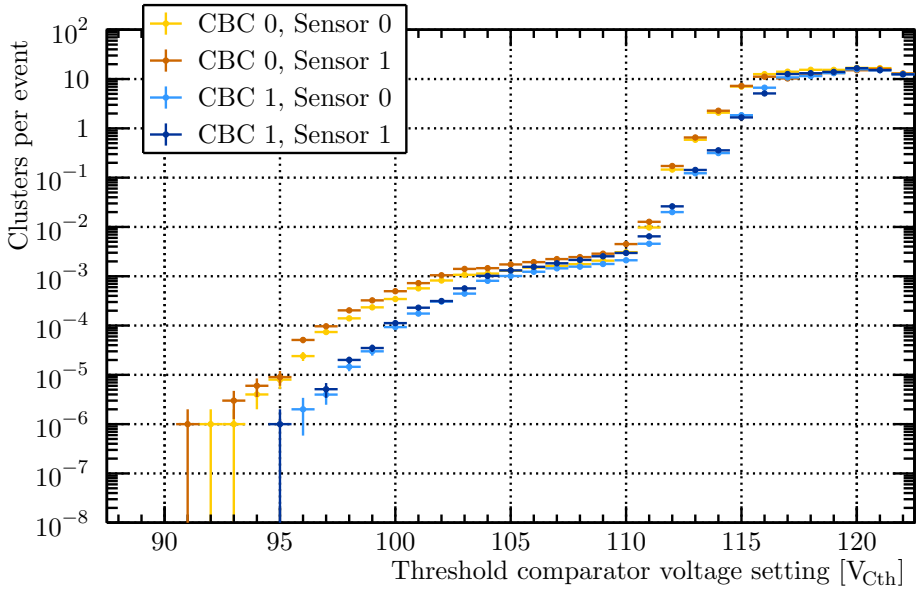

Figure 2.12. *Measured number of clusters per event versus threshold for a* V_{Cth} *scan with a CBC2 mini module, that was exposed to fluorescent radiation from a tin foil being irradiated by the primary X-rays.*

per event goes to zero, as can be predicted. Table 2.1 also dictates, that the photon rate is highest for zinc's Kα photons and is roughly inversely proportional to the photon energy. This manifests itself in the plots as the height of the second plateau. The higher the Kα rate, the higher the number of clusters per event at the plateau.

In the case of zinc however, Figure 2.9, there is no clear second plateau visible. Moreover, the data approximates the background scan of Figure 2.6, although the V_{Cth} at which the mini module stops measuring signal seems to be higher by circa $7\,V_{Cth}$. The relatively long tail of the zinc data compared to the background scan might be explained by the X-rays being reflected by the zinc metal foil, but the detailed modeling of this effect is outside the scope of this thesis. From this plot it seems the signal of zinc is very close to the noise of the mini module and therefore it can not be seen. This is further confirmed by the toy Monte-Carlo model later in this chapter in Section 2.4. For that reason, zinc can not be used to find a calibration factor for the V_{Cth} in Section 2.3.6.

For each scan the curves for the two CBCs look different. Each CBC is wire-bonded to both sensors. Apart from the sensors positioned on top of each other, they are in principle expected to behave similarly, since the two chips come from the same production batch, are mounted on the same circuit and share the same power supply and reference voltage. However, due to the 130 nm technology chip difference of less than 10 % are normal.

The only difference in response between the two sensors, comes from the fact that the top sensor can shield the bottom sensor from a portion of the Kα photons. This can be quantified by looking at the attenuation factor of X-rays with the energies used in the measurement. For the 270 µm thick sensors in the module, the attenuation factor of tin photons is computed as

$$\begin{aligned} F_a &= \frac{\mu}{\rho} \cdot \rho \cdot d \\ &= 2.866\,\mathrm{cm}^2\,\mathrm{g}^{-1} \cdot 2.32\,\mathrm{g\,cm}^{-3} \cdot 270\,\mu\mathrm{m} \\ &= 0.180 \end{aligned} \tag{2.6}$$

where μ/ρ is the attenuation per density, ρ is the density of silicon and d is the thickness of the sensor. Similarly for silver and molybdenum this gives 0.238 and 0.465 respectively. When looking at the curves of for instance CBC 0 and Sensor 0 and CBC 1 with Sensor 0, the attenuation factor, which decreases with growing energy, can be observed. For the tin case, Sensor 0 has roughly a factor of 0.2 clusters per event less than Sensor 1.

2.3.3. Cluster size

In the previous section it is concluded that because of the lack of a sharp transition in the number of clusters per event at the signal threshold, there must be charge sharing between the strips. By looking at the average cluster size versus V_{Cth}, the charge sharing process can be better understood. This is shown in Figure 2.13, where the cluster size is given in number of strips.

Between $113\,V_{Cth}$ and $117\,V_{Cth}$ the cluster size increases, because at lower thresholds noise hits start to be likely enough that they merge into larger clusters. At the lowest threshold between $117\,V_{Cth}$ and $122\,V_{Cth}$, the cluster size reduces rapidly, due to the high noise occupancy at that regime, with the CBC2 being operated well outside of its specifications. For the remainder of the scan, the cluster size is constantly equal to one.

The cluster size as a function of V_{Cth} can be explained by a charge sharing model in which only a small fraction of the charge deposited in a strip, is going to the neighbors. Such that when the threshold is high, only the strip with the largest fraction of the charge is detected to have a hit. An illustration of this model is given in Figure 2.14a.

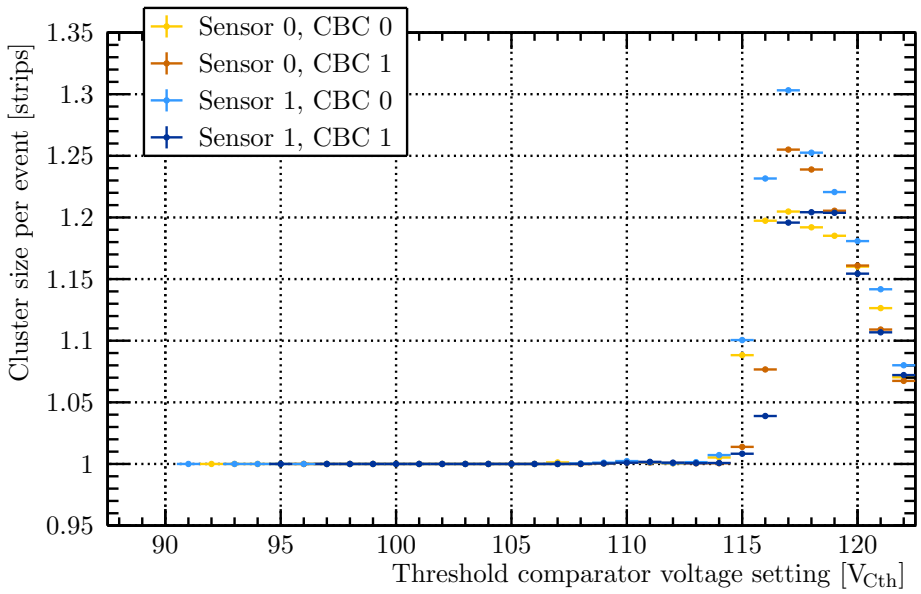

Figure 2.13. *Average cluster size versus threshold for a V_{Cth} scan with a CBC2 mini module while it was exposed to fluorescent radiation from a tin foil, irradiated by an X-ray source.*

The charge carrier dynamics in the sensor are quite complex and can be generally described with a simulation taking into account the electric field in the sensors, as well as the charge deposition by the ionizing particle and a model of the front-end amplifier. However, the general behavior can be reproduced with the following, drastically simplified model.

It can be assumed that when a particle hits exactly between two strips, the charge is shared evenly, and when it hits exactly below a strip implant there is no sharing. Between those two locations, the charge sharing is taken to decrease or increase linearly, as in Figure 2.14b. This model proves to be sufficiently accurate in the determination of the signal threshold which is demonstrated in Section 2.3.5. A more sophisticated charge sharing model is presented in Section 2.5.4.

(a) *Model 1.* **(b)** *Model 2.*

Figure 2.14. *Two different models for charge sharing between the strips of the CBC2 mini module.*

2.3.4. Subtracting the contribution from background radiation

As was measured with the background scan presented in Section 2.2, in addition to the Kα X-rays, background radiation is detected. The background should be removed from the signal before further analysis. The energy distribution of the primary X-rays is not precisely known and they cause an overestimation of the signal. Removing the background is achieved by

measuring the hit rates during a threshold scan, and then subtracting the background hit rates in Figure 2.6, bin by bin from each of the scans with the different metal foils.

The results of this procedure are shown in Figures 2.15 to 2.17. Taking into account that during the background scan it can not be avoided to measure the noise as well, the noise is also mostly removed from the scans. As in the case of silver, Figure 2.16, the data points in the noise region between 115 V_{Cth} to 120 V_{Cth}, have a large uncertainty, sometimes reflected in the estimated statistical error that is shown as error bars. The systematic error is also large in this region because between each measurement, the conditions may be slightly different, which is the root cause of systematic errors. This is not relevant for the measurement, as the noise region is well separated from the signal region.

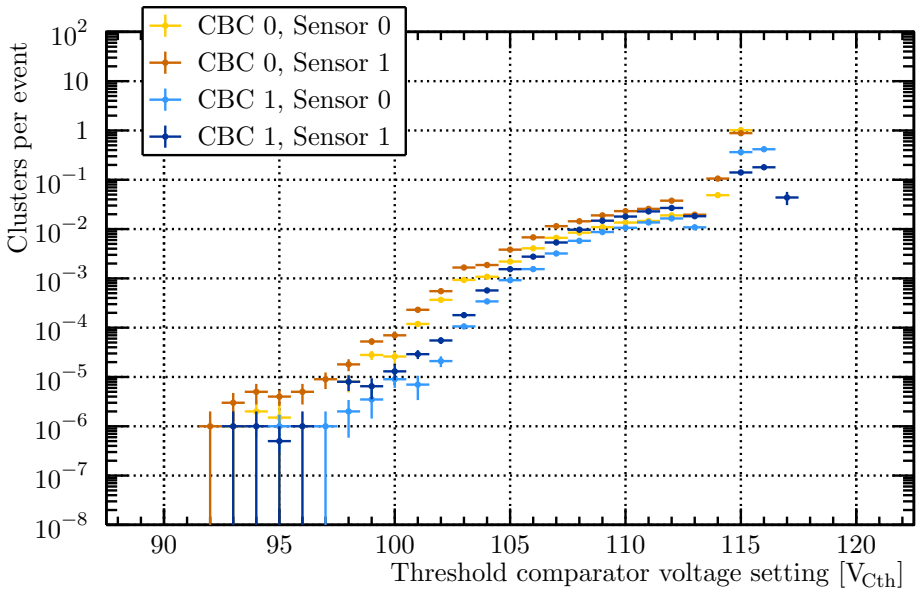

Figure 2.15. *The signal from fluorescent radiation of a molybdenum metal foil, that was irradiated by an X-ray source, measured by the CBC2 mini module.*

2.3.5. Finding signal thresholds for different Kα photons

Based on the observations in Section 2.3.2, it is concluded that the strips in the mini module share the charge that is released in the silicon by radiation. Consequently, there is no sharp drop in number of clusters per event observed when the threshold exceeds the signal, with the number of clusters per event gradually decreasing towards zero with the threshold approaching the limit value $V_{T,S}$.

To explain this phenomenon, a simple charge sharing model is adopted, illustrated in Figure 2.14b, which will be further discussed in Section 2.4.2. This model does not include noise and therefore the tail of the signal most be excluded from the fit. With this model, the signal threshold can be determined by fitting a linear function to the measured signal, before extrapolating the fit to find the threshold at zero number of clusters per event. This linear relation is given by

$$N_{\text{Clusters}}(V_T) = aV_T + b \tag{2.7}$$

where N_{Clusters} is the number of clusters for a given threshold V_T, a is the slope and b the offset.

In order to identify the fit limits with a well-defined procedure, a first linear fit is performed on each signal between 110 V_{Cth} and 115 V_{Cth}. Then the intercept with the threshold axis V_0

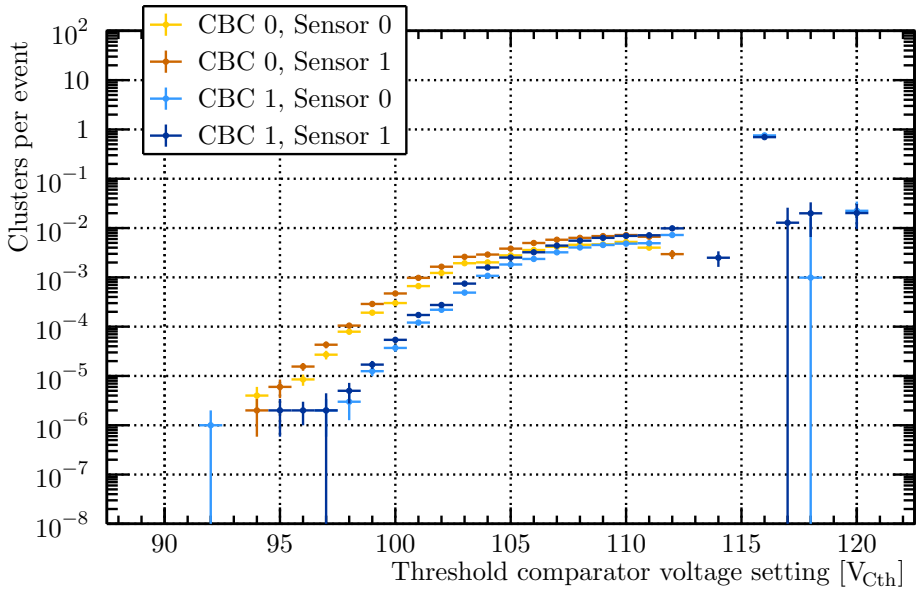

Figure 2.16. *The signal from fluorescent radiation of a silver metal foil, that was irradiated by an X-ray source, measured by the CBC2 mini module.*

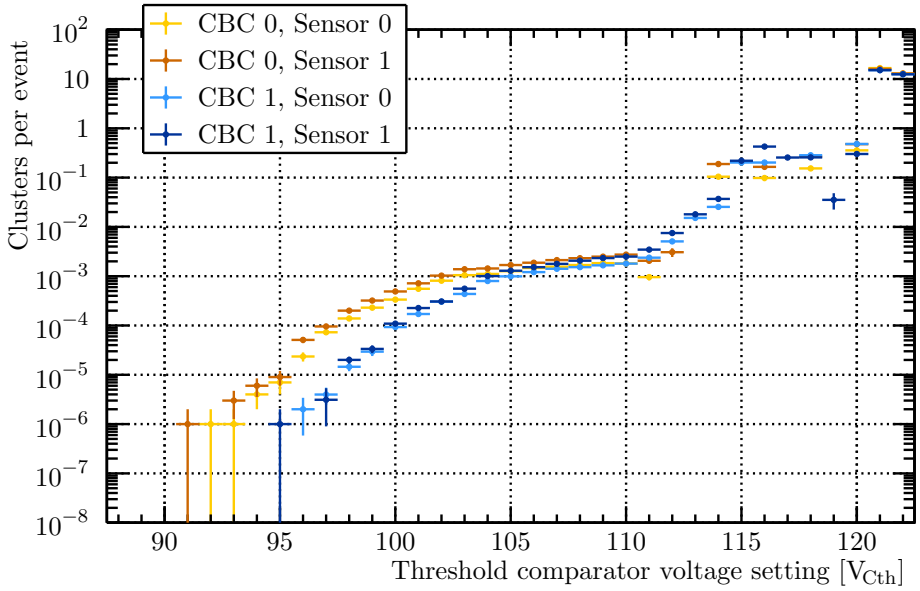

Figure 2.17. *The signal from fluorescent radiation of a tin metal foil, that was irradiated by an X-ray source, measured by the CBC2 mini module.*

is extracted, to estimate where the number of clusters per event goes to zero. Subsequently another fit is carried out between 110 V_{Cth} and the $V_0 + 2\,V_{Cth}$. The second fit is not carried up to V_0 because the noise in the signal is expected to smoothen the measured signal rate curves towards V_0. The distance of 2 V_{Cth}, corresponding to the measured noise, allows for neglecting this effect. The V_{Cth} intercept, $V_{T,S} = -b/a$, is the threshold value that corresponds to the signal.

For each metal the results of this second set of fits are shown in Figures 2.18 to 2.20 for CBC 0-Sensor 0. The error on the signal and background rates is taken to be given purely by statistics and governed by the Poisson distribution. It is then propagated to the distributions, which are fit here. It has to be noted that in the signal region, the contribution of the background is very small and therefore the error is mainly given by the signal measurements. All the results are summarized in Tables 2.2 to 2.4. For both CBCs, the results of the two fits, one per sensor that is wire-bonded to the CBC, are the same within the statistical uncertainties.

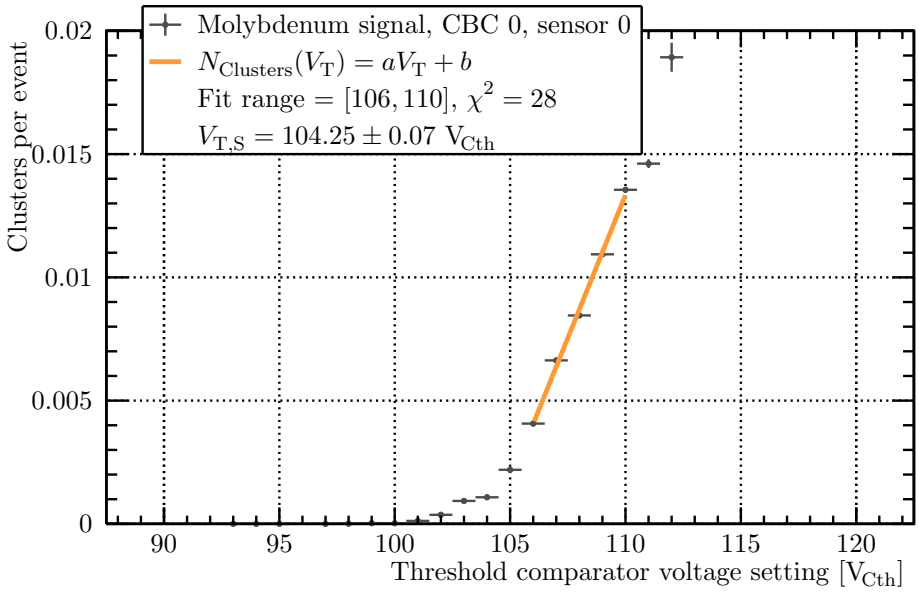

Figure 2.18. *Fitting a linear function to the molybdenum signal in Figure 2.15.*

Table 2.2.
Results of fitting a linear function to the molybdenum signal, that was measured by different CBC-sensor combinations.

CBC	**Sensor**	**Slope** a e/V_{Cth}	**Constant** b e	**x-intercept** $V_{T,S}$ V_{Cth}
0	0	$(2.32 \pm 0.04) \times 10^{-3}$	$(-2.42 \pm 0.04) \times 10^{-1}$	104.25 ± 0.07
0	1	$(3.96 \pm 0.05) \times 10^{-3}$	$(-4.13 \pm 0.06) \times 10^{-1}$	104.23 ± 0.05
1	0	$(2.52 \pm 0.03) \times 10^{-3}$	$(-2.67 \pm 0.03) \times 10^{-1}$	105.71 ± 0.03
1	1	$(4.29 \pm 0.04) \times 10^{-3}$	$(-4.53 \pm 0.04) \times 10^{-1}$	105.73 ± 0.025

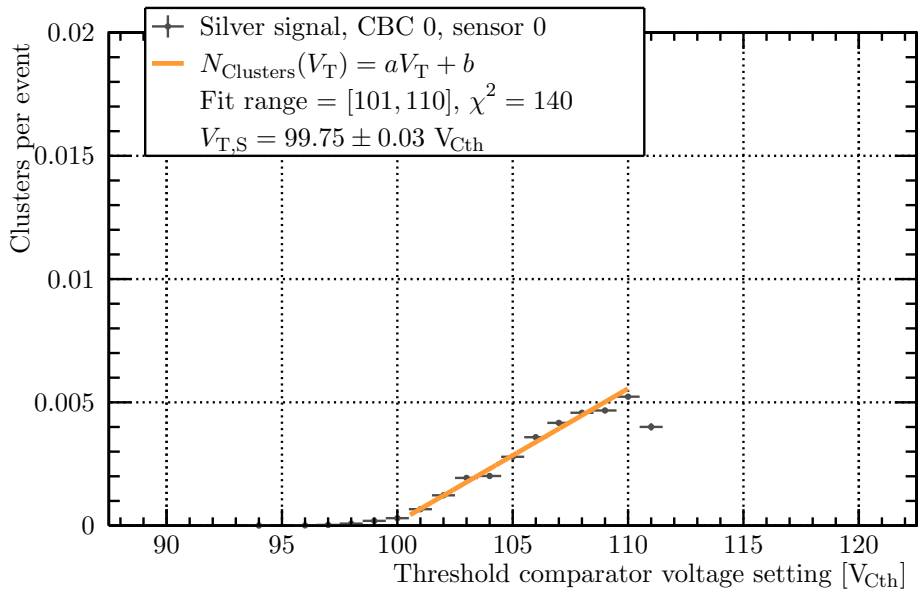

Figure 2.19. *Fitting a linear function to the silver signal in Figure 2.16.*

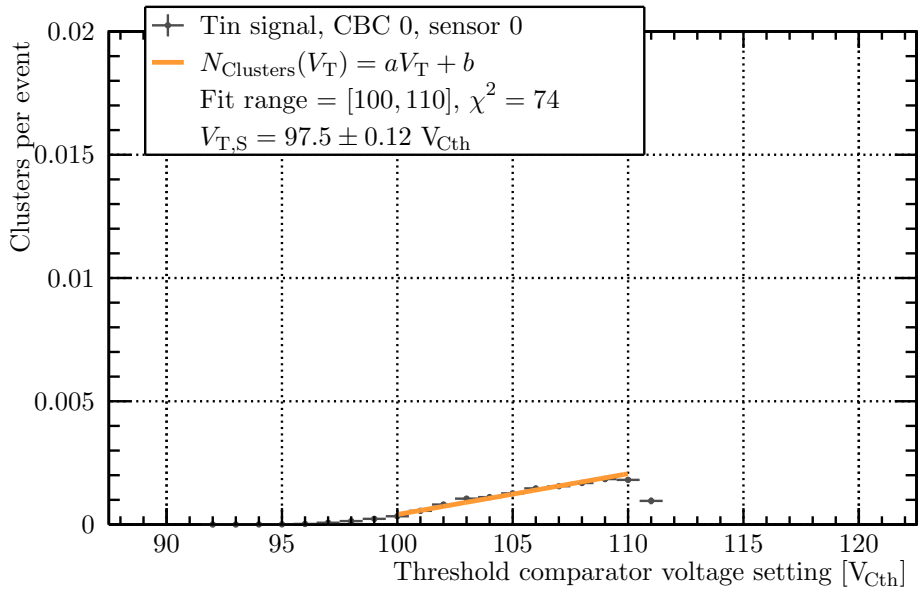

Figure 2.20. *Fitting a linear function to the tin signal in Figure 2.17.*

2.3.6. Estimation of calibration value for CBC2 threshold

The signal resulting from the photons expressed in number of electrons, as function of the signal thresholds found in the previous section, are plotted in Figures 2.21 to 2.24. A linear relation is found of which the slope c is the number of electrons generated in silicon that equals to one V_{Cth} unit. Each plot shows a different CBC-sensor combination. The fourth point in the plot is the pedestal that was measured with the Ph2_ACF, at zero signal. The yellow line is a linear fit to the data points, defined as

$$N_{\text{Electrons}}(V_{\text{T}}) = cV_{\text{T}} + d \tag{2.8}$$

Table 2.3.
Results of fitting a linear function to the silver signal, that was measured by different CBC-sensor combinations.

CBC	Sensor	Slope a $e/\mathrm{V_{Cth}}$	Constant b e	x-intercept $V_{\mathrm{T,S}}$ $\mathrm{V_{Cth}}$
0	0	$(5.42 \pm 0.05) \times 10^{-4}$	$(-5.40 \pm 0.05) \times 10^{-2}$	99.75 ± 0.03
0	1	$(7.62 \pm 0.05) \times 10^{-4}$	$(-7.60 \pm 0.87) \times 10^{-3}$	99.76 ± 0.06
1	0	$(6.62 \pm 0.07) \times 10^{-3}$	$(-6.77 \pm 0.14) \times 10^{-2}$	102.28 ± 0.095
1	1	$(9.50 \pm 0.16) \times 10^{-4}$	$(-9.73 \pm 0.17) \times 10^{-2}$	102.44 ± 0.08

Table 2.4.
Results of fitting a linear function to the tin signal, that was measured by different CBC-sensor combinations.

CBC	Sensor	Slope a $e/\mathrm{V_{Cth}}$	Constant b e	x-intercept $V_{\mathrm{T,S}}$ $\mathrm{V_{Cth}}$
0	0	$(1.65 \pm 0.03) \times 10^{-4}$	$(-1.61 \pm 0.03) \times 10^{-2}$	97.6 ± 0.12
0	1	$(2.26 \pm 0.04) \times 10^{-4}$	$(-2.21 \pm 0.04) \times 10^{-2}$	97.7 ± 0.10
1	0	$(1.80 \pm 0.22) \times 10^{-5}$	$(-1.79 \pm 0.23) \times 10^{-3}$	99.78 ± 0.04
1	1	$(2.40 \pm 0.26) \times 10^{-5}$	$(-2.40 \pm 0.26) \times 10^{-2}$	99.91 ± 0.04

where d is the maximum threshold, in electrons, that can be applied by the CBC. Values of both c and d are written in each of the legends of the graphs. Within the statistical uncertainty, the combination CBC 0-Sensor 0 has the same calibration factor as the combination CBC 0-Sensor 1. The difference between CBC 0 and CBC 1 are within the expected 10 % variation.

Since the original χ^2 of the fits was in the order of ∼40, it can be concluded that the uncertainties of each signal threshold were underestimated. This is due to the fact that the systematic errors of the threshold measurements are not used. Through the use of the normalized χ^2, a good estimation of the uncertainties on the calibration values c is made *a posteriori*.

The normalized χ^2 is obtained by performing a first linear fit and then multiplying by the χ^2 per degree of freedom. A second fit is then performed and shown here. By construction, the new $\chi^2 = 2$ equals the number of degrees of freedom.

In Figure 2.9, the zinc signal is not visible. With a calibration value of $335\,e\,{\mathrm{V_{Cth}}}^{-1}$ for CBC 0-Sensor 0, the noise measured in number of electrons, three sigma away from the pedestal, equals $2.88 \times 312 \times 3 \approx 2696$. A zinc photon releases $8640/3.6 \approx 2400$ electrons in silicon. Thus when the threshold is $3\,\sigma$ away from the noise at $111\,\mathrm{V_{Cth}}$, the zinc signal is not detectable, explaining the observations in Figure 2.9.

2.3.7. Variations in gain of different CBC2s

The strip-to-strip and chip-to-chip gain variation are both expected to be in the order of 10 %, due to the 130 nm CMOS technology used to produce the CBC2. To check whether the difference in $\mathrm{V_{Cth}}$ between CBC2s is within 10 %, data taken with a full size, sixteen CBC2 chips module was analyzed [53]. During those measurements, the $\mathrm{V_{Cth}}$ DAC setting was varied

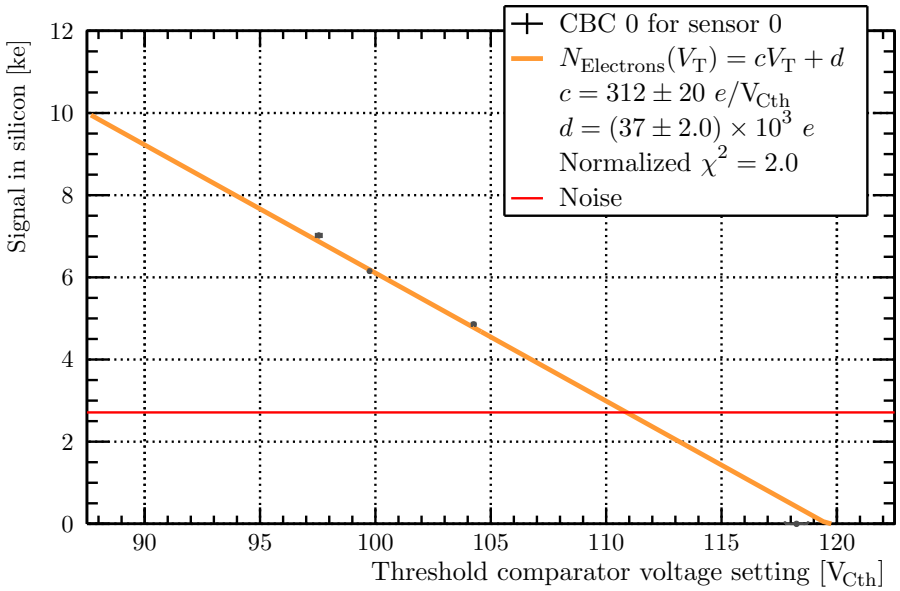

Figure 2.21. *Fitting a linear function to the signal thresholds, versus signal in the silicon sensors resulting from fluorescent radiation, for CBC 0 and Sensor 0.*

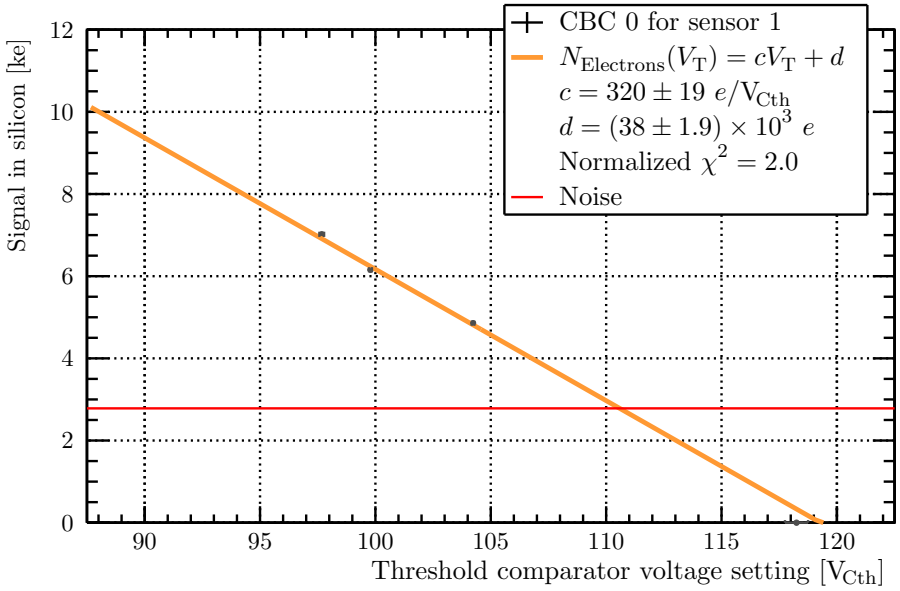

Figure 2.22. *Fitting a linear function to the signal thresholds, versus signal in the silicon sensors resulting from fluorescent radiation, for CBC 0 and Sensor 1.*

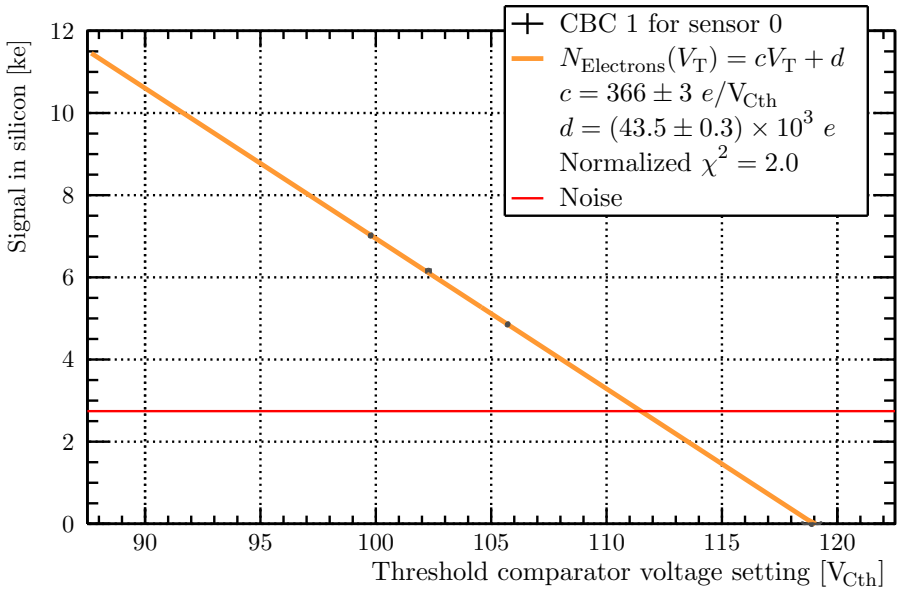

Figure 2.23. *Fitting a linear function to the signal thresholds, versus signal in the silicon sensors resulting from fluorescent radiation, for CBC 1 and Sensor 0.*

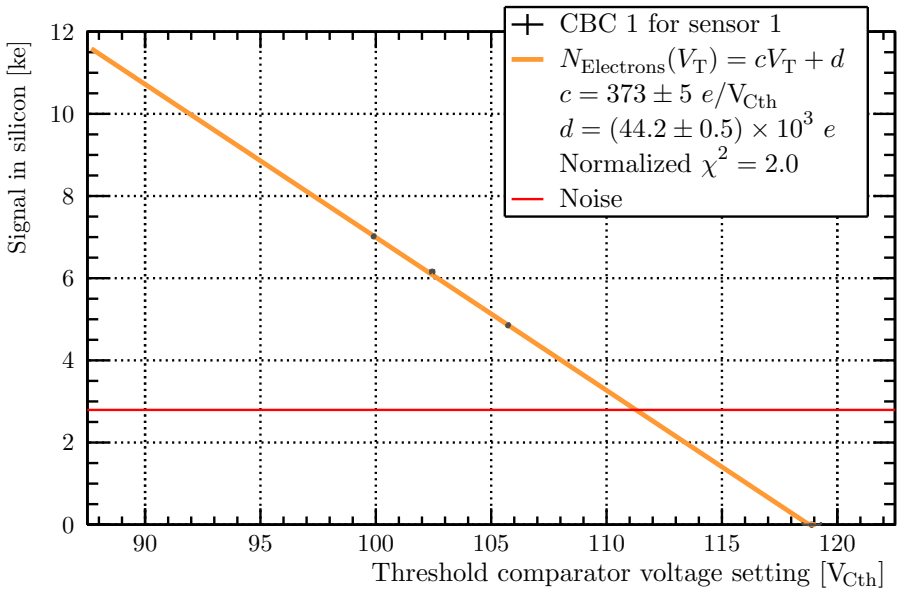

Figure 2.24. *Fitting a linear function to the signal thresholds, versus signal in the silicon sensors resulting from fluorescent radiation, for CBC 1 and Sensor 1.*

while the threshold voltage was measured, as shown in Figure 2.1. This measurement makes use of a testing feature present in the CBC2 that allows to probe the internal voltage of different lines, one at a time, on a pad of the chip by means of an internal analogue multiplexer [42]. This pad is wire-bonded to a dedicated line on the CBC2 hybrid. The measurements are shown in Figure 2.25, where each CBC2 is plot in a different color, the lines are linear fits to the data points.

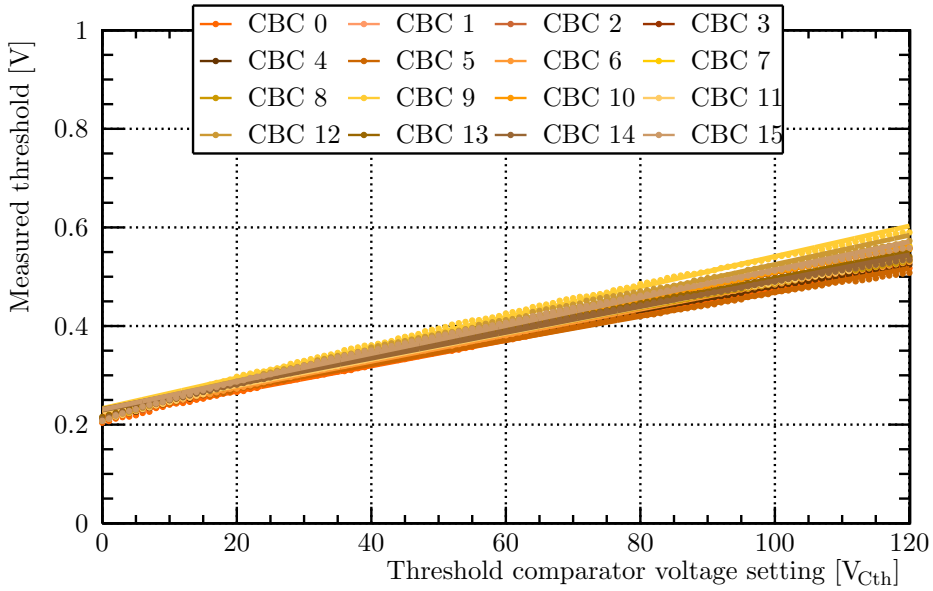

Figure 2.25. *Measured threshold comparator voltage versus threshold comparator voltage setting, for sixteen CBC2 chips in a full size CBC2 prototype module.*

The CBC2 was designed such that a V_{Cth} unit equals ~25 mV. For the sixteen CBC2 chips in the full size module, the average was found to be $(27.0 \pm 1.3)\,\mathrm{mV}\,{V_{Cth}}^{-1}$. Therefore, the difference is less than 10 %.

The residuals between the data points and the fit are also calculated for each CBC, and plotted in Figure 2.26. They are in the order of 1×10^{-4} and thus it can be concluded that the gain of the CBC2 is linear, especially for the region between 80 V_{Cth} and 100 V_{Cth} where the signals of the Kα photons are measured.

2.3.8. Results for single channels

For completeness, the data of the threshold scans are sorted by individual channels in Figures 2.27 to 2.29. These plots only show the signals detected by the different strips, the background is subtracted here. The red line is the threshold needed to suppress noise less than 3σ from the pedestal.

For each strip the signal threshold is determined using the same procedure as for the CBC-sensor combinations described in Section 2.3.5. The resulting distributions of the number of channels versus the signal threshold are given in Figure 2.30. Each color represents a different Kα photon. The same pattern is visible as in the other sections; the gain is different for the two CBCs. In the legend, the average and corresponding standard deviation for each distribution are written. It matches well with the data in Tables 2.2 to 2.4. The standard is a few percent, meaning that the strip-to-strip differences well below 10 %.

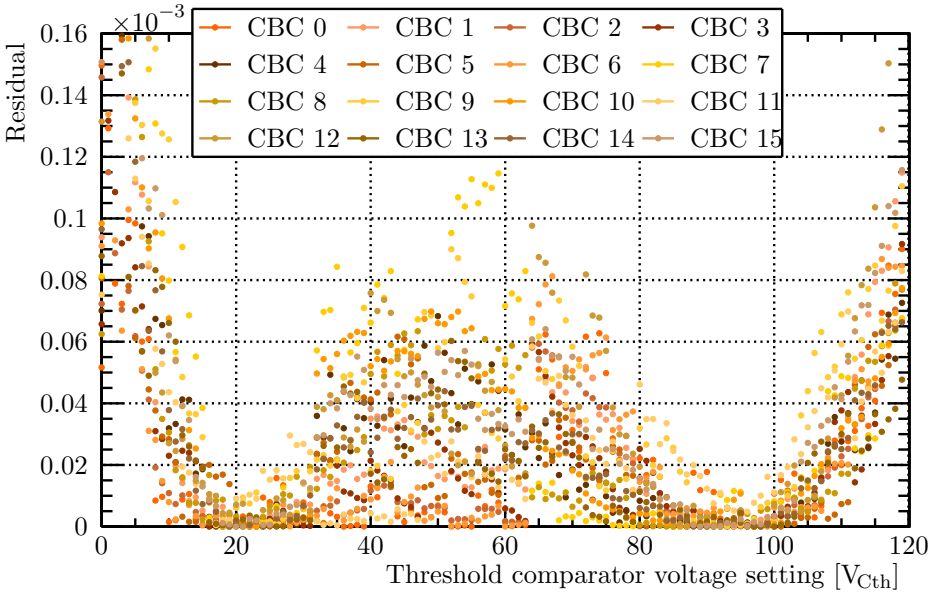

Figure 2.26. *Residuals of each threshold measurement shown in Figure 2.25, with respect to the fitted lines.*

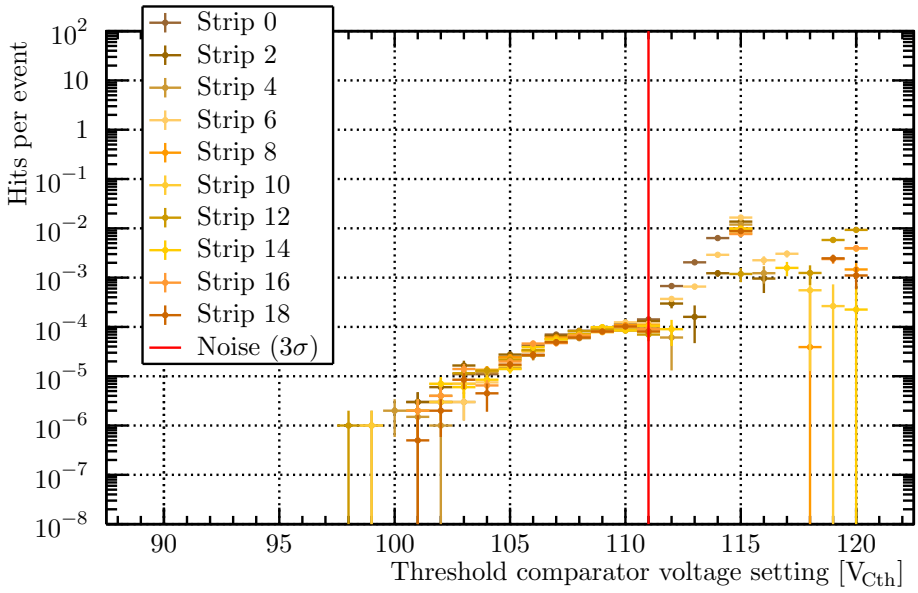

Figure 2.27. *Molybdenum signal in individual strips of the CBC2 mini module.*

2.4. Simulating the threshold scans

To better understand the measurements performed on the CBC2 chips, a simulation was developed with a simple toy Monte-Carlo model at the basis. For each simulated event the noise is modeled either by taking a Gaussian distribution, or by using the background distribution in Figure 2.6. For each strip, the code picks a value from the chosen distribution at random, which is the noise of that strip in that event. This is discussed in more detail in Section 2.4.1.

Based on the Kα energy, the signal in a strip of the CBC2 mini module is calculated and added to the noise. This is accomplished by working out the probability P_{hit} of the random

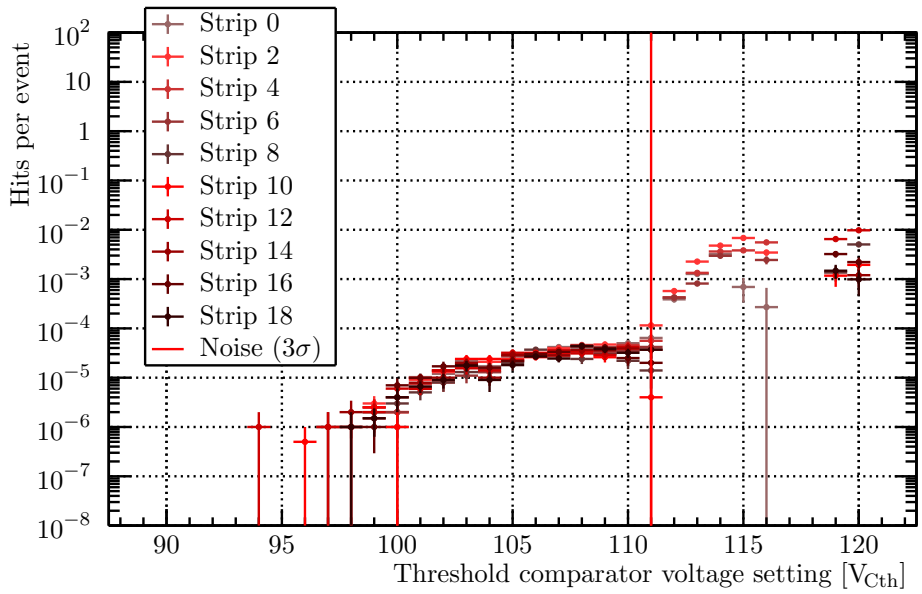

Figure 2.28. *Silver signal in individual strips of the CBC2 mini module.*

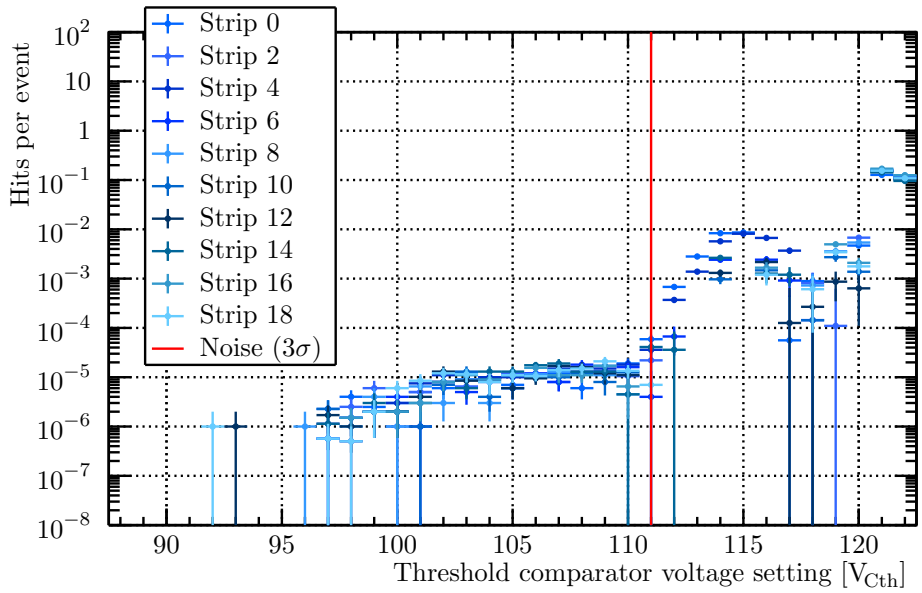

Figure 2.29. *Tin signal in individual strips of the CBC2 mini module.*

triggers coinciding with a signal as

$$P_{\text{hit}} = \frac{R_{\text{photons}}}{f_{\text{clock}}} \cdot d_{\text{strip}} \cdot l_{\text{strip}} \tag{2.9}$$

where R_{photons} is the photon rate given in Table 2.1, f_{clock} is the 40 MHz clock frequency of the CBC, d_{strip} is the strip pitch and l_{strip} the length of the strip. If P_{hit} is smaller than a random number between 0 and 1, the signal is triggered on and its amplitude is added to the noise that was selected before.

The height of the signal is also determined by the charge sharing. It is simply modeled by taking a random number between 0 and 1, and taking it as the charge sharing fraction.

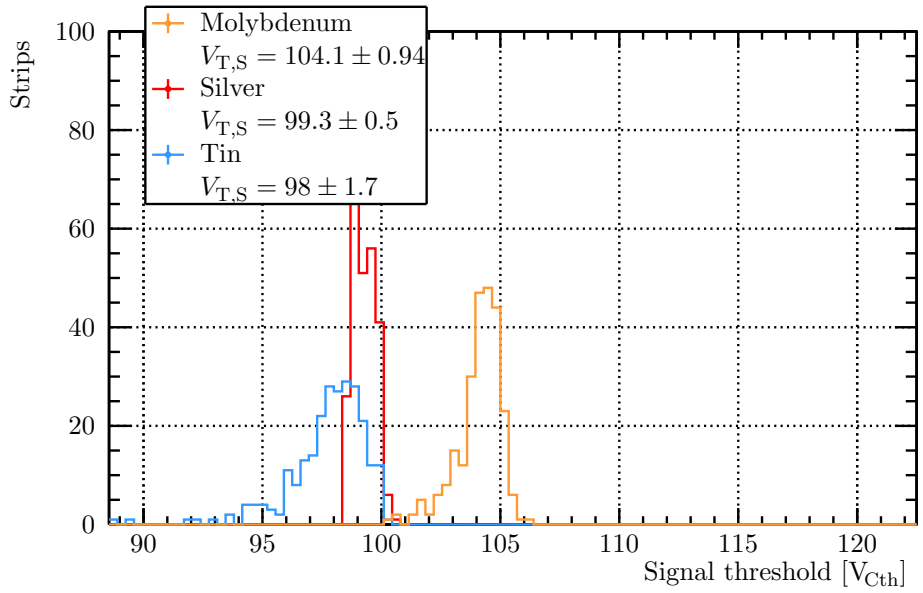

(a) *CBC0.*

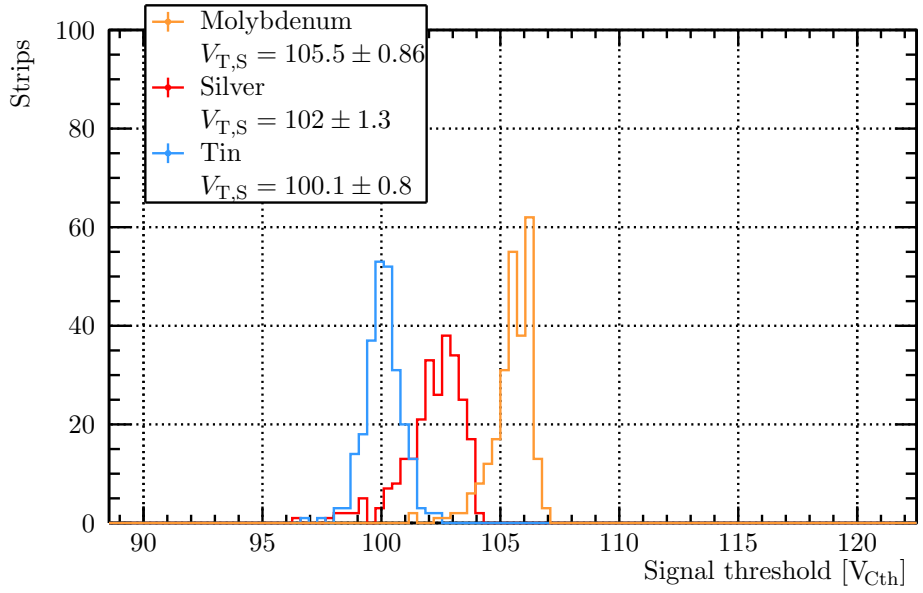

(b) *CBC1.*

Figure 2.30. *Number of channels versus the signal threshold in VCth units. The top plot shows all the channels in CBC 0 and the bottom plot is for CBC 1. The different colors represent the different fluorescent signals.*

Then the signal energy E_{signal} of the strip containing the signal, is multiplied by this fraction. The neighboring strip receives a signal of $E_{\text{signal}} \cdot (1 - F_{\text{chargesharing}})$, where $F_{\text{chargesharing}}$ is the charge sharing fraction. The difference between charge sharing and no charge sharing is further discussed in Section 2.4.2.

Finally the signal plus noise are compared to the threshold. If their sum is larger, a hit is registered. This is repeated a million times per V_{Cth}, until the scan is complete. The results of the different energy Kα photons are examined in Section 2.4.3. For completeness, the V_{Cth} calibration value obtained from the simulations is compared to the measured values in Section 2.4.4.

The input parameters of the simulation come from measurements with the CBC2 mini module, measurements with BPix modules and literature. The Gaussian distribution for the noise, has mean and sigma from the measurements in Section 2.1.1. The background is measured with the X-rays, Section 2.2, and the signal energies are taken from reference literature [51] and rates expected with various metal targets from measurements performed with the same equipment for the CMS Phase-1 Upgrade Pixel [54]. To convert the signal to a V_{Cth} value in the simulation, the calibration value measured on CBC 1-Sensor 1 is used. No simulation parameter was tuned to the data, except the background and noise signal distribution and the calibration of CBC 1-Sensor 1.

2.4.1. Simulation of noise and background

Figure 2.31 shows the results of simulating the noise in the CBC2 mini module in blue and the background simulation for when it is exposed to background X-rays from the Phywe XR 4.0 Expert Unit in orange. The measurements, previously shown in Section 2.2, are also shown in this plot.

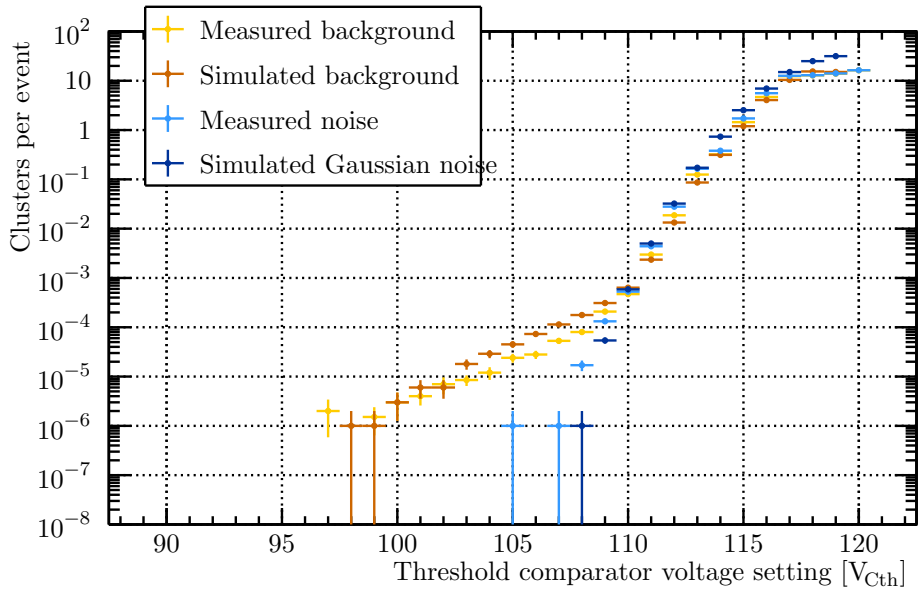

Figure 2.31. *Simulation of the CBC2 mini module's noise and background from the primary X-rays in the Phywe XR 4.0 Expert Unit.*

Both the noise and the background simulation follow the same pattern as the measured data. The simulated noise matches the data very well in the region between 110 V_{Cth} and 114 V_{Cth}. For lower thresholds, higher V_{Cth}, the occupancy in the mini module is too high for the CBC

to function properly. This is not taken into account in the simulation which results in a higher number of clusters per event for the simulation of Gaussian noise of thresholds settings higher than $117\,\mathrm{V_{Cth}}$.

2.4.2. Simulating the charge sharing

The effect of charge sharing on the signal distribution can be easily shown using the simulation. This is presented in Figure 2.32 where the simulation results are given in linear and logarithmic scale. The blue markers represent the simulation in which there is charge sharing between the strips and the orange ones are for the simulation without charge sharing. When the charge in the silicon is not shared, the signal plateau is more pronounced, as well as the point where the threshold becomes higher than the signal. The smearing of the signal for both charge sharing cases and is more clearly observed in Figure 2.32a, comes from the noise of the CBC2 mini module.

2.4.3. Simulating fluorescent signals in a CBC2 mini module

Figure 2.33 shows the results of the simulated number of clusters in the CBC2 mini module, while being exposed to Kα photons, generated by illuminating a zinc foil with X-rays. Two simulations are shown in orange and yellow; orange for the model with only Gaussian noise and the zinc Kα photon energy as input and the yellow curve showing the results of modeling the background radiation from the X-ray tube and the Kα energy. They are compared to the measured data which have blue markers.

The simulation with the background X-rays taken into account matches the data very well. In Section 2.3.6 it is estimated that the zinc signal is not detectable, as the energy from its Kα is less than $3\,\sigma$ away from the pedestal. This is also visible in the simulation shown in Figure 2.33, where threshold scan curves with the zinc target and with the background only overlap. Moreover, for the simulation that takes not into account the background, there is no signal plateau visible only noise, confirming that the zinc signal can not be used to determine the $\mathrm{V_{Cth}}$ calibration value.

In Figures 2.34 to 2.36, the other simulated signals are plotted. They match the measured data well qualitatively, but there are quantitative differences. In the noise regions, the simulations give larger number of clusters per event because the CBC2 behavior at high occupancy is not included in the model. In the signal region, from $110\,\mathrm{V_{Cth}}$ downwards, some of the simulations give a higher number of clusters per event while others are lower. This can be explained by the fact that the Kα photon rate is not known well enough.

In addition, in the tail of the signals differences between the simulation and the measurements are observed. In this toy Monte-Carlo a very simple charge sharing model is used which can explain this. An improvement is proposed in Section 2.5.4, where data taken with an $^{241}_{95}\mathrm{Am}$ source are used to better model the charge sharing.

2.4.4. Calibration curve for the simulations

Following the same procedure as in Section 2.3.5, the signal thresholds are computed from the simulation results. They are given in Table 2.5, where they are compared to the measured signals as well. The simulation seems to be off by $\sim 0.4\,\mathrm{V_{Cth}}$, which can be expected from the results in Section 2.4.3. It is most likely caused by the simple charge sharing model.

With the signal thresholds and the signal energies, the $\mathrm{V_{Cth}}$ calibration value of the simulated CBC2 mini module was calculated, see Figure 2.37. With measurements, a calibration value of $373 \pm 5\,e\,{\mathrm{V_{Cth}}}^{-1}$ was found, the simulation predicts $(390 \pm 15)\,e\,{\mathrm{V_{Cth}}}^{-1}$. Within the statistical uncertainty of the simulation and the measurement the same calibration value was found. This

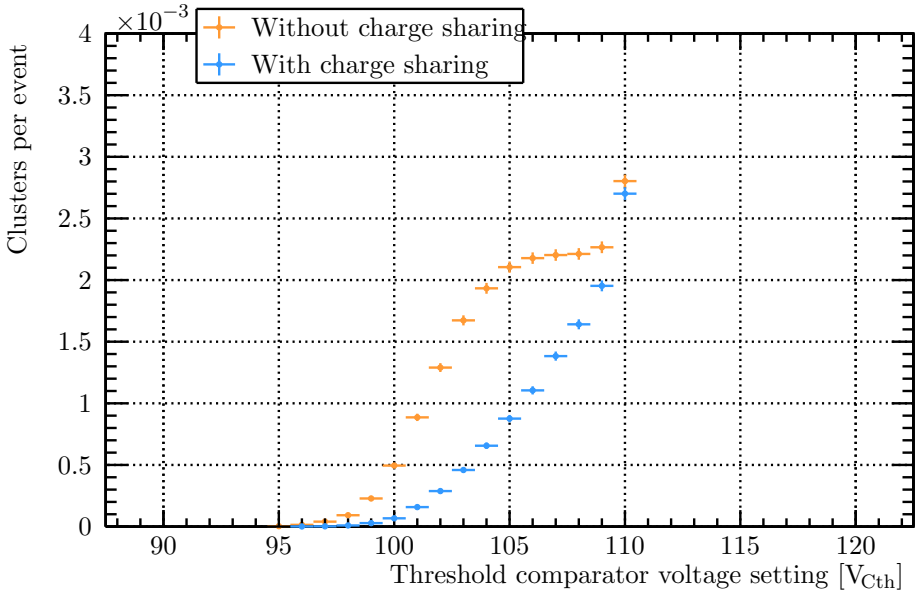

(a) *Linear scale.*

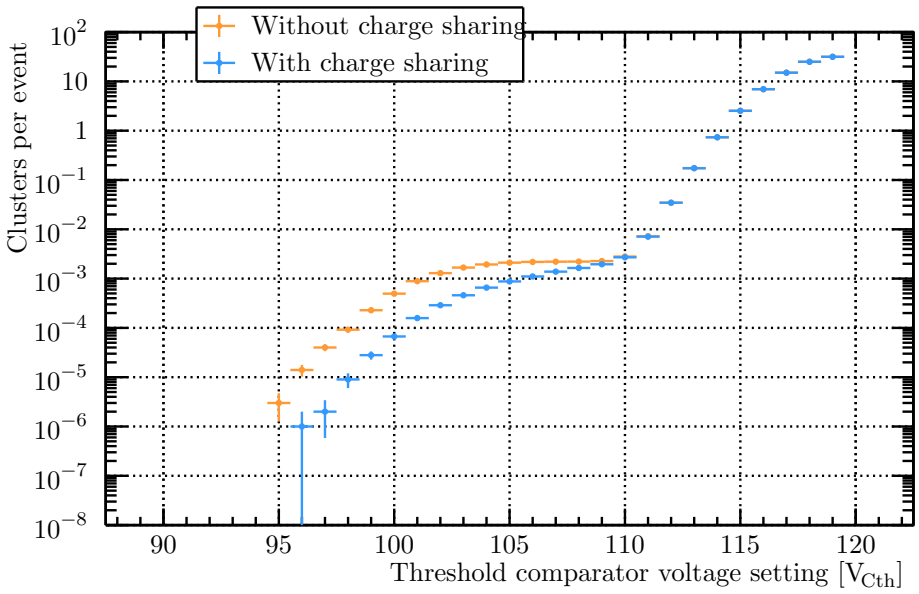

(b) *Logarithmic scale.*

Figure 2.32. *Simulation of a fluorescent signal in a CBC2 mini module, that was produced by irradiating a tin foil with X-rays, with or without charge sharing between its silicon strips.*

Table 2.5.
Results of fitting a linear function to different simulated Kα photon signals in a CBC2 mini module.

CBC	**Sensor**	**Metal**	**Measured signal** S_{meas} V_{Cth}	**Simulated signal** S_{sim} V_{Cth}
1	1	Molybdenum	105.73 ± 0.025	105.20 ± 0.03
1	1	Silver	102.44 ± 0.08	102.02 ± 0.03
1	1	Tin	99.91 ± 0.04	99.51 ± 0.05

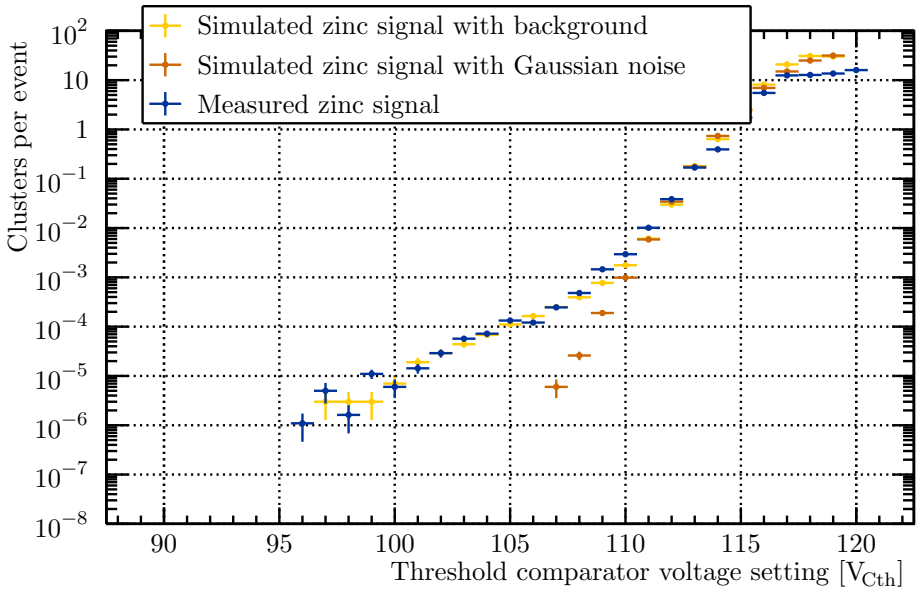

Figure 2.33. *Simulation of of a fluorescent signal that was produced by irradiating a zinc foil with X-rays, as seen by a CBC2 module.*

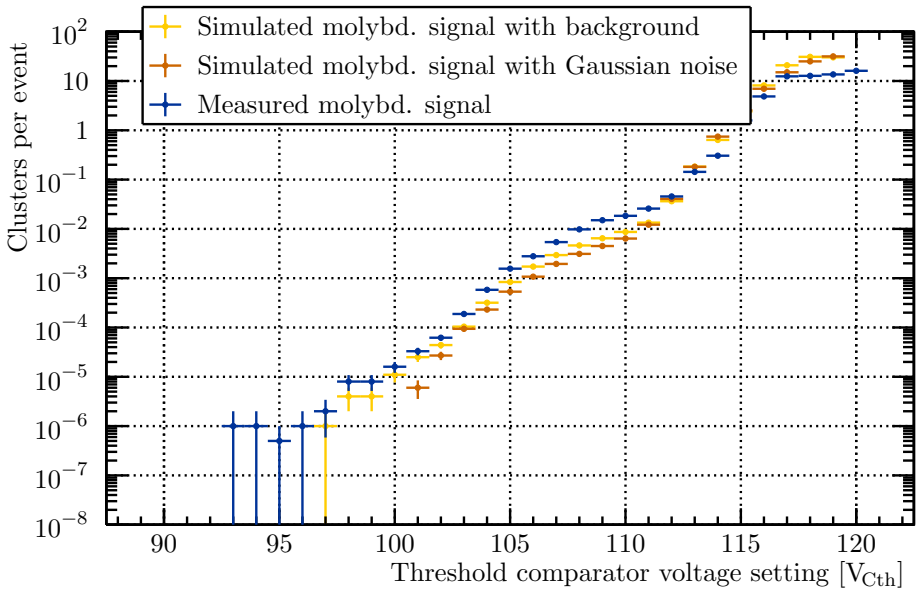

Figure 2.34. *Simulation of of a fluorescent signal that was produced by irradiating a molybdenum foil with X-rays, as seen by a CBC2 module.*

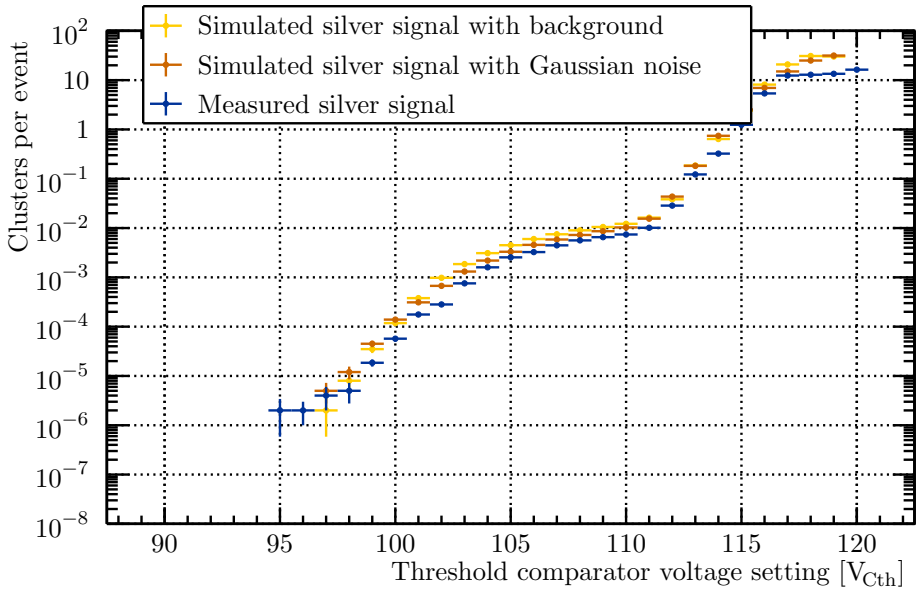

Figure 2.35. *Simulation of of a fluorescent signal that was produced by irradiating a silver foil with X-rays, as seen by a CBC2 module.*

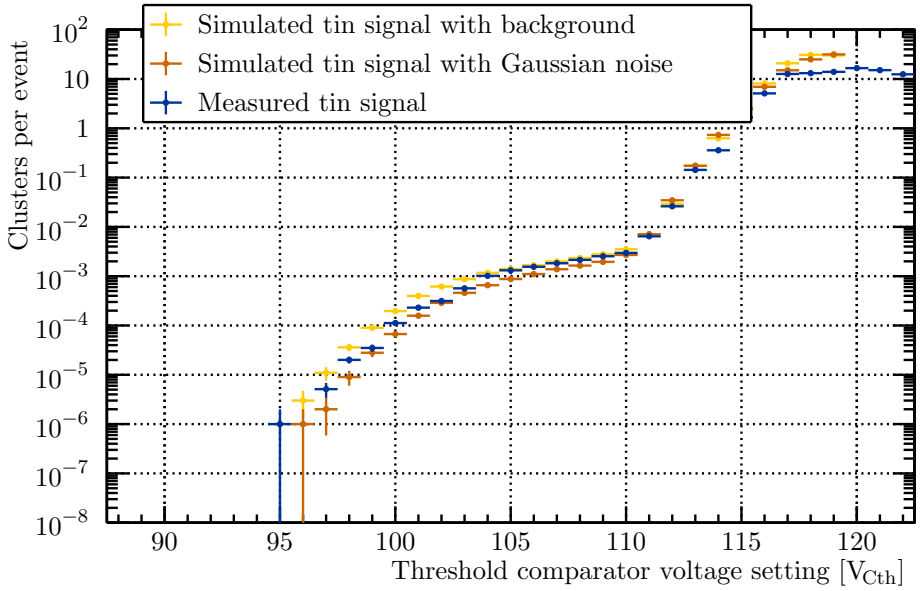

Figure 2.36. *Simulation of of a fluorescent signal that was produced by irradiating a tin foil with X-rays, as seen by a CBC2 module.*

means that the simulation can be used to predict measurements of low energy photon signals, with the CBC2 mini module. Since the difference between the simulation and the measurement is 5 %, this is taken as the uncertainty of the simulation for now.

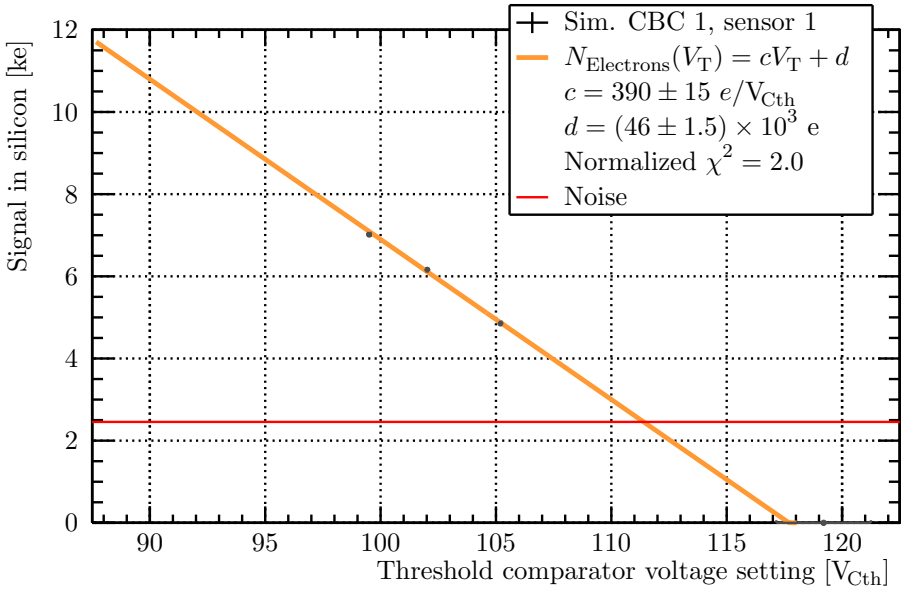

Figure 2.37. *Fitting a linear function to the simulated signal thresholds in* V_{Cth} *DAC units, versus the number of electrons that corresponds to the signal in silicon, produced by fluorescent radiation of different energies.*

2.5. V_{Cth} calibration with a radioactive source

Radioactive sources, emitting either β or γ radiation can potentially be used for the V_{Cth} calibration as well. This is studied in the following subsections.

2.5.1. Choosing a radioactive source

An advantage of β sources is that they can be triggered on before, or after they hit the silicon detector. A disadvantage of β sources is that the energy spectrum of the β's is very wide. This is a result of the three-body decay during which they are formed, shown in Equations (2.10) and (2.11) [55].

$$\text{p} \longrightarrow \text{n} + \beta^- + \overline{\nu}_{\text{e}} \tag{2.10}$$

$$\text{n} \longrightarrow \text{p} + \beta^+ + \nu_{\text{e}} \tag{2.11}$$

Illustrations of energy spectra of β decays are given in Figure 2.38, where it is shown that there is a difference between the spectra of β^+ and β^-. The maximum energy of the spectrum E_{max}, is usually given as a measure of the energy of the β particles.

A commonly used β source is $^{90}_{38}\text{Sr}$. It decays into $^{90}_{39}\text{Y}$ while releasing a β^- particle and an anti-neutrino [17, p. 521]. In turn, $^{90}_{39}\text{Y}$ decays to a β^-, an anti-neutrino and $^{90}_{39}\text{Zr}$, which is stable and does not decay further. The maximum energy of the $^{90}_{38}\text{Sr}$ decay is 0.546 MeV, that of ^{90}Y is 2.283 MeV.

In order to be able to use the $^{90}_{38}\text{Sr}$ source for V_{Cth} calibrations, a procedure has to be implemented to select β particles of a certain energy. This is complicated, as a spectrometer or

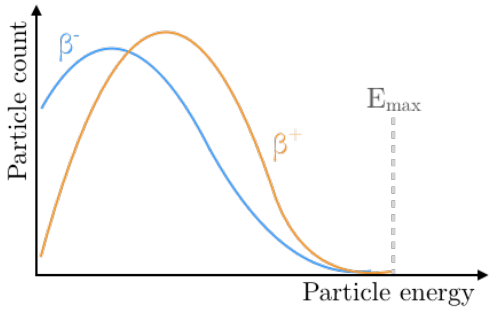

Figure 2.38. *Illustration of an energy spectra of β decay [55].*

calorimeter needs to be added to the setup, and only if the energy resolution is good enough in the order of ∼2 %, the signal can be used for calibration. Even when this would be implemented, the energy loss of the electrons happens according to a Landau distribution. In contrary to the photon case, they are not fully absorbed by the silicon after the first interaction. This makes it very difficult to extract the signal threshold from measurements with $^{90}_{38}$Sr .

Therefore, $^{241}_{95}$Am was selected, which, next to an α particle, emits γ radiation with a narrow energy distribution peaking at 60 keV. This energy is higher than the highest energy measured with the characteristic X-rays, which is an advantage because with a higher energy, a larger portion of the V_{Cth} range is covered. The α particles coming from the source, are shielded by a titanium capsule that the source is contained in.

2.5.2. Simulating a signal from $^{241}_{95}$Am

To prepare for measurements with $^{241}_{95}$Am, the toy Monte-Carlo simulation was used again. Figure 2.39 shows the simulation of a threshold scan with a CBC2 mini module, while it was irradiated by γ photons with an energy of 60 keV. The noise was assumed to be Gaussian with a pedestal of 118.9 V_{Cth} and noise of 2.5 V_{Cth}, see Section 2.1.1. Background radiation is not expected for this kind of measurement. The same charge sharing model was assumed as for the Kα photons, see Figure 2.14b. For the photon rate, 10 kHz cm^{-2} was chosen.

With this rate, the region between 110 V_{Cth} and 120 V_{Cth} is dominated by the noise, which is the same for the fluorescent Kα photons. From 110 V_{Cth} downward, the signal is visible as a clear plateau, followed by a linear decrease between 95 V_{Cth} and 75 V_{Cth}. A fit to determine the expected signal threshold, $V_{T,S_{Am}}$, is shown in Figure 2.40. Because the accuracy of the model is estimated to be around 5 %, the signal threshold for $^{241}_{95}$Am γ photons and the CBC 1-Sensor 1 combination is estimated to be between 73 V_{Cth} and 80 V_{Cth}. This means that the $^{241}_{95}$Am source can be used for V_{Cth} calibrations, which are described in the next section.

2.5.3. Calibration of a CBC2 mini module with $^{241}_{95}$Am

For the V_{Cth} calibration with $^{241}_{95}$Am, the same method is applied as for the calibration with Kα photons. First a threshold scan is taken with the CBC2 mini module while it is exposed to the γ photons from a 37 MBq $^{241}_{95}$Am source. For each step in the scan, 6×10^6 triggers were send to ensure enough hits in each strip. This is verified by the plot in Figure 2.41, where it can be seen that the sensor was uniformly illuminated.

With the results from the threshold scan shown in Figure 2.42, the signal thresholds, $V_{T,S_{Am}}$, were computed with the fitting procedure described in Section 2.4.3, but with different fit ranges. To determine the fit ranges, the first fits were performed between $[75, 83]V_{Cth}$, because at 83 V_{Cth} the number of clusters per event starts to decrease and at 75 V_{Cth} both CBC's still

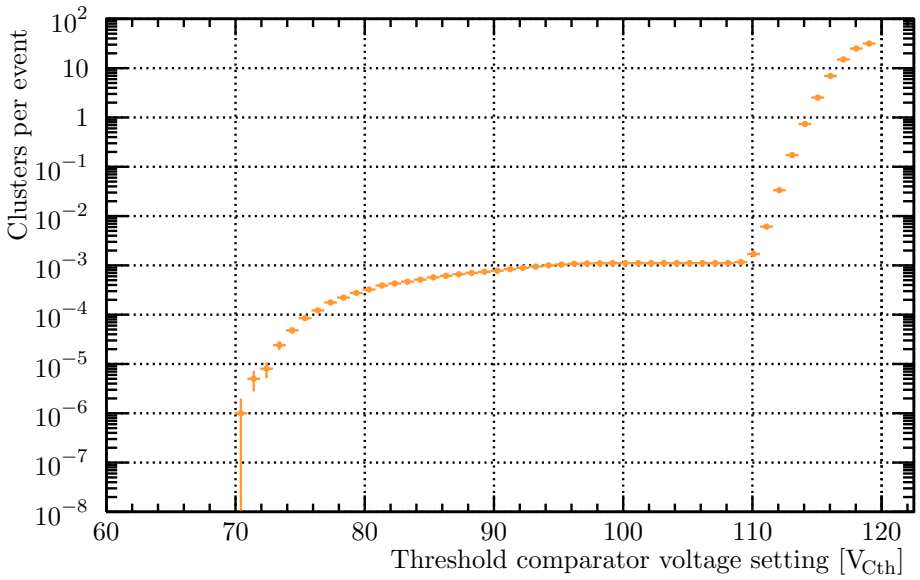

Figure 2.39. *Simulation of a* V_{Cth} *scan with a CBC2 mini module, while it was exposed to* γ *radiation from a* 37 MBq $^{241}_{95}Am$ *source. The result is shown in number of clusters per event versus threshold setting.*

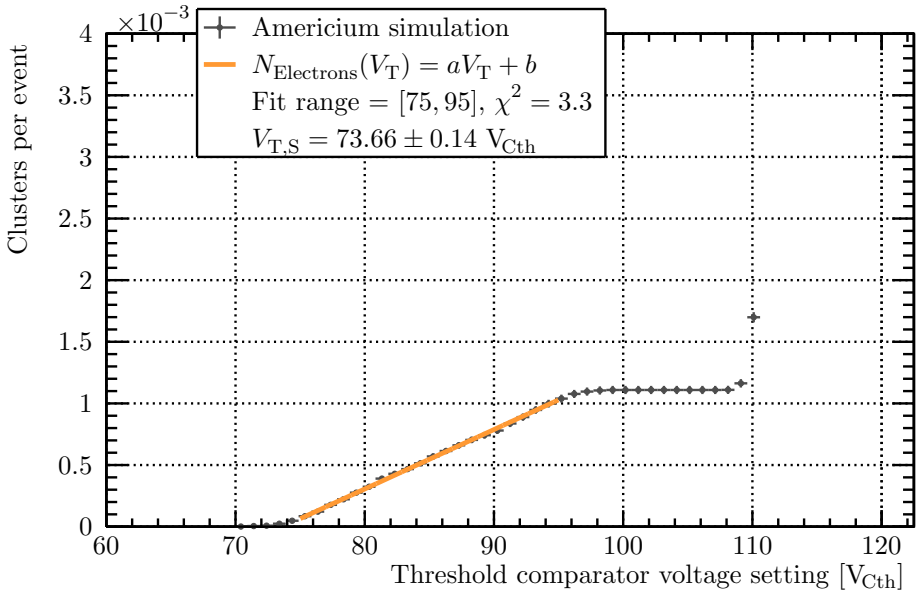

Figure 2.40. *Result of fitting a linear function, to the simulation of a signal in a CBC2 mini module, while it was exposed to a* 37 MBq $^{241}_{95}Am$ *source.*

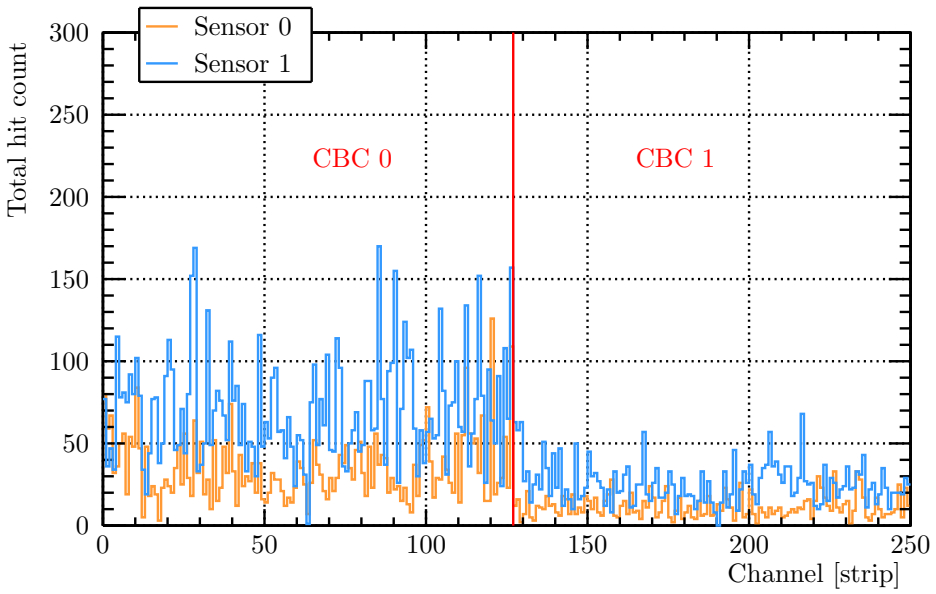

Figure 2.41. *Total hit count per channel in the CBC2 mini module, while it was being illuminated by γ radiation from a* 37 MBq $^{241}_{95}Am$*source, at* 110 V_{Cth}.

have a significant number of clusters per event. Just like in the fluorescent photon case, by extrapolating this fit to the threshold axis, V_0 is found. Then the lower limit of the final fit is $V_0 + 2\,V_{Cth}$, to not ensure that the smearing of the signal by the noise is neglected. Since there is no background radiation, the fits can be directly performed on the results from the $^{241}_{95}Am$, see Figure 2.43. The results from all the signal threshold fits are summarized in Table 2.6.

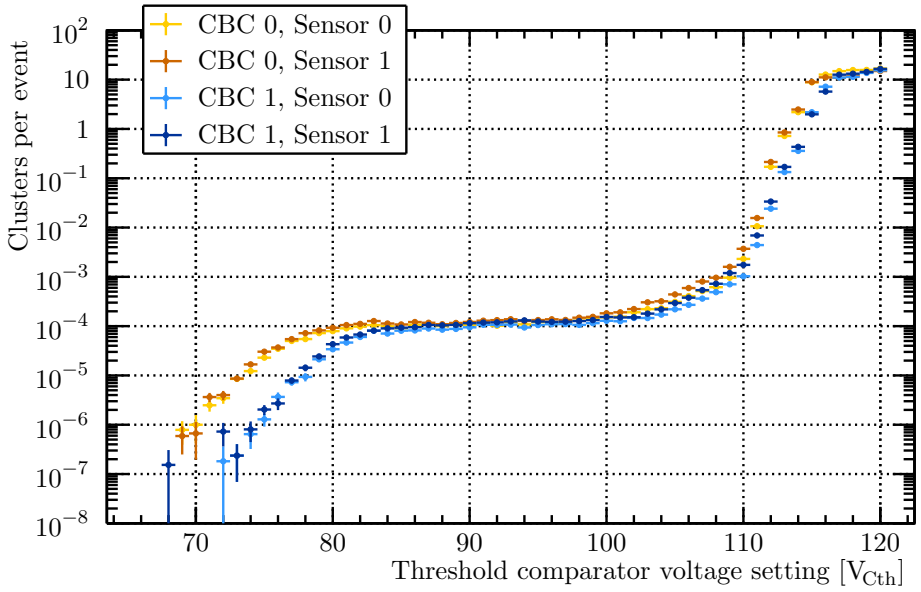

Figure 2.42. *Measured number of clusters per event versus threshold, for a V_{Cth} scan with a CBC2 mini module, while it was exposed to γ radiation from a* 37 MBq $^{241}_{95}Am$ *source.*

As the plots in Figure 2.43 are giving in linear scale, it can be seen that the signal plateau is not as constant as it appears in Figure 2.42. This should be investigated in the future to check

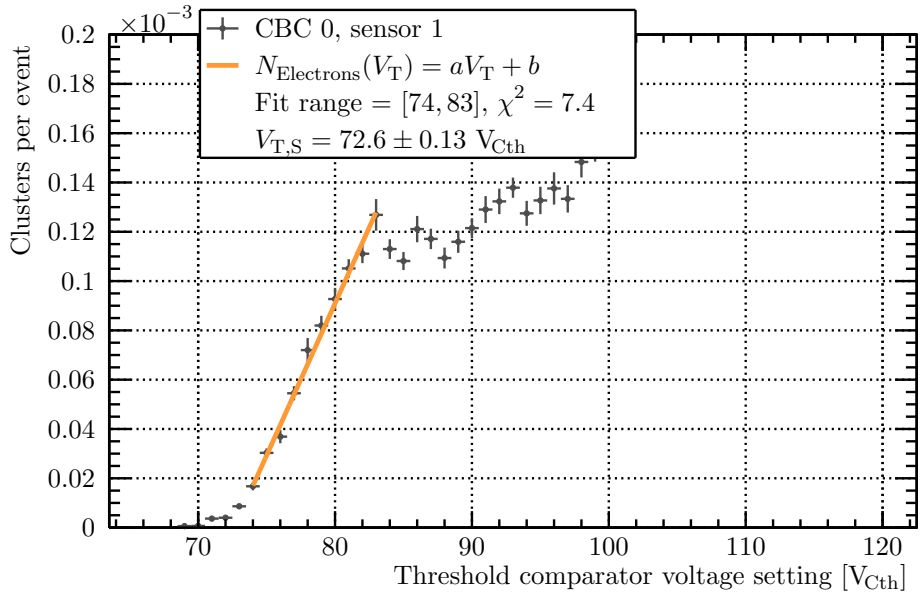

(a) *CBC 0-Sensor 1.*

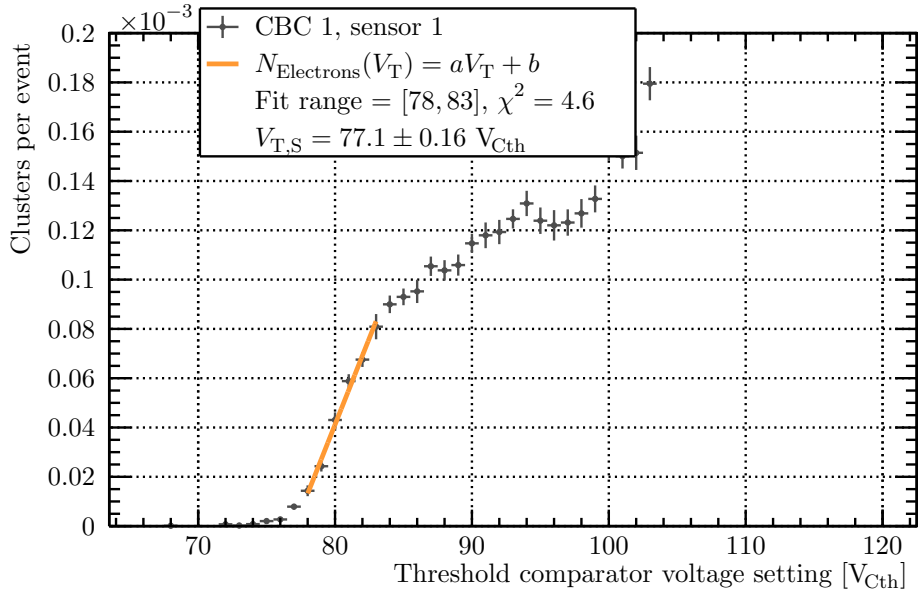

(b) *CBC 1-Sensor 1.*

Figure 2.43. *Results of fitting a linear function to the ${}^{241}_{95}$Am signals measured by the two CBC2's in the mini module.*

whether this is due to having not enough events per scan step or if there is some other cause for this observation.

For CBC 0-Sensor 0, the signal in silicon from the ${}^{241}_{95}$Am signal, as well as the signals from the Kα scans versus their respective signal thresholds, are plotted in Figure 2.44. As before, the V_{Cth} calibration value was estimated by fitting a linear function to the calibration curve, this time adding the signal measured with the ${}^{241}_{95}$Am source. For all four groups of CBC-sensor combinations the calibration results are given in Table 2.7.

Table 2.6.
Results of fitting a linear function to the $^{241}_{95}Am$ signal, that was measured by different CBC-sensor combinations.

CBC	Sensor	Slope a e/V_{Cth}	Constant b e	x-intercept $V_{T,S}$ V_{Cth}
0	0	$(1.10 \pm 0.03) \times 10^{-5}$	$(-8.00 \pm 0.23) \times 10^{-4}$	72.8 ± 0.12
0	1	$(1.23 \pm 0.03) \times 10^{-5}$	$(-9.00 \pm 0.26) \times 10^{-4}$	72.8 ± 0.12
1	0	$(1.31 \pm 0.06) \times 10^{-5}$	$(-1.01 \pm 0.05) \times 10^{-3}$	77.3 ± 0.14
1	1	$(1.40 \pm 0.07) \times 10^{-5}$	$(-1.08 \pm 0.06) \times 10^{-3}$	77.1 ± 0.16

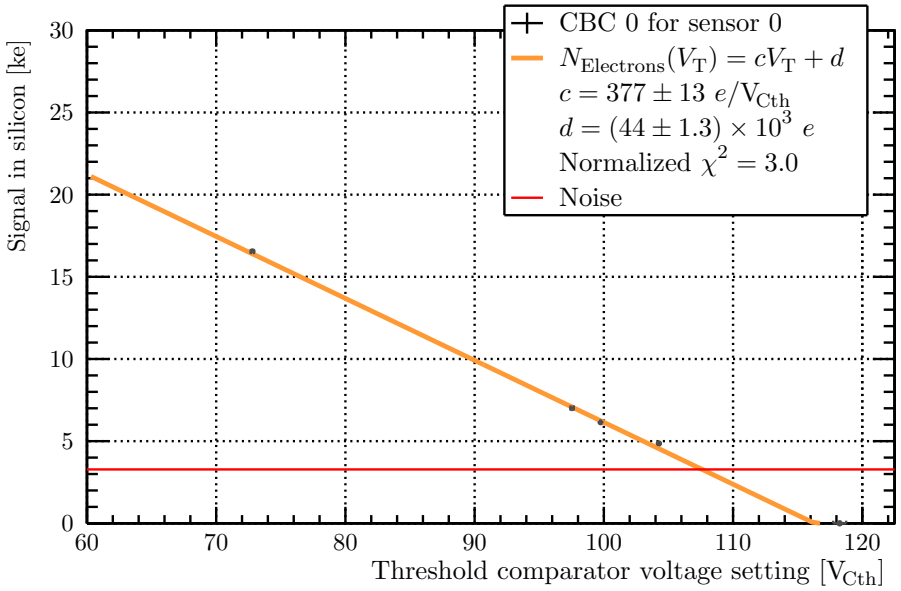

Figure 2.44. *Fitting a linear function to the signal thresholds in V_{Cth}, versus the number of electrons released in silicon by fluorescent radiation of different energies and the γ photons from the $^{241}_{95}Am$ source, for CBC 0-Sensor 0.*

Table 2.7.
Results of fitting a linear function to the photon signals versus the thresholds in V_{Cth}, for all four CBC-sensor combinations.

CBC	Sensor	Calibration value c e/V_{Cth}	Constant d V_{Cth}
0	0	377 ± 17	$(4.10 \pm 0.13) \times 10^4$
0	1	373 ± 11	$(4.40 \pm 0.11) \times 10^4$
1	0	402 ± 13	$(4.70 \pm 0.13) \times 10^4$
1	1	396 ± 11	$(4.70 \pm 0.13) \times 10^4$

Again, within the statistical uncertainty, for the two different sensors wire-bonded to the same CBC2, the same calibration value is found and a different calibration value is found for the two different CBCs. However, the calibration values in Table 2.7 are 6 % higher than the ones obtained with only fluorescent photons. This will be discussed in more detail in Section 2.6, where the different signals are compared to each other.

2.5.4. Cluster size, charge sharing and uncertainty of simulation

With the $^{241}_{95}$Am data, the charge sharing model used in the simulations can be improved by looking at the average cluster size versus the threshold. If a large fraction of the charge deposited in a strip is shared with its neighbors, the average cluster size is large too. Following the same logic, if only a small fraction of the charge is shared, small clusters dominate. It is easier to study this sharing fraction with a large signal, like the signal coming from the $^{241}_{95}$Am γ photons. This is because if the charge sharing fraction is small, a larger signal is needed to observe its effects.

Figure 2.45 shows the average cluster size versus the threshold, of a V_{Cth} scan with a CBC2 mini module, while it was exposed to γ photons from a 37 MBq $^{241}_{95}$Amsource. Between 111 V_{Cth} and 122 V_{Cth} the same pattern is observed as for the tin measurement in Figure 2.13. Between 110 V_{Cth} and 98 V_{Cth} a bump is observed that is not clearly visible in the Kα measurements. This can be explained by the higher energy, and thus the larger signal in the silicon by $^{241}_{95}$Am signal.

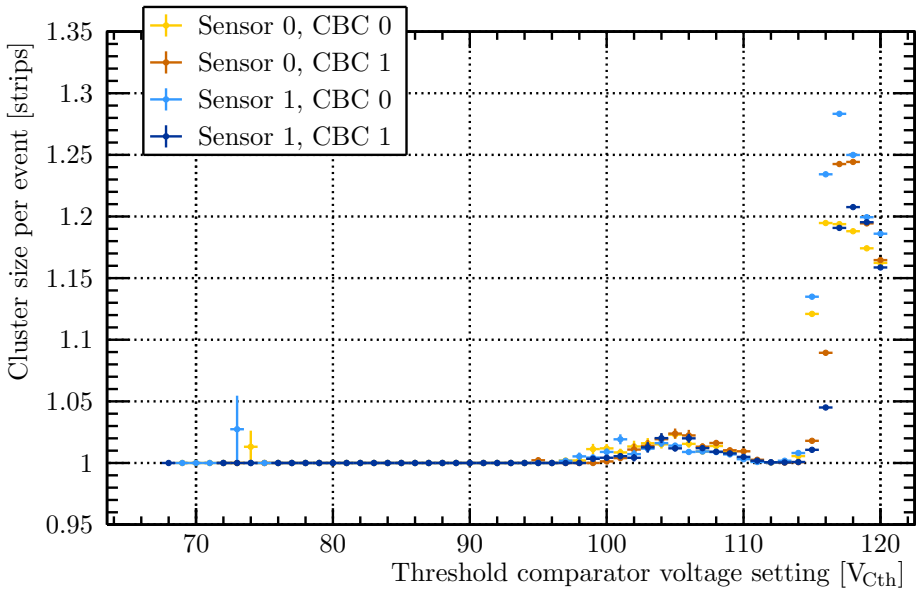

Figure 2.45. *Average cluster size versus threshold for a* V_{Cth} *scan with a CBC2 mini module, while it was exposed to* γ *radiation from a* 37 MBq $^{241}_{95}$*Am source.*

Based on these results, a new model is proposed. It includes a charge sharing region, the region in the strip where charge is shared, and a charge sharing fraction, which is the amount of the charge that is being shared if a hit is located in the charge sharing region. This is illustrated in Figure 2.46 where the model is shown in Figure 2.46a and the effect of the charge sharing on the number of clusters per event versus the threshold in Figure 2.46b. The charge sharing region is given by α and the charge sharing fraction in the region α, is referred to as β.

The threshold range where the number of clusters per event decreases due to the charge sharing, is as wide as the signal $V_{T,S}$, times the sharing fraction, β. The threshold at which the

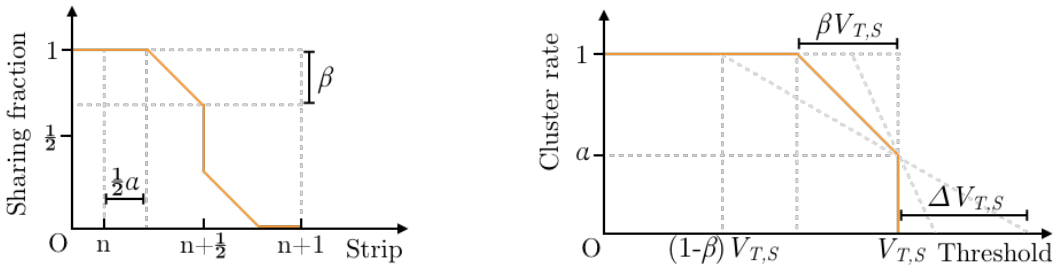

(a) *Model 3.* **(b)** *number of clusters per event versus for model 3.*

Figure 2.46. *A more realistic charge sharing model that takes a charge sharing region, α, and the charge sharing fraction, β, into account.*

charge sharing starts affecting the cluster size is given by $(1-\beta)V_{\mathrm{T,S}}$. Therefore the slope of the charge sharing, S_{CS}, can be written as in Equation (2.12).

$$\begin{aligned} S_{\mathrm{CS}} &= \frac{\Delta R_{\mathrm{Cluster}}}{\Delta V_{\mathrm{T,S}}} \\ &= \frac{1-\alpha}{V_{\mathrm{T,S}} - (1-\beta)V_{\mathrm{T,S}}} \\ &= \frac{1-\alpha}{1-1+\beta} \cdot \frac{1}{V_{\mathrm{T,S}}} \\ S_{\mathrm{CS}} &= \frac{1-\alpha}{\beta V_{\mathrm{T,S}}} \end{aligned} \tag{2.12}$$

In Equation (2.12), R_{Cluster} is the number of clusters per event. The uncertainty on the simulated signal using this new model, $\Delta V_{\mathrm{T,S}}/V_{\mathrm{T,S}}$, is given by Equation (2.13).

$$\begin{aligned} \frac{\Delta V_{\mathrm{T,S}}}{V_{\mathrm{T,S}}} &= \frac{\Delta V_{\mathrm{T,S}}}{\Delta R_{\mathrm{Cluster}}} \cdot \Delta R_{\mathrm{Cluster}} \cdot \frac{1}{V_{\mathrm{T,S}}} \\ &= \frac{\beta V_{\mathrm{T,S}}}{1-\alpha} \cdot \alpha \cdot \frac{1}{V_{\mathrm{T,S}}} \\ \frac{\Delta V_{\mathrm{T,S}}}{V_{\mathrm{T,S}}} &= \frac{\alpha\beta}{1-\alpha} \end{aligned} \tag{2.13}$$

With this new simulation the values of α and β can be found by tuning them to measured data. This is attempted by deploying a simple least squares optimization. By simulating the number of clusters per event and the cluster size for the whole range of $\alpha = [0,1]$ and $\beta = [0,1]$, and calculating the difference between the simulation and the measured data, a set of α and β for which the simulation best matches the measurement is obtained.

The results of a first optimization of α and β are shown in Figure 2.47, where β is plotted versus $1-\alpha$. The gray-scale indicates how well the measurement matches the simulation, the lighter the color, the better the match. Even though the results look very noisy and there is no clear minimum visible, a global minimum is found at $1-\alpha = 0.96 \Leftrightarrow \alpha = 0.04$ and $\beta = 0.49$. With these parameters, the uncertainty on the simulated signal threshold is $0.04 \times 0.49/0.96 \times V_{\mathrm{T,S}} = 0.019 \cdot V_{\mathrm{T,S}}$.

The results for number of clusters per event and cluster size versus threshold, for when these values are used in the toy Monte-Carlo simulation, are shown in Figures 2.48 and 2.49. The yellow curves show the results with the new model in Figure 2.46 and the orange curves show the results with the original model, see Figure 2.14b. The blue curves represent the

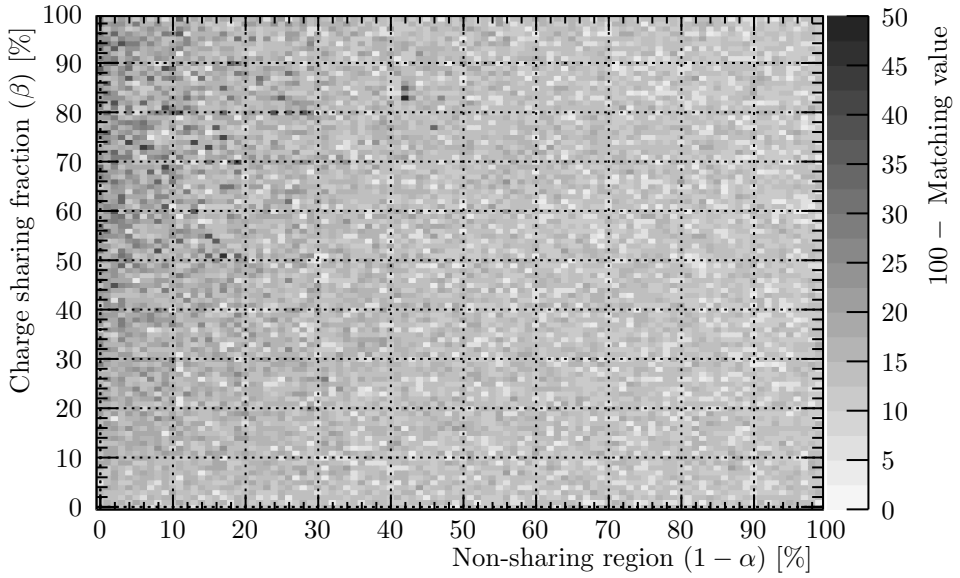

Figure 2.47. *Results of a least squares optimization of the α and β parameters of the charge sharing model in Figure 2.46. The global minimum is found at $1-\alpha = 0.04$ and $\beta = 0.49$.*

measured $^{241}_{95}$Am threshold scan. While simulations with both charge sharing models do not accurately represent the measurement, the new model with $\alpha = 0.04$ and $\beta = 0.49$ matches the measurement better, especially in the range between $100\,\mathrm{V_{Cth}}$ and $110\,\mathrm{V_{Cth}}$.

From these plots it can be seen that the optimization does not take the whole range of the threshold scan into account properly. From $90\,\mathrm{V_{Cth}}$ downward, the number of clusters per event goes down vastly, causing it to be less important in the optimization. Hence, another optimization was executed, where instead of taking the difference between the measured number of clusters per event and the simulated one, first the logarithm of both are calculated before they are subtracted from each other. The results are similar to Figure 2.47; the global minimum found here is at $1-\alpha = 0.89 \Leftrightarrow \alpha = 0.11$ and $\beta = 0.22$. The resulting error on the signal threshold is therefore $0.11 \times 0.22/0.89 \times V_{\mathrm{T,S}} = 0.03 \cdot V_{\mathrm{T,S}}$.

The simulation results with $\alpha = 0.11$ and $\beta = 0.22$, are given in Figures 2.50 and 2.51. As can be seen in Figure 2.50, the number of clusters per event versus threshold is now modeled very well with this charge sharing model. For the cluster size versus threshold however, the quality of the simulation is decreased; the bump for the cluster size is very narrow compared to the measure cluster size bump.

This exercise shows that the model described here is probably too simplified to correctly describe the charge carrier dynamics in the sensor, but at the same time, it can be tuned to correctly reproduce the edge of the signal spectrum. Simulating the number of clusters per event versus threshold accurately, is more important than the cluster size. Hence, the $^{241}_{95}$Am signal threshold was extracted from this simulation of the CBC 1-Sensor 1 combination and the result is shown in Figure 2.52 and found to be $76.2 \pm 0.23\,\mathrm{V_{Cth}}$. Taking the 3 % uncertainty on the signal into account, this is the same as the measured signal threshold of $77.1 \pm 0.16\,\mathrm{V_{Cth}}$.

In addition, the four fluorescent photons were simulated again with this model, and the signal thresholds from this simulation were estimated with the linear fits. The results of these threshold scan simulations are presented in Figure 2.53, and the signal thresholds are summarized in Table 2.8. Similar to the simulation with the original model illustrated in

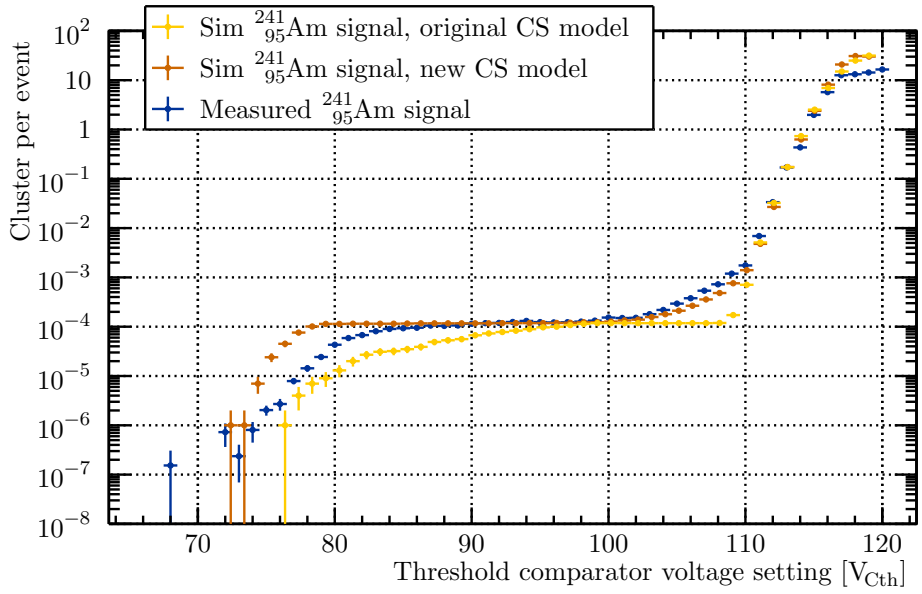

Figure 2.48. *Comparing a number of clusters per event measurement in blue to two simulations with different charge sharing models, of a* V_{Cth} *scan of a CBC2 mini module, while it was exposed to* γ *radiation from a* 37 MBq $^{241}_{95}Am$ *source. For the new CS model,* $\alpha = 0.04$ *and* $\beta = 0.49$ *were used.*

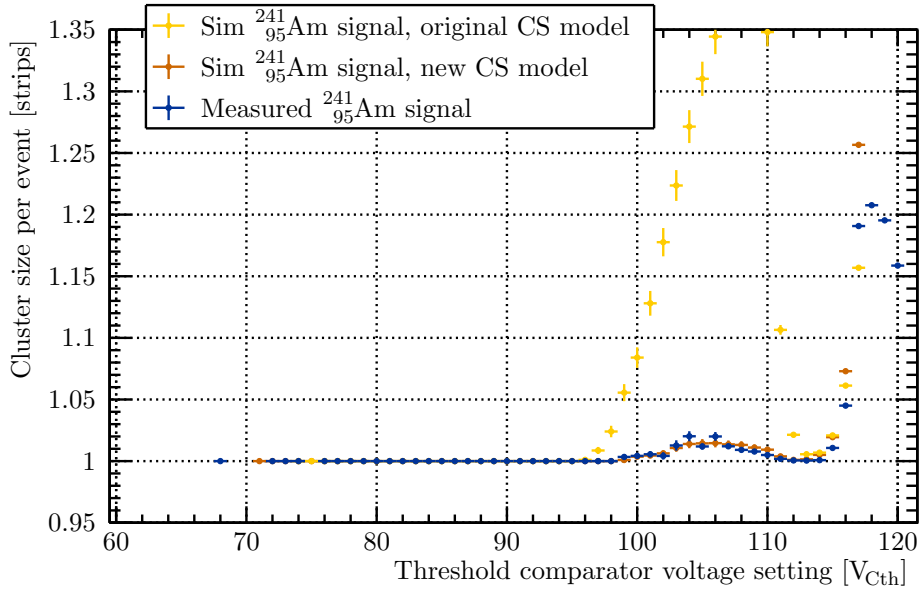

Figure 2.49. *Comparing measurement to two simulations of the average cluster size versus threshold, for a* V_{Cth} *scan with a CBC2 mini module, while it is exposed to* γ *radiation from a* 37 MBq $^{241}_{95}Am$ *source. For the new CS model,* $\alpha = 0.04$ *and* $\beta = 0.49$ *were used.*

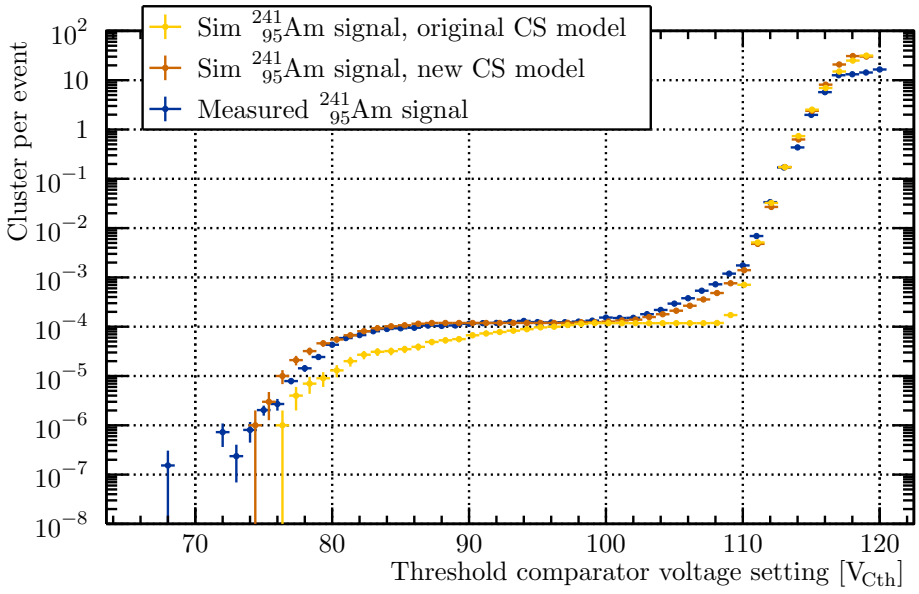

Figure 2.50. *Comparing a number of clusters per event measurement in blue to two simulations with different charge sharing models, of a* V_{Cth} *scan of a CBC2 mini module, while it was exposed to* γ *radiation from a* 37 MBq $^{241}_{95}Am$ *source. For the new CS model,* $\alpha = 0.11$ *and* $\beta = 0.22$ *were used.*

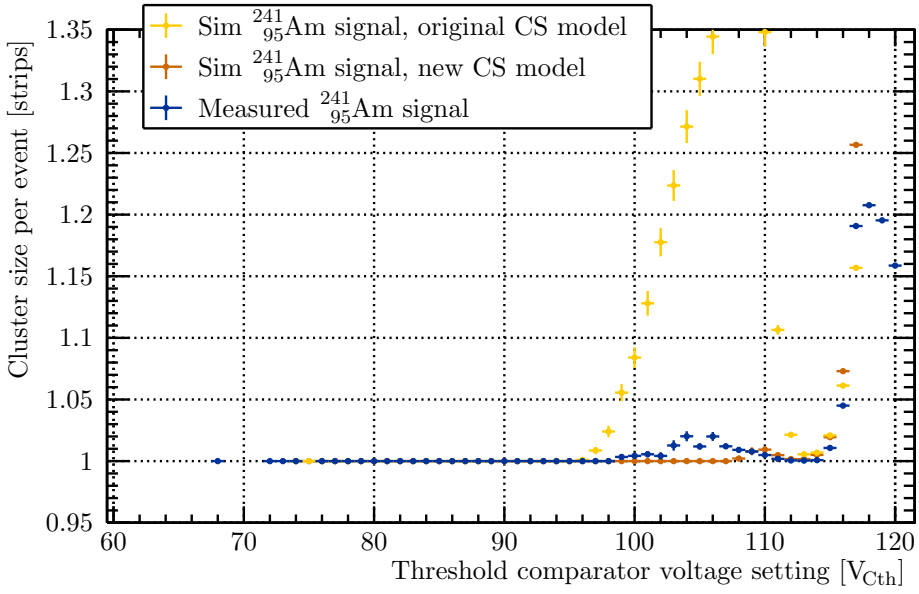

Figure 2.51. *Comparing measurement to two simulations of the average cluster size versus threshold, for a* V_{Cth} *scan with a CBC2 mini module, while it is exposed to* γ *radiation from a* 37 MBq $^{241}_{95}Am$ *source. For the new CS model,* $\alpha = 0.11$ *and* $\beta = 0.22$ *were used.*

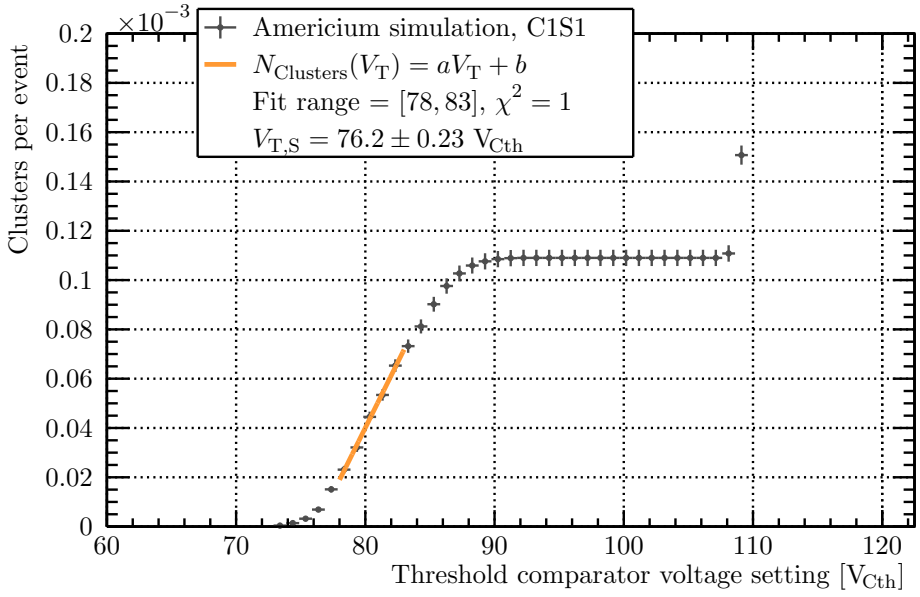

Figure 2.52. *Fit to the simulated ${}^{241}_{95}Am$ signal in the CBC2 mini module, with $\alpha = 0.11$ and $\beta = 0.22$.*

Figure 2.14b (see Table 2.5), the simulation underestimates the signal thresholds. The resulting calibration curve with calibration value $377 \pm 13\, e\, \mathrm{V_{Cth}}^{-1}$ is shown in Figure 2.54.

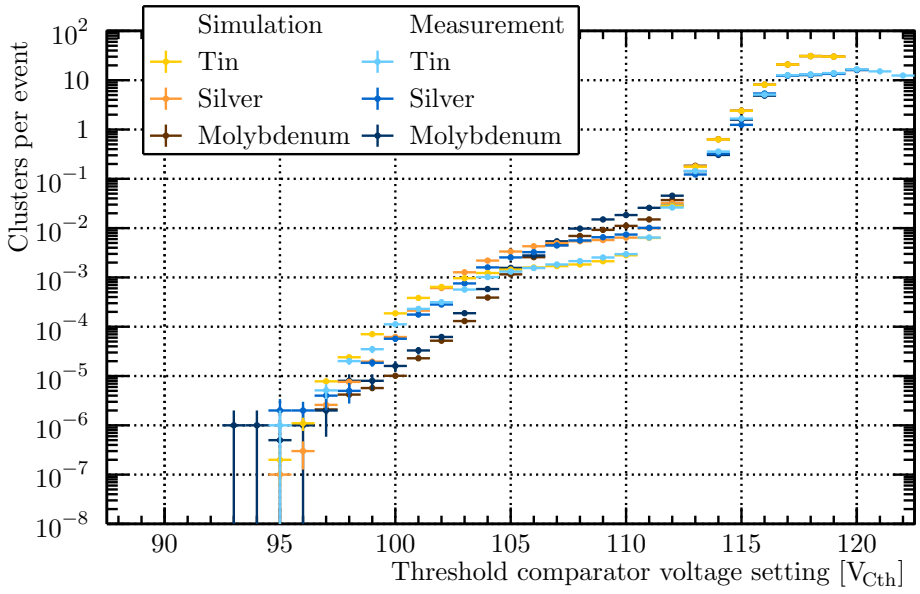

Figure 2.53. *Results of the threshold scan simulations with the CBC mini module, while it was being exposed to the four fluorescent photon signals.*

Except for in the ${}^{241}_{95}$Am photon case, the new calibration does not improve the original simulation with more than 1 %. This is probably caused by the fact that the charge sharing model was tuned to the ${}^{241}_{95}$Am threshold scan, the fluorescent photon signals were not taken into account during the optimization.

Table 2.8.
Results of fitting a linear function to different simulated Kα photon signals in a CBC2 mini module, with $\alpha = 0.11$ and $\beta = 0.22$.

CBC	S	Metal	Measured signal S_{meas} V_{Cth}	Simulated signal S_{sim} V_{Cth}
1	1	Molybdenum	105.73 ± 0.025	104.84 ± 0.010
1	1	Silver	102.44 ± 0.08	101.19 ± 0.010
1	1	Tin	99.91 ± 0.04	99.18 ± 0.0017
1	1	$^{241}_{95}$Am	77.1 ± 0.16	76.2 ± 0.23

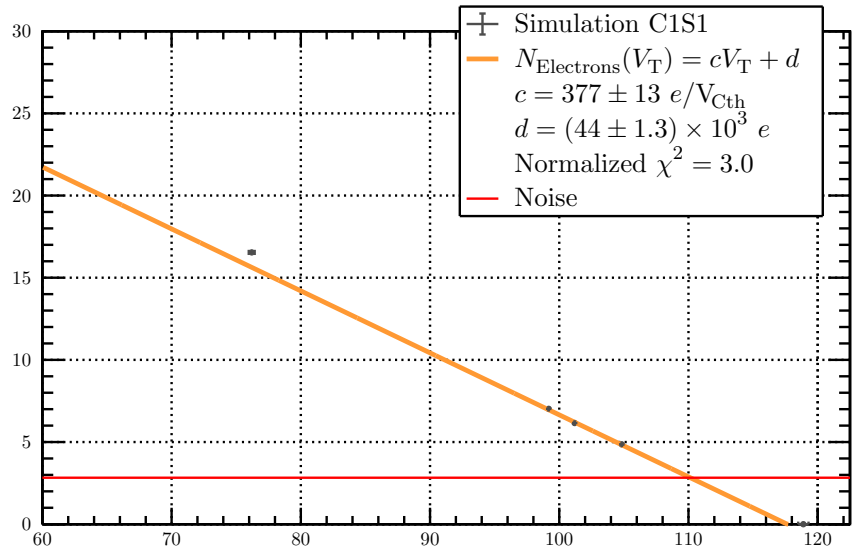

Figure 2.54. *Calibration curve from the simulation with $\alpha = 0.11$ and $\beta = 0.22$.*

2.6. Comparing different calibration signals

To evaluate the V_{Cth} calibration, three measurements are available: the pedestal measurement (Ped), the three fluorescent Kα signals (Fluo) and the americium signal (Am). These measurements are compared here in five combinations: Fluo, Fluo+Ped, Fluo+Am, Fluo+Am+Ped, Am+Ped. These combinations are plotted in Figures 2.55 and 2.56.

It has to be noted that for combinations including fluorescent measurements, the error on the fit for V_{Cth} was evaluated by re-scaling χ^2/N_{dof} as noted above, whereas for the combination Am+Ped (since $N_{dof} = 0$ implies there is no way of checking the measurement linearity) the error on the calibration is directly propagated form the estimated error on Am and Ped. This means that the error estimate for the Am+Ped combination cannot be directly compared to those of the combinations including Fluo.

The same measurements are rearranged in Figure 2.56 to compare different sensors connected to each CBC. Two sensors connected to the same CBC, are compatible within the statistical uncertainty, and the differences between the CBCs are on the order of 10 %. Moreover, Figure 2.56 shows a comparison of the different combinations of signals. For each CBC-sensor combination, the fits that include $^{241}_{95}$Am are compatible within the statistical errors. Similarly,

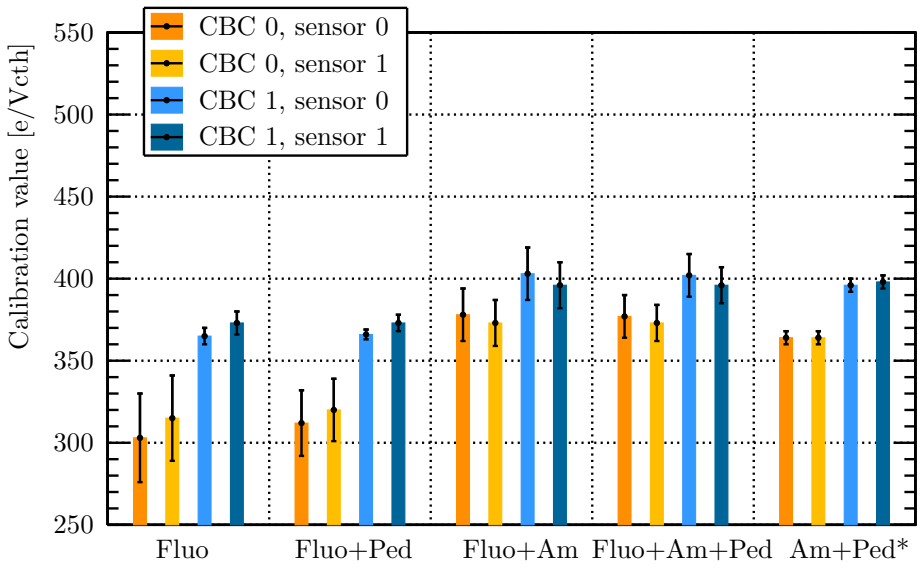

Figure 2.55. *Comparing calibration results of different combinations of signals. (*) Error bars are obtained by re-scaling* $\chi^2/N_{dof} = 1$ *for all measurements except Am+Ped.*

the two fits without $^{241}_{95}$Am are consistent with each other, but they are not in agreement with the other three fits. This might be explained by the signal range that is different between the two groups. The points in the two fits without $^{241}_{95}$Am have signals between 0 keV and 25 keV, while the others have signals between 0 keV and 60 keV.

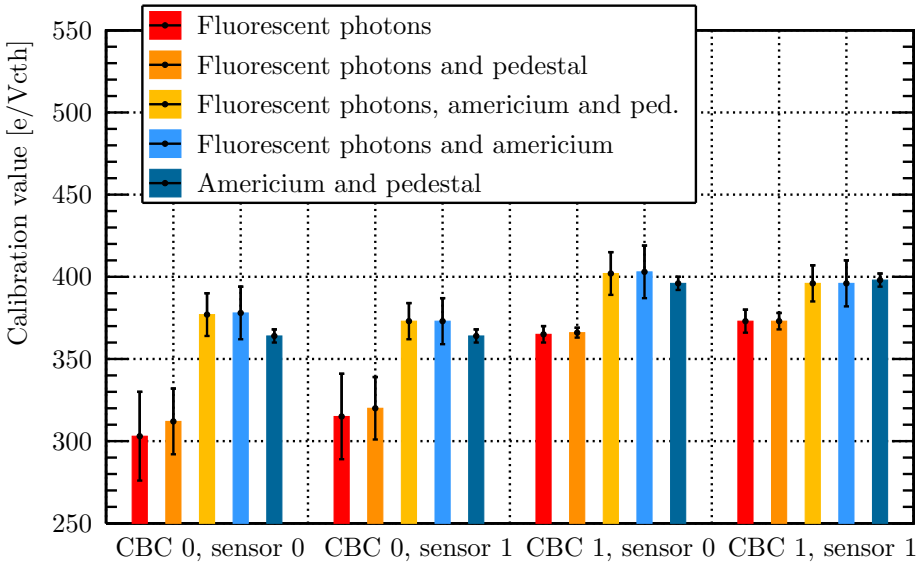

Figure 2.56. *Comparing calibration results of different combinations of signals, for different CBC-sensor combinations.*

2.7. CBC3 calibration

The CBC3, has a 10 bit threshold register. This means that each V_{Cth} unit corresponds to ∼1 mV, which is roughly 130 e. The CBC3's V_{Cth} DAC setting is perfectly linear with the threshold voltage, see Figure 2.57 [44]. This eases the V_{Cth} calibration for a CBC3 chip as only one measurement with one well-defined signal, should in principle be enough to measure its gain. Since $^{241}_{95}$Am has the highest signal energy, it is the best candidate for CBC3 V_{Cth} calibrations.

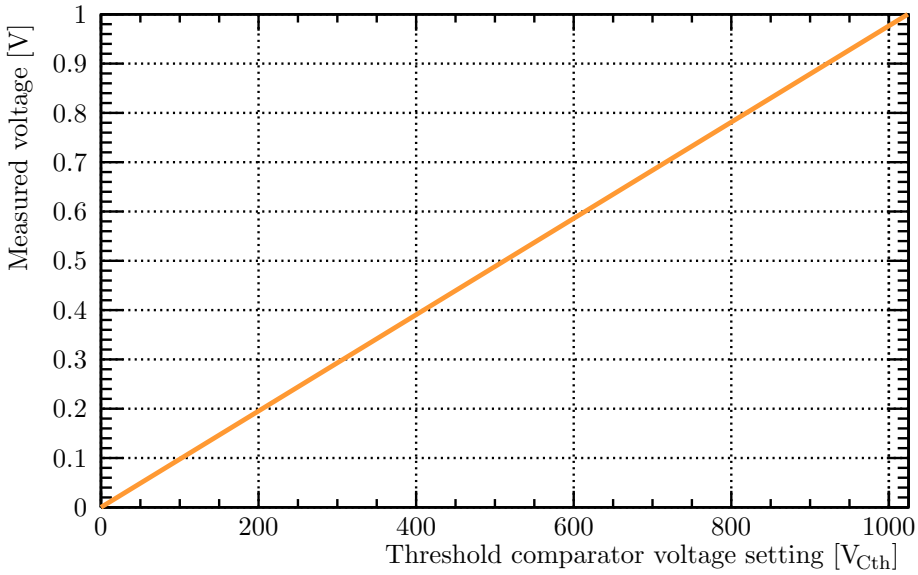

Figure 2.57. *Measured threshold comparator voltage versus the threshold comparator voltage setting in* V_{Cth}*, of a CBC3 chip [44].*

An improved version of the toy Monte-Carlo is implemented to simulate the CBC3 chip [56]. The core of the simulation is the same; noise and signal are randomly picked from their respective distributions, and their sum is compared to the threshold. The same charge sharing model as for the CBC2 was used with $\alpha = 0.11$ and $\beta = 0.22$. But to have a more realistic model, before the signal and noise are compared to the threshold, the CBC3 front-end's response to the noise plus the signal is calculated via the use of an RC-RC-CR model.

The Laplace transforms of CR- and RC-filters are given in Equations (2.14) and (2.15) where τ is the time constant of the filter.

$$F_{\mathrm{RC}}(s,\tau) = \frac{1}{1+\tau s} \tag{2.14}$$

$$F_{\mathrm{CR}}(s,\tau) = \frac{\tau s}{1+\tau s} \tag{2.15}$$

The analog pulse of the CBC3 front-end logic is the integrated Laplace transform of the product of two RC-filters and one CR filter. It can be derived by using polar expansions, resulting in $f(r,\theta,\tau,t)$, as described in Equation (2.16). Here t is the time, τ is the time constant of the RC and CR filters and r and θ are the amplitude and angle of the polar expansions.

$$f(r,\theta,\tau,t) = \exp^{-t/\tau}\left(\frac{t}{\tau}\right)^2 \sum_{N=0}^{\infty} f_N(r,\theta,\tau,t)\,, \tag{2.16}$$

with

$$f_N(r,\theta,\tau,t) = \frac{r^N}{\tau^{2N}(N+2)!}\sum_{i=0}^{N}(\cos\theta)^{N-i}(\sin\theta)^i\sum_{i=0}^{N}(-1)^i a_{N,i}t^{N-i}\tau^i\,. \tag{2.17}$$

The parameters of the pulse of the analog part of the CBC3 front-end, are obtained by fitting the expression in Equation (2.16) to a measured test pulse from the CBC3. The resulting pulse is shown in Figure 2.58. In the simulation this pulse shape is used to calculate the CBC3 front-end's response to noise and signal, that are randomly picked, just like before.

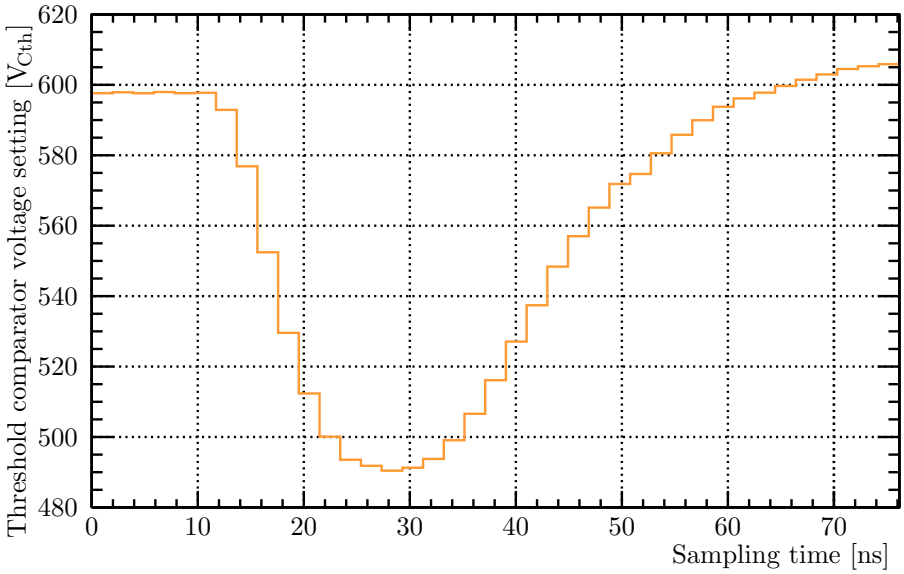

Figure 2.58. *Simulation of a pulse shape of a signal processed by a CBC3 amplifier, in threshold comparator voltage setting versus pulse delay. This pulse shape is based on a fit to a measured CBC3 test pulse.*

The pulse is then compared to the V_{Cth} setting applied, to determine for how many clock cycles it was above threshold. This is the binary output of the CBC3 front-end logic.

Another upgrade made to the model is the implementation of the Hit Detect Logic of the CBC3 of which the different settings are explained in Figure 1.19. In the simulation, the number of clock cycles the signal was above threshold from the previous step, is taken as HDL input. Depending on the HDL setting chosen, the final output of the CBC3 is calculated.

With this CBC3 model, a simulation of a threshold scan with a CBC3 module, while it was exposed to γ photons from a 37 MBq $^{241}_{95}$Am source, is given in Figure 2.59. The different colors represent the different outcomes depending on the HDL setting selected. On the horizontal axis, the pedestal subtracted threshold is given. The pedestal of the CBC3 is around 590 V_{Cth} with a noise of ~6.5 V_{Cth}. Thus it is expected that the $^{241}_{95}$Am signal is found at $60\,\text{keV}/3.6\,\text{eV}\,e^{-1}/130\,e\,V_{Cth}{}^{-1} \approx 128\,V_{Cth}$.

Measurements with a CBC3 module and an $^{241}_{95}$Am source have not been performed yet, but from beam test data with a CBC3 mini module, a calibration value of $128\,e\,V_{Cth}{}^{-1}$ is obtained [57, 58], which is compatible with the design specifications.

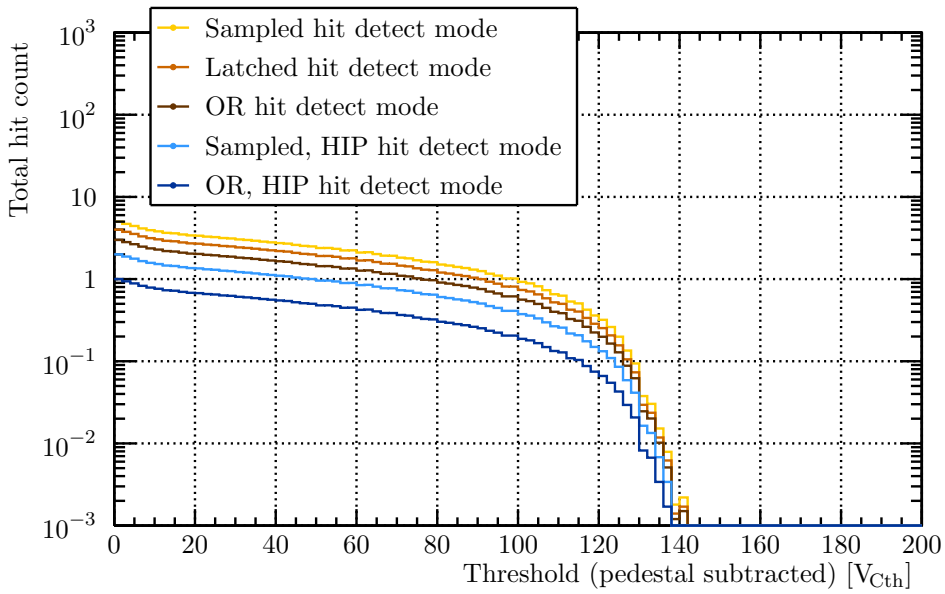

Figure 2.59. *Simulation of the number of clusters per event versus threshold comparator voltage, for a* V_{Cth} *scan with a CBC3 mini module, when exposed to gamma radiation from an* $^{241}_{95}Am$ *source. Different colors show the results for different Hit Detect Logic settings.*

2.8. Proposal for CBC calibration during production

Both calibration signals discussed before in this chapter, are signals that can be used for V_{Cth} calibrations. However, the measurements discussed here do not seem to produce compatible results with the CBC2 mini module, see Section 2.6. Nonetheless, it is expected that for CBC3, the results of threshold scans with Kα photons and γ photons will produce consistent data. This is firstly foreseen, because the CBC3's measured threshold is absolutely linear with the V_{Cth} setting. Secondly, since the CBC3 can self-trigger on incoming signals, the systematic uncertainties on the threshold scan results will be smaller, because of the heavily reduced measuring time needed for each step in a V_{Cth} scan. Based on these expectations, a V_{Cth} calibration procedure for during CMS Phase-2 Outer Tracker Module production is proposed below.

Initially, calibrations with both Kα photons and $^{241}_{95}$Am γ photons should be executed for a small number of modules ($\sim$10). The results of these calibrations have to be compared as in Section 2.6. If the results are in agreement, it can be concluded that the CBC3 V_{Cth} calibration can be achieved through the use of $^{241}_{95}$Am γ photons alone.

For the remainder of the modules, it has to be checked whether the differences in V_{Cth} calibration values, justify the calibration of just a fraction of the CMS Phase-2 Outer Tracker Modules. If the differences in V_{Cth} calibration values are significant, it should be considered to calibrate all CMS Phase-2 Outer Tracker Modules individually. If that is not the case, calibrating a fraction of modules that is large enough to be a good representation of the CMS Phase-2 Outer Tracker detector, will save a lot of time during production.

2.9. Conclusion

The research described in this chapter, was aimed at finding a procedure to calibrate the V_{Cth} threshold setting of a CBC, during the production of CMS Phase-2 Outer Tracker Modules.

The expected calibration value in $e\,\mathrm{V_{Cth}}^{-1}$ for a CBC2, is around $343\,e\,\mathrm{V_{Cth}}^{-1}$. For a CBC3 chip the expected value is $\sim 125\,e\,\mathrm{V_{Cth}}^{-1}$.

Two sources of well-defined signals were tested, and it can be concluded that with both of them the above mentioned calibration can be performed in the following way. First a threshold scan is taken while the module is being exposed to one of the signals. When looking at the number of clusters per event versus the threshold, the signal $\mathrm{V_{Cth}}$ can be found by fitting a linear function, and extrapolating the result to find the $\mathrm{V_{Cth}}$ at which the number of clusters per event is zero. The was demonstrated in Section 2.3.5.

For CBC2s in a mini module, the average calibration value found was $(367 \pm 12)\,e\,\mathrm{V_{Cth}}^{-1}$. From beam test data with a CBC3 mini module, the CBC3 $\mathrm{V_{Cth}}$ calibration value was found to be $125\,e\,\mathrm{V_{Cth}}^{-1}$.

For most combinations of the signals, used to study CBC2 $\mathrm{V_{Cth}}$ calibration, the calibration values are compatible. For the cases that are not consistent, it was argued that the different energy ranges of the signal combinations and the systematic uncertainties for the different methods can explain the discrepancies. This is expected to be better in the CBC3 case, because the CBC3 can self-trigger. This reduces the time needed to perform a full threshold scan, thereby lowering the systematic uncertainties. On top of that the measured threshold voltage of the CBC3, is exactly linear with $\mathrm{V_{Cth}}$.

At the end of the chapter, a strategy for $\mathrm{V_{Cth}}$ calibration of the many CMS Phase-2 Outer Tracker Modules was proposed, with the objective to calibrate only a fraction of the modules with ${}^{241}_{95}\mathrm{Am}$. First it should be verified with a small number of modules, that when calibrating CBC3 with Kα and ${}^{241}_{95}\mathrm{Am}$ signals, both kinds of photons result in the same calibration value. If that is the case, then the other modules only need to be calibrated with ${}^{241}_{95}\mathrm{Am}$. This will save a lot of time, compared to when each module has to be calibrated with both Kα and ${}^{241}_{95}\mathrm{Am}$ photons. In order to be able to save even more time, the differences in $\mathrm{V_{Cth}}$ calibration values between different CBCs, have to be evaluated in order to determine if each module has to be calibrated, or if only calibrating a fraction of them would be enough.

With the intend to further deepen the understanding of the CBCs, two simulations were established as well; one for CBC2 modules and the other for CBC3 modules. The CBC2 toy Monte-Carlo simulation was validated with data from the threshold scans, performed during the $\mathrm{V_{Cth}}$ calibration tests. While doing so, a charge sharing model was proposed, with which it was possible to predict the number of clusters per event versus threshold very accurately. The uncertainty on the predicted signal threshold is around 3 %. The CBC3 simulation still has to be validated with data from either ${}^{241}_{95}\mathrm{Am}$ measurements or beam test results.

3. Preparing for High Rate Beam Tests

In this chapter, the design, construction, commissioning and testing of a new high rate beam telescope for CMS is presented. The aim of the research was to build a setup that can be used to (stress) test CMS Phase-2 Outer Tracker prototype modules in beam test experiments, at CERN or other beam test facilities.

Most beam test facilities also provide a beam telescope [10, 59] for testing tracking detectors. These do usually not meet the requirements for high rate stress tests with CMS Phase-2 Tracker prototypes, as their readout and triggering frequencies are too low (below a few tens of kilo Hertz). Therefore a dedicated CMS telescope was build at CERN, and tested at the SPS beam test facility .

Any device that is tested in a beam telescope will from here on out be referred to as the Device Under Test, or DUT.

3.1. A new CMS high rate telescope: CHROMIE

The new CMS Phase-2 Tracker Modules will have 750 kHz trigger rate capabilities and a 25 ns integration time (see Section 1.6.2). To qualify and test these modules in beam tests, ideally they would be tested at nominal operation rate and beyond, to be able to fully characterize them before they will be used in CMS.

In beam test facilities in Europe that have a beam energy of more than a few GeV, normally have EUDET telescopes available for users [60]. Therefore, and because most beam tests with CMS Tracker prototypes in the past were performed with EUDET telescopes, they will be used as an example as to why a new high rate telescope dedicated to CMS Tracker prototypes was needed. The telescope was initially designed with Phase-2 OT modules in mind, however it can also be used for Phase-2 IT module beam tests, as well as beam tests with tracker modules of other experiments.

Because the Phase-2 Outer Tracker modules have a binary output, a large number of thresholds has to be scanned to quantify a signal, see Chapter 2. Ideally, the limiting factor of these measurements would be the maximum trigger rate that the module can handle, which is in the MHz regime. This is more than a hundred times faster than the current EUDET readout rate of around ∼9 kHz [61]. On top of that, the integration time of the Mimosa planes used in this type of telescope is 113 µs, which is almost ∼4600 times slower than the Outer Tracker prototypes (25 ns). This results in a large pile-up of thousands of tracks in the telescope if the prototypes would be tested at nominal rate.

As high rate tests (MHz) are vital in qualifying the new Phase-2 Tracker modules, it was decided to make a new high rate beam telescope designed for the use with CMS Phase-2 Tracker prototypes. The design of the telescope is based on CMS BPix modules, left over from the CMS Phase-1 Inner Tracker production. They have the same integration time as the Phase-2 prototypes and can handle particle fluxes up to 200 MHz cm^{-2}. This is well above the maximum particle flux expected for example for the 2S Outer Tracker modules, which will receive around 10 MHz cm^{-2}, and the PS modules which will receive 50 MHz cm^{-2} in CMS at nominal pile-up of 200. As a comparison, EUDET telescopes can manage a maximum of 1 MHz cm^{-2}.

A collection of grade-C quality modules was made available for this purpose. Phase-1 Inner Tracker modules were graded A to C during the production. Modules of grade A and B were

used for the detector construction or kept as spares. Often, grade-C means that a module has dead areas or a lot (tens of thousands) of noisy pixels in a readout chip. To compensate for these defects, the telescope is constructed with eight planes in total. Based on a straight line fit, and the $100 \times 150\,\mu m^2$ pixel size of the modules , the track pointing resolution of the telescope is expected to be better than 14 µm in the horizontal direction, and better than 10 µm in the vertical direction.

An additional advantage that comes with using BPix modules, is that their readout is CMS standard. This simplifies the design of the telescope readout and electronics. Furthermore it makes the integration of CMS Tracker prototypes in the telescope readout straightforward. The telescope is referred to as the CMS High-Rate telescOpe MachInE, or CHROMIE.

3.2. Design of the new telescope

The description of the design of the CHROMIE telescope is split into five parts. First the mechanics design is explained in Section 3.2.1. This includes the box surrounding the telescope, the control and monitoring of temperature and humidity, the design of the automated DUT stand, the frames and rails to mount the telescope modules and its auxiliary electronics and the scintillators for triggering. Second the electronics design is explained (Section 3.2.2), which covers everything from the telescope modules to hardware of the auxiliary electronics and the back-end firmware. This is followed by the cabling of the telescope and the triggering scheme, in Section 3.2.3 and Section 3.2.4 respectively. In Section 3.2.5, the software packages for readout, data analysis and simulation of the telescope are described.

3.2.1. Mechanics design

A rendered, three-dimensional image of the telescope mechanics design, is presented in Figure 3.1. The basis of the mechanical support of the CMS High Rate Telescope, consists of so-called aluminum Bosch profiles [62]. These are the horizontal and vertical aluminum bars observed in the image.

Aluminum panels are bolted to the frame of the telescope, to turn it into a closed box. It provides shielding from light in the experimental area, as well as protection against electromagnetic interference [63]. To further ensure darkness within the box, the aluminum sheets are painted black on the inside. Patch panels are mounted on the aluminum walls, to accommodate cables and fibers that link the telescope to service racks. The dimensions of the box are $1300 \times 1100 \times 595\,mm^3$

Another reason why the telescope is placed inside a box, is that it allows for accurate monitoring and control of the temperature and humidity around the telescope and DUT. The BPix modules that the telescope is built with, have never been irradiated. From previous experiences with the same detectors in a high rate beam test, it is known that a data set with good statistics can be collected at a flux of $>100\,MHz\,cm^{-2}$, with limited effect on the dark current. Therefore the telescope can be operated at room temperature.

When operating the telescope, the modules as well as the service electronics produce a relevant amount of heat ($\sim$10 kW) that must be removed in order to keep the temperature in the box below 25 °C. This is achieved with commercially available computer fans hung from the ceiling of the telescope's box. They circulate the air inside. Considering the power consumption of each telescope arm calculated to be less than 20 W, and the large aluminum structure surrounding the telescope, the excess heat is removed easily. Cooling for DUTs is provided separately through tubes in patch panels. It will be designed for each new version DUT, and is therefore not part of the telescope's design.

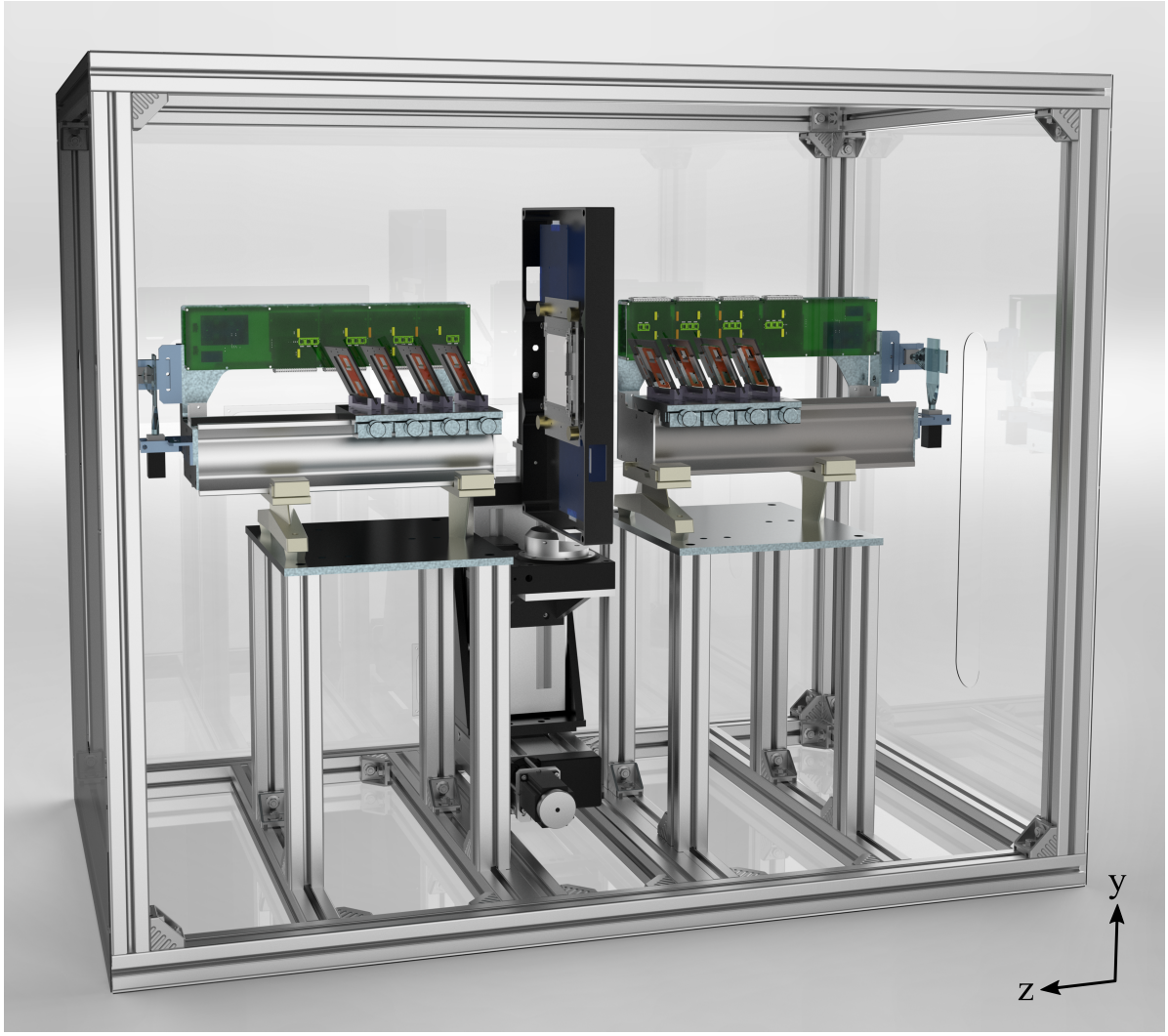

Figure 3.1. *Full view of the mechanics design of CHROMIE. The particle beam would normally come in on the right side of the telescope, and leave on the left, following the positive z-direction. Pointing up vertically is the positive y-axis, and pointing into this drawing horizontally is the positive x-axis. Rendering in KeyShot [64].*

The telescope's box is also equipped with temperature and humidity sensors for environmental monitoring. These are connected to Programmable Logic Controllers (PLCs). The PLCs can be programmed to create interlocks and circuit breakers for safe running conditions, like having the temperature below 25 °C and the leakage current of each module below 20 µA.

An enlarged image of the DUT in the center of the telescope and its mounting stages is presented in Figure 3.2. The DUT shown here, is a full-size, 2S module prototype (see Section 1.6.2), used in a series of beam tests at CERN [8]. It is chosen as a model DUT, because with its $52 \times 20 \times 4\,\mathrm{cm}^3$ dimensions, it is the largest prototype that is foreseen to be tested in the telescope. The telescope mechanics are designed such that a total of five of these full-size 2S modules can be placed in its center. In that case, the five DUTs can not be rotated around their common y-axis; they have to be installed parallel to the global xy-plane.

Under the influence of the magnetic field in the CMS detector, particles will impinge on the Outer Tracker modules at different incident angles, depending on transverse momentum (p_T). The CMS environment is reproduced, by rotating the DUT around an axis at a right angle with respect to the incoming particle test beam. For this reason, when installing less, or

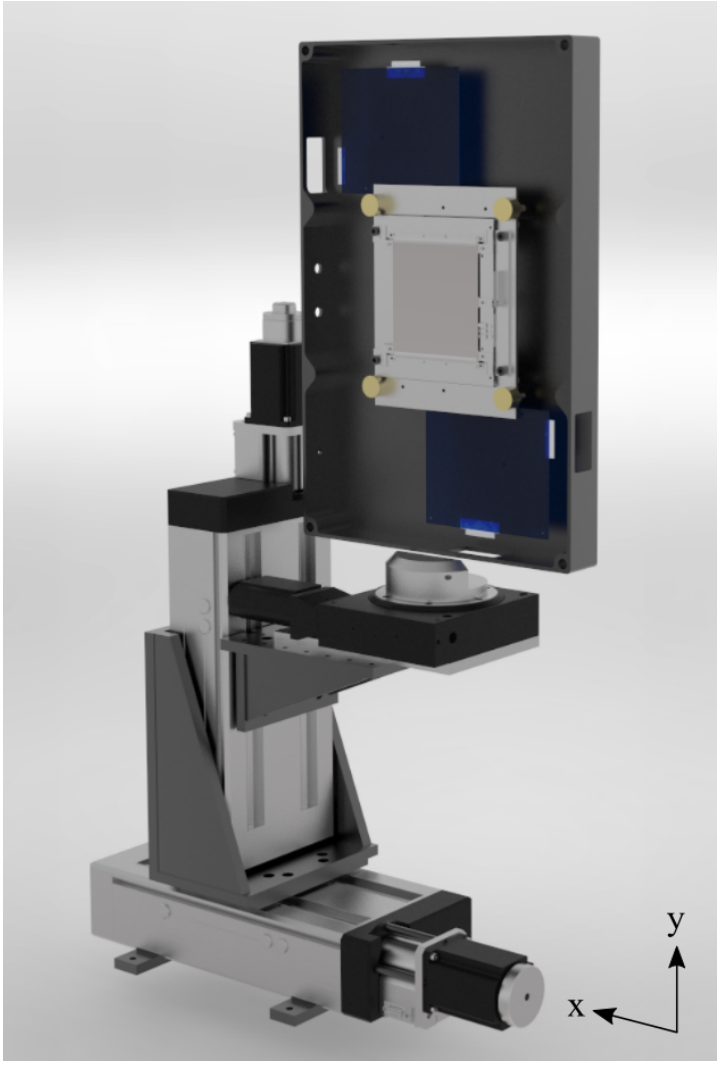

Figure 3.2. *Design of the mounting piece for the DUT(s), and the actuators that can rotate, and translate the DUT. Rendering in KeyShot [64].*

smaller DUTs in the telescope, they can be rotated around their common y-axis by means of a motorized rotational stage that is remotely controlled. It is a PI, M-062.DG actuator, that rotates 360° around its central axis, in steps of 0.96 µrad, or 5.5×10^{-5}° [65]. A single axis controller for DC motors, the PI Mercury C-863 [66], controls the actuator. The rotational stage holds a mounting piece, that is designed to mount DUTs on.

The rotational actuator is placed on two automated, remotely controlled linear stages. The bottom linear actuator is bolted to the aluminum supports of the telescope box. The linear actuators can move in the global x- and y-directions, defined in Figure 3.10. These Standa 8MT295, long-travel, motorized linear stages, can make steps with a minimum size of 12.5 µm at a range of 140 mm [67]. A 8SMC5.USB two-axis controller for stepper and DC motors is used for both linear stages [68]. Both the rotational and the linear actuators, can be seen in Figure 3.2 as well.

Through the use of linear stages, alignment of a DUT with respect to the beam and the telescope can be achieved without entering the experimental area. This saves time, as various DUTs with different dimensions, can all be aligned after installation in the telescope, without manual intervention. Thanks to the 140 mm range, it also permits for the irradiation of the

whole active surface of the sensors of a DUT, which is used when studying the response of different areas of the module's sensor.. This can be as large as $10\,\mathrm{cm}^2$ in the full-size 2S case, even though the beam spot size is usually in the order of a few mm^2.

Four telescope planes are placed on either side of the DUT, see Figure 3.1. They are all aligned to, and centered on the global z-axis, which is is parallel to the beam direction. Since the BPix modules are grade-C, see Section 3.1, it is chosen to have eight planes in total. This allows for having at least six points per reconstructed track, as dead areas in modules are preempted by having redundant planes.

This configuration, with a DUT in between two telescope arms, is very standard among beam telescopes. It is beneficial to the spatial resolution with which the position of a hit in the DUT can be predicted, because the track measured by the telescope can be interpolated to the DUT. This is opposed to placing a DUT in front or behind the telescope, where the track has to be extrapolated to find the hit in the DUT, which is usually less accurate.

A close-up view of an arm of the telescope is given in Figure 3.3. In that image it can be seen that each telescope plane exists of two BPix modules, which amount to an active area of the telescope of $32.4 \times 64.8\,\mathrm{mm}^2$ per plane. They are glued back-to-back, on a custom build aluminum frame. The Sylgard glue that is applied [69] remains gel-like after curing, and it is radiation hard up to 1 MGy, at which point it starts to loose elasticity. This leaves the possibility of removing a module from a frame, without significantly damaging it. A small aluminum clamp prevents the destruction of a module when accidentally pulling on the sacrificial cable.

The frames are fixed in mounting blocks, which position the modules at a 30° angle around their local x-axes, and 20° around their local y-axes. The magnitude of the angles are chosen to maximize the spatial resolution [70]. By placing the planes under an angle, the charge sharing between the sensor's pixels becomes more pronounced, and the average cluster size will be larger. Due to the fact the the output of the modules is analog and therefore the charge received by each pixel in a cluster very well known, the cluster position can be calculated very accurately. With these angles, the cluster size in the respective x and y-directions is expected to be around 2 pixels.

Each telescope mounting block is screwed onto a cradle that can slide over a rails. These aluminum Newport rails and cradles, are commercial pieces that are very accurately machined (10^{-1} mm tolerances), because they are designed for optical bench top experiments that depend on high precision positioning of parts [71]. This is an advantage, as precise mechanical alignment of the telescope planes, eases the software alignment later on during the data analysis.

The auxiliary electronics of the telescope, are drawn in green in Figure 3.3 as well. These motherboards (MBs) are discussed in more detail in Section 3.2.2. They are placed right next to the rails, parallel to the beam direction, because the sacrificial cables connected to the modules are only 26 cm long. Considering that the telescope modules are easily damaged by handling, it is chosen to leave these cables attached, contrary to replacing them by longer twisted pair cables which is standard for the CMS Inner Tracker.

The other objects installed on the rails, are the scintillators and photomultipliers, for triggering the telescope and DUT. The scintillator material selected, is EJ200 (BC408) [72] and the PMs are H11900 Photosensors from Hamamatsu [73].

There are four scintillators in total, two on either end of the telescope. By triggering on the coincidence of signals of all four scintillators, the purity of the trigger signal approaches 99 %. Each scintillator has a surface area of $67 \times 34\,\mathrm{mm}^2$, the same size as the active area of a telescope plane. On each side, one scintillator is mounted horizontally and the other vertically.

During the design process, for two scintillators the light guide was mistakenly connected to the short sides the scintillating material. Therefore, the overlap of scintillators on one end of the telescope is only $34 \times 34\,\mathrm{mm}^2$. If, for the one scintillator on each end, the light guide would

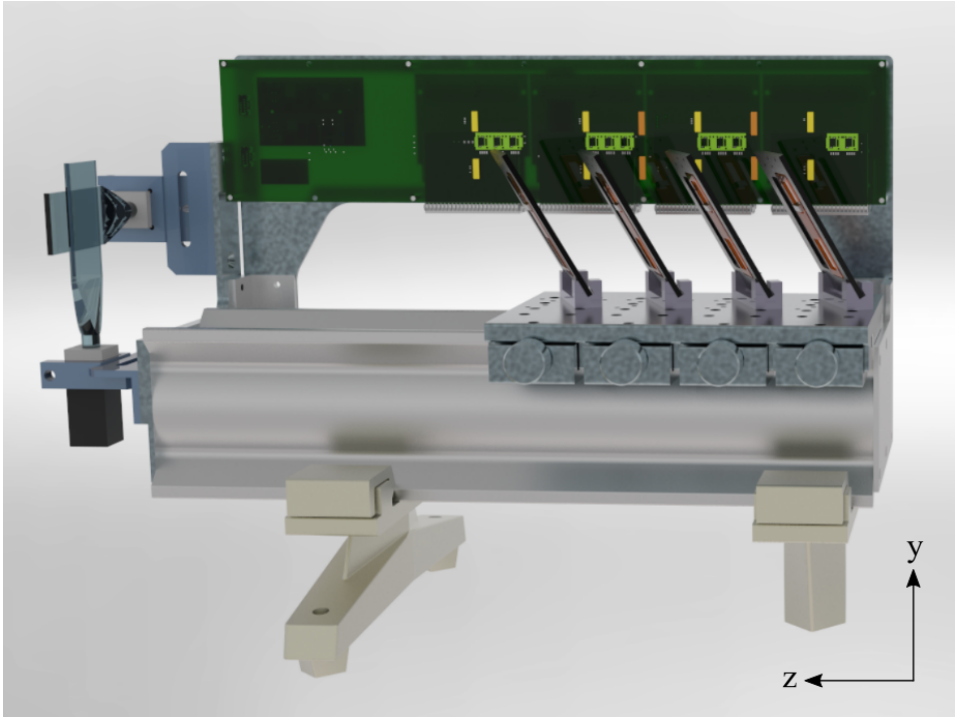

(a) *Front view.*

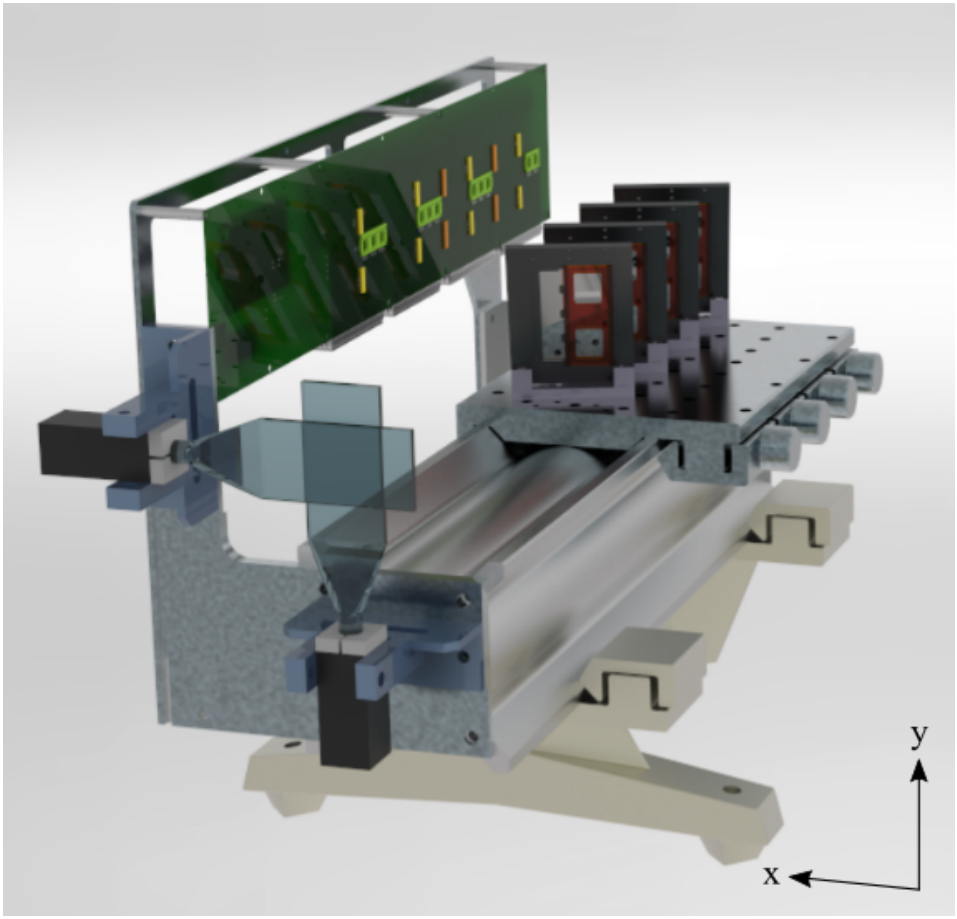

(b) *Side view.*

Figure 3.3. *Telescope rails with cradles for the telescope planes. On one end of the rails, two scintillators are installed. The auxiliary electronics boards of the telescope in green, are fixed parallel to the rails. Rendering in KeyShot [64].*

have been connected to the long end of the plastic, the overlap would have been $32.4 \times 67\,\mathrm{mm}^2$, which is the same size as the active area of a telescope plane.

The PMs connected to the scintillators are held in position by clamps that are screwed to very simple custom rails. This allows for moving them either up and down or left and right, depending on which scintillator is concerned. This is useful when studying the triggering efficiency of the setup.

3.2.2. Electronics design

A diagram of the electronics design of CHROMIE is given in Figure 3.4. It is based on the DAQ of the CMS Phase-1 Inner Tracker [31, 74], explained in Section 1.5. The telescope DAQ is mostly CMS standard, because the telescope was designed to test CMS Tracker modules. This reduced the design effort of the telescope electronics to a minimum. In this section, only the differences between the telescope electronics and the CMS Phase-1 Inner Tracker are clarified.

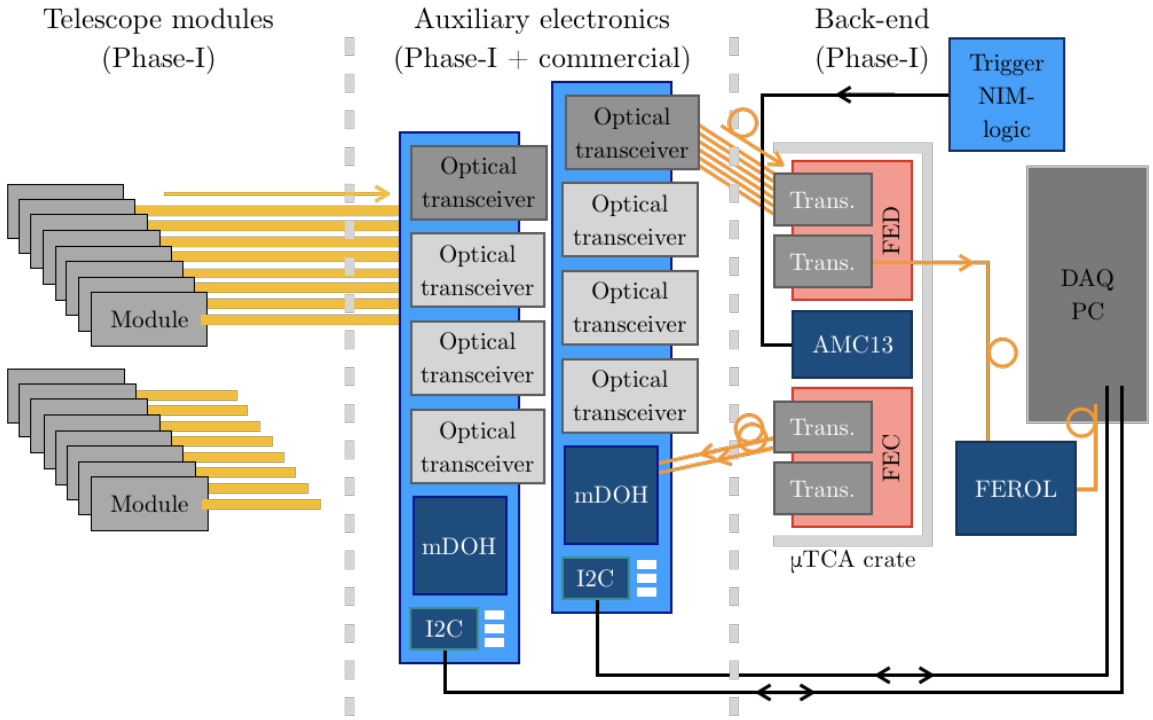

Figure 3.4. *A schematic overview of the DAQ of CHROMIE. Yellow lines represent flat ribbon cables, providing electrical connections. The orange lines represent optical fibers, and the black lines electrical links. The arrows on each link indicate the direction of the signals.*

From left to right in Figure 3.4, the modules, the auxiliary electronics which are both inside the telescope box, and the back-end electronics are drawn. The differences with the Phase-1 Inner Tracker DAQ are mostly in the auxiliary electronics, which are referred to as Service Tube Electronics in CMS. It contains the same electronics pieces as for the Inner Tracker, except for the CCU and DC-DC-converters, see Figure 1.8.

The auxiliary electronics or Motherboards of the telescope, are drawn in Figure 3.5. The MB design is similar to the Service Tube Electronics, however it is more compact in size. The CCU and DC-DC-converters are replaced by commercially available components in the form of an Adafruit FT232H Breakout I^2C master [75] and simple power regulators.

A major adjustment between the service tube electronics and the motherboards, is the replacement of the deprecated POHs. These optical transceivers are substituted by Small

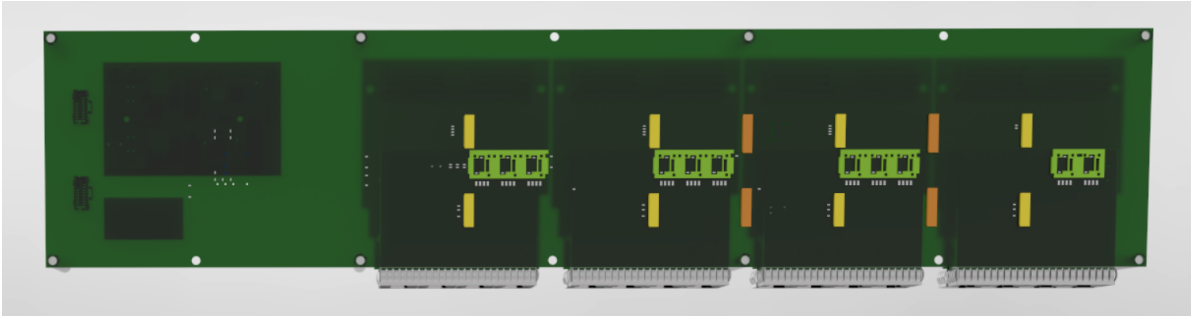

(a) *Front view.*

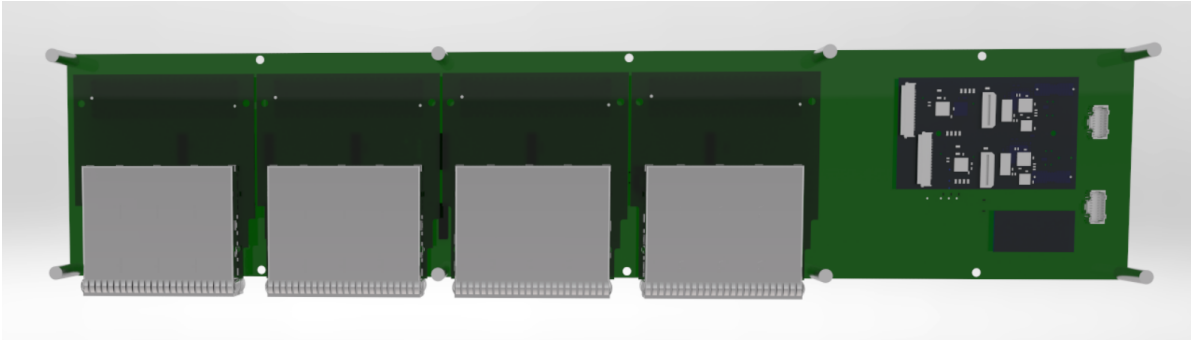

(b) *Back view.*

Figure 3.5. *A front and back view of the telescope's auxiliary electronics, referred to as the motherboard. Rendering in KeyShot [64].*

Form-factor Pluggable (SFP) transceivers on FMC boards, that can be plugged directly into the back of the motherboards, see Figure 3.5b. The grey square objects in that image, are the SFP cages that can carry a total of eight single-mode, 1310 nm 1.25 $\frac{\text{Gbit}}{\text{s}}$ FC/GBE, duplex SFP transceivers [76].

In all, four 8SFP-FMCs can be connected to the motherboard. Depending on which Inner Tracker layer BPix modules are used in the telescope, one or more 8SFP-FMCs are installed. Since the telescope modules are from layer 3, the data density leaving the modules is lower than for layer 1-2 modules [31]. Therefore, only one 8SFP-FMC is required per telescope arm.

On the right side of the MB in Figure 3.5b, the DOH motherboard is connected which hosts an mDOH. The small dark square in the bottom right of the figure is the I^2C master. It plugs into the motherboard and it is linked to a control PC. The connectors for low voltage power to the modules and the motherboard, and the high voltage module bias, are located on the outermost right, visible as white squares.

The modules attach to the front of the motherboards, seen in Figure 3.5a. Their connectors are marked with orange and yellow rectangles. The eight layer 3 BPix modules of a telescope arm connect to the orange connectors, the yellow connectors are for layer 1-2 modules.

The back-end electronics of the telescope is CMS standard. The differences between the telescope's and the Inner Tracker back-end, are the absence of the Tracker FEC and TCDS card. The Tracker FEC controls the CCU rings, which are not used in the telescope. The TCDS board is replaced by NIM logic modules in a NIM crate.

The firmware used for the FED and FEC cards, are `fed version 15.3` and `fec version 1.2` respectively. The AMC13 firmware for the Kintex chip is `AMC13T1v0x225b_7k325t.mcs`. For the Spartan it has a firmware version that is not standard, namely `AMC13T2v0x0032_6slx45t.mcs`. This firmware has a feature that is used to take the to-TTL-converted triggers from the NIM

modules as an input on the AMC13's L1A LEMO connector. Moreover it can output the AMC13 clock on the clock LEMO connector, so that the triggers can be synchronized to it.

3.2.3. Cabling scheme

Figure 3.4 not only demonstrates the different electronics components of the CHROMIE telescope, but also the links between them. The details of the telescope cabling are disclosed in this section.

From left to right, the first connection in the diagram of Figure 3.4 is the sacrificial cable between the module and the motherboard. This is a 26 cm long, flat ribbon, Molex Premo-Flex Cable Jumper [77]. This is an electrical link. The SFPs convert the signals from the modules from electrical to optical, and ship it out via 0.5 m long F-OUT PCORD 12xSM MPOF(12) to 12XLC/PC fibers. The LC connector of this fiber plugs into the SFP, and the MPO side in a patch panel on the inside of the telescope wall. On the outside, an MPO to MPO M-FIBRE PCORD 12xSM fiber links the patch panel to the FED.

The control signals sent to the modules from the FEC, arrive at the motherboard via fibers as well. Inside the telescope, a 0.5 m long F-OUT PCORD 12xSM MPOF(12) to 12XMU/PC connects the fibers from mDOH to the patch panel. On the other side of the patch panel a F-OUT PCORD 12xSM MPOF(12) to 12XLC/PC fiber attaches to the FEC. Both the FED and the FEC fibers on the outside of the telescope are 40 m long.

The I^2C master on the motherboard connects to a computer directly via a Micro B USB to USB2.0 cable. The last two connectors on the motherboard are for module and motherboard power and module bias. The power is supplied over an eight-pin Power Mate Cable Assembly from the manufacturer Samtec [78]. The module bias is provided via the same kind of cable assembly with a four pin connector. The eight and four pin connectors plug into the motherboard, and the cables are soldered directly to the patch panels on the inside of the telescope walls. On the outside there are banana connectors for the low voltage power, and Safe High Voltage (SHV) connectors for the high voltage bias.

On the back-end side, two fibers are needed to connect the FED to the FEROL, and the FEROL to the DAQ pc. Both these fibers are OM3 Multimode, LC to LC. The triggers coming from the NIM logic travel over standard coaxial LEMO cables to the AMC13.

3.2.4. Trigger logic

Figure 3.6 presents a schematic view of the trigger NIM logic used for the telescope. The negative output of the scintillators is the input of the discirminator NIM module on the the left side of the scheme. On the right, the AMC13 is drawn which receives the (a)synchronous trigger as an input on its L1A connector. It also outputs the clock that is used to synchronize the triggers to.

The discriminators on the left take the output of the scintillators, and compare it to a threshold. The threshold level is chosen by counting the number of pulses from the PM during a given time, without a signal present and comparing it to the number of pulses when a radioactive source is placed on the scintillator. The output of the discriminator is a NIM pulse of which the width can be varied manually.

Then all four NIM pulses go to a coincidence unit, which outputs another NIM pulse upon coincidence between either two, three or four of the PM signals, depending on the settings of the unit. This NIM pulse is the asynchronous trigger that can be send directly to the AMC13, after being converted to TTL logic levels.

To obtain a sychronous trigger signal, the clock of the AMC13 is converted to NIM logic. Then it is shaped by another discriminator unit (on the left), after which it is send through a

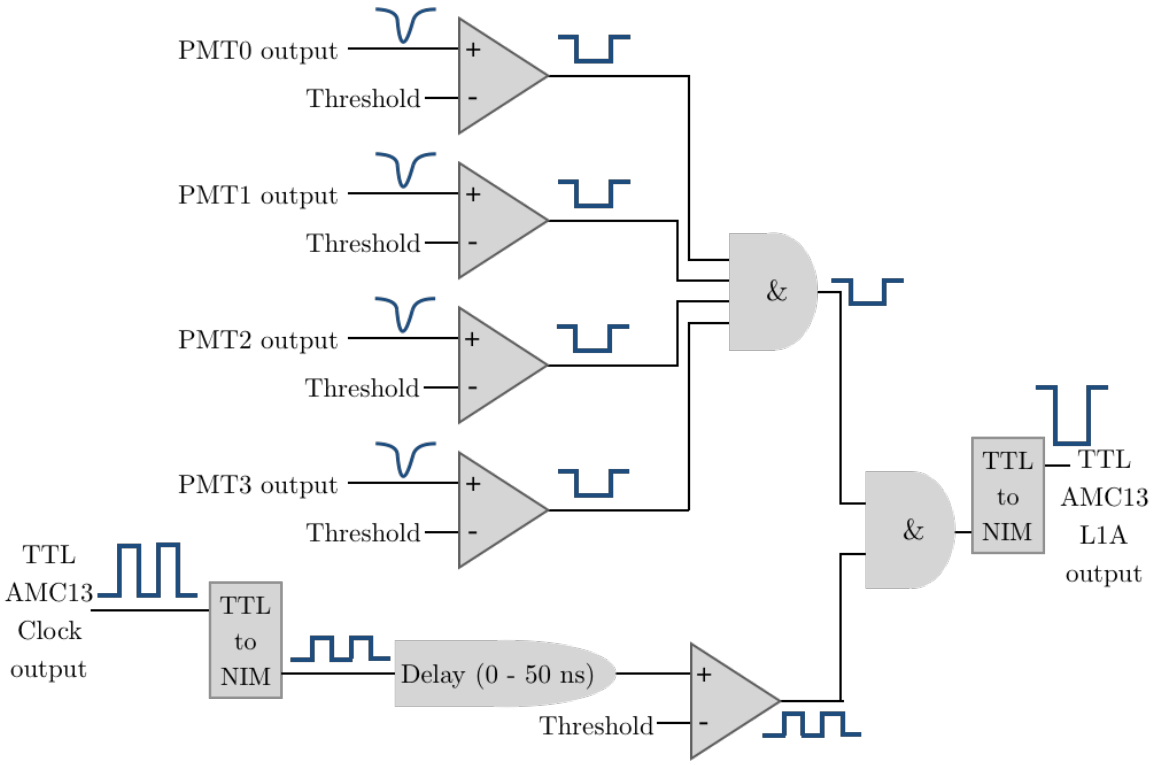

Figure 3.6. *Trigger logic for the CHROMIE triggering system.*

delay unit before it goes into a second coincidence unit (right-hand side of the scheme). If there is coincidence between the asynchronous trigger and the rising edge of the clock, a synchronous NIM trigger is outputted. This has to be converted back to TTL logic before it can be accepted by the AMC13.

The delay module can be used to select a phase between the clock and the asyncrhonous trigger, that reduces the time jitter of the synchronous trigger to a minimum. The jitter on the synchronous trigger was measured to be 5 ns, before entering the AMC13.

The counters in the center of the diagram are used for diagnostics purposes. When testing the trigger logic, a radioactive source is placed on the scintillators and the number of triggers are counted for different configurations.

3.2.5. Software

Just like the modules and the electronics, the DAQ and data analysis software of the CHROMIE telescope are based on CMS standard software. The DAQ software is the Pixel Online Software (POS, [79, 80]) embedded in the Cross-DAQ framework (XDAQ, [81]), and CMSSW is exploited for simulation and data analysis purposes.

An I^2C library is added to POS, to extend its use for the telescope [82]. Furthermore, the `PixelTrkFECSupervisor` is reworked, such that it can send commands to the Adafruit I^2C master as well as to the CCU ring. In addition, the code for the Delay25 calibration is updated, to accommodate the new telescope features.

In order to be able to use CMSSW for the simulation and data analysis of the telescope, its geometry is implemented in the CMSSW XML format. The already existing XML descriptions of BPix modules are applied in the telescope's geometry files. Based on the geometry, CMSSW can reconstruct events measured with the telescope, or obtained from CMSSW simulations. This is referred to as the local reconstruction of events.

CMSSW has tools for track finding and alignment too, however this is currently not yet supported for the telescope. Instead, a custom made tracking and alignment code is used. A more detailed description of this code is provided in Section 3.7.

3.3. System tests and integration of the telescope readout

Before installation of all the electronics components in the telescope box, system tests were executed to verify that a module could be controlled and read out by the full telescope DAQ chain. It proceded in a few stages, which are illustrated in Figure 3.7.

First the back-end electronics were set up. Once all the back-end hardware could be properly configured by the software, the motherboard with all its components was added to the setup and tested. Next, a module was connected to the motherboard, and by manually varying Delay25 settings, a configuration was found for which communication with the module was established. Finally the fiber between the motherboard and the FED was attached to complete the chain. A detailed explanation follows in the next paragraphs.

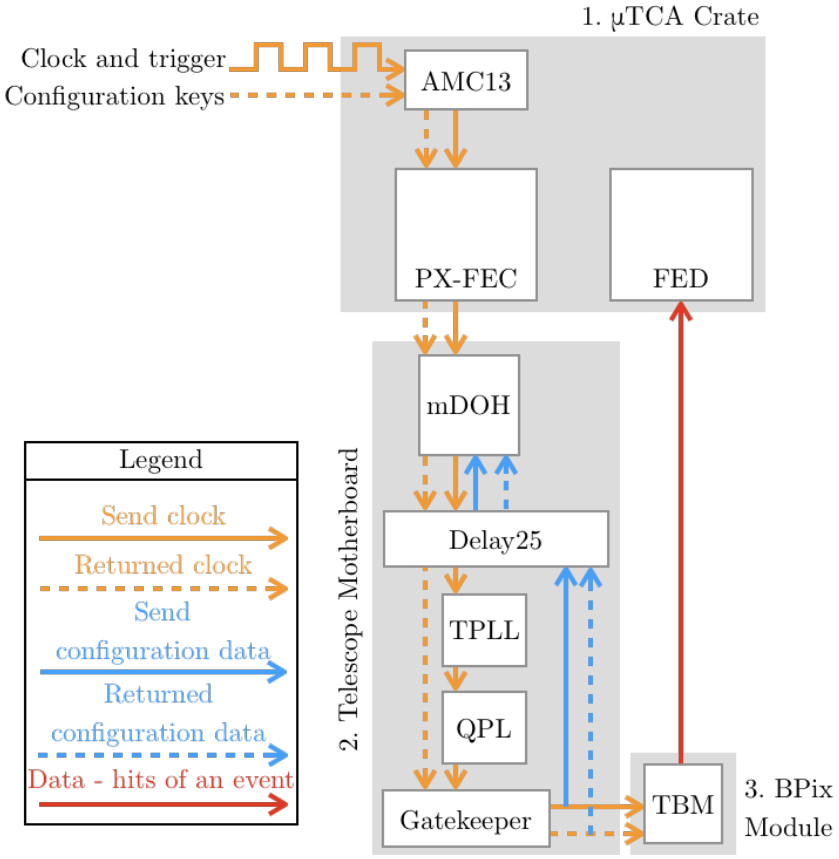

Figure 3.7. *Paths that configuration signals travel from the FEC to the motherboard, and finally the module. The arrow to the FED illustrates where the event data from the modules eventually travels to.*

To start with, the µTCA crate was setup and all the µTCA cards, as well as the AMC13, were installed. After the correct versions of the firmware were flashed, the POS and XDAQ software were used to configure the boards. They only configure if all the settings in the POS configuration files are written up correctly. Testing the configuration files of the software is an important first step during the DAQ testing.

When each of the components of the back-end electronics was correctly configured, the motherboard was connected to the FEC via optical fibers, see Section 3.4. As can be seen in Figure 3.7, both the configuration keys and the clock and trigger, travel from the AMC13 to the modules, via the mDOH, the Delay25 chip, the T/QPLL and the gatekeeper before they arrive at the modules [83–85]. Additionally, they are returned to the Delay25 directly, right after the gatekeeper, which can be used as a confirmation that the signals can travel up to the modules.

For the I^2C protocol to function, a well-defined time shift between the clock and the I^2C data is required. This is accomplished via the use of the Delay25 chip, which can add a delay to both the send and return lines in order to align the signals to the clock. Both the send clock (SCK) and the send data (SDA) line can be probed on the motherboard to verify that they have arrived right before the modules. The return lines can be scoped on the optical fibers leaving mDOH.

This is seen in Figure 3.8; the send clock is the bottom yellow and the return clock is the top blue curve. By changing the Delay25 settings, the return clock was delayed by 12.5 ns with respect to the send clock in that figure.

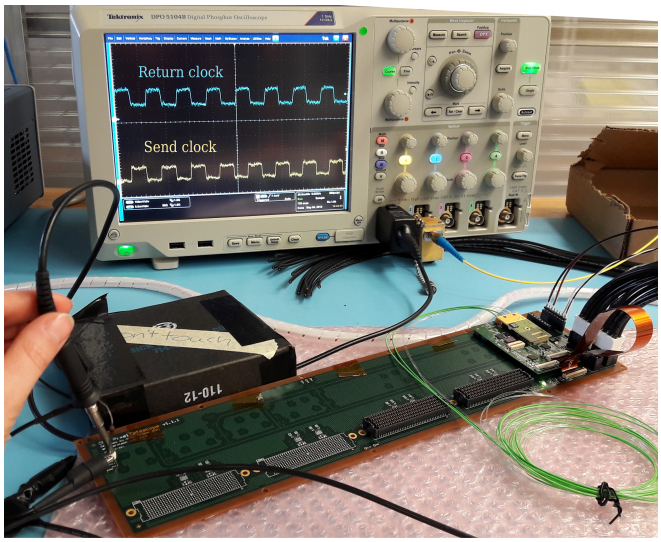

Figure 3.8. *The send clock (bottom yellow) probed on the motherboard and the return clock scoped on the return clock fiber (top blue).*

Once I^2C communication was established, one module was connected to the motherboard. At a given SCK, the SDA delay was varied manually until a setting was found with which the module could be configured. This was validated by monitoring the current of the analog module power. When configured, a BPix module draws ∼600 mA of current on the analog line, while if it is not (correctly) configured, it draws only ∼80 mA.

Subsequently to the successful configuration of the module, the fiber between the associated SFP on the MB and the FED was attached. Upon issuing the configuration of the system through the software, the FED will adjust the phase between the incoming and outgoing light of the bi-directional optical link. If all components in the DAQ chain are accurately configured, the FED will find the correct phase adjustment settings which are outputted on the DAQ computer's screen. Together with the increase in analog power consumption, this proved that the full DAQ chain was made operational.

3.4. Construction

Before assembling the telescope, the grade-C, layer 3 BPix modules were selected from a set of ∼40 modules that were made available for the telescope. Common problems of grade-C modules are a large fraction of dead pixels, or even dead readout chips or high leakage current or IV-curve. As a result of these issues, roughly half of the available grade-C modules could not be used in the telescope. The other half was tested and calibrated with a Digital Test Board (DTB) and pixel expert analysis and readout (pXar) software, [86–88]. Based on these test results, a final selection of telescope modules was made. For more information on testing and calibrating the modules with DTBs and pXar, see Section 3.5.1.

The selected modules were then glued onto the module frames, of which a picture is shown in Figure 3.9. It shows one module glued to a frame, leaving an open space for a second module. After curing the glue for 24 h, the telescope plane was finalized by gluing a second module to the other side of the frame.

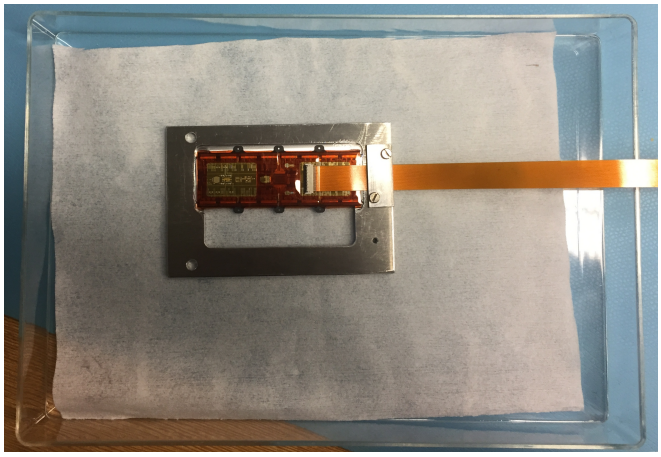

Figure 3.9. *One module glued on a telescope frame. A second module was later glued to the back of same frame to complete a telescope plane.*

Following the assembly of the mechanical structures of the telescope the motherboards were mounted on their supports, and the cabling was put in place according to the plan laid out in Section 3.2.3. Then, the telescope planes were fixed on their cradles one by one. Before going to the next plane, the two modules would be configured separately, to confirm that each module was connected to the right optical fiber. At every iteration, the analog current of the modules was monitored to verify that this was the case.

Since some modules have dead pixels and even dead areas, the modules were placed in the telescope such that the dead areas would not overlap with each other from the beam's point of view. This resulted in the module locations, displayed in Figure 3.10. This gives a side view of the telescope with the DUT in the middle. The right arm is called the Upstream arm and on the left is the Downstream arm. Each arm has Layers 0 to 3, with layer 0 always being on the outermost downstream side. A plane has an Inside (I) and an Outside (O) module, where the Inside module is closest to the auxiliary electronics. The red coordinate system, specifies the global coordinates that are adopted from CMSSW. On the bottom of the module map, the numbering of the ROCs in a BPix module is demonstrated as well. The telescope modules are identified by the readout through a hardware address. A summary of the module identification scheme is given in Appendix A.

A photograph of the fully constructed telescope is displayed in Figure 3.11a. Both telescope arms and their auxiliary electronics are visible in this photograph. The fans cooling the

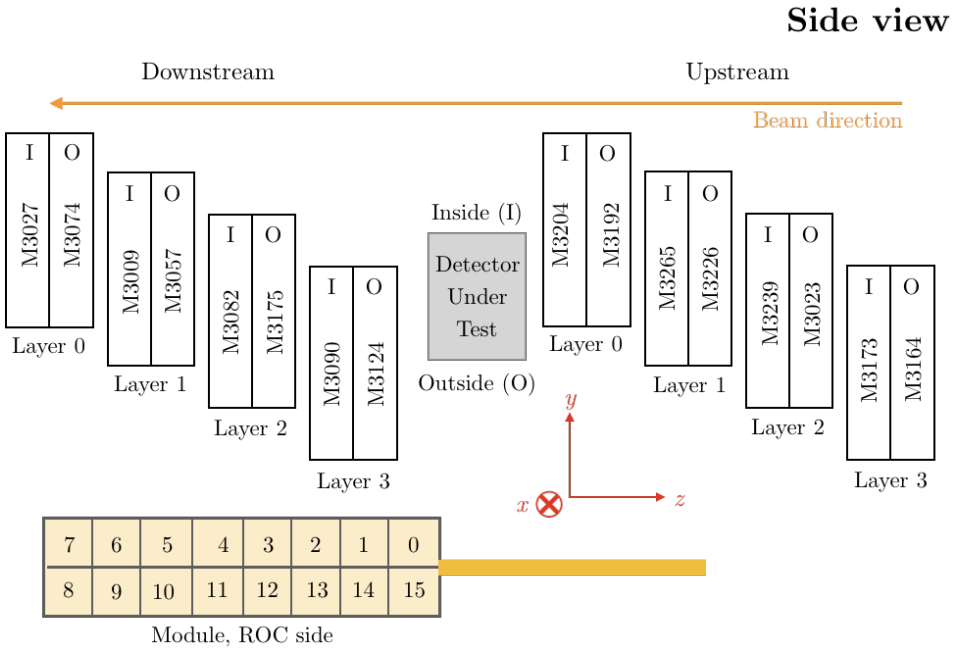

Figure 3.10. *A map with the locations of each module as it was installed in the telescope. The red coordinate system shows the CMSSW coordinates. The arrow at the top of the image specifies the beam direction.*

telescope can be seen hanging from the ceiling. The colored fibers bringing control signals to and leading data away from the modules, show up throughout the image. The rotational stage in the center does not hold a DUT in this photograph. It can be identified by a silver colored round plate in the center of the bottom of the photograph. In Figure 3.11b a close-up photograph of the downstream arm is shown. The four telescope layers in this arm can be seen mounted on the cradles that can slide over the aluminum rails in the bottom of the photograph. The green printed circuit board in the back of the photograph is the motherboard to which the sacrificial cables of the modules are connected. From the back of the motherboard the SFP cages stick out and the optical fibers are plugged into them.

3.5. Calibration of the telescope

Five steps were involved in the calibration of CHROMIE which are all explained in more detail in the subsections below. First individual modules were calibrated via the use of a DTB and pXar software, before they were installed in the telescope [89, 90]. This is explained in Section 3.5.1. After the modules had been mounted in the setup, first the Delay25 had to be tuned, see Section 3.5.2. This was followed by the calibration of the calibration pulse delay, CalDel, described in Section 3.5.3. Next was the calibration of the threshold, which is illustrated in Section 3.5.4. The final step was the calibration of the pixel gain of which the values are used during the offline reconstruction of clusters, as described in Section 3.5.5.

The Delay25 tuning, calibration pulse delay and threshold calibration and the gain calibration are all performed using the POS software [79, 80, 91]. The first round of calibrations was done in the lab to ensure that the telescope's modules were all in good working order since installing them in the telescope. When the telescope was moved to a beam area, it was calibrated again before data taking commenced, to validate that all modules were still functioning well.

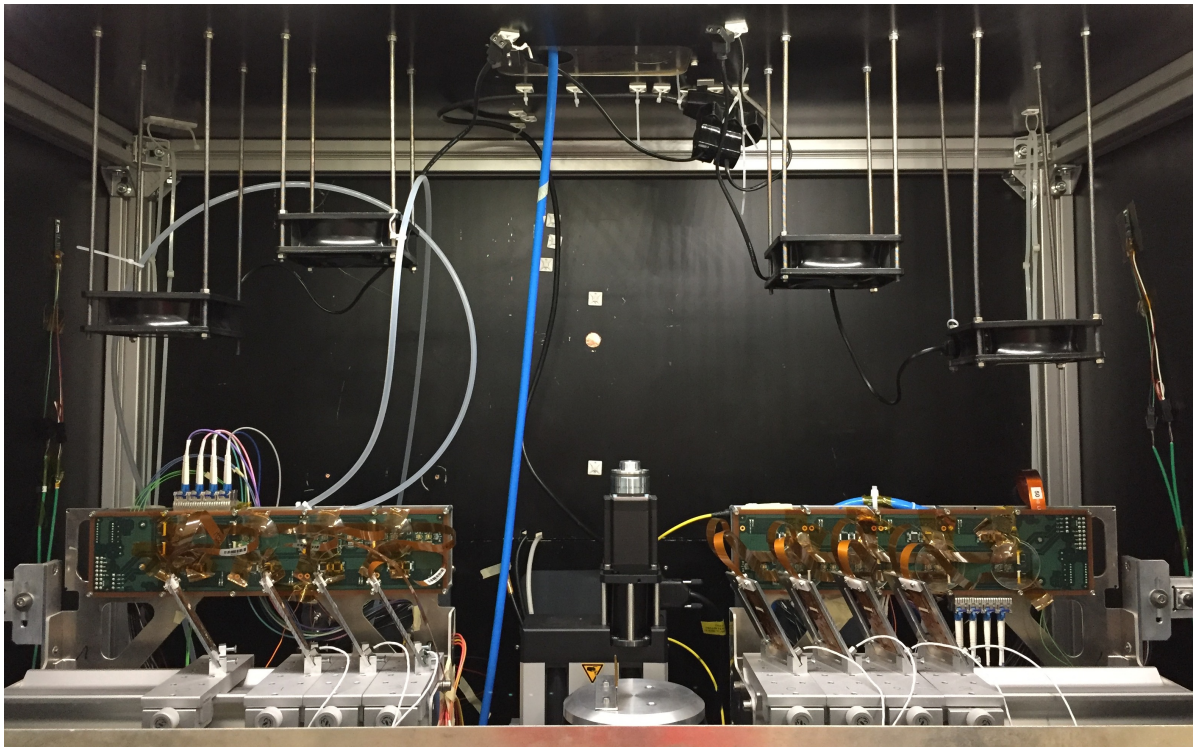

(a) *A full-view of the CHROMIE Telescope.*

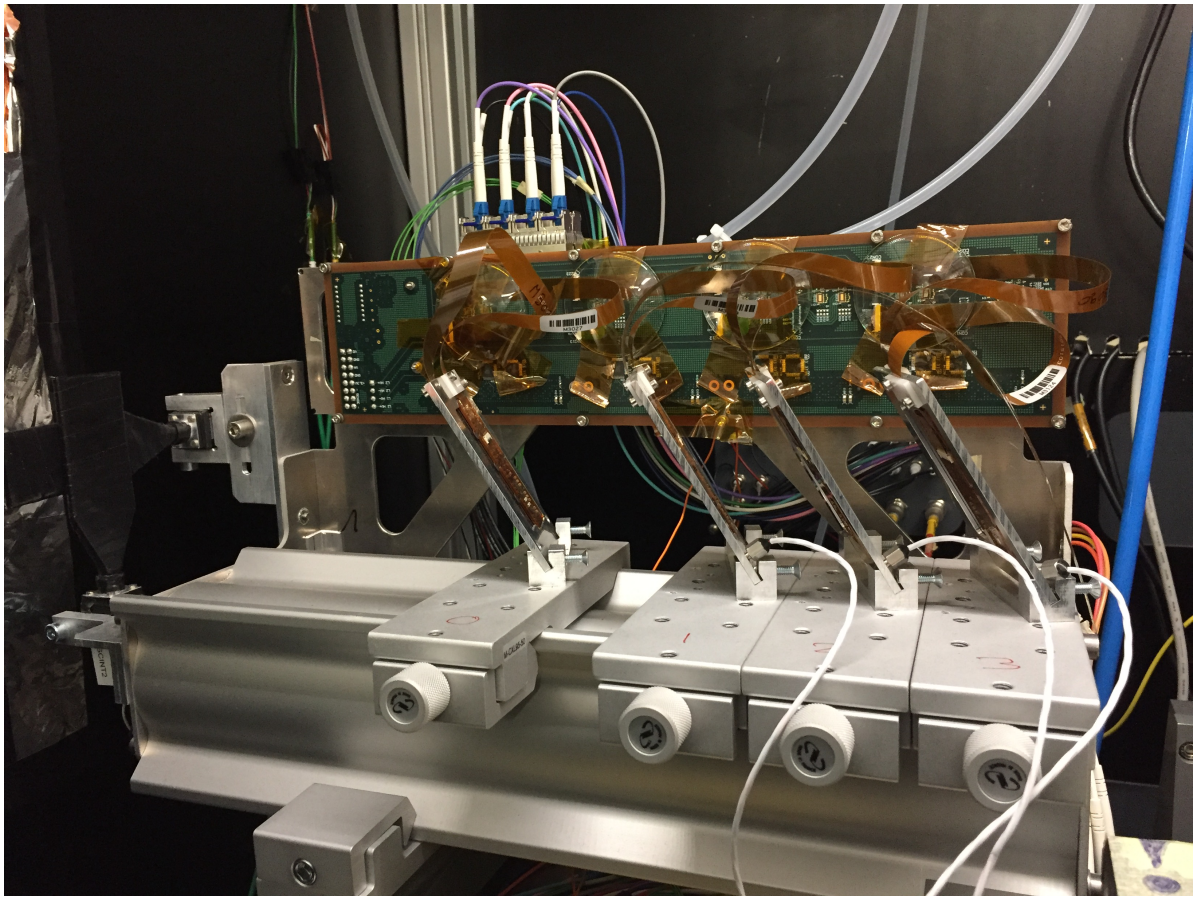

(b) *A close-up view of the downstream arm of the CHROMIE telescope.*

3.5.1. pXar calibrations

pXar calibrations are performed to obtain initial values for the DAC settings of the modules. This includes the threshold comparator voltage level ($V_{ThrComp}$), the global threshold scale (V_{trim}) and the trim bits per individual readout channel. For BPix modules, threshold and calibration pulse height are expressed in V_{Cal} DAC units. Therefore the first thing that has to be determined is the quantity of a V_{Cal} unit expressed in number of electrons. This was achieved in a similar manner as for the CBC2 mini module, which was explained earlier in Chapter 2. The intricate details of this procedure for BPix modules, are laid out in [54, 87].

Once the V_{Cal} unit for a given module is calibrated, $V_{ThrComp}$, V_{trim}, as well as the pixel trim bits are tuned. This process is called trimming. During this operation, $V_{ThrComp}$ is set in such a way that the pixel with the lowest threshold is above the target threshold. Then V_{trim} and the trim bits are tuned such that the threshold distribution of all channels is as narrow as possible. The result is a uniform response to a fixed signal over the whole module.

The settings found with the DTB and pXar were then converted to make them readable by POS so that they could be used when the modules are operated in the telescope.

3.5.2. Tuning of the Delay25 settings

To configure the telescope modules, I^2C commands are used that are send by the FEC. These signals travel back an forth via the Delay25 chip, which adds a delay to their arrival time (see Figure 3.7). To guarantee that the I^2C data can be properly decoded, the phase between the data lines and the clock needs to be correctly adjusted. Seeing that I^2C signals are used to configure modules, it is the first calibration that had to be executed once the modules were installed in the telescope.

The results of a Delay25 calibration of the telescope are shown in Figure 3.12. The most important settings are the SDA and RDA, which represent the delay on the send data and return data respectively. For a given delay on the clock line, consecutive signals are sent over the data line, and the number of times they return is counted. This is done iteratively, while SDA and RDA are varied until a working point is found.

In Figure 3.12 the grey dots mark where signals return successfully after sending. The bigger and darker the dot, the more often a signal actually returns for a given set of values; black dots mean that a 100 % of the send signals returns. The yellow dot represents the point that the algorithm in POS had chosen to have ideal delay times. It finds a point in the center of a good region where a 100 % of signals returns, to be as far away from lesser efficient settings as possible.

Two diagonal shapes with dark centers are observed in the plot. This is because for each clock cycle, a similar region is found for which the I^2C protocol works properly. The diagonal shows the relation between the delay on the send data and the delay on the return data, which are obviously correlated.

3.5.3. Calibration pulse delay

The module threshold calibration depends on the calibration pulse, which is send by the ROCs. Whether a pixel detects the input charge or not, depends on its pulse height and on the time the readout chip is triggered after the pulse was send. This is depicted in Figure 3.13 where it can be seen that only if the combination of both the trigger latency and the calibration pulse delay is right, the signal is detected. Therefore, the optimal delay of the calibration pulse (CalDel) needs to be determined first.

Figure 3.14 shows the result of a Calibration Delay (CalDel) calibration. It is a plot of the trigger latency in clock cycles, versus CalDel, showing the number of pulses that are actually

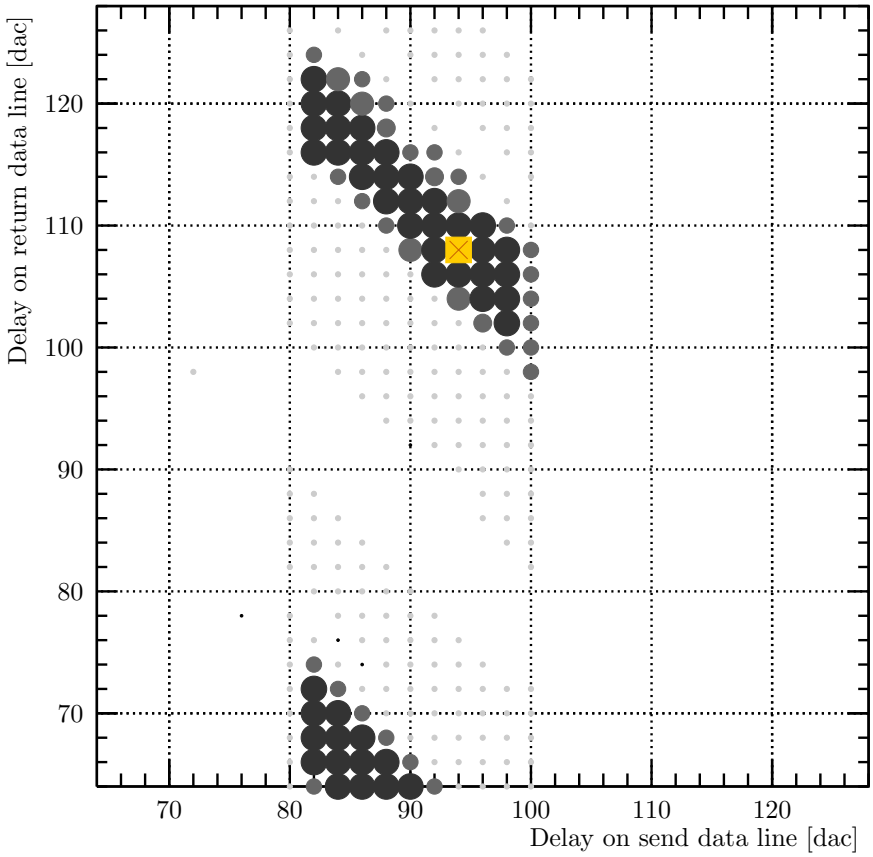

Figure 3.12. *Example result of a Delay25 calibration of the telescope. The gray and black dots represent the amount of times the send signal actually returned for a set of SDA and RDA values. The black marks represent* 100 % *of the send signals returned, and the smaller and grayer the dot, the less times the send signal returned. The yellow marker in the center shows the settings that have been selected by the calibration algorithm of the Pixel Online Software.*

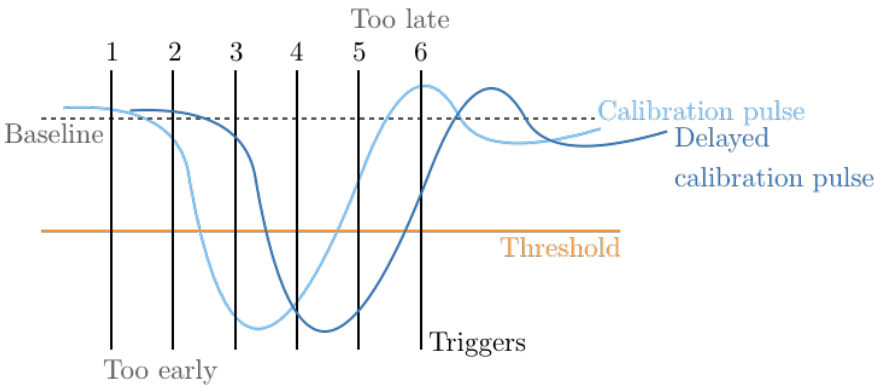

Figure 3.13. *Illustration of how the latency between the calibration pulse and the trigger affects whether the signal is being detected or not. For the first calibration pulse (light blue), only for trigger numbers three and four the signal is detected. However when the calibration pulse is delayed (dark blue), triggers four and five result in the signal being detected.*

detected by the ROC (the efficiency) in different shades of grey. A two-dimensional scan is ran, and at each scan step a calibration pulse with a large pulse height and a given delay and trigger latency, is injected into the pixel. The amount of times a hit was detected is plotted in Figure 3.14. The orange cross indicates the best combination of settings according to the software. For a given trigger latency, the algorithm picks a calibration delay at the beginning of the efficient range. This ensures that signals that are less strong, and thus take longer to cross the threshold, can still be detected. A trigger latency step is one clock cycle long, or 25 ns. Consequently, each time the the calibration pulse is delayed by 25 ns, the ability to detect a hit with 100 % efficiency moves to the next trigger latency setting. This results in a diagonal pattern as is visible in Figure 3.14.

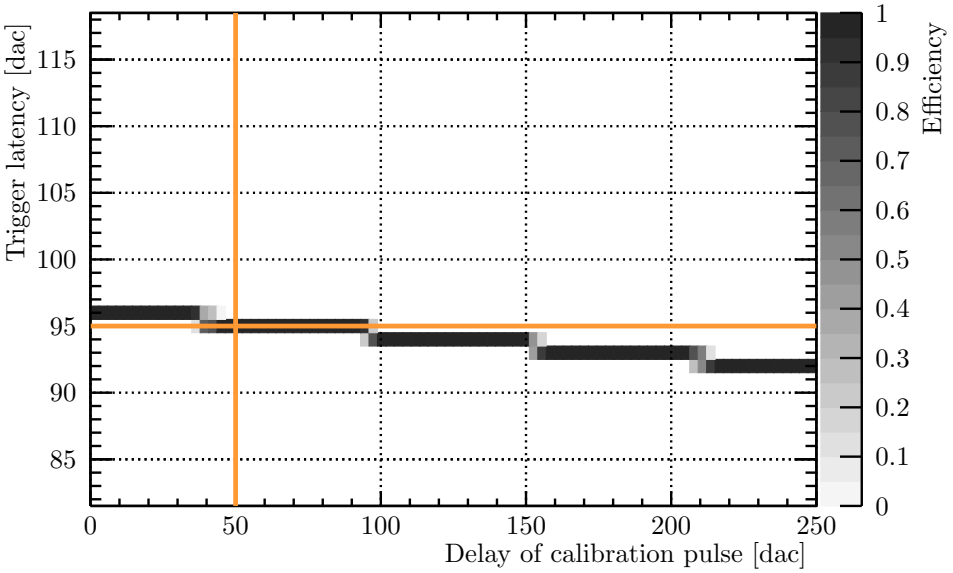

Figure 3.14. *Trigger latency versus calibration pulse delay after a calibration pulse delay scan with a telescope module. The orange cross shows which settings the algorithm picks.*

3.5.4. Threshold calibration

The threshold setting, $V_{ThrComp}$, is calibrated with the calibration pulse. A result of a threshold calibration with the telescope is shown in Figure 3.15. It shows a two dimensional scan of the $V_{ThrComp}$ setting versus the CalDel. The grey scale gives the efficiency of the ROC detecting a signal after the calibration pulse is sent. The top of this so-called tornado plot has a straight horizontal shape. This is the baseline of the calibration pulse. Since the pulse is negative, the higher the $V_{ThrComp}$, the lower the threshold. The right side of the contour can be seen as the rising edge of the negative signal. For a decreasing CalDel the pulse is seen going back in time, which makes up for the characteristic shape of the plot. For low thresholds, and thus high $V_{ThrComp}$ (above 130 $V_{ThrComp}$ in Figure 3.15), the efficiency is zero because of the dead time of the pixels. The algorithm selects the optimum threshold, by choosing a point 40 $V_{ThrComp}$ units below the top of the tornado plot, in the middle of the CalDel range. In Figure 3.15, this is indicated by orange lines.

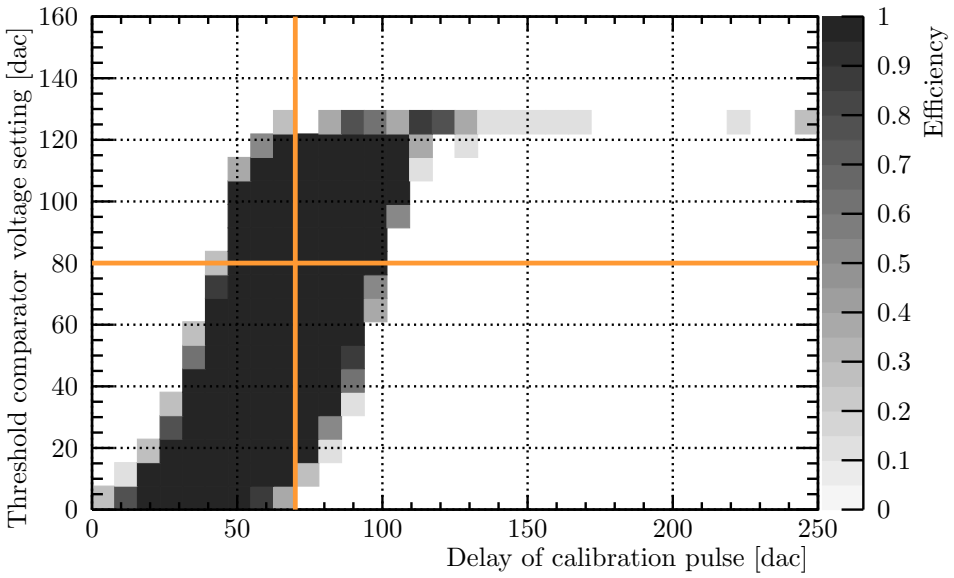

Figure 3.15. *A so-called tornado plot obtained with the telescope DAQ and a telescope module. It shows the threshold comparator voltage setting versus calibration pulse delay after the threshold calibration. The orange cross shows the settings that the algorithm selected.*

3.5.5. Gain calibration

The gain of a pixel is a measure of the pulse height of its output signal, for a known input charge. For a large part of the V_{Cal} range, the pixel response is proportional to the injected charge. When the pixel response reaches its maximum, a plateau is observed in the gain. This is shown in Figure 3.16, where the output pulse height in ADC is plotted as function of V_{Cal} .

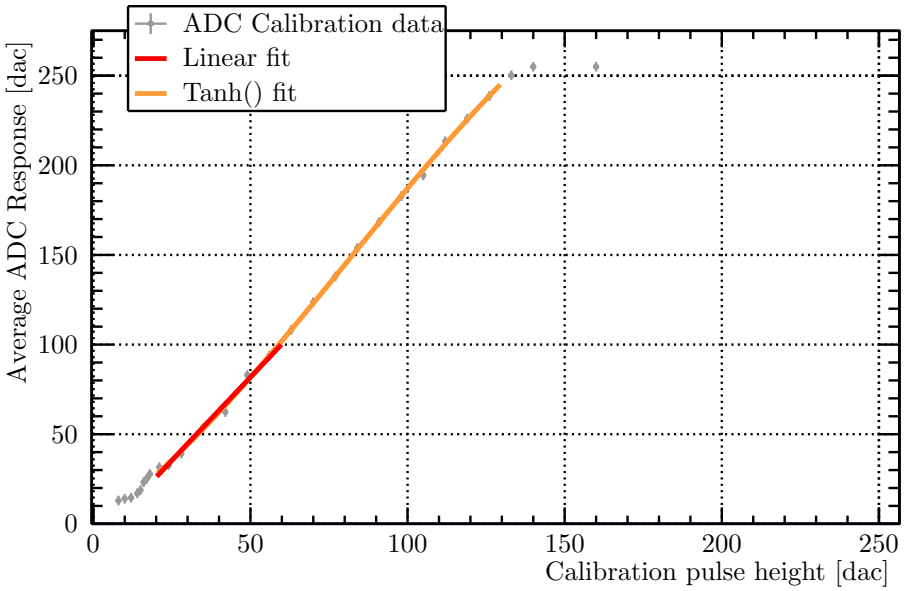

Figure 3.16. *Average ADC response versus* V_{Cal} *after the gain calibration of a telescope module.*

In order to determine the gain and the pedestal of each pixel, the pixel output in ADC counts is measured for different input charges. This is done in the firmware by looping over each pixel, while sending multiple calibration signals with increasing pulse heights. Then the software performs a fit to the linear part of the data, yielding the gain (slope) and the pedestal (offset). Either a linear function, or a tanh() function are used to fit. Results of both are shown in Figure 3.16 as well.

Later in the offline analysis of telescope data the gain calibration values are used to reconstruct clusters, where the pixel pulse height in ADC counts is converted into charge. The exact location of a cluster is found by looking at the amount of charge each pixel in a cluster measured.

3.6. Telescope commissioning

For the commissioning of the telescope, CHROMIE was taken to the H6A beam line at the SPS. It was installed on a so-called DESY table, that has a large flat surface which can be remotely controlled to move horizontally and vertically [92]. This provided the possibility to align the telescope to the beam, without having to enter the experimental area. Moreover, the telescope could be brought in and out of the beam, which was advantageous during the commissioning process, as in case of problems a calibration could be repeated without the interference of the beam particles.

During the calibrations in the beam area, it was observed that two modules in the telescope could not be configured anymore, namely M3057 and M3175. Several different efforts, with for instance different Delay25 settings or connecting only one of the two not responding modules were tried, none leading to a solution. Therefore they were physically disconnected from the telescope motherboards, to prevent damage from applying bias voltage to not configured modules.

3.6.1. Diagnostics tools

During commissioning, a few diagnostics tools were used to prove that the telescope was working correctly, or to debug problems. It is always paramount to monitor the analog current drawn by the modules, to ensure that they are configured well. On top of that, the FED has to have found a good working point for sending and receiving data over the optical fibers, which can be checked by looking at the FED phases printed out by the POS.

Then there is the `pixel_dashboard.py` tool that monitors the status of the FED firmware [93]. The FED can either be `READY` (`RDY`), `BUSY` (`BSY`) or `OUT OF SYNC` (`OOS`) [94]. Whenever it is in the `RDY` state, data can be taken without any complications. When it is `BSY`, its buffers are most likely full, and it is busy shipping out data to the FEROL. Usually it should recover from this state as soon as the buffers have been emptied. The `OOS` state is more serious, this means that the number of events coming from the modules does not match the number of events that the FED has counted. It can usually be recovered from by sending a re-synchronization command in between triggers. If the system does not recover after the re-synchronization, the dashboard tool provides information in the form of error statements, to investigate the problem.

A few possible errors can be distinguished. For instance the Time Out (TO) error, which can be seen in the dashboard tool if it occurs. This happens when the FED is expecting data from a module because it has received a trigger, but no event data has arrived after a specific amount of time. After 254 TO errors, the FED is programmed to go out of sync. A different error occurs when there is a mismatch between the event number from the module and the event number from the FED. This is called an Event Number Error (ENE) and it can also be monitored with the dashboard tool.

The dashboard tool can be used during the operation of the telescope since it is an online tool. At the end of each run, the FED also sends an error status file to the DAQ PC, which can be analyzed offline to find a summary of the status of the FED and the errors that occurred during the run.

3.6.2. Cooling problems

After construction it was observed that the sacrificial cables were moving excessively under the influence of the moving air created by the fans. As this can lead to the destruction of the cables caused by metal fatigue, it was decided to turn the fans off. Due to the fact that the modules were not irradiated before, this should normally not cause any harm to them.

After the first few hours of running the telescope without the fans turning, the modules did not configure anymore and also the FED phases were not found correctly. This was attributed to the overheating of the SFPs and the warming up of one or a few ASICs on the motherboard, causing them to behave differently. The telescope was turned off immediately, and the cooling protocol of the telescope was revised.

To establish air circulation in the telescope without moving the module's cables, the fans were turned up-side down. This assures air circulation without the fans blowing directly towards the modules, instead they extract the air away from them. Nonetheless, this did not provide enough cooling power aimed at the laser drivers, and thus tubes leading pressurized air directly to the SFPs were installed. The tubes were positioned in such a manner, that the air forced through the tubes did not go in the direction of the modules. In addition, additional temperature and humidity sensors were installed on the SFP cages and the module frames, to measure the temperature more accurately.

With this new cooling scheme in place, nor the SFPs, neither the ASICs on the MB would overheat, and safe telescope operation was guaranteed by monitoring the temperature sensors on the SFP cages and the module frames.

3.6.3. Problems during initial runs

After the remaining fourteen modules were configured and calibrated (modules M3057 and M3175 were disconnected at this point), the telescope was moved into the beam to take the first data with MIP particles coming from the SPS. During the first runs with the telescope, as soon as the triggers would start to arrive at the FED (Section 3.2.4), the FED either went to the `OOS` or `BSY` state. From the dashboard tool it was determined that when the FED flaged `OOS`, it was caused by a few modules having ENEs. The `BSY` was not understood in the beginning, so at first the ENE problem were debugged.

To understand the `OOS` problem of the telescope, first the sequence of errors was analyzed more carefully with the help of the offline FED error data. It was found that each time the FED went to `OOS`, first most of the modules would cause for a TO error, and from that moment on they would have ENEs. This can be understood by seeing that whenever a module times out, by the time the FED receives the event data it has already received the next trigger. This was observed in the offline error data, where the event number of each module and the FED are given as well.

To fix the `OOS` problem, the modules that had TO+ENEs were removed from the readout, after which a new run was taking without them. During this run, the FED went to `OOS` as well, now because of other modules having TO+ENEs. Again these modules were removed from the DAQ chain and a new run was taken. This was repeated until a run could be taken, for which the system was operating stably. At that moment, only two modules were left in the DAQ,

but the FED remained RDY throughout the duration of a run, during which a large number of events ($\sim 1 \times 10^7$) was taken.

This behavior of having TO+ENEs when more than two modules were used to take data, signaled a timing problem of for instance an incorrect trigger latency setting. Therefore a trigger latency scan was taken, which is presented in the next section.

3.6.4. Scanning the latency

After the initial round of commissioning which resulted in two modules that could be ran stably, a trigger latency scan was carried out. The objective of this scan is to find a latency setting at which the highest number of clusters would be registered by the modules. This improves the overall readout, as it aids the modules to send the data out to the FED within the expected time frame.

The results of the latency are given in Figure 3.17. For most of the values in the trigger latency scan range, the number of clusters per event was ~0. Except for between latency 30 and 35 clock cycles, where there was a peak observed at 32 clock cycles. In bin 33, clusters were found as well, which was due to the jitter on the trigger. The jitter was measured to be 5 ns before the AMC13. The jitter on the trigger after processing by the AMC13, can be estimated by varying the delay on the clock before the trigger is synchronized to it, and looking at the cluster rate in the telescope for different clock delays. Due to time constraints, this scan has not been performed.

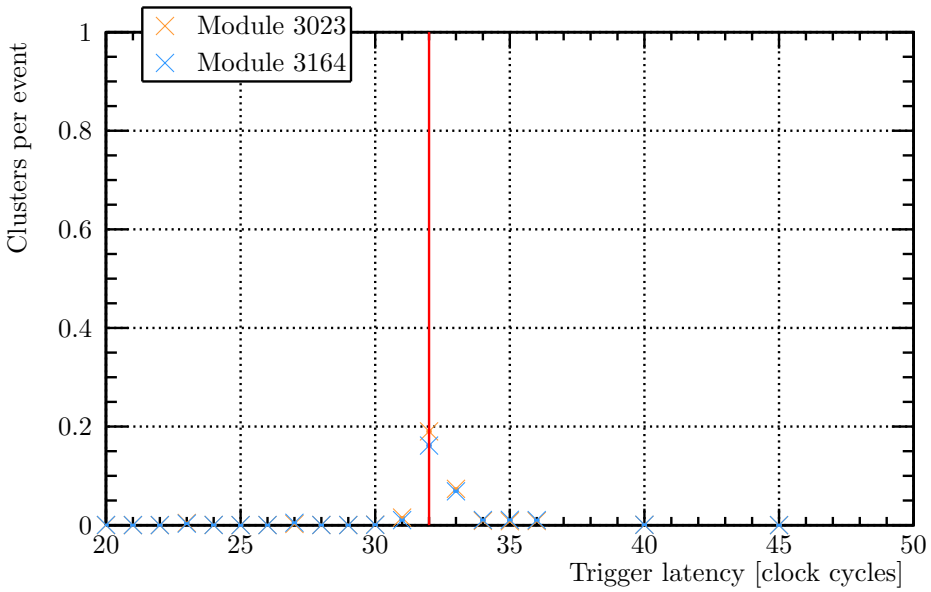

Figure 3.17. *The number of clusters per event versus the trigger latency, while the telescope was taking data in the H6A beam line of CERN's SPS. Only two modules were included in the readout during this scan.*

The number of clusters per event at 32 clock cycles is close to 0.2 in Figure 3.17. If the beam was aligned exactly on the center of the telescope planes, 0.5 clusters per event would be expected per module. If there is an overlap between the modules, the expected cluster rate in a module is slightly bigger than 0.5 and it is proportional to the area of overlap. Therefore the results in Figure 3.17 indicate that the beam was not centered on the middle of each telescope plane, as only in 20 % of the triggers, clusters are found in modules M3023 and M3164 (see Figure 3.10).

With this latency setting, more and more modules were added back to the readout, and while taking runs with all these detector configurations, the FED would not go out of sync. With all the modules in the Upstream arm back in the readout, another trigger latency scan was performed with only eight steps around the 32 clock cycles latency setting. The results are shown in Figure 3.18. Again, the trigger latency with the most clusters per event is at 32 clock cycles as expected, and a smaller number of clusters is found in the bins on either side of bin 32.

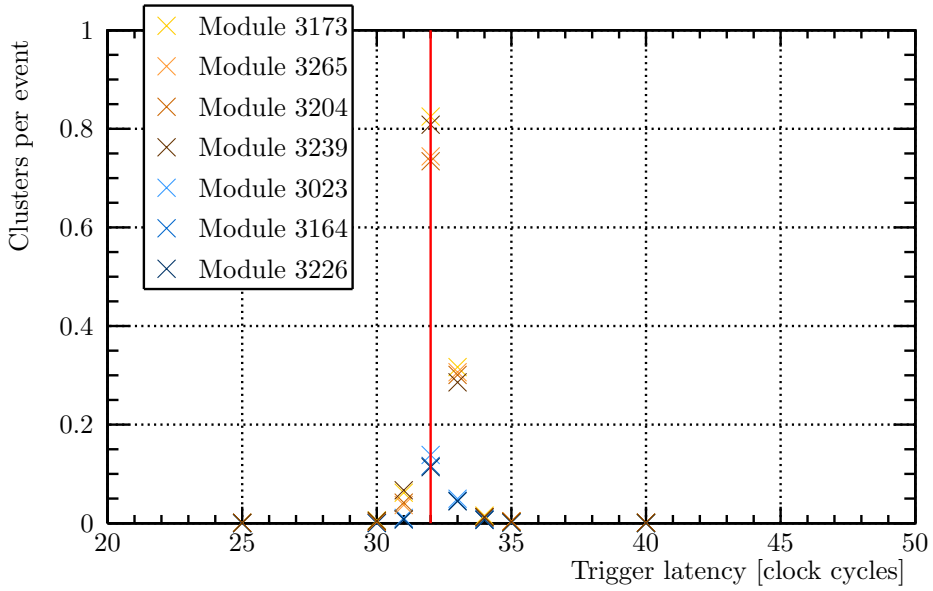

Figure 3.18. *The number of cluster per event versus the trigger latency, while the telescope was taking data in the H6A beam line of CERN's SPS. All eight modules of the Upstream arm were included in the readout during this scan. The results of M3192 are not included in this plot because the large amount of noisy pixels in the module heavily effect the number of cluster in each event to much.*

In Figure 3.18, there is a clear difference between the modules close to the auxiliary electronics (Inside, see Figure 3.10), and the modules on the Outside. The Inside modules have a maximum cluster rate around 0.75, while the Outside modules have on average 0.15 clusters per event at the correct trigger latency. This can be explained by the beam position that is off-center, and mostly covering the Inside modules which is confirmed in Figure 3.19. It displays the number of hits accumulated in modules M3164 and M3173, during the run with a trigger latency of 32 clock cycles. Most of the hits are recorded in the Inside module M3173. When the maximum cluster rates in the Inside and Outside modules are added up, a trigger efficiency of 90 % is obtained. This is caused by the trigger jitter of the system; a significant number of cluster is still detected in the two bins beside the bin at 32 clock cycles.

During the latency scans, the FED would often go into the `BSY` state, as was observed before. It was discovered that this was caused by using the wrong type of optical fiber. Right after the construction of the telescope, one of the fibers between the FED, the DAQ PC and the FEROL was a single-mode fiber while both fibers should have been multi-mode, see Section 3.2.3. At some point during the commissioning, both fibers were switched for single-mode fibers, which was not known at the time. After this exchange the FED would be `BUSY` all the time for each run. When this was realized, both of fibers were replaced again by multi-mode fibers and the problem disappeared. This all can be explained by the FED not being capable of shipping the

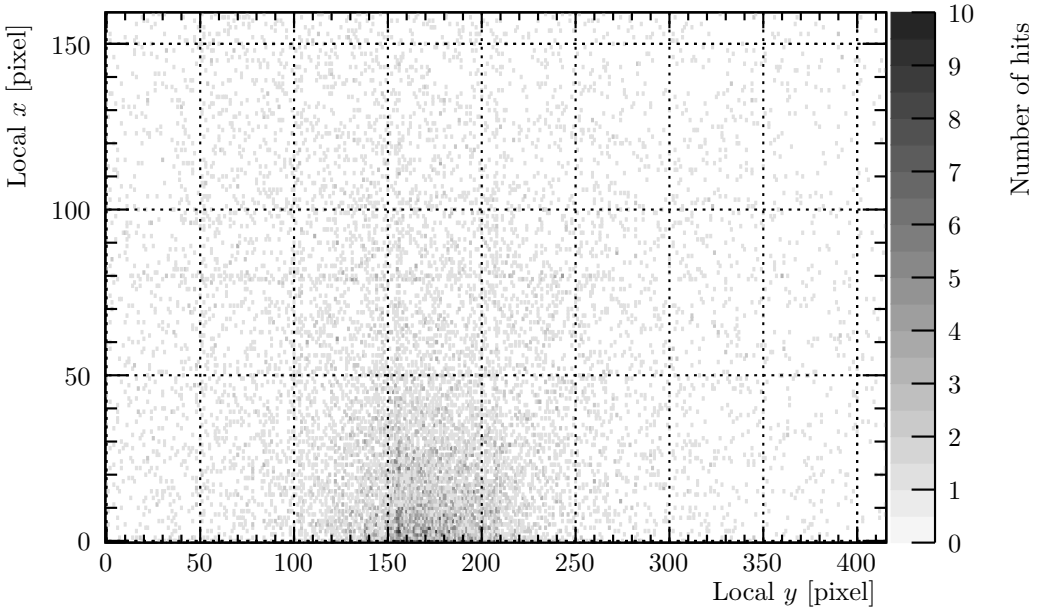

(a) *Module 3164.*

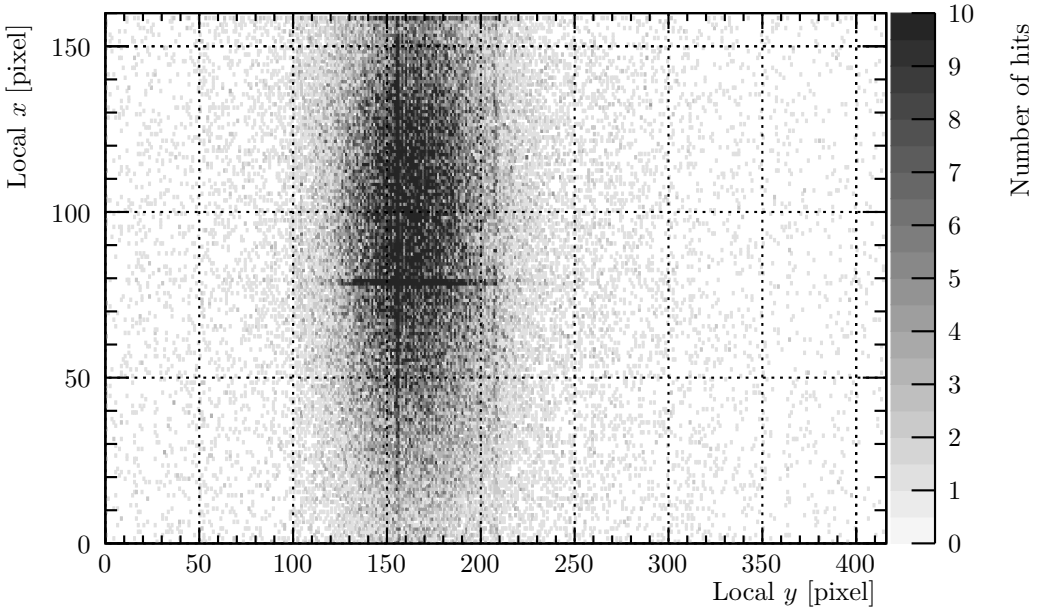

(b) *Module 3173.*

Figure 3.19. *Number of hits in module M3164 and M3173, accumulated during a test beam run with the telescope, during a run at nominal trigger latency of* 32 *clock cycles. During the latency scan, the beam mostly hits one half of the telescope.*

data out fast enough with single-mode fibers and thus it goes into the BSY state and never recovers from it.

3.6.5. Synchronizing all the telescope modules

With the OOS problem solved for the Upstream arm, a new cooling system and the replacement of the single-mode fibers by multi-mode fibers, data was collected with all the modules in the telescope included in the readout, except for M3057 and M3175. Two modules, M3090 and M3082, in the telescope would still cause the FED to go out of sync as a consequence of a Time Out followed by numerous Event Number Errors. Of these two modules, module M3090 had less TO+ENEs counts than M3082. It is important to note that regardless of the TO+ENE errors, the FED will continue to send data to the back-end PC. What was observed was that for all modules except for the M3090 and M3082, the local reconstruction of the data looked normal.

By looking at the fiber numbers to which these modules are linked in Table A.1, it was realized that they were connected to the lowest to fiber numbers in the system, namely 3 and 5. For each event, the FED firmware is expecting data of the module connected to the lowest fiber number first. The remainder of the data is ordered by fiber number as well. Taking this into account, it appeared as if there was a delay in the system which was too short, since the FED was awaiting data from M3082 and M3090 for a while, but it was taking too long and thus it threw a Time Out error.

Such a delay in the FED firmware could not be identified at the time. Therefore the problem was solved in a differently by adding an artificial delay to the system. This was accomplished by including module M3057 (connected to fiber 1) back into the detector configuration files of the POS software such that the FED was expecting data from that module first, without it being physically connected to the motherboard. Therefore, the FED will wait for data from that channel first, and when it is not receiving any it throws a TO and moves on the the next module in line, which is M3082. This means that the telescope could be operated with all modules running synchronously, however the FED would always send OOS signals. To overcome this, for each run the correlation between hit positions in different layers was checked to make sure that the modules were running synchronously.

The results of a run taken with all fourteen functional modules in the telescope readout are shown in Figure 3.20. It shows the cluster density in $\mathrm{cm}^{-2}\,\mathrm{event}^{-1}$, of each telescope module. The coordinates in this figure are from the global coordinate system which is also implemented in CMSSW. Every frame in the figure shows two modules in one of the telescope planes.

For each module, except for M3057 and M3175 which were physically disconnected, clusters were found and the shape of the beam was clearly observed. From this graph, noisy ROCs are identified as black square shapes. The white line between two modules is a result of the CMSSW telescope geometry that does not take into account the overlap between the modules at the moment.

3.6.6. Masking noisy ROCs

In Figure 3.20, the noisy ROCs and pixels dominate the cluster density plot. The noisy pixels and ROCs have an influence on the efficiency of the tracking during the offline analysis and therefore they have to be masked. This can be achieved either in the data acquisition, the local reconstruction in CMSSW, or the offline analysis.

Masking noisy ROCs and pixels in the data acquisition, can be approached with different settings. One possibility is raising the threshold of the front-end to the highest possible level. This threshold level may not be higher than the noise level and therefore ineffective. Another

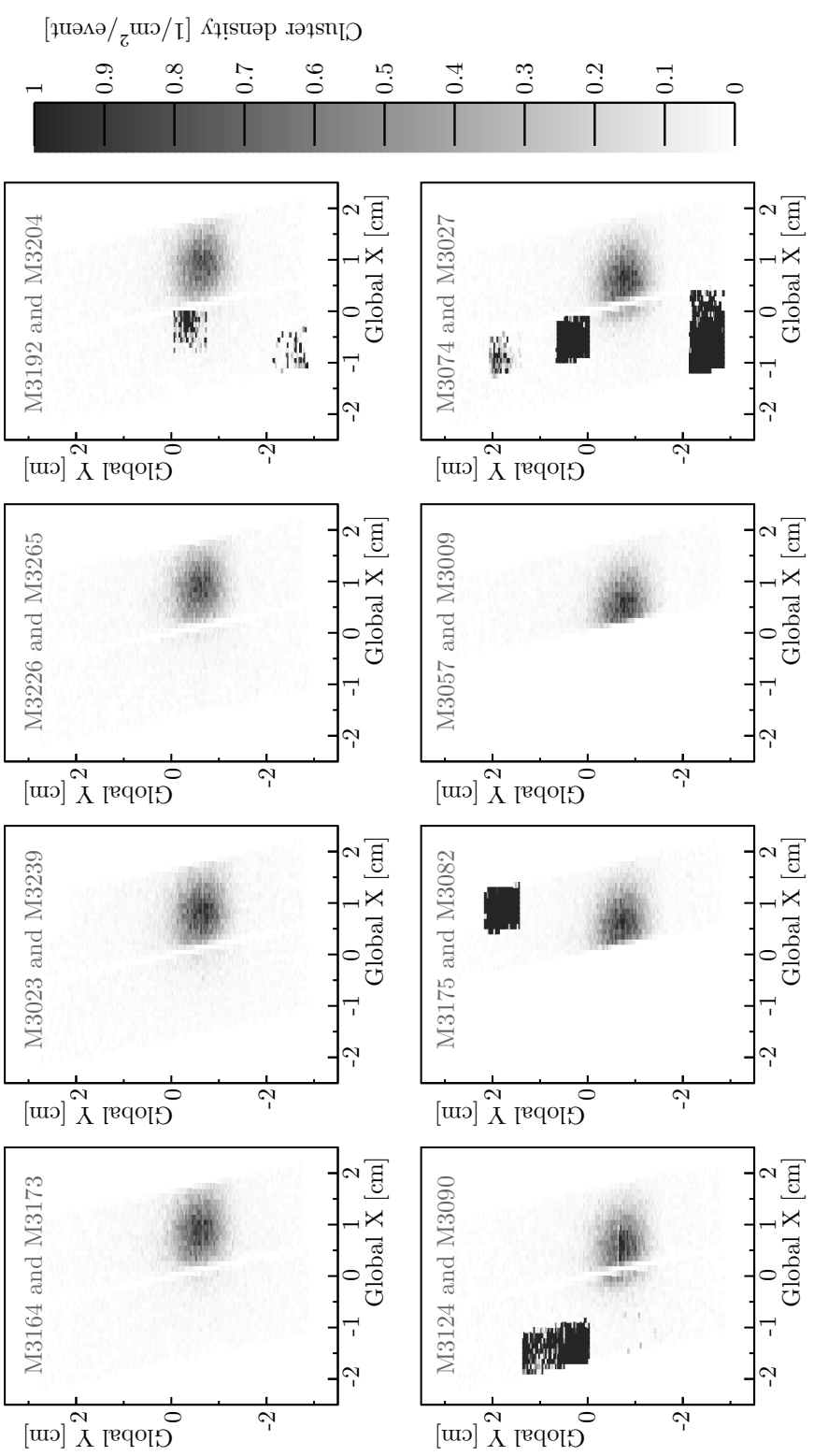

Figure 3.20. *The cluster density in each module of the telescope, obtained during one of the first runs with all the modules in the telescope readout, at the H6A beam line in SPS. The telescope run number is* 100 257.

option is removing half a module from the readout by removing its FED channel from the detector configuration file in POS, which is too rigorous in most cases. Individual ROCs can be removed from the DAQ as well by changing the value of the ROCs `ChipContReg` register in the `daq` configuration file of the targeted module in POS to 2.

The last option was chosen for the noisy areas in the telescope, and the result is shown in Figure 3.21. Instead of firing constantly, the masked areas wouldn't send data anymore. This improves the overall data quality that the telescope produces. Two noisy regions could still be found in M3192 regardless of the settings that were tried for that module. As a consequence, these noisy pixels had to be masked during the offline analysis.

During the exercise of finding the right settings to mask a region or a ROC in the telescope DAQ, it was found that module M3074 and M3124 were switched either in the DAQ or the analysis software.

At some point during the commissioning the telescope had to be moved to a table that could not be remotely controlled, by reason of the limited availability of DESY tables in the experimental hall at the SPS. Therefore, the telescope could not easily be aligned to the beam anymore. This is the cause of the off-centered beam that can be observed in the rest of the data in this thesis.

3.6.7. Correlation between telescope hits in different planes

To validate that the commissioning of the telescope was successful, the correlation between cluster positions in different telescope layers was studied. The cluster position correlations between two modules on the same side of the telescope are shown in Figures 3.22 to 3.25. The first two plots for the x and y-direction respectively, are from the Inside modules in Layer 2 and 3 of the Upstream arm. These are followed by the two plots comparing the Inside modules of Layer 3 Upstream to Layer 0 Downstream, which are the two outermost layers of the telescope. Finally, the same four plots are shown for the Outside modules in Figures 3.24 and 3.25.

In each of the plots there is a strong correlation found between the two different modules that are compared. Due to the beam dimensions and the rectangular shape of the telescope planes, the correlation in the graphs for the local x, are clearly visible throughout the whole range. This is in contrast to the local y plots, because the modules are longer in that direction and the beam does not cover the whole range. All the off-diagonal, light gray dots, are most likely off-time particles.

Because of the difference in number of pixels in the x and y directions, the bin size in the x plots is larger than in the y plots. In Figure 3.25b, there are a few empty regions due to ROCs that were masked in the readout as they were too noisy.

The number of correlation counts found in the Inside modules is higher than the count of the Outside modules. This was due to the beam alignment with respect to the telescope planes being off-center. Figure 3.21 can be referred to for an accurate view of the beam position on the telescope. There the beam is almost centered on the Inside telescope modules. This also results in a more smooth looking cluster correlation plot for the Inside part of the telescope, compared to a rougher picture from the Outside modules.

From the plots it can be observed that there is an almost perfect one-to-one correlation between two modules in different layers, and therefore the rotations between modules with respect to each other are minimal. This is because the telescope's cradles and rails were machined very precisely. There are, however, shifts in x and y between the modules, which is most likely the result of the frames of the telescope planes that are produced with a lower accuracy.

In Figure 3.24b, an off-diagonal shadow is observed at a slightly different angle. This is found in other correlation plots between modules in the Upstream arm as well. It is not yet

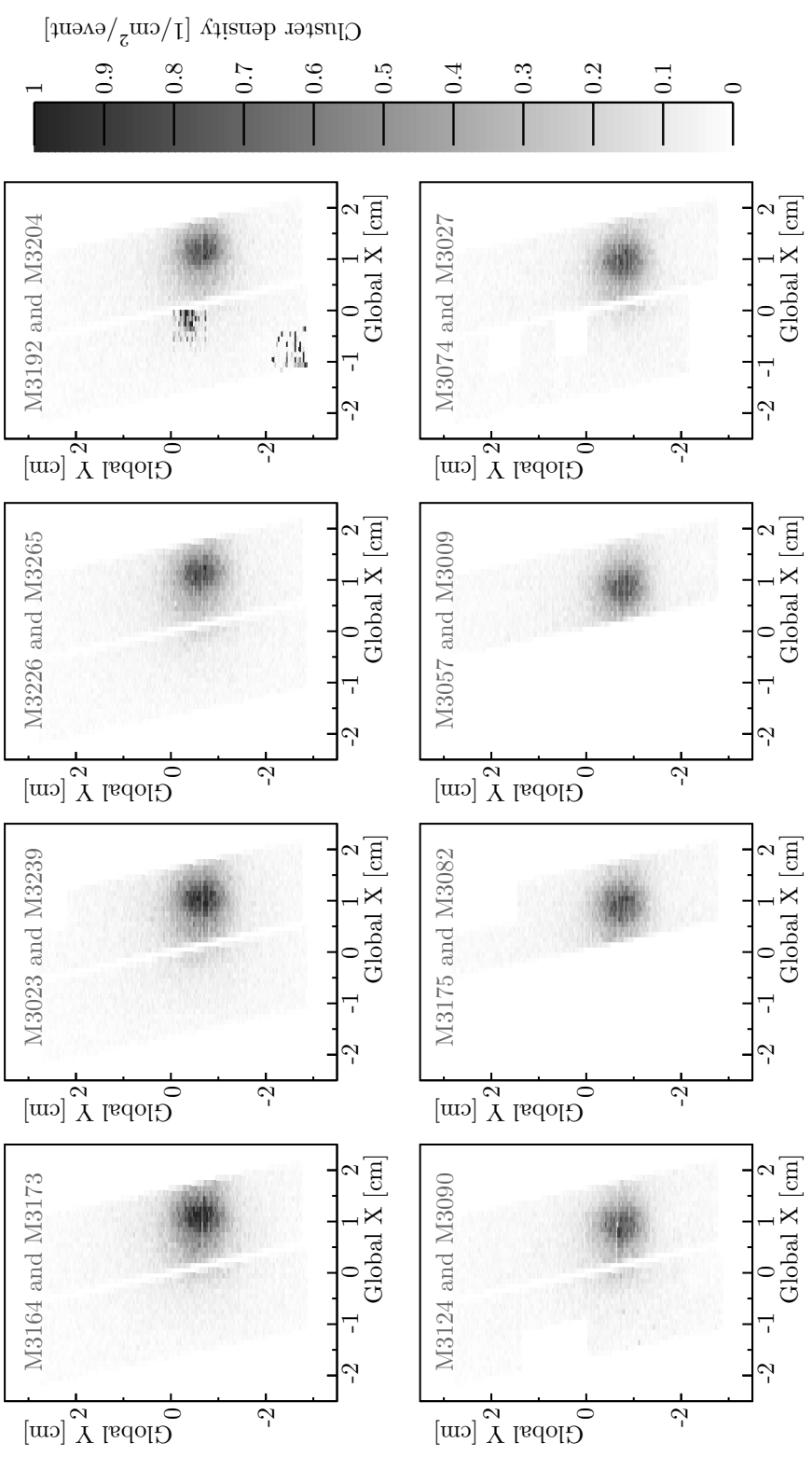

Figure 3.21. *The cluster density in each module of the telescope, obtained during one of the first runs with all the modules in the detector configuration, at the H6A beam line in SPS, after most of the noisy ROCs were successfully masked. The telescope run number is* 100 333.

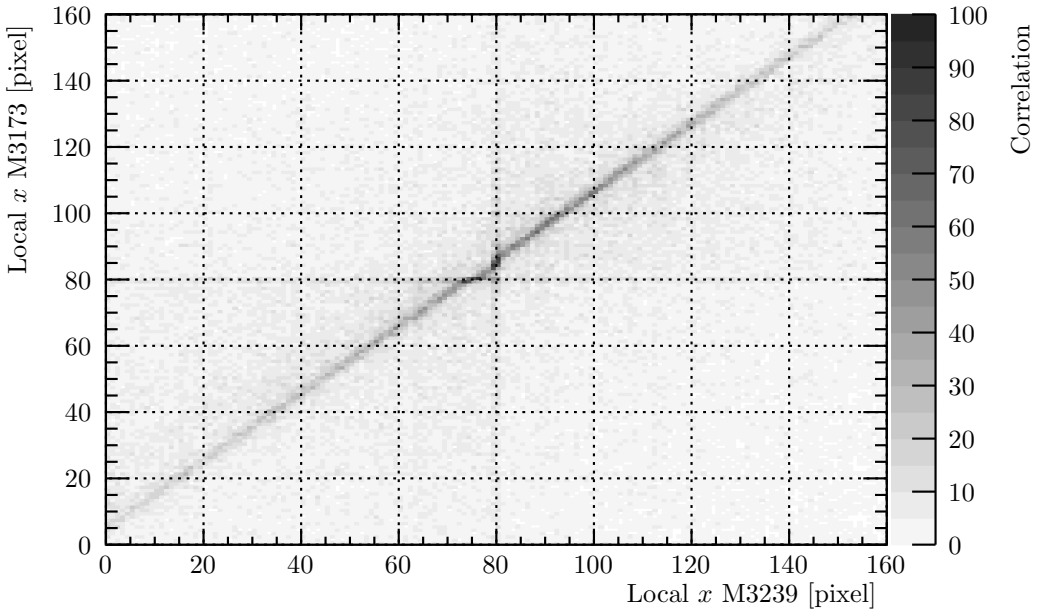

(a) *Local x.*

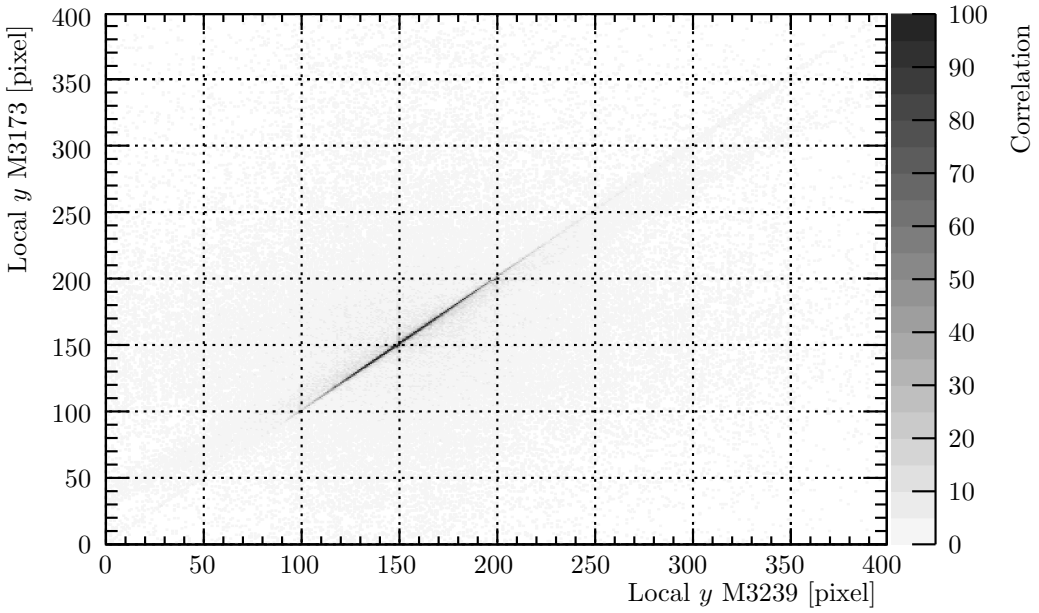

(b) *Local y.*

Figure 3.22. *Hit correlation between module M3173 and M3239, in Upstream Layer 3 and Layer 2. This data is from run 100333.*

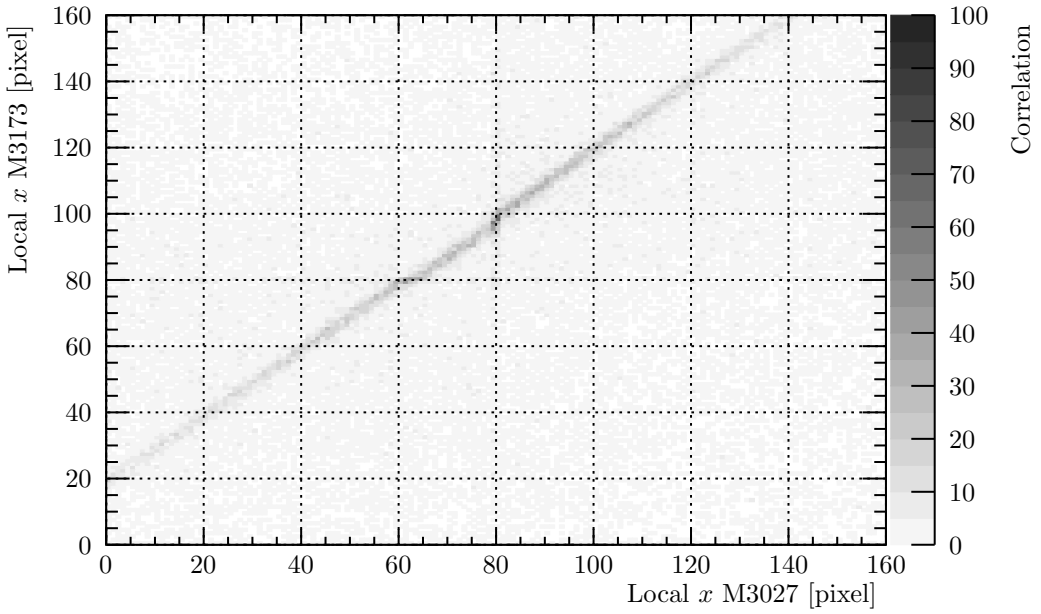

(a) *Local x.*

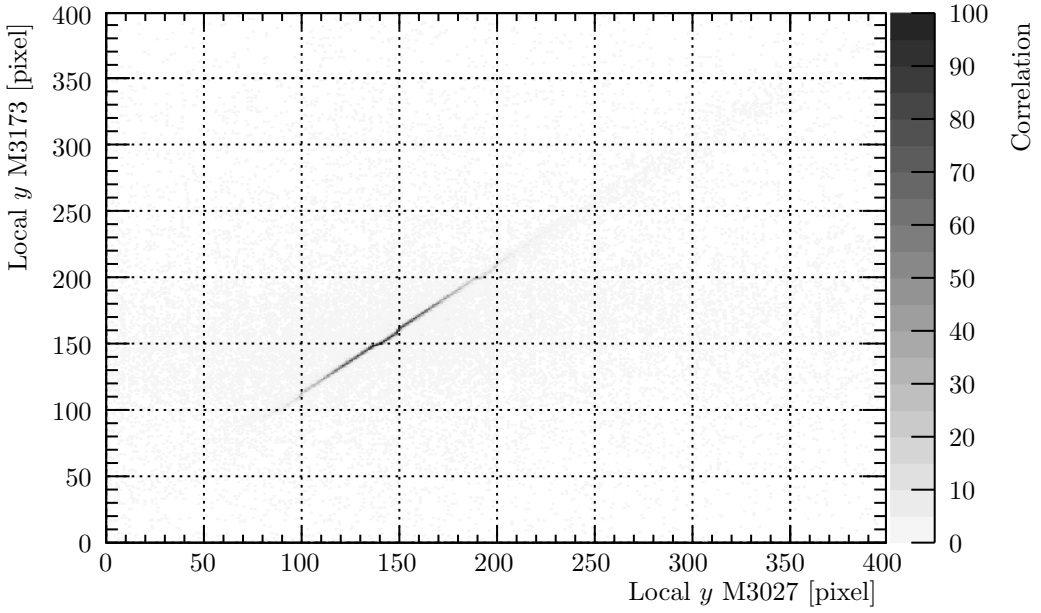

(b) *Local y.*

Figure 3.23. *Hit correlation between module M3173 and M3027, in Upstream Layer 3 and Downstream Layer 0. This data is from run 100333.*

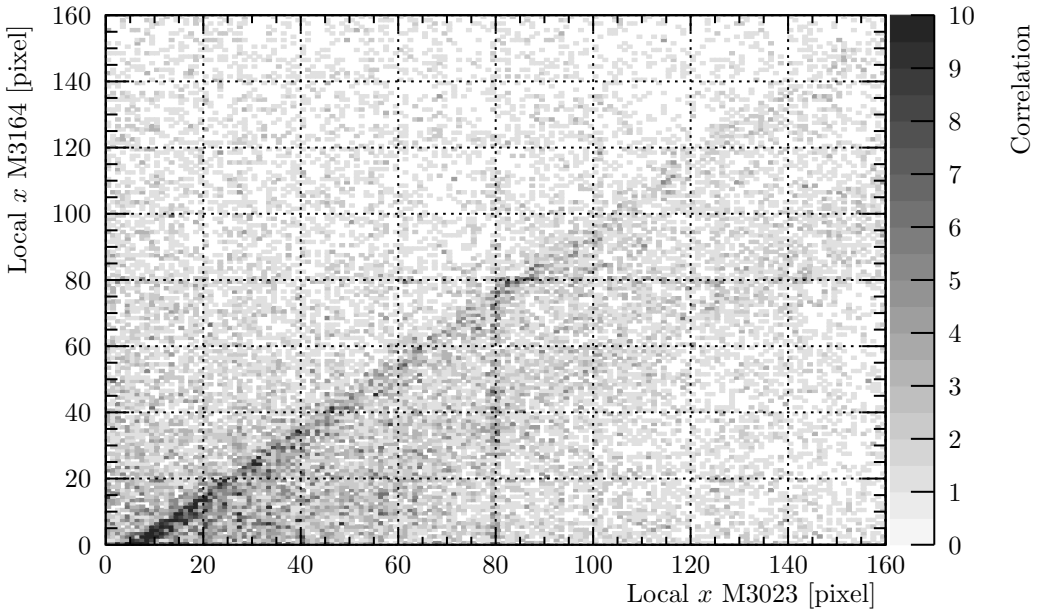

(a) *Local x.*

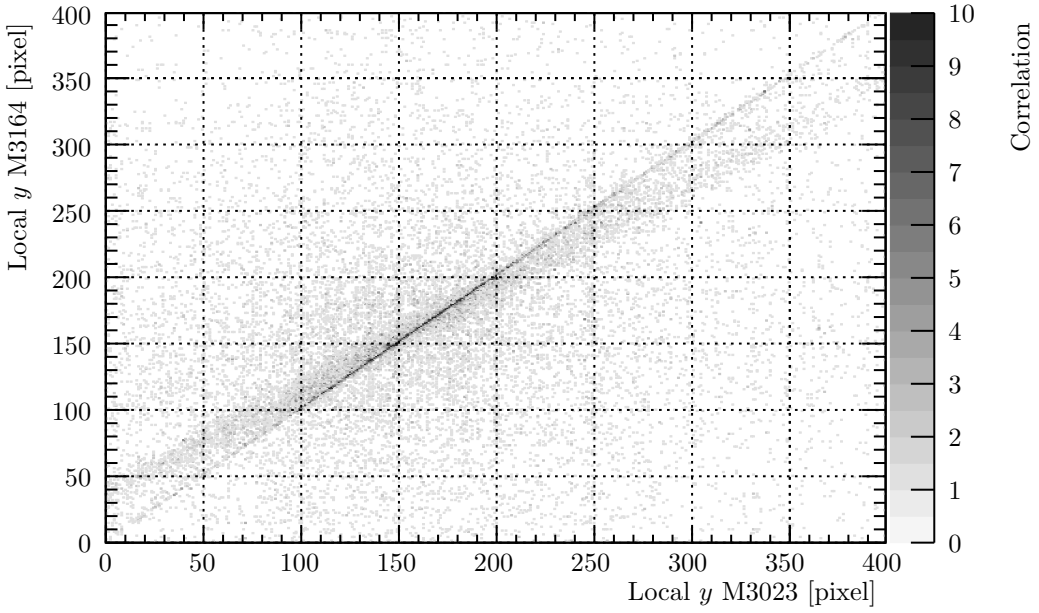

(b) *Local y.*

Figure 3.24. *Hit correlation between module M3164 and M3023, in Upstream Layer 3 and Layer 2. This data is from run 100333.*

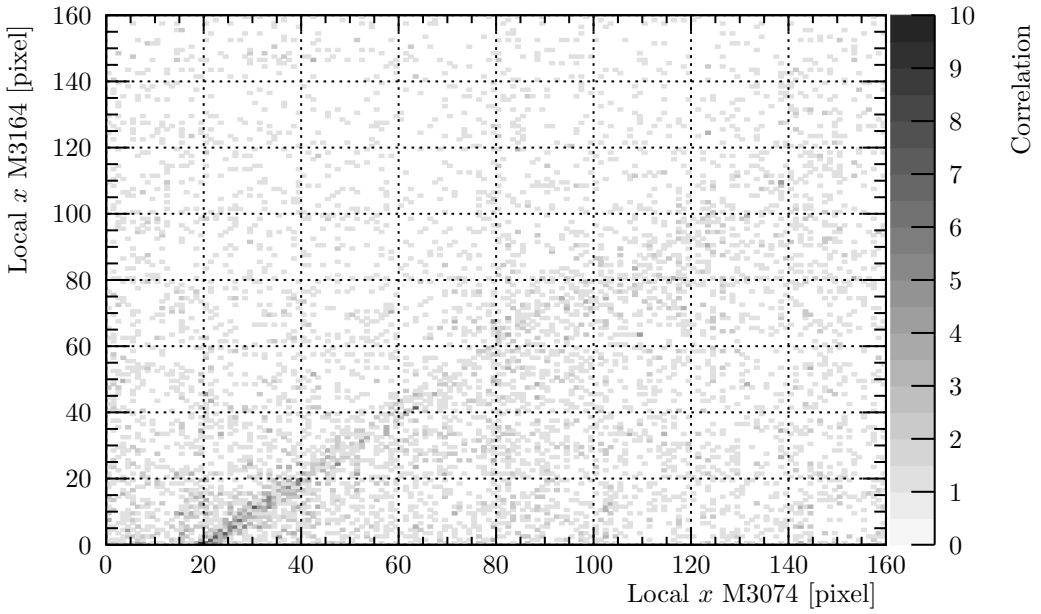

(a) *Local x.*

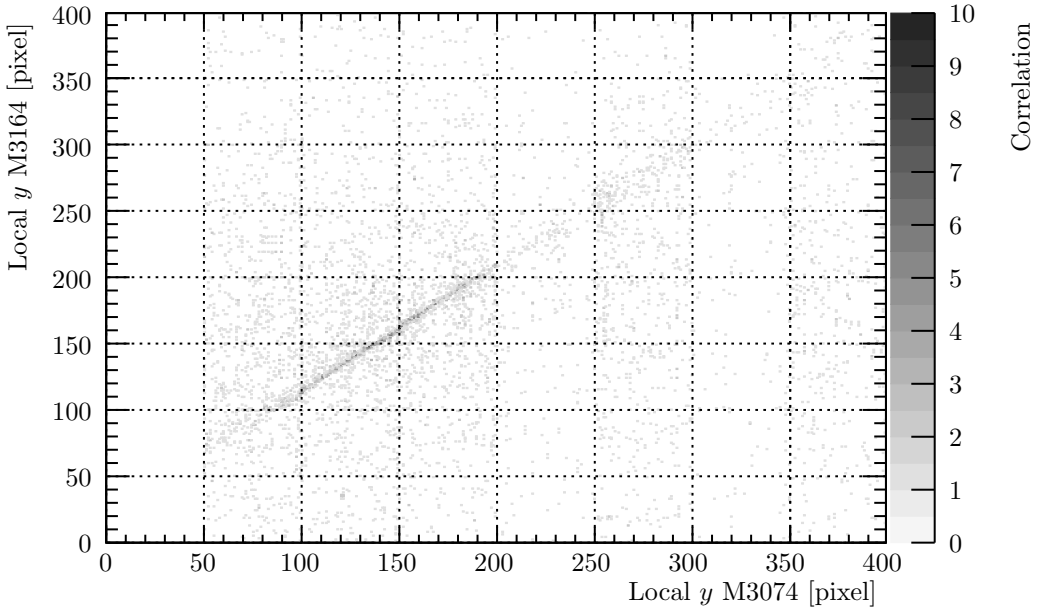

(b) *Local y.*

Figure 3.25. *Hit correlation between module M3164 and M3074, in Upstream Layer 3 and Downstream Layer 0. This data is from run 100333.*

understood why this shadow appears in the plots; it might be caused by the beam halo at the SPS.

Next, the hit correlations in local x and local y are shown in Figure 3.26. The module planes were designed to have a small overlap in the local x-direction of 2 mm. Still, from the correlation plot in Figure 3.26 no correlation between hits in modules M3164 and M3173 is found, and thus it can be concluded that there is no overlap. After measuring an empty aluminum frame and calculating the overlap between the sensitive areas of the modules, it was found that the sensitive areas are actually not overlapping but touching. Taking into account the rotation of the planes around the local y-axis, there is actually a very small gap of 1 or 2 mm between the two modules, as seen from the beam. Therefore, the two sides of the telescope (Inside and Outside) are treated separately in the analysis, as if there were two telescopes positions very closely together.

In Figure 3.26a a cross-shape is observed in the center of the image. Each axes of the cross is located at a ROC's edge, where each pixel is double in size. Hence, the cross-shape is cause by a binning effect: the bins on the ROC's edge should be twice as large than all the other bins. By carefully examining the other correlation plots in Figures 3.22 to 3.25, this same shape can sometimes be observed. In the plots for the hit correlation in y there are multiple cross-shapes because there are eight ROCs in the y-direction.

The correlation plots presented in this section are proof that with the telescope data, tracks can be reconstructed and thus that the telescope commissioning was successful. In the next section follows a more detailed analysis of the telescope data of run 100 333. For future reference, the correlation plots for the other modules are given in Appendix B.

3.7. Analyzing the first telescope data

The analysis of the telescope data occurs in a three successive steps. First is the local reconstruction of raw telescope data and clustering in CMSSW, then track finding is initiated and finally the software alignment is executed. The latter two are both performed with a home-made code and all three stages are discussed below in their respective subsections.

3.7.1. Clustering

The local reconstruction and clustering performed with CMSSW, results in the global coordinates of each cluster and its properties like charge and size of a cluster. These are all discussed in more detail below. The run that these plots are a result of is number 100 333. The beam profile during this run is shown in Figure 3.21 of the previous section.

Due to of the telescope alignment with respect to the beam, the cluster rate measured by the the Inside modules is lower than what the Outside modules measured. This results in a lower cluster count for those Inside module, and is visible in all plots in this section. Therefore, it will not be mentioned for each individual case described below. For this analysis, the standard CMS BPix pixel gain was used. The gain that was measured with the telescope (see Section 3.5.5) was not yet made available in CMSSW at the time of this analysis. In each plot, the modules on the Inside are indicated by orange tones and the Outside modules by blue tones. As a reminder, there are only fourteen modules in each plot since two modules were physically disconnected from the telescope readout.

Figure 3.27 shows the cluster charge in kilo electrons, versus the number of clusters. For modules M3192 and M3124, a peak at low cluster charge, below a 10 ke, is observed. Most of these clusters are from noisy pixel in those modules that were not masked in the readout. This means that the cluster charge can be used to remove clusters from the data that are most likely

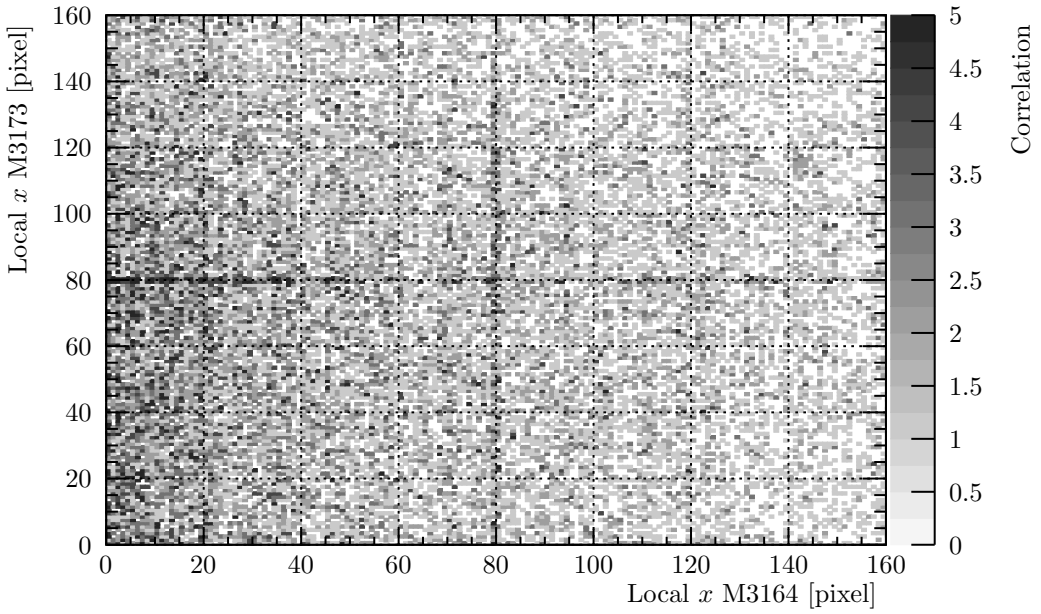

(a) *Local x.*

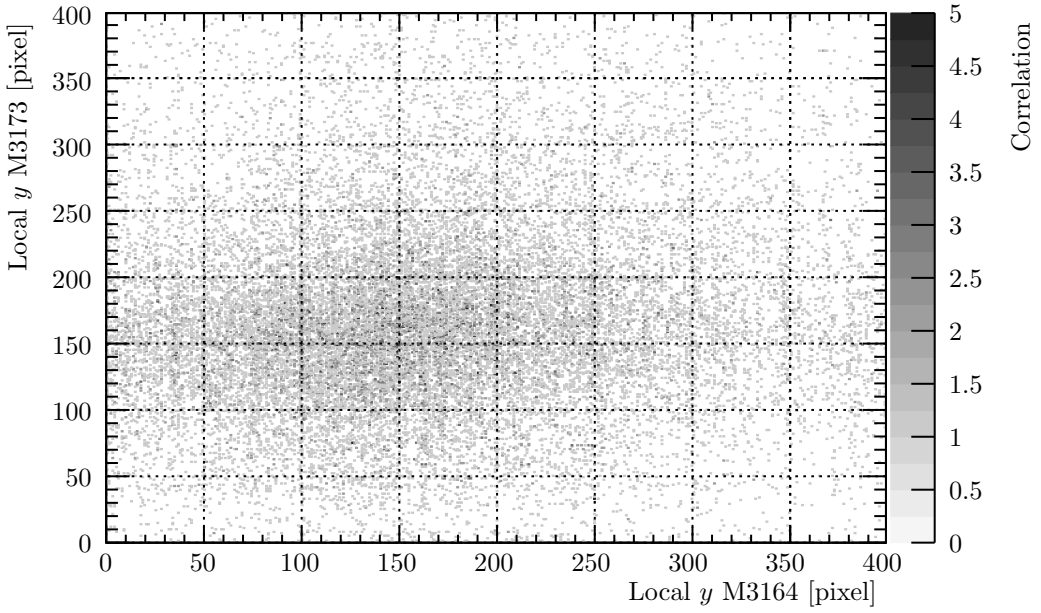

(b) *Local y.*

Figure 3.26. *Hit correlation between module M3164 and M3173, both in Upstream Layer 3. This data is from run 100333.*

noise or background. Hence, for all the other plots in this section, clusters with a charge below 8 ke are removed from the data.

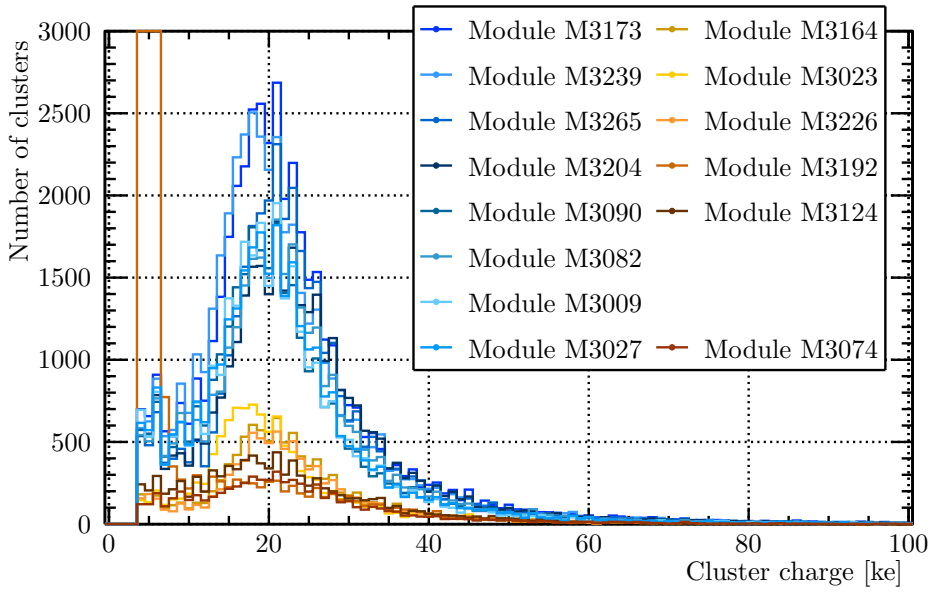

Figure 3.27. *Measured cluster charge in electrons versus the number of clusters, during run* 100 333.

Except for the noisy pixels in modules M3192 and M3124, the histograms for each individual module seem to follow a Landau distribution, as expected. For Minimum Ionizing Particles traveling through 300 µm thick silicon, the Most Probable Value (MPV) of the Landau distribution is around 250 eV µm^{-1} with a full-width-half-maximum (FWHM) of 36 eV µm^{-1} [17, p. 450]. Expressed in number of electrons, the MPV is ∼20 k*e* and the FWHM ∼3 keV.

Figure 3.28 shows the charge distributions for modules M3164 and M3173. On top of the histograms Landau distributions with an MVP of 20 keV and a FWHM of 3 keV was plotted. For both M3164 and M3173 the data match the Landau distribution closely. The differences between the Landau and the data stem from the background and noise that can not be easily subtracted from these distributions.

The number of clusters versus the number of events, per module, are shown in Figure 3.29. Because of the triggering efficiency of 90 % (see Section 3.6.4), and the fact that there are two modules in a telescope layer, a large peak is found at 0 clusters. As expected, the number of clusters distributions follow Poisson distributions.

The global x, y and z cluster positions of all clusters accumulated during run 100 333 are shown in Figures 3.30, 3.32 and 3.33. These positions are calculated in CMSSW based on the linear average of the analog charge information of each pixel in the cluster, also referred to as the barycenter calculation. When looking at the global x cluster position distributions, two groups of modules are observed as can be expected from the physical positions of the Inside and Outside modules. A telescope plane is almost 4 cm wide, which explains the lowest and highest cluster position in this plot. The overlap in the center comes from the 20° angle around a plane's local y cluster positions, see Figure 3.31.

For obvious reasons, the global y cluster position distributions of clusters in different modules, are overlapping completely. The beam width in the y-direction was ∼1 cm which is also found in this plot. The tails of the y distributions come from the beam halo.

Figure 3.33 shows the global z cluster positions. The separation between the Upstream and Downstream modules is clearly visible. Apart from that, it can be seen that the planes were

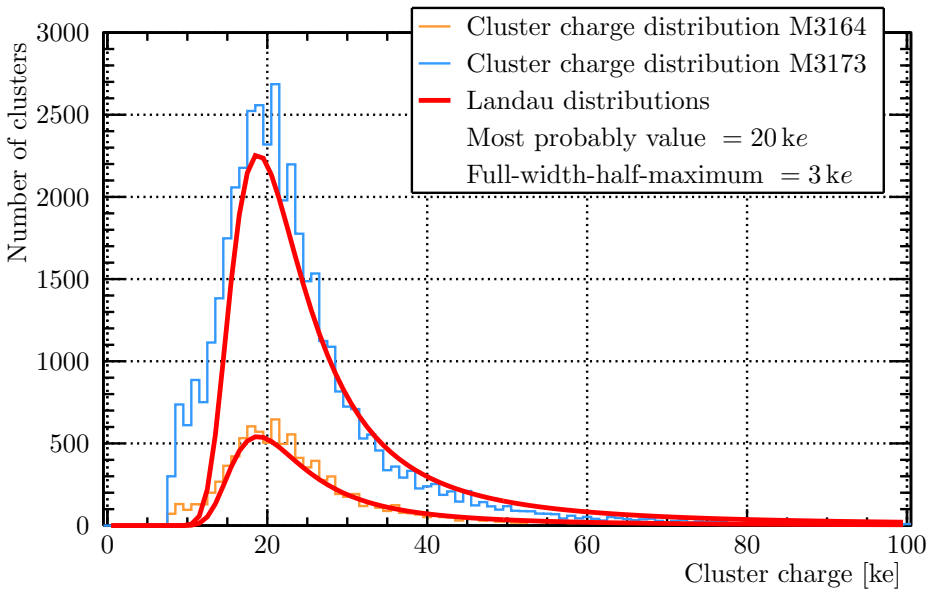

Figure 3.28. *Landau distribution of cluster charge in kilo electrons, measured by M3173, during run* 100 333.

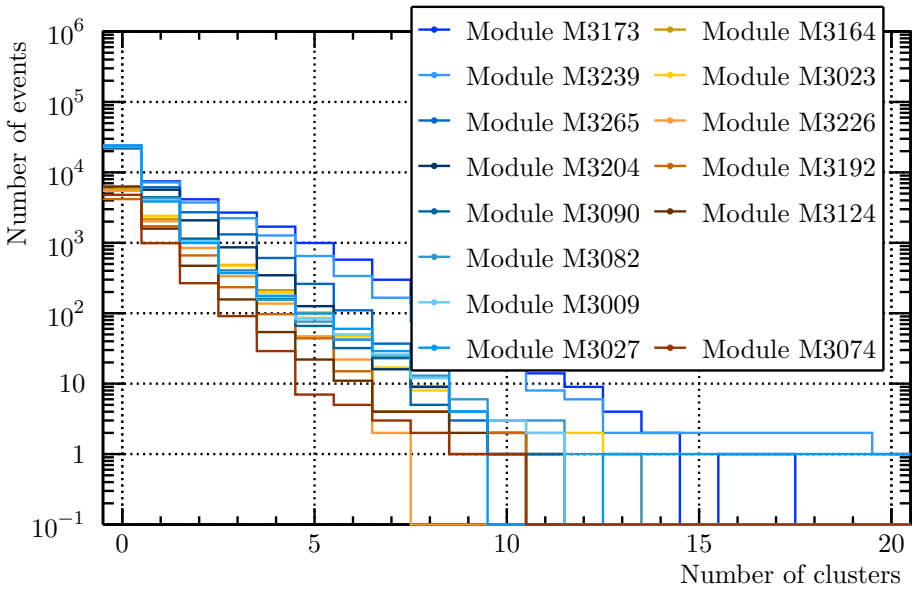

Figure 3.29. *Number of clusters per module, during run* 100 333.

equispaced during this run. Between each plane on an arm the distance was 5 cm. For each module, the z cluster position is distributed around the center of the module. If the angle around the local x of each telescope layer is exactly 30°, then the width of the distribution should be $\sin(30°) \cdot 6.66\,\text{cm} = 3.33\,\text{cm}$. In Figure 3.33 the width of each module distributions is very close to 3.33 cm. However, it has to be noted that these plots were made before the software alignment of the telescope planes.

Figures 3.34 to 3.36 show the total cluster size, the cluster size in the local x-direction and the cluster size in the local y-direction respectively. Each cluster is at least 1 pixel in size,

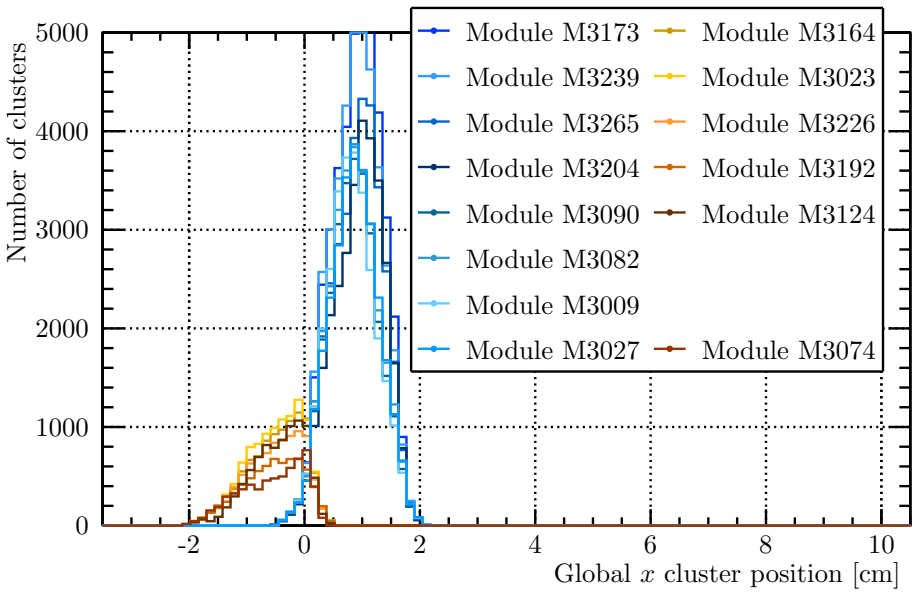

Figure 3.30. *Global x-position versus the number of clusters, during run* 100 333*. The colors indicate which module is concerned.*

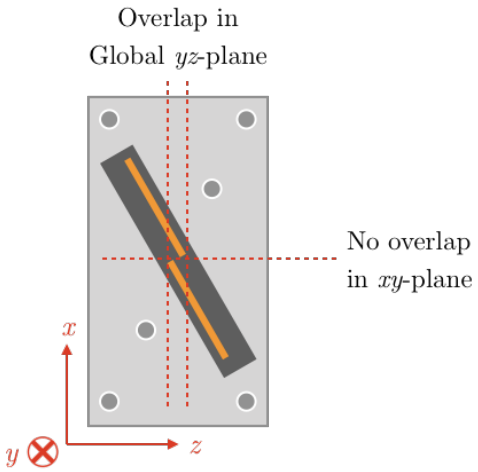

Figure 3.31. *A top view of a telescope plane on a cradle showing the overlap in global x.*

but most clusters are bigger than 1 pixel. This is caused by the charge sharing between the pixels, which is enhanced in the telescope by the respective angles around x and y. On average, the total cluster size (Figure 3.34) is bigger than the cluster sizes in the x and y-directions respectively, which is to be expected since the total cluster size takes both the pixels in x and y-direction into account. Most clusters have a size of 2 pixels in both the x and y-direction, which is expected from the magnitude of the angles around x and y [70].

3.7.2. Tracking

Based on the global coordinates of each cluster in an event, an algorithm was implemented for the track reconstruction of CHROMIE telescope events. In view of there being no overlap between the Inside ($+x_{global}$) and Outside ($-x_{global}$) modules, these two sides were considered

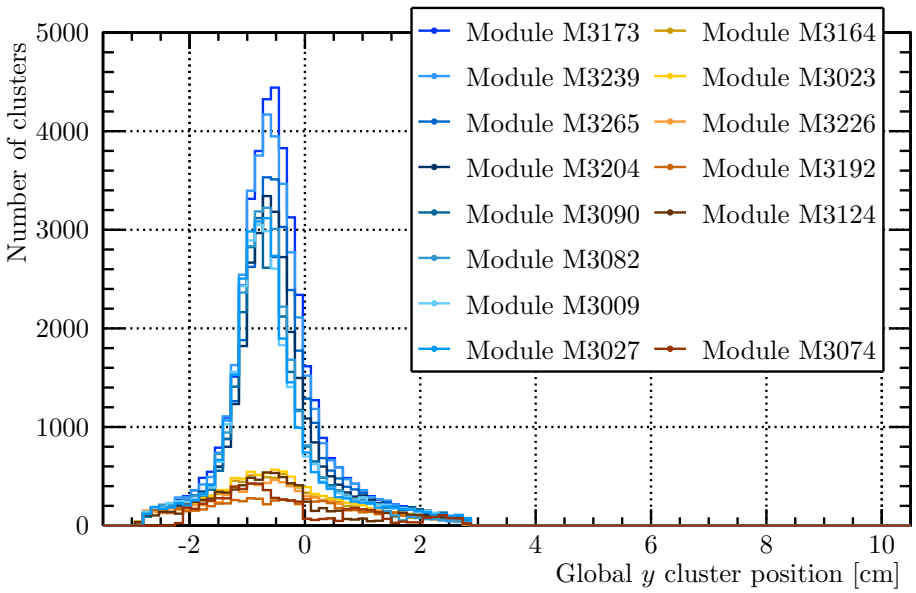

Figure 3.32. *Global y-position versus the number of clusters, during run* 100 333.

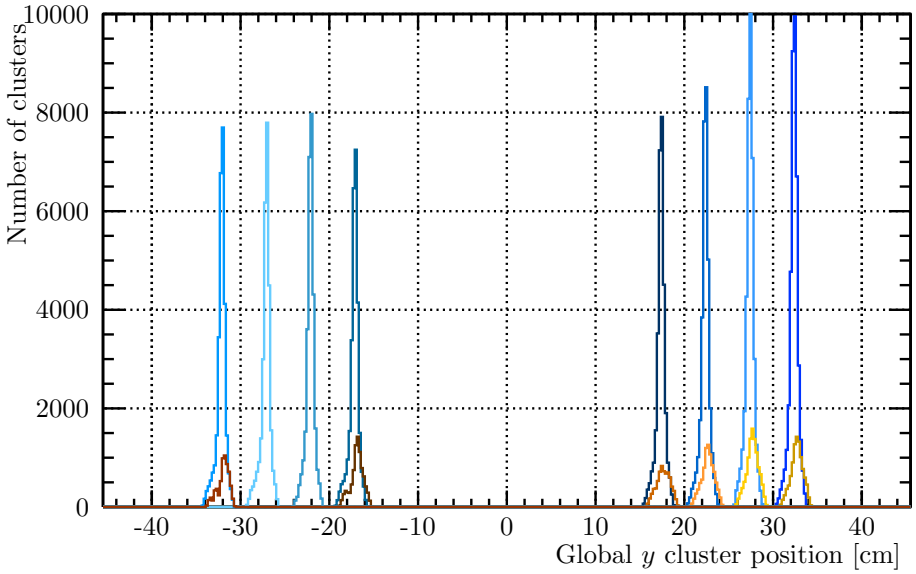

Figure 3.33. *Global z-position versus the number of clusters, during run* 100 333. *See the legend of Figure 3.32 for the color coding.*

separately during tracking and alignment. Tracks that crossed from the Inside modules of the telescope to the Outside modules were discarded.

Figure 3.37 shows the total number of clusters per telescope event. It peaks at 8 clusters for the Inside modules, while for the Outside modules, most events have 6 or less clusters, since modules M3057 and M3175 were disconnected. If an event had a track in the Inside modules with more than 6 clusters, this was either because of noisy pixels, or the track switched at some point from the positive x-side to the negative x-side modules. In the latter case the track was neglected in the next part of the tracking analysis.

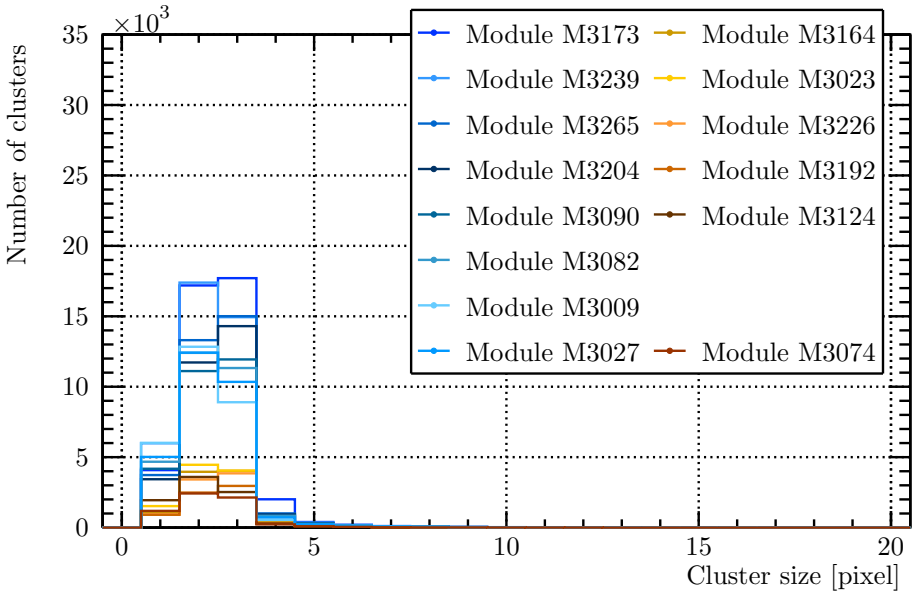

Figure 3.34. *Cluster size in number of pixels, during run* 100 333.

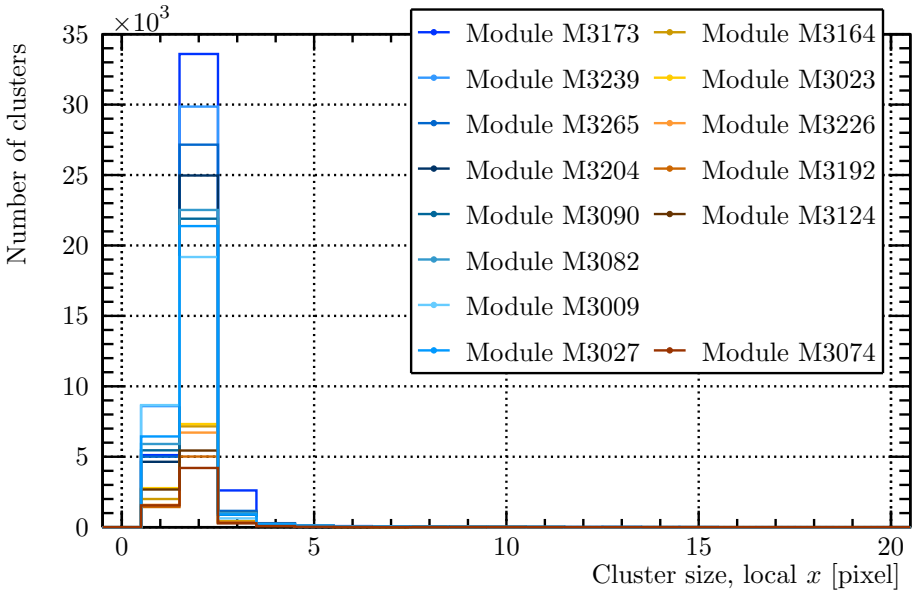

Figure 3.35. *Cluster size in the local x-direction, in number of pixels, during run* 100 333.

The home-made tracking code is set up as follows. For each event, the tracking algorithm checks if there are at least four unique telescope layers that detected a cluster. For those events, the code iterates over the unique layers and at each iteration, a seed track is constructed with the cluster(s) in the current layer, and the cluster(s) in the next layer. The seed track is obtained by

$$x_{\text{track,global}} = az_{\text{global}} + b \tag{3.1}$$

$$y_{\text{track,global}} = cz_{\text{global}} + d \tag{3.2}$$

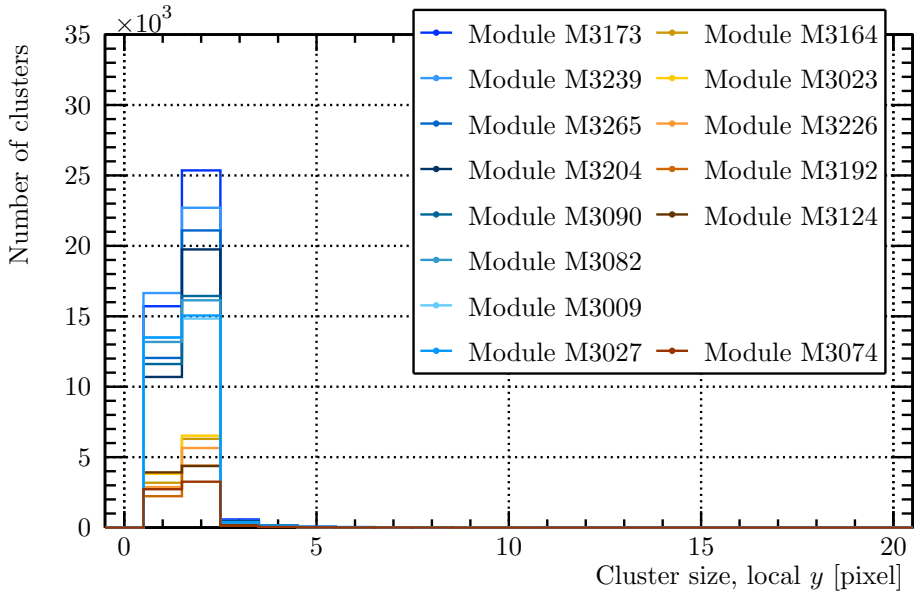

Figure 3.36. *Cluster size in the local y-direction, in number of pixels, during run* 100 333.

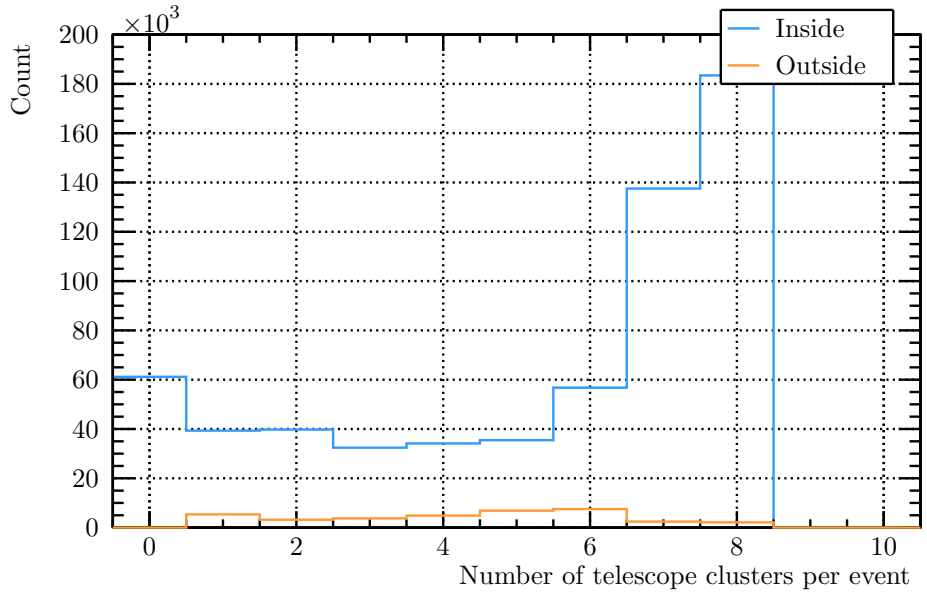

Figure 3.37. *Total number of clusters in a telescope event, during run* 100 333. *The blue distribution is for the Inside modules, and the orange histogram for the Outside modules.*

were $x_{\text{track,global}}$ and $y_{\text{track,global}}$ are the track coordinates, a, b, c and d the track parameters and z_{global} is the global z-axis.

Then for each event with four unique layers, the code loops over all of the two-layer seed tracks, to try an increase the track with clusters from the other modules. First, the track is extrapolated to the next layer on the downstream side of the two seed modules. It searches for clusters in that layer within a given acceptance window around the extrapolated track position. Before alignment, this acceptance window has a cone-shape, with a radius that grows with the z-position of the next plane, by 10 mm per meter. If there are multiple clusters

within the acceptance window, only the cluster that is closest to the track is used for the track reconstruction

To the now three clusters, a fit is carried out with Equations (3.1) and (3.2) to recalculate the track parameters. Then the track is extrapolated again to the next layer, and again, new track parameters are estimated based on the newly added cluster. This is repeated for all telescope layers with clusters in the event. First it tries all layers downstream of the seed layers and then all modules upstream. If this final track has at least four clusters in four unique layers, and if at least one of the clusters is in an upstream module, and another one in a downstream module, it is accepted as a track.

If there were more than one seed tracks in an event, the algorithm selects the track with the most clusters in individual layers. Therefore, by definition there is maximally one track per event. This choice is justifiable by looking at Figure 3.37, the maximum number of clusters in the whole telescope, during run 100 333, was 8, which means that there can be at most one track per event.

Both the track parameters and the cluster information were stored and used for the alignment which is explained in the next section. Figure 3.38 shows the number of clusters per track, after the software alignment of the telescope, for both the $+x_{global}$ and the $-x_{global}$ modules. As expected, tracks in the Inside modules had a maximum of 8 clusters associated to them and for the Outside modules this number was 6. Due to the fact that the number of tracks in the inside modules was low, and the number of clusters associated with them was 6 or lower, the software alignment of those modules proved to be difficult which is explained in the next section. For future beam tests it is very important that the beam is centered on the telescope planes, and not just one of the two modules in a plane.

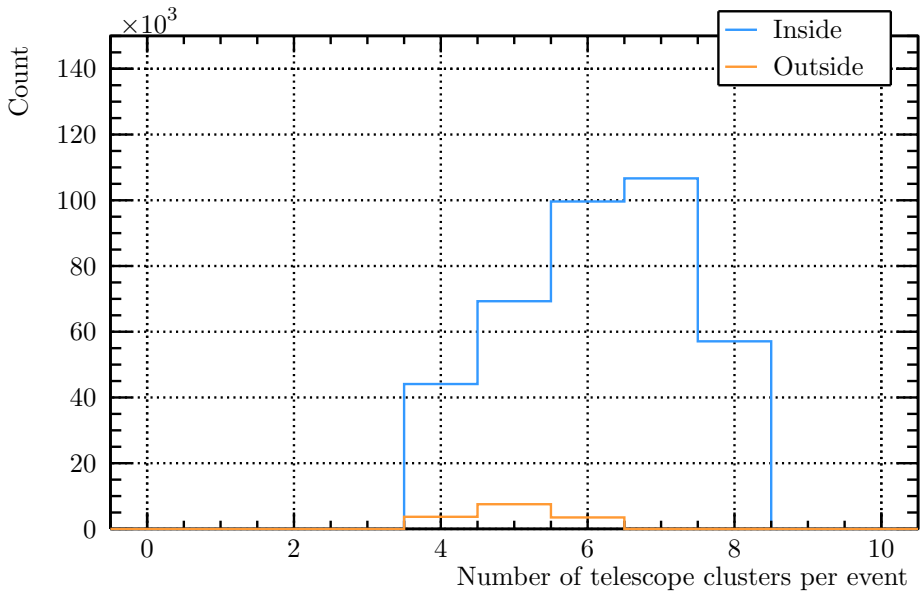

Figure 3.38. *Total number of clusters in a telescope track, during run* 100 333*. The blue distribution is for the Outside modules, and the orange histogram for the Inside modules.*

The tracking efficiency (after software alignment, described in the next section) is summarized in Table 3.1. The tracking efficiency is defined here as the number of tracks with n clusters or more, divided by the number of events with at least n clusters in n different layers. When tracks are accepted with at least 4 clusters in 4 unique layers, the tracking efficiency is 84 % at $+x_{global}$ and 62 % at $-x_{global}$. Table 3.1 is, as it were, a summary of what happens when

the number of clusters in Figure 3.38 would be divided, bin by bin, by the number of clusters in Figure 3.37. The efficiency of the Outside modules is lower because this side misses two modules and is therefore difficult to align properly with software.

Table 3.1.
Tracking efficiency, after software alignment of the telescope planes, of the tracking code presented in this section.

Number of clusters per event	**Tracking efficiency $+x_{global}$ modules** η_{track} %	**Tracking efficiency $-x_{global}$ modules** η_{track} %
4	84	62
5	80	58
6	69	28
7	51	
8	31	

It must be noted that a tracking efficiency of 100 % is not possible for the CHROMIE telescope for a number of reasons. First of all, there are dead areas, of in some cases several ROCs per module. Secondly there is a large amount of noisy pixels (more than 40 000) in two modules, which is significant compared to the 66 880 pixels in a readout chip. On top of that there is a triggering inefficiency of 10 %. All of these effects influence the tracking efficiency of the telescope negatively.

3.7.3. Software alignment and telescope resolution

The software alignment of the telescope is based on the unbiased residuals between the extrapolated track position on each plane, and the position of the cluster in that layer that is associated with the track. For all tracks in a run, the unbiased residual distributions are calculated in both the global x and y direction.

During the alignment, all clusters in a run are moved until the χ^2 of all tracks is minimized. The χ^2 is used to compute the difference between the cluster positions and the extrapolated track locations based on Pythagoras' theorem

$$\chi^2 = \sum_{i=1}^{N_{\text{Clusters}}} (x_{\text{t,i}} - x_{\text{c,i}})^2 + (y_{\text{t,i}} - y_{\text{c,i}})^2 \,, \tag{3.3}$$

where i is the index of a cluster, N_{Clusters} the total number of clusters in an event, $x_{\text{t,i}}$ and $y_{\text{t,i}}$ the extrapolated track position on the plane containing cluster i and $x_{\text{c,i}}$ and $y_{\text{c,i}}$ are the cluster position.

The software alignment uses the `fminunc` function from Matlab for the minimization of Equation (3.3). It performs unconstrained minimization, based on the Trust Region algorithm [95]. The allowed positional shifts of each cluster, are translations along the local x and y and rotations around the global x, y and z axis.

This is illustrated in Figure 3.39 that shows the different reference frames and vectors used to obtain the minimized cluster positions. First the local frame of a module is moved to the origin of the global frame. Than the global frame is rotated around x_{global}, y_{global} and z_{global} after which the local frame is moved back to its original position. Lastly, it is translated in the local x and y direction.

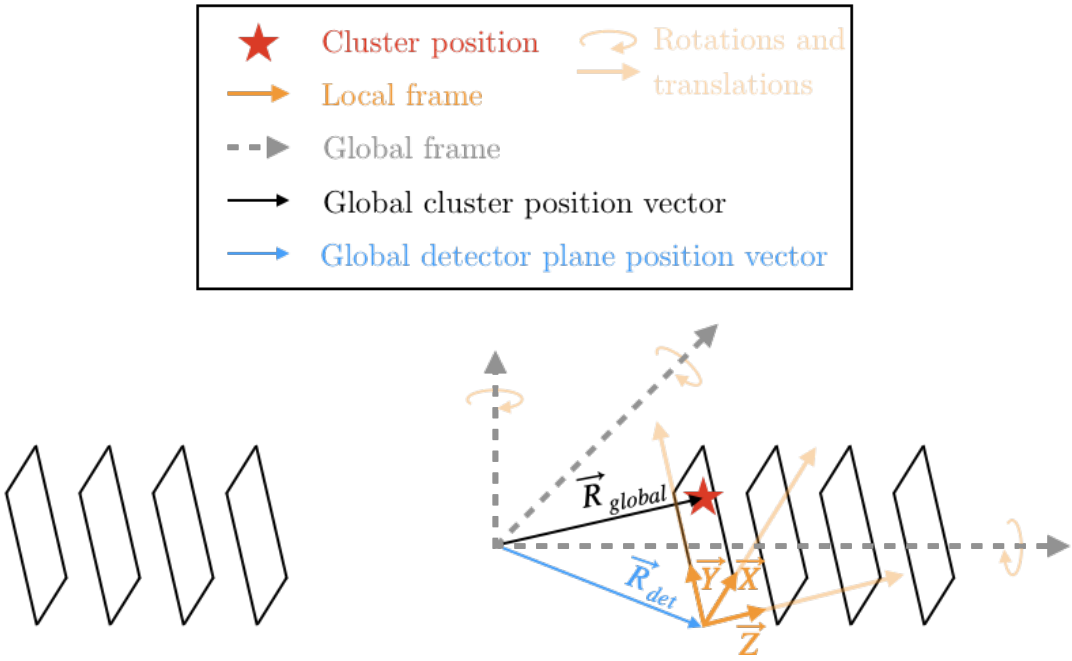

Figure 3.39. *The different reference frames and vectors used to perform the software alignment. The $\vec{R}_{global}$ is calculated by CMSSW, see Section 3.7.1. The vector $\vec{R}_{det}$ is defined between the origin of the local frame and the origin of the global frame. The allowed positional changes are indicated by yellow arrows.*

These transitions are described mathematically by Equation (3.4), where $\vec{R}_{global}$ is the original cluster position, $\vec{R}'_{global}$ the new cluster coordinates, $\vec{R}_{detector}$ the vector to the origin of the local frame, $\mathbf{M}(\theta, \phi, \psi)$ the rotation matrix that allows for rotations around all three global axes and $\vec{Y}\,dy$ and $\vec{X}\,dx$ the translations in the local x and y.

$$\begin{aligned}\vec{R}'_{global} = \mathbf{M}(\theta,\phi,\psi)\{\vec{R}_{global} - \vec{R}_{detector}\} \\ + \mathbf{M}(\theta,\phi,\psi)\vec{Y}\,dy + \mathbf{M}(\theta,\phi,\psi)\vec{X}\,dx + \vec{R}_{detector}\end{aligned} \tag{3.4}$$

The rotation matrix is given by

$$\mathbf{M}(\theta,\phi,\psi) = \mathbf{M_x}(\psi)\mathbf{M_y}(\phi)\mathbf{M_z}(\theta) \tag{3.5}$$

with

$$\mathbf{M_x}(\psi) = \begin{bmatrix} 1 & 0 & 0 \\ 0 & \cos\psi & -\sin\psi \\ 0 & \sin\psi & \cos\psi \end{bmatrix} \tag{3.6}$$

$$\mathbf{M_y}(\phi) = \begin{bmatrix} \cos\phi & 0 & \sin\phi \\ 0 & 1 & 0 \\ -\sin\phi & 0 & \cos\phi \end{bmatrix} \tag{3.7}$$

$$\mathbf{M_z}(\theta) = \begin{bmatrix} \cos\theta & -\sin\theta & 0 \\ \sin\theta & \cos\theta & 0 \\ 0 & 0 & 1 \end{bmatrix} \tag{3.8}$$

The χ^2 minimization is called three times, after which the tracking algorithm is evoked again to reconstruct tracks based on the new cluster positions. Each time the acceptance window of the tracking is reduced because at each step the misalignment is very likely to be

less than in the previous iteration. With the new tracks, the minimization of χ^2 is executed three times again. The tracking and χ^2 minimization are alternated until χ^2 does no longer change. The acceptance window cones have radii 10 mm per meter, 4 mm per meter, 3 mm per meter and 3 mm per meter for the first four iterations of three sets of χ^2 minimization and track reconstruction. Then it changes from a cone-shaped acceptance window to a cylindrical shape, with a radius of 150 µm for the remainder of the software alignment.

Figure 3.40 gives the value of χ^2 after each minimization cycle, during the software alignment performed with data from runs 100 333 to 100 335. After fifteen iterations the χ^2 did not decrease further. As is explained above, the acceptance window size changes after cycle 2, 5 and 11 and the track reconstruction was only called after three χ^2 minimization cycles. This is consistent with the sudden drops in the plot. Moreover, Figure 3.41 shows the χ^2 distribution of all the tracks reconstructed from run 100 333 to 100 335, after the software alignment.

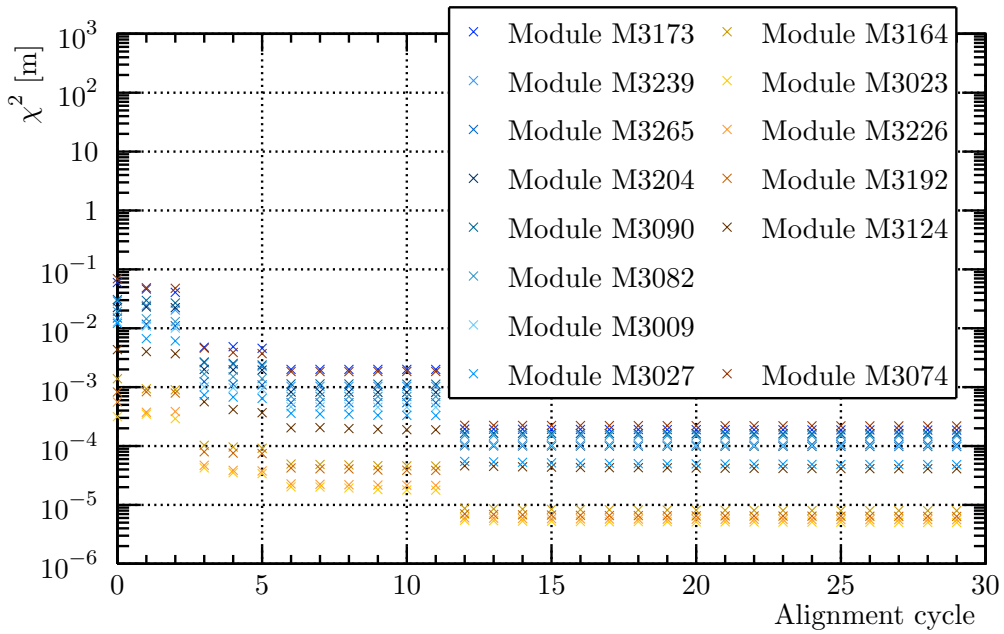

Figure 3.40. *Chi-squared value versus the alignment cycles with tracks from run* 100 333*,* 100 334 *and* 100 335*.*

After the software alignment, the misalignment of each module is computed of which a summary is shown in Table 3.2, which gives the different misalignment values for translations along x, y and rotations around x, y and z. For most modules, the misalignment in rotation was less than a degree around x and less than a few degrees around y and z. The translational misalignment was usually less than a millimeter.

After the software alignment, the unbiased residuals for x and y respectively, were calculated again. For modules M3204 and M3192 they are plotted in Figures 3.42 and 3.43 respectively. They are both positioned in the upstream layer that is closest to the DUT. For each plot, the unbiased residuals were split in two. There is one distribution for clusters that have a cluster size of 1 pixel and a distribution for clusters of cluster size 2 pixels in the given direction. There were more clusters with a cluster size 2, which is consistent with charge sharing between the pixels.

The sum of two Gaussian functions was fitted to each unbiased residual distribution to be able to make an estimation of the single point resolution at each detector plane. Since the cluster positions are calculated by CMSSW based on the charge measured of each pixel, the

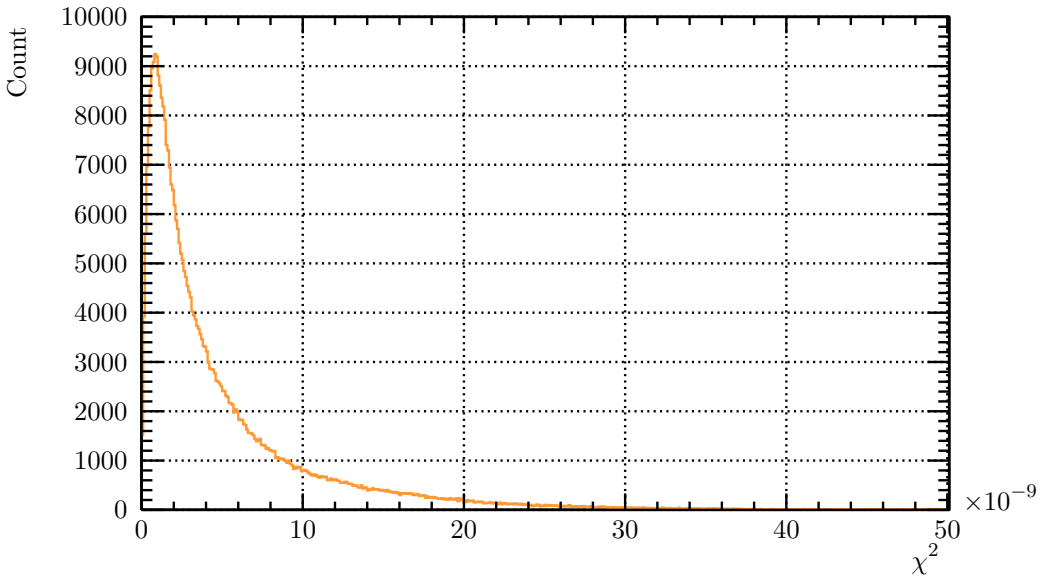

Figure 3.41. *The χ^2 distribution of all the tracks in runs* 100 333 *to* 100 335.

Table 3.2.
The misalignment of each telescope module computed with data from run 100 333 *to* 100 335.

Module	**Rotation around x** ψ °	**Rotation around y** ϕ °	**Rotation around z** θ °	**Transl. along x** x_{trans} mm	**Transl. along y** y_{trans} mm
M3173	−0.5896	+5.0372	−1.6117	+0.7867	+0.4550
M3164	−0.6520	+3.6747	−1.5869	+0.1746	−0.1230
M3239	+0.2595	+2.8759	−1.8977	+1.2034	+0.6373
M3023	+0.1495	+1.8908	−1.6593	+0.7039	+0.1172
M3265	−0.2640	+3.7084	−1.9376	+0.0648	+0.2414
M3226	−0.3244	+2.7138	−1.6963	−0.2003	−0.2879
M3204	−0.3551	+3.6747	−2.1063	−0.6927	+0.3345
M3192	−0.5586	+2.7001	−2.0445	−0.9726	−0.2433
M3090	−0.8789	+3.6237	−1.5080	+0.6416	+0.2111
M3124	−1.3968	+2.9307	−1.7433	+0.9832	−0.4088
M3082	−0.4554	+4.1518	−1.5844	+0.3592	+0.3402
M3009	−1.014	+2.6771	−1.6704	+0.7141	+0.4451
M3027	−0.2949	+4.2053	−1.8518	−0.9104	+0.2554
M3074	−0.7725	+3.7166	−1.5249	−0.3888	−0.0508

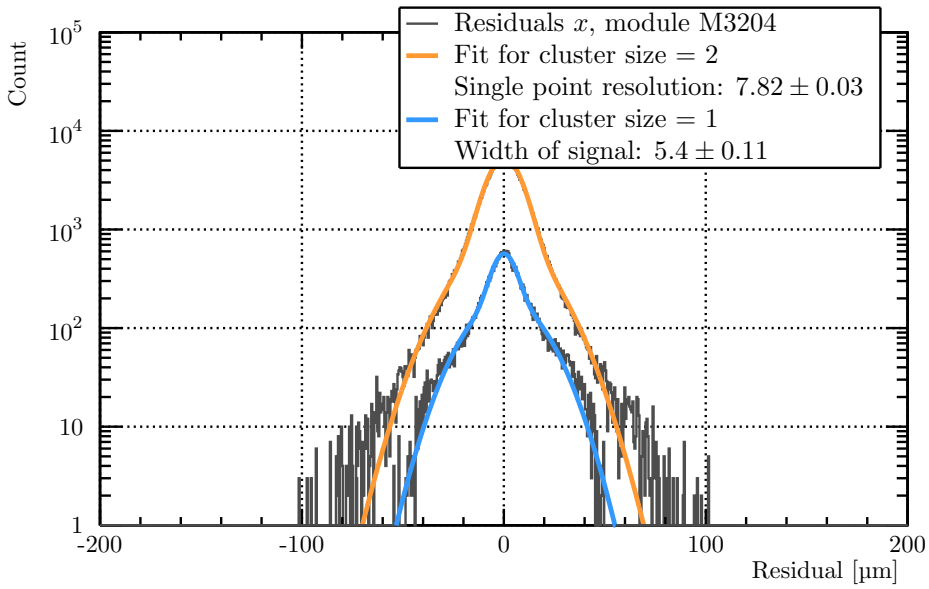

(a) *Global x.*

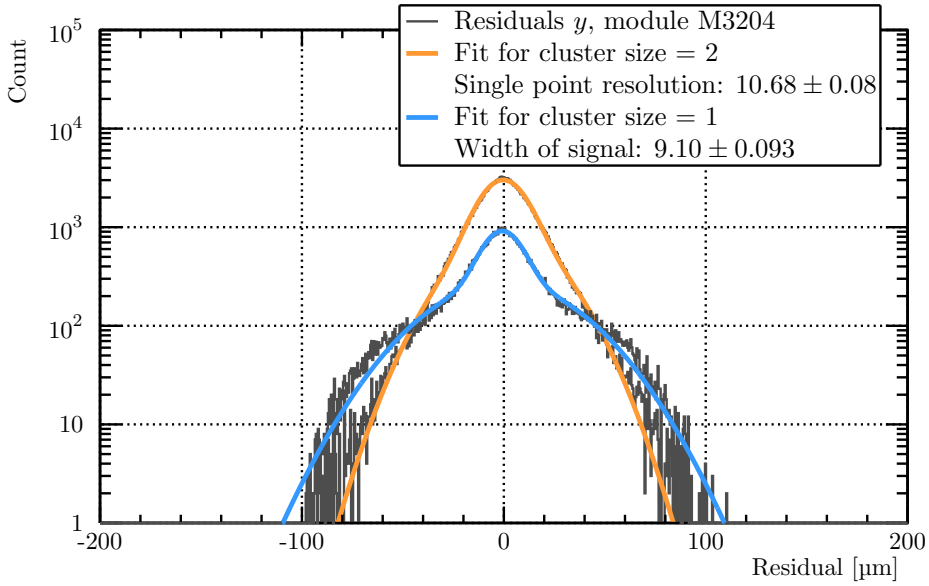

(b) *Global y.*

Figure 3.42. *Fits to the unbiased residuals distributions with cluster size 1 pixels (blue) and 2 pixels (orange), between the cluster position on module M3204 ($+x_{global}$) and the track interpolated on the detector plane. The data is shown in grey, and the estimated resolution is given in the legend.*

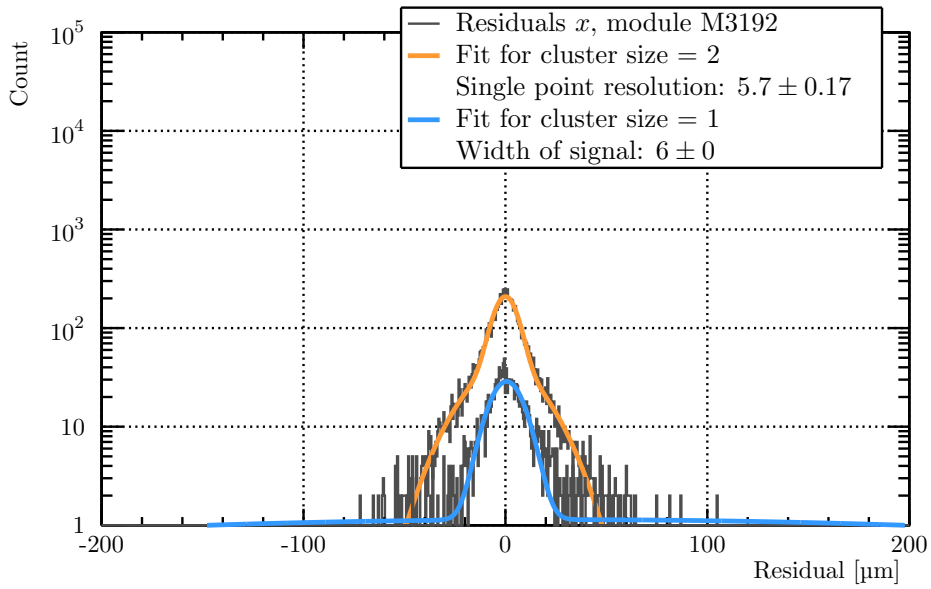

(a) *Global x.*

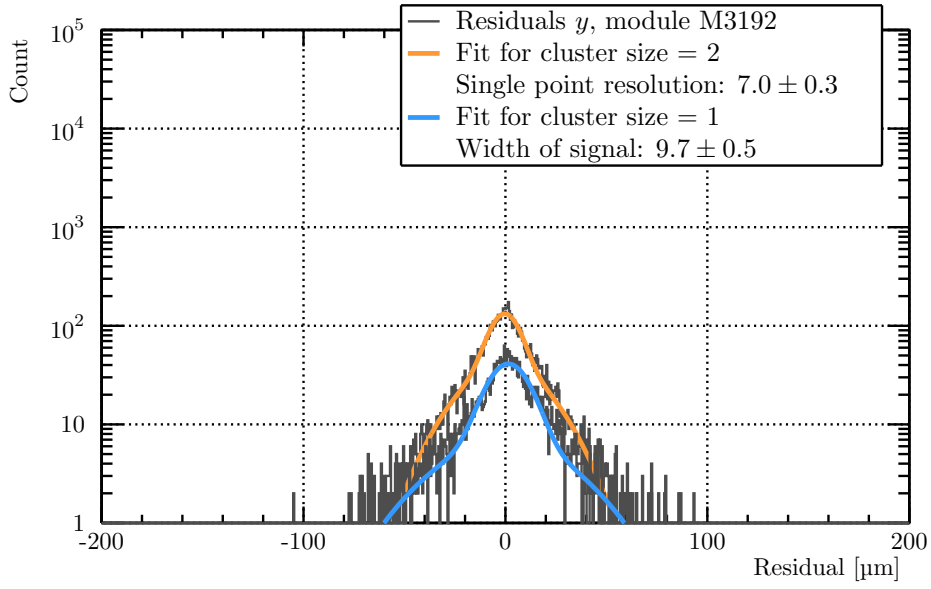

(b) *Global y.*

Figure 3.43. *Fits to the unbiased residuals distributions with cluster size 1 pixels (blue) and 2 pixels (orange), between the cluster position on module M3192 ($+x_{global}$) and the track interpolated on the detector plane. The data is shown in grey, and the estimated resolution is given in the legend.*

cluster positions are known with sub-pixel accuracy and they are randomly distributed. Hence, the signal can be modeled by a Gaussian distribution of which the sigma is a measure of the resolution. The background is most likely due to noise, off-time particles and many other processes, and thus it is also approximated by a Gaussian. The fits are represented by orange and blue curves in Figures 3.42 and 3.43.

The single point resolution of a telescope module is defined here as the sigma of the Gaussian with the narrowest width of the fit to the unbiased residual distribution of clusters with a size of 2 pixels. The single point resolutions in x and y for modules M3204 and M3192 are given in the plots of Figures 3.42 and 3.43. For all other modules an overview is given in Table 3.3 below. The corresponding plots are in Appendix C.

Table 3.3.
A summary of the residual fits and the single point resolution of the telescope modules.

Module	**Single point resolution, x** σ_x µm	**Single point resolution, y** σ_y µm	**Width of x background** B_x µm	**Width of y background** B_y µm
M3173	7.19 ± 0.03	9.43 ± 0.07	18.4 ± 0.12	20.53 ± 0.099
M3164	7.2 ± 0.13	8.9 ± 0.29	21.0 ± 0.94	19.9 ± 0.6
M3239	6.99 ± 0.04	9.42 ± 0.08	16.0 ± 0.11	19.91 ± 0.094
M3023	6.9 ± 0.25	10.4 ± 0.4	15.4 ± 0.7	21 ± 1.1
M3265	7.64 ± 0.03	9.92 ± 0.07	18.1 ± 0.12	21.8 ± 0.12
M3226	7.0 ± 0.24	7.4 ± 0.3	17.7 ± 0.6	20.1 ± 0.5
M3204	7.82 ± 0.03	10.68 ± 0.08	19.2 ± 0.12	22.9 ± 0.14
M3192	5.7 ± 0.17	7.0 ± 0.3	18.0 ± 0.5	20.5 ± 0.6
M3090	6.54 ± 0.03	8.65 ± 0.086	18.3 ± 0.13	21.2 ± 0.11
M3124	5.9 ± 0.14	8.0 ± 0.20	62 ± 2.6	72 ± 4
M3082	7.19 ± 0.03	11.24 ± 0.08	19.9 ± 0.13	25.0 ± 0.15
M3009	7.33 ± 0.04	10.36 ± 0.090	24.8 ± 0.18	27.3 ± 0.20
M3027	14.48 ± 0.07	19.9 ± 0.18	37.4 ± 0.22	41.6 ± 0.24
M3074	25.6 ± 0.85	37 ± 1.3	95 ± 5	154 ± 29

There were a few modules with a relatively low resolution above 12 µm, namely M3124 and M3074 in the $-x_{global}$, downstream quadrant. This may be explained to be a result of the missing modules in downstream layers 2 and 3 and the low statistics for that side of the telescope. For future beam tests these layers should be swapped with others to spread the dead areas in the telescope better and improve the tracks on the $-x_{global}$ side of the telescope.

Excluding modules M3124 and M3074, the resolution in y is slightly lower than in x since the pixel size is larger in the y direction by 50 µm. For the x direction, the average single point resolution of a module is 7.24 ± 0.08 µm and for y it is 10.0 ± 0.21 µm. This is well below $100/\sqrt{12} = 29$ µm in x and $150/\sqrt{12} = 43$ µm for y, because the cluster charge is taken into account for the cluster position estimation in CMSSW.

Based on the uncertainty propagation of a straight line fit, the tracking resolution σ_{track} at $z_{global} = 0$ is defined as

$$\sigma_{track} = \sqrt{\sum_{i}^{N} \frac{\sigma_i^2}{N}} \tag{3.9}$$

with i being the index of the layers in the telescope, N the total number of layers in the telescope and σ_i the single point resolution of plane i. Excluding the downstream layer 0 with module M3124 and M3074, this gives a tracking resolution in x of $\sigma_{track} = 7\,\mu m$ and in y of $\sigma_{track} = 10\,\mu m$.

3.8. Pilot beam test with a CBC3 mini module

To verify that the telescope can be used for beam tests with CMS Tracker Upgrade module prototypes, a pilot beam test was completed with a 2CBC3 mini module (see Section 1.6.2) in the same H6A area of the SPS test beam facility. This module was already tested in a beam at Fermilab, in November of 2017 [57]. The results of this beam test campaign are used to compare to this pilot beam test.

3.8.1. Installing the DUT in the telescope

The mini module's aluminum frame was mounted on the rotational stage via the use of an L-shaped, aluminum adapter piece. A photograph of the CBC3 DUT after the installation in the telescope is presented in Figure 3.44.

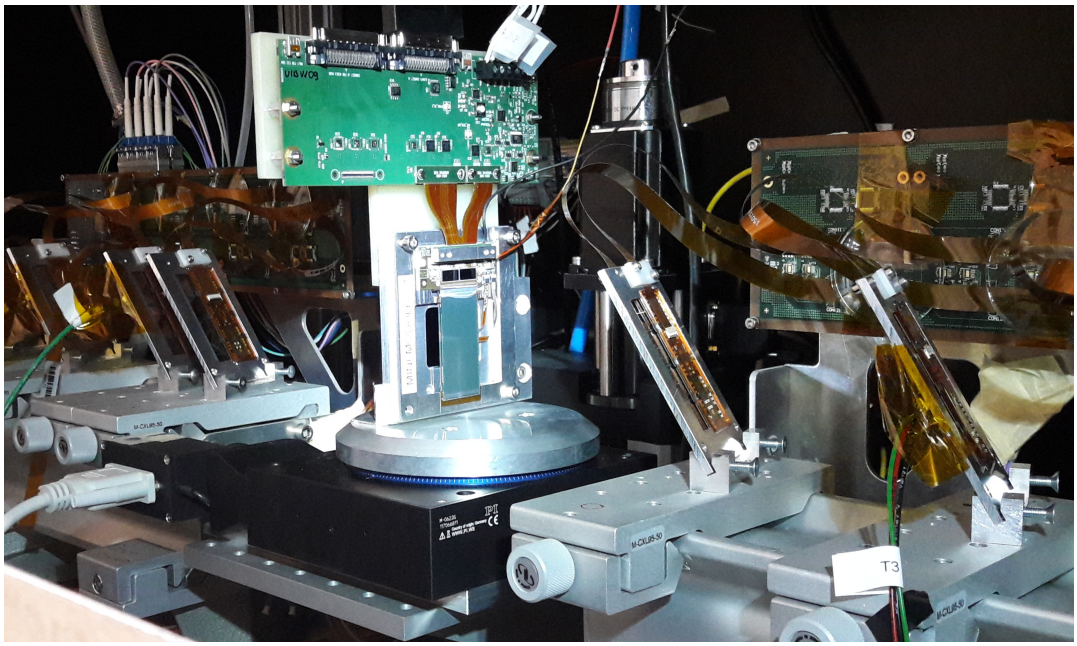

Figure 3.44. *A CBC3 mini module installed in the CHROMIE telescope.*

A plastic, L-shaped plate screwed to the aluminum frame of the mini module supported the Universal Interface Board (UIB). This interface board connects to the 2CBC3 hybrid of the mini module. The power and data cables from the power supplies and the back-end cards attach to the UIB. A rectangular window in the ceiling of the telescope box was used to allow the DUT cables to leave the telescope enclosure. It was covered with a thick black cloth to prevent light from entering the setup. The mini module was positioned at a 90° angle with respect to the beam axis for the whole duration of the pilot beam test.

Two laboratory power supplies were used for low voltage power and high voltage bias. The µTCA card for the mini module's DAQ was placed in the µTCA crate of the telescope to allow for simultaneous triggering of both. Since the CBC3 mini module had not been irradiated before it did not need extra cooling.

During this pilot beam test, the threshold of the CBC3 chips of the mini module was scanned between 570 V_{Cth} and 500 V_{Cth}. Because of time constraints, a full threshold scan of with the CBC3 mini module could not be completed. On top of that, the beam was not properly focused and aligned on the telescope, which leaves only a few runs that can be analyzed. The results of the pilot beam test are explained in the next sections, but first the synchronization of the readout is discussed.

3.8.2. Synchronizing the DUT with the telescope

As the readout of the telescope and the readout of the CBC3 mini module were in the same µTCA crate, clock and triggers could be sent simultaneously to both by the AMC13. This is illustrated in Figure 3.45. The µDTC and the DAQ PC were linked to each other via an ethernet cable. Between the mini module and the back-end a 3 m long HDR cable was used to transport the data from the module to the µDTC.

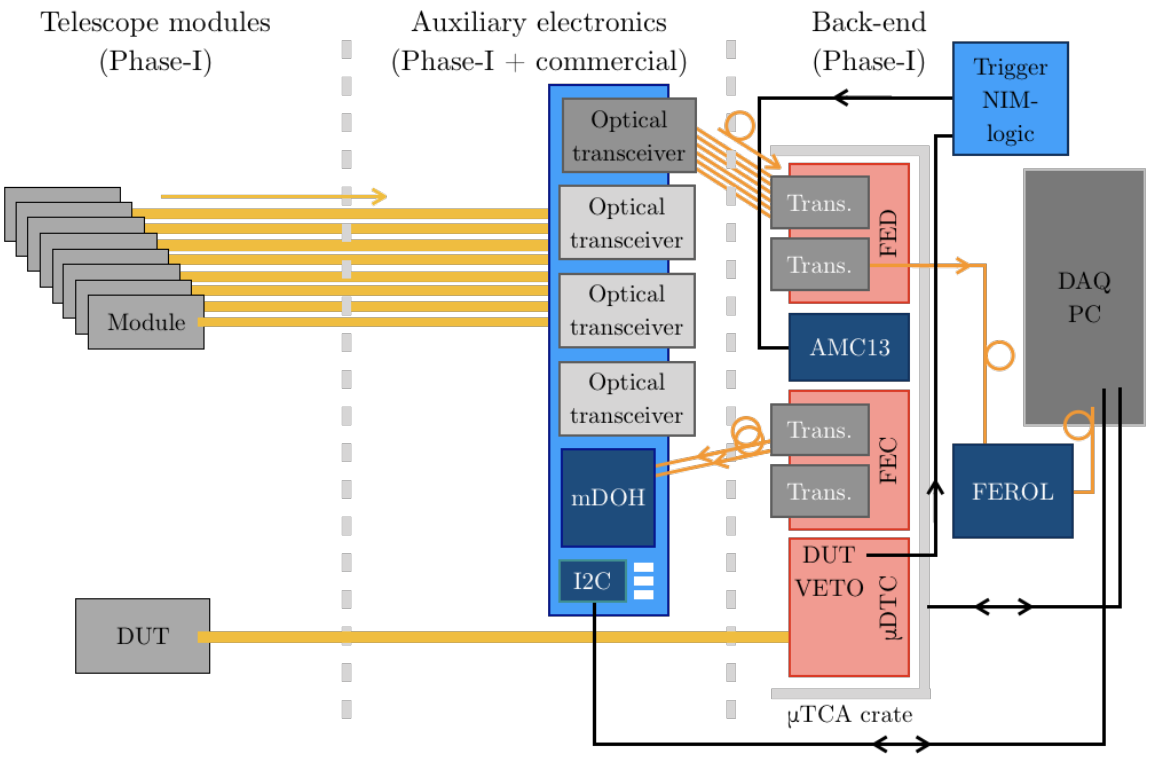

Figure 3.45. *A schematic view of the combined DAQ of CHROMIE and the CBC3 mini module. Yellow lines represent flat ribbon cables, providing electrical connections. The orange lines represent optical fibers, and the black lines electrical links. The arrows on each link indicate the direction of the signals.*

Two different FMCs were used in the DUT readout, an LPC+ FMC for the HDR cable connector and a custom made LA12 FMC that was used to send a veto signal to the NIM logic. When the mini module readout was busy, the veto signal was high. The veto of the DUT was send to the trigger NIM logic of CHROMIE. This is shown in Figure 3.46. The coincidence unit of the trigger and the clock has a veto input and as long as it is high the unit produces no output.

Including the veto, the two readout systems were synchronized in the following way. First the triggering was stopped via the software of the AMC13. Then both the telescope and the DUT were configured through their separate readout software packages. If both were configured

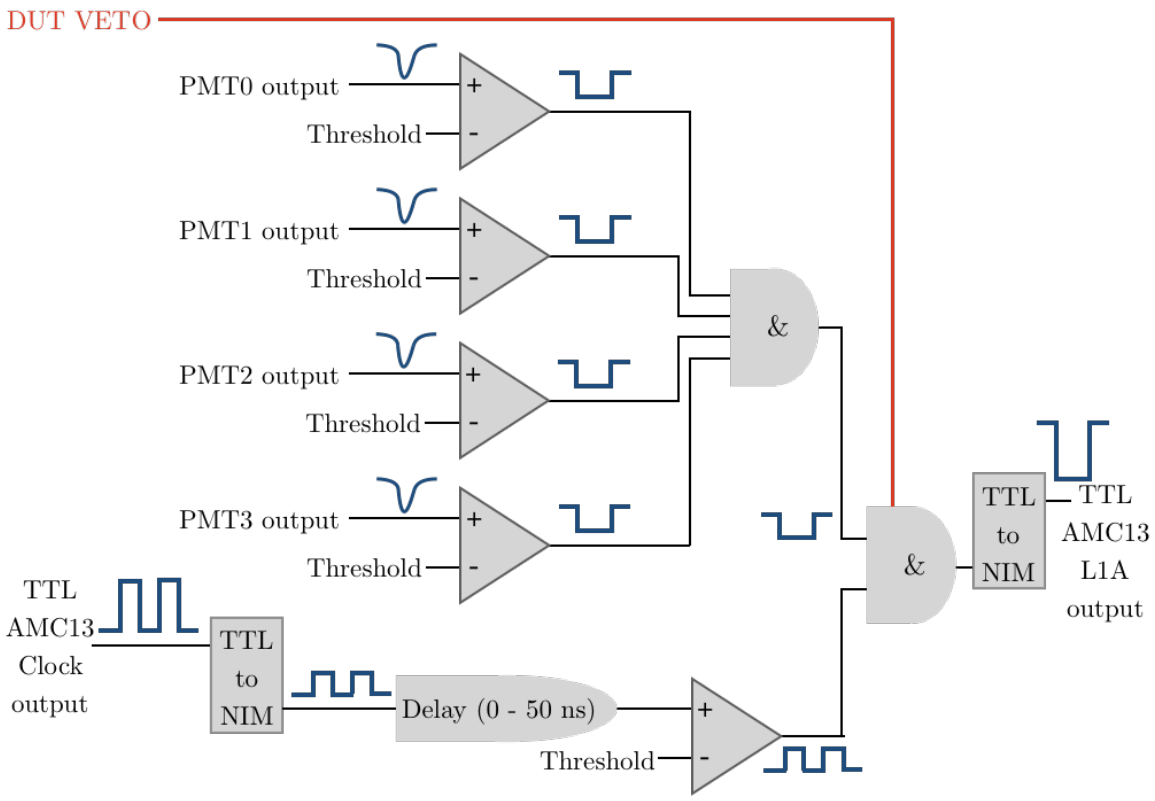

Figure 3.46. *Trigger logic of the CHROMIE triggering system with the DUT included. Whenever the mini module was unable to receive triggers it send a VETO signal to the trigger logic.*

correctly, the triggering would be started with the AMC13 software. At the end of a run, the triggers were stopped first, and then the respective readouts of the telescope and DUT were turned off. The synchronicity of the two was confirmed by looking at the correlation between the extrapolated track positions on the CBC3 module and the its cluster positions.

3.8.3. Results from the pilot beam test: synchronization

Figure 3.47 shows the correlation between the extrapolated track's x-position on the DUT and the x-position of the clusters detected by the mini module on Sensor 0 and 1 respectively. This was before any software alignment of tracks or DUT. There was a clear correlation visible with a large offset in the order of a centimeter. This offset was a result of the DUT's position with respect to the telescope's z-axis.

The physical misalignment between the DUT's xy-plane and the telescope's xy-plane is demonstrated in Figures 3.48 and 3.49. Here the track's x-position on $z_{global} = 0$ (DUT location) and the cluster position on the DUT are shown respectively. During the pilot beam test the telescope measured the whole beam while the CBC3 mini module only measured half.

Due to time constraints no effort was made to align the DUT to the beam with the help of the motorized stages. This makes it difficult to understand from the pilot beam test data whether the DUT failed to detect a cluster when a track was reconstructed because of its geometry, or because of an inefficiency of the mini module. Even more so because the position of the DUT in the y-direction is not known as it has strip sensors.

In an ideal situation, the DUT's y-location with respect to the beam could have been optimized. By varying the y-position with the vertical linear actuator while monitoring the

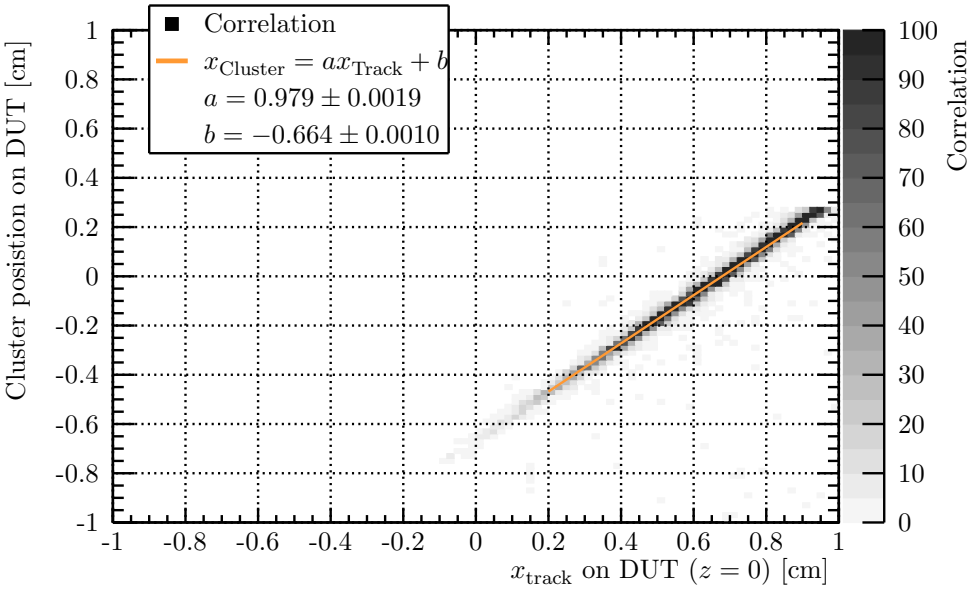

(a) *Sensor 0.*

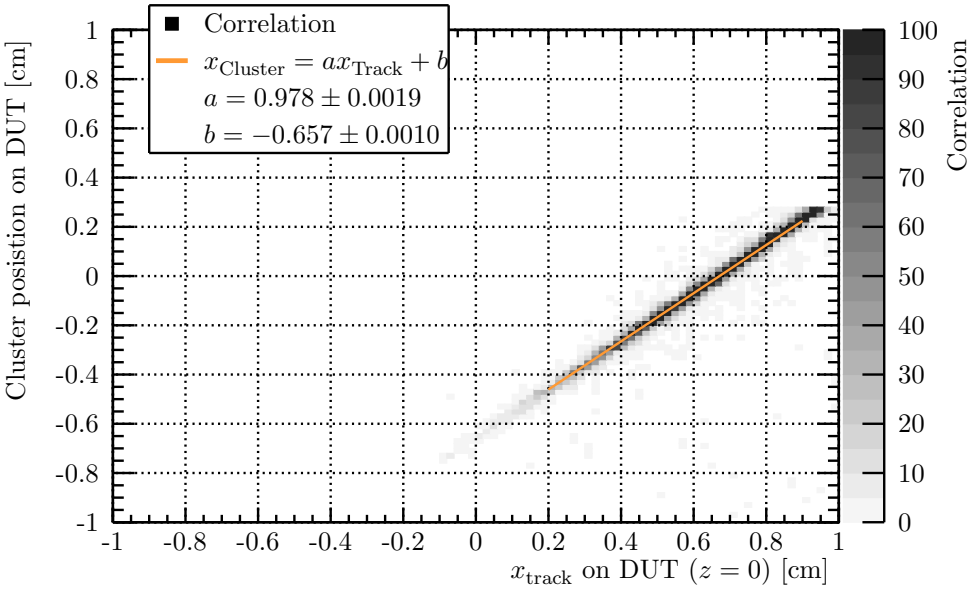

(b) *Sensor 1.*

Figure 3.47. *Correlation between the cluster position on DUT Sensor 1 and the interpolated track x-position from the telescope, before telescope and DUT software alignment, during run* 100 334 *of the pilot beam test.*

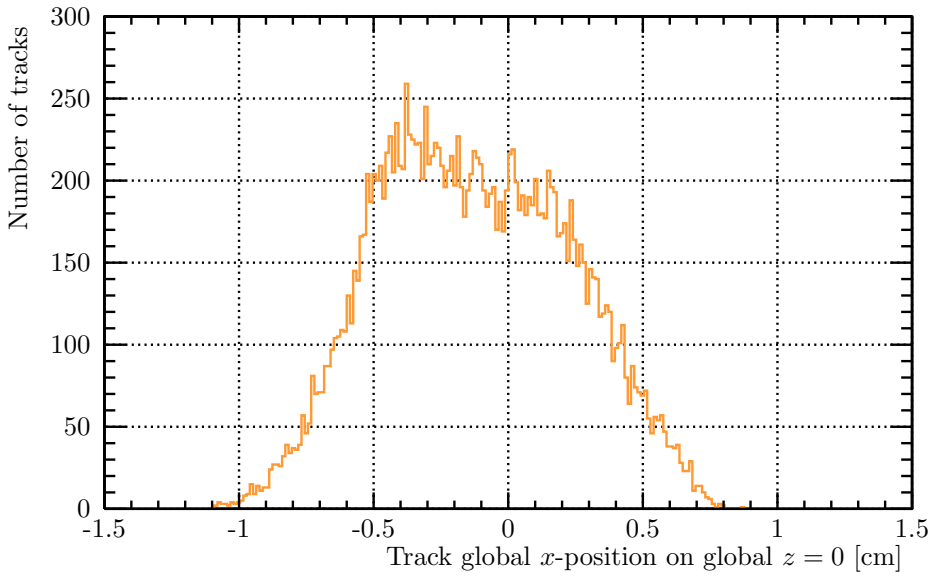

Figure 3.48. *The track x-positions on global $z = 0$, during run* 100 334.

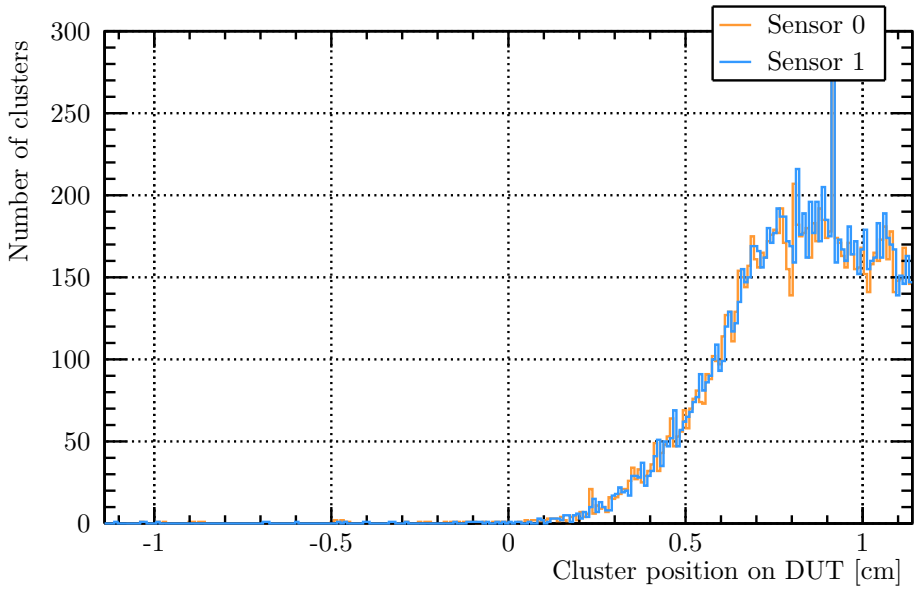

Figure 3.49. *Cluster x-positions in the DUT, during run* 100 334. *The clusters in Sensor 0 are in orange and the clusters in Sensor 1 in blue.*

number of hits in both sensors, the beam could have been scanned. Normally the DUT would be then placed on the y-position that results in the most hits, for obvious reasons.

3.8.4. Results from DUT measurements

Figure 3.50 displays the number of clusters per event in DUT Sensor 0 (orange) and 1 (blue) respectively. Both sensors measured almost the same number of cluster per event. Each sensor detected zero clusters in 30 % of the events. This can be explained by the position of the DUT with respect to the beam.

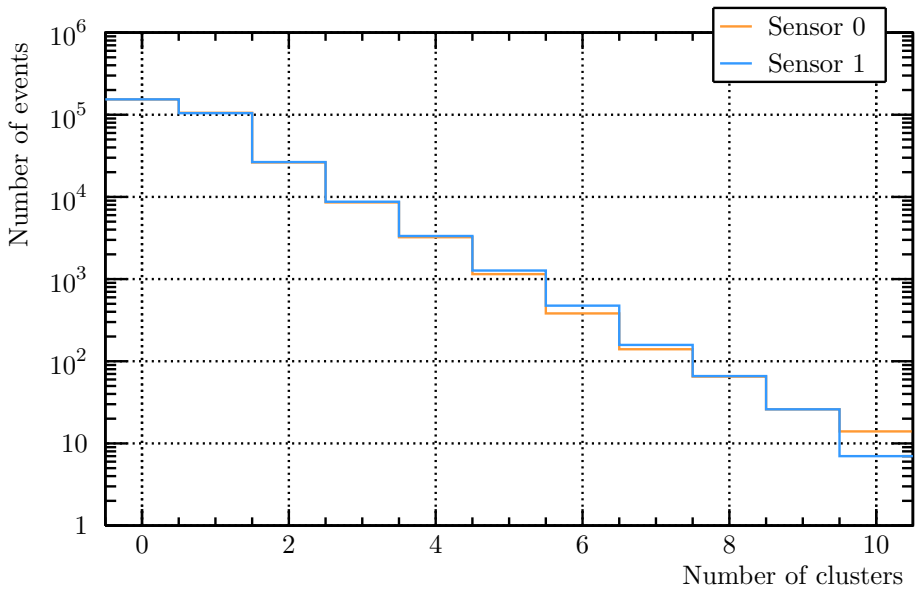

Figure 3.50. *Cluster width in number of strips, for Sensor 0 and Sensor 1 respectively, measured during run* 100 321.

Figure 3.51 shows the cluster size during the pilot beam test in DUT Sensor 0 (orange) and Sensor 1 (blue). The DUT sensor planes were positioned at a 90° angle with respect to the beam axis. Therefore, most clusters measured by the DUT were expected to have a cluster size of 1 strip, because there is no additional charge sharing as a result of geometry. This explains the large peak at cluster size 1 in the plot.

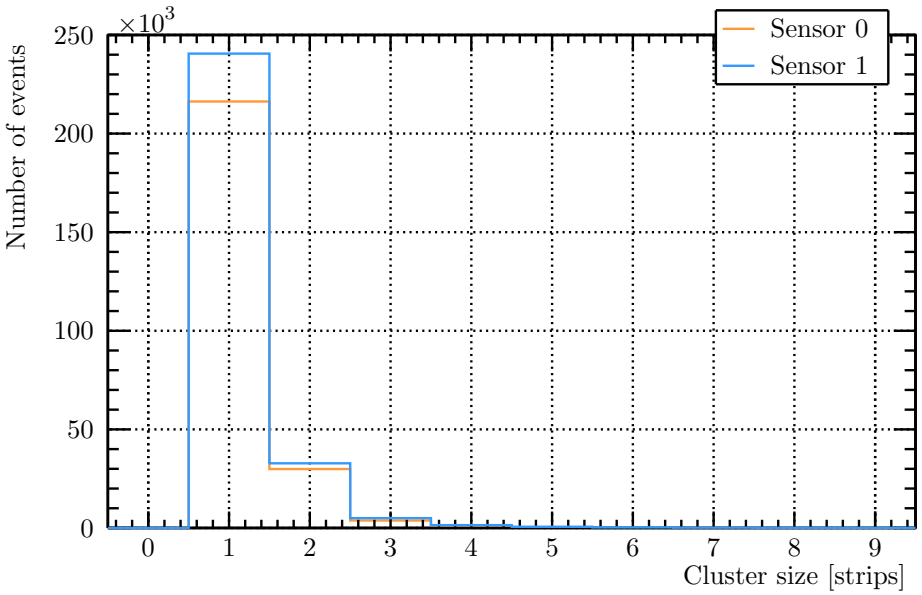

Figure 3.51. *Cluster size in number of strips for Sensor 0 (orange) and Sensor 1 (blue) respectively, measured during run* 100 334.

After the telescope track reconstruction, see Sections 3.7.2 and 3.7.3, the DUT was aligned with respect to the tracks with the same software. Since the mini module has strip sensors, the

positional changes in the DUT were limited to translations in the DUT's local x-direction, and rotations around it's local y and z-axis. The misalignment of the DUT's sensors is summarized in Table 3.4. The difference in rotation around z between the two sensors, estimated with the software alignment based on tracks from the CHROMIE telescope is 0.0605°. In addition, it was estimated that there is a shift along x between the sensors of 60 µm.

Table 3.4.
Summary of the misalignment of the CBC3 mini module's sensors.

Sensor	**Rotation around y** ϕ °	**Rotation around z** θ °	**Translation along x** x_{trans} mm
0	0.0	+0.9821	+13.9592
1	0.0	+1.0426	+13.8995

The unbiased residuals of the DUT clusters with 1 strip cluster size with respect to the tracks that point to them are shown in grey in Figure 3.52 for both Sensor 0 and Sensor 1. Since the CBC3 has binary readout the cluster position can not be known more accurately than $90/\sqrt{12} = 26$ µm. This is the expected resolution of the module's sensors. This also means that the resulting residual distributions are more square-shaped. They can be fit by a box-shaped function (two step functions) convoluted with a Gaussian. The Gaussian function accounts for the smear of the edges of the box shape caused by the tracking resolution and the measurement error of the DUT. The fit for Sensor 0 is shown in orange in Figure 3.52 and the fit for Sensor 1 is shown in blue.

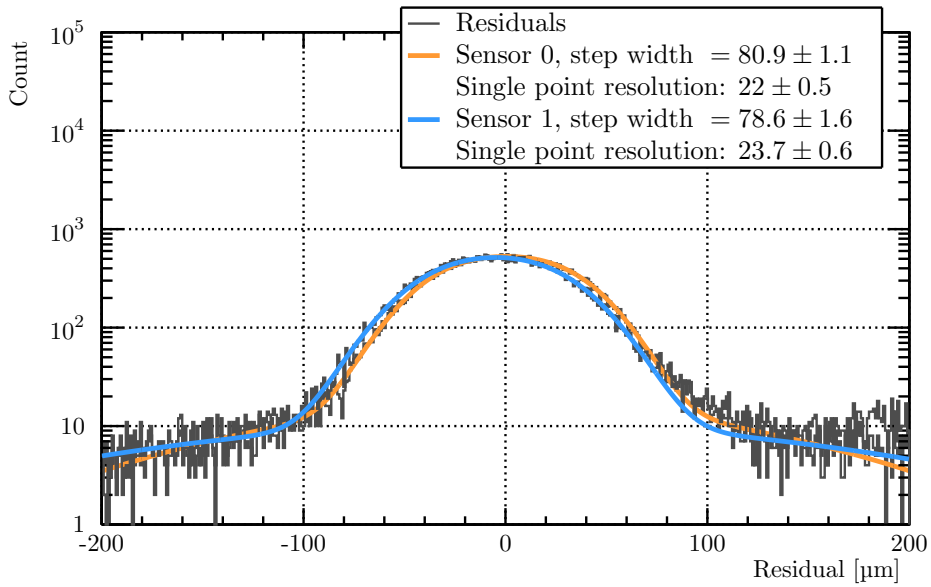

Figure 3.52. *Fits to the unbiased residuals of the DUT clusters with cluster size 1 between the cluster position on the DUT's sensors and the track interpolated on the DUT sensor planes measured during run* 100 334. *The data are shown in grey, the fit for Sensor* 0 *in orange, and the fit for Sensor* 1 *in blue.*

The width of the step function gives the sensitive area of a strip in which the particle must hit to produce one-strip clusters. Outside of this sensitive area there is charge sharing which results in clusters of more than 1 strip size. Therefore, this width is not equal to the strip pitch of 90 µm. In Figure 3.52 it can be seen that for Sensor 0 this sensitive area was measured

to be $(80.9 \pm 1.1)\,\mu m$, and $(78.6 \pm 1.6)\,\mu m$ for Sensor 1. Hence, the expected measurement error, or resolution for 1-strip clusters of the DUT's Sensor 0 was $80.9\sqrt{12} = 23\,\mu m$, and $78.6\sqrt{12} = 23\,\mu m$ for Sensor 1.

The Gaussian distribution of the fit is the square sum of the measurement error of the DUT and the error on the track position. The error on the track position is given by the tracking resolution of the telescope. The tracking resolution was measured to be $7\,\mu m$ in the horizontal direction (Section 3.7.3) which is parallel to the strip pitch. Thus, the 1-strip resolution of the DUT can be defined as in (3.10). As a result, the measured 1-strip resolution of Sensor 0 was $(21.0 \pm 1.2)\,\mu m$, and for Sensor 1 it was $(23.0 \pm 1.7)\,\mu m$.

$$\sigma_{DUT} = \sqrt{\sigma^2_{Gaussian} - \sigma^2_{Track}} \tag{3.10}$$

During a beam test campaign at Fermilab in November 2017 with the same module the resolution was measured to be $(23.9 \pm 0.3)\,\mu m$ [57]. The resolution that was measured with the CHROMIE telescope was the same within the statistical uncertainty for Sensor 1 while for Sensor 1 it within 2 standard deviations from the Fermilab beam test results.

From the results of the pilot beam test with the CHROMIE telescope it was concluded that the telescope can be used to reconstruct tracks from particle beams for the use of studying CMS Phase-2 Outer Tracker Modules. CHROMIE was used in a mini beam test with an RD53A module after this pilot. The preliminary results of that mini beam test are presented in Appendix D.

3.9. Conclusion

A new beam telescope, designed for high-rate tests ($>200\,MHz\,cm^{-2}$) with CMS Phase-2 Tracker modules, has been constructed and tested at CERN. Based on the results of a pilot beam test, it is concluded that the telescope is functional and can be used for its design purpose.

With the telescope, tracks from beam particles can be reconstructed, to use for testing DUTs. The single point resolution in the global x at a module is on average $7.24 \pm 0.08\,\mu m$ and in y the average is $10.0 \pm 0.21\,\mu m$. This translates into a tracking resolution at $z_{\text{global}} = 0$ of $\sigma_{\text{track},x} = 7\,\mu m$ and in y of $\sigma_{\text{track},x} = 10\,\mu m$.

3.10. Future improvements to the CHROMIE

Throughout this chapter suggestions have been made as to what needs to be improved on the telescope. These are summarized in this section, in the order they were previously discussed in.

First of all the cooling and powering of the telescope have to be improved. At the time of writing, the cooling consists of a few computer fans and pressurized air directed at the SFPs on the motherboards. This is sufficient but very impractical as it requires a few bars of pressure to provide to needed cooling power.

The powering now consists of two remotely controlled laboratory power supplies. At the moment there are no safety measures implemented to for instance protect against overpowering or applying the bias voltage when the ROCs were not configured yet. This needs to be improved in order to make it safe for the telescope to be operated by many different users.

At present the delay to prevent the FED from going out of sync has not been identified yet (see Section 3.6.5). This needs to be fixed by identifying the settings in the FED firmware that are responsible for the timing between the trigger and the readout, and changing those accordingly.

Related to the readout staying synchronized is the triggering. At the moment the trigger logic is based on NIM modules that can not be controlled or changed remotely. Additionally, there is no triggering and clock control system, that monitors the state of the FED to verify that it did not go OOS or BUSY during a run. Such a control system is usually also able to stop triggering and send a resync command to the firmware to allow for the run to be finished without problems. Especially for high rate tests such a system is needed as the trigger rates will be very high.

By looking at the hit position correlation between two modules in the same plane it was concluded that there was no overlap in the local x-direction between modules in the same layer. This can be fixed by changing the angle of each plane around the local y. It will help with the resolution of the telescope as it will make it easier for the two modules in a plane to be aligned.

Finally there are currently two modules in the telescope that can not be communicated with, and are potentially broken beyond repair. It needs to be investigated in a lab if these modules are actually broken or if there is a problem with the setting somewhere in the readout software. Whether they are dead or not, the position of the layers with the modules in them should be changed because right now they are next to each other and on the same x_{global} side of the telescope. If they can be recovered, swapping them reduces the risk of having large gaps in the telescope in case they break again. If they are in fact broken, changing their position is obvious.

4. Conclusion

During this research, prototype silicon sensor modules for the upgrade of the CMS tracking detector were characterized in two studies. First, a calibration procedure was developed for the gain calibration of the prototype readout chip that is connected to the silicon sensors. Second, a setup for testing the prototypes in a particle beam at a high-rate was designed, constructed, and tested.

The gain calibration procedure, which was developed during this study, can be explained as follows. The gain of the binary readout chip is the relation between the energy of a particle that traverses the silicon sensor, and the amount of charge that is collected by the readout chip because of that. To determine the gain, the silicon tracker prototype for CMS was exposed to different fluorescent photon sources with a monochromatic energy while executing a threshold scan with the binary readout chip. In the threshold scan, the threshold at which the signal of a fluorescent photon source can no longer be measured corresponds to the photon's energy because the binary readout will only produce a logical 1 when the signal is larger than the threshold.

A linear calibration curve was obtained by plotting the threshold values corresponding to the different fluorescent photon energies versus the photon energies. The gain was extracted from this curve by determining the slope of the curve such that the threshold unit of the readout chip could be expressed in amount of signal produced by a photon of a given energy, and it was expressed in number of electrons.

The average calibration value of the readout chips in the prototype silicon tracker module that was used in this study was found to be $367 \pm 12\,e$ per unit of threshold. The variation in calibration value of the individual silicon strips of the sensor was within 10 %. This was explained to be the result from the technology used to produce the readout chips. To further investigate the chip-to-chip differences data were analyzed from measurements with another silicon tracker prototype that had sixteen readout chips. The differences between these sixteen chips were within 10 % as well.

To obtain a better understanding of the measurements a toy Monte-Carlo simulation was developed. It was capable of predicting the signal threshold for a photon of a given energy with a 5 % accuracy. The simulation took as input the energy of the photon, the measured calibration value of a readout chip, and the measured noise and baseline of the prototype silicon module. The simulation included a simple charge sharing model that was tuned with data attained from measurements with the silicon tracker prototype that was used to measure a threshold scan while it was being exposed to photons from radioactive americium.

A procedure was proposed for the calibration of the threshold setting of CMS silicon tracker modules' readout chips during their mass-production, which is scheduled to start at the end of the year 2020. This proposal included performing calibrations with a large set ($\sim$100) of readout chip prototypes to first make a better evaluation of quantitative differences between the chips. Based on those measurements a decision can be made to either calibrate all chips, or just a fraction of them.

Since the prototype silicon tracker modules of CMS are designed for the upgrade of the LHC they need to be tested while they are being exposed to high particle fluxes of up to $100\,\mathrm{MHz\,cm^{-2}}$. This is achieved in beam test facilities where particle tracks that are reconstructed with data from beam telescopes are compared to the hits in the prototypes. Standard beam telescopes

are not functional at these high particle fluxes because their readout speed is to low. Therefore, a new telescope designed for prototype silicon tracker modules for the upgrade of CMS was build and tested at CERN.

This new beam telescope had eight layers. Each layer contained two CMS silicon pixel modules that were left over from the production of the last upgrade of the inner most part of the CMS tracker. The two pixel modules in a layer had a total silicon sensor area of $32.4 \times 64.8\,\mathrm{mm}^2$. In between the fourth and the fifth telescope layer a prototype silicon tracker module could be placed such that reconstructed tracks from the telescope data could be interpolated to the prototype module to compare to the particle cluster positions that it measured.

After the construction and calibration of the telescope it was placed in a particle beam of the SPS beam test facility at CERN. With the particles in the beam the telescope was fully commissioned. This was verified by the almost one-to-one correlation between the locations of hits in different telescope layers. Then a silicon tracker prototype was placed in the center of the telescope to verify that the telescope could be used effectively in beam tests. To accomplish this the readouts of the two systems were synchronized before data taking began. The almost one-to-one correlation between the interpolated tracks of the telescope and the particle hit positions of the prototype tracker module demonstrated that the telescope was fully functional and ready for use in the high particle flux beam tests it was designed for.

An analysis code was produced to reconstruct tracks from the telescope data. With that analysis code the spatial resolution of the telescope was determined to be 7 µm in the horizontal and 10 µm in the vertical measurement axis. Reconstructed tracks from tests with the prototype silicon tracker module of CMS were compared to the clusters found in the prototype. It was found that the spatial resolution of that prototype module was (21.6 ± 0.5) µm for one of the silicon sensors and (23.7 ± 0.6) µm for the other silicon sensor in the module. This same result was previously found in a beam test elsewhere with the same module confirming the successful commissioning of the telescope.

Bibliography

[1] "LHC Machine". In: *JINST* 3 (Aug. 14, 2008). Edited by Lyndon R Evans and Philip Bryant. This report is an abridged version of the LHC Design Report (CERN-2004-003), S08001. 164 p. DOI: 10.1088/1748-0221/3/08/S08001. URL: http://cds.cern.ch/record/1129806.

[2] ATLAS collaboration. "The ATLAS Experiment at the CERN Large Hadron Collider". In: *JINST* 3 (Aug. 14, 2008). Also published by CERN Geneva in 2010, S08003. 437 p. DOI: 10.1088/1748-0221/3/08/S08003. URL: http://cds.cern.ch/record/1129811.

[3] CMS Collaboration. "The CMS experiment at the CERN LHC. The Compact Muon Solenoid experiment". In: *JINST* 3 (Aug. 14, 2008). Also published by CERN Geneva in 2010, S08004. 361 p. DOI: 10.1088/1748-0221/3/08/S08004. URL: http://cds.cern.ch/record/1129810.

[4] ALICE Collaboration. "The ALICE experiment at the CERN LHC. A Large Ion Collider Experiment". In: *JINST* 3 (Aug. 14, 2008). Also published by CERN Geneva in 2010, S08002. 259 p. DOI: 10.1088/1748-0221/3/08/S08002. URL: http://cds.cern.ch/record/1129812.

[5] LHCb Collaboration. "The LHCb Detector at the LHC". In: *JINST* 3.LHCb-DP-2008-001. CERN-LHCb-DP-2008-001 (Aug. 14, 2008). Also published by CERN Geneva in 2010, S08005. DOI: 10.1088/1748-0221/3/08/S08005. URL: http://cds.cern.ch/record/1129809.

[6] David Barney. "CMS Detector Slice". CMS Collection. Jan. 2016. URL: https://cds.cern.ch/record/2120661.

[7] Werner Herr and Bruno Muratori. *Concept of luminosity*. Technical report. CERN, 2006. DOI: 10.5170/CERN-2006-002.361. URL: https://cds.cern.ch/record/941318 (visited on Aug. 19, 2019).

[8] CMS Collaboration. *The Phase-2 Upgrade of the CMS Tracker*. Technical report CERN-LHCC-2017-009. CMS-TDR-014. Geneva, Switzerland: CERN, June 2017. URL: https://cds.cern.ch/record/2272264.

[9] D Noll, V Bencini, J B Lallement, et al. "Linac 4 source extraction and low energy beam transport study". In: *AIP Conf. Proc.* 2011.1 (2018), 080026. 3 p. DOI: 10.1063/1.5053381. URL: https://cds.cern.ch/record/2675881.

[10] Daniel Jean Simon. "The CERN PS complex: a versatile particle factory". In: *Joint Accelerator Conferences* CERN-PS-96-019-DI (Apr. 19, 1996), page 4. URL: http://cds.cern.ch/record/305985.

[11] John Bertram Adams. *A design of the European 300 GeV research facilities*. Geneva, Switzerland: CERN, 1970. URL: https://cds.cern.ch/record/1220684.

[12] CERN. *Design study of a proton-antiproton colliding beam facility*. Technical report CERN-PS-AA-78-3. Geneva, Switzerland: CERN, 1978. URL: https://cds.cern.ch/record/518868.

[13] Giulio Stancari, Valentina Previtali, Alexander Valishev, et al. "Conceptual design of hollow electron lenses for beam halo control in the Large Hadron Collider". In: FERMILAB-TM-2572-APC, CERN-ACC-2014-0248 (2014). arXiv: 1405.2033 [physics.acc-ph].

[14] Corinne Pralavorio. *Record luminosity: well done LHC*. CERN. Nov. 3, 2017. URL: http://cern.ch/go/QPj8 (visited on Aug. 12, 2019).

[15] Lucio Rossi and Oliver Brüning. *The High Luminosity Large Hadron Collider: the new machine for illuminating the mysteries of Universe*. Advanced series on directions in high energy physics. Hackensack, New Jersey: World Scientific, 2015. ISBN: 9789814675468. DOI: 10.1142/9581. URL: http://cds.cern.ch/record/1995532.

[16] CMS Collaboration. *CMS Physics: Technical Design Report. Volume 1: Detector Performance and Software*. Technical Design Report CMS CERN-LHCC-2006-001. There is an error on cover due to a technical problem for some items. Geneva, Switzerland: CERN, 2006. URL: http://cds.cern.ch/record/922757.

[17] M. Tanabashi, K. Hagiwara, K. Hikasa, et al. "Review of Particle Physics". In: *Phys. Rev. D* 98 (3 Aug. 2018). DOI: 10.1103/PhysRevD.98.030001. URL: https://link.aps.org/doi/10.1103/PhysRevD.98.030001.

[18] CMS Collaboration. "Detector drawings". CMS-PHO-GEN-2012-002, CMS Collection. Mar. 2012. URL: https://cds.cern.ch/record/1433717.

[19] V Karimäki, M Mannelli, P Siegrist, et al. *The CMS tracker system project: Technical Design Report*. Technical Design Report CMS CERN-LHCC-98-006. Geneva, Switzerland: CERN, 1997. URL: https://cds.cern.ch/record/368412.

[20] CMS Collaboration. *The CMS tracker: addendum to the Technical Design Report*. Technical Design Report CMS CERN-LHCC-2000-016. Geneva, Switzerland: CERN, 2000. URL: https://cds.cern.ch/record/490194.

[21] Philippe Bloch, Robert Brown, Paul Lecoq, and Hans Rykaczewski. *Changes to CMS ECAL electronics: addendum to the Technical Design Report*. Technical Design Report CMS. Geneva, Switzerland: CERN, 2002. URL: https://cds.cern.ch/record/581342.

[22] CMS Collaboration. *The CMS hadron calorimeter project: Technical Design Report*. Technical Design Report CMS CERN-LHCC-97-031. Geneva, Switzerland: CERN, 1997. URL: https://cds.cern.ch/record/357153.

[23] CMS Collaboration. *The CMS magnet project: Technical Design Report*. Technical Design Report CMS CERN-LHCC-97-010. CERN, 1997. URL: https://cds.cern.ch/record/331056.

[24] CMS Collaboration. *The CMS muon project: Technical Design Report*. Technical Design Report CMS CERN-LHCC-97-032. Geneva, Switzerland: CERN, 1997. URL: https://cds.cern.ch/record/343814.

[25] Frank Hartmann. *Evolution of silicon sensor technology in particle physics; 2nd ed.* Springer tracts in modern physics. Berlin, Germany: Springer, Dec. 2017. DOI: 3319644343. URL: http://cds.cern.ch/record/2292029.

[26] L. Cadamuro. "The CMS Level-1 trigger system for LHC Run II". In: *Journal of Instrumentation* 12.03 (Mar. 2017), pages C03021–C03021. DOI: 10.1088/1748-0221/12/03/c03021. URL: https://doi.org/10.1088%2F1748-0221%2F12%2F03%2Fc03021.

[27] *Introduction into VME standard*. Wiener Power Electronics. Linde 18, D - 51399, Burscheid (Germany). URL: http://cern.ch/go/6Wht (visited on May 2019).

[28] *Optical readout and control systems for the CMS Tracker*. Volume 1. Nov. 2002, pages 233–237.

[29] C Paillard, C Ljuslin, and A Marchioro. "The CCU25: a network oriented communication and control unit integrated circuit in a 0.25 μm CMOS technology". In: (2002). DOI: 10.5170/CERN-2002-003.174. URL: http://cds.cern.ch/record/593914.

[30] Katja Klein. *The CMS Silicon Strip Tracker - Overview and Status*. Presented during a DCMS Meeting. Aachen, Germany: Physikalisches Institut B, RWTH, Jan. 20, 2006. URL: http://cern.ch/go/jwF9 (visited on Aug. 20, 2019).

[31] CMS Collaboration. *CMS Technical Design Report for the Pixel Detector Upgrade*. Technical report CERN-LHCC-2012-016. CMS-TDR-11. CERN, Sept. 27, 2012. URL: https://cds.cern.ch/record/1481838.

[32] H. C. Kästli. "Frontend electronics development for the CMS pixel detector upgrade". In: *Nucl. Instrum. Meth.* A731 (2013), pages 88–91. DOI: 10.1016/j.nima.2013.05.056.

[33] Edward Bartz. "The token bit manager chip for the CMS pixel readout". In: (2003). DOI: 10.5170/CERN-2003-006.185. URL: https://cds.cern.ch/record/720634.

[34] M Friedl, M Pernicka, and H Steininger. "The phase-1 upgrade of the CMS Pixel Front-End Driver". In: *Journal of Instrumentation* 5.12 (Dec. 2010), pages C12054–C12054. DOI: 10.1088/1748-0221/5/12/c12054. URL: https://doi.org/10.1088%2F1748-0221%2F5%2F12%2Fc12054.

[35] Dominique Gigi, Jean-Marc Andre, Ulf Behrens, et al. "The FEROL40, a microTCA card interfacing custom point-to-point links and standard TCP/IP". In: *PoS* TWEPP-17 (2017), 075. 5 p. DOI: 10.22323/1.313.0075. URL: https://cds.cern.ch/record/2312401.

[36] *Micro Telecommunications Computing Architecture Short Form Specification*. PICMG. Sept. 2006. URL: http://cern.ch/go/6BJZ (visited on May 2019).

[37] *FEC-CCS: A common front-end controller card for the CMS detector electronics*. 2006, pages 179–184. URL: http://doc.cern.ch/yellowrep/2007/2007-001/p179.pdf.

[38] E Hazen, A Heister, C Hill, et al. "The AMC13XG: a new generation clock/timing/DAQ module for CMS MicroTCA". In: *Journal of Instrumentation* 8.12 (Dec. 2013), pages C12036–C12036. DOI: 10.1088/1748-0221/8/12/c12036. URL: https://doi.org/10.1088%2F1748-0221%2F8%2F12%2Fc12036.

[39] *The CMS Timing and Control Distribution System*. Oct. 2015, pages 1–3. DOI: 10.1109/NSSMIC.2015.7581984.

[40] J Varela. *Timing and synchronization in the LHC experiments*. Technical report CMS-CR-2000-012. Geneva: CERN, 2000. DOI: 10.5170/CERN-2000-010.77.

[41] *PIMG 3.0 Revision 3.0 AdvancedTCA Base Specification*. 3rd edition. PICMG. Apr. 2015. URL: http://cern.ch/go/c8x6 (visited on May 2019).

[42] Davide Braga. *CBC2 (CMS Binary Chip 2) User Guide 1.1*. Science and Technology Facilities Council. Mar. 22, 2013. URL: http://cern.ch/go/p78z.

[43] Kirika Uchida and Mark Raymond. *Private communication about the common-mode noise problem in CBC2*. May 23, 2019.

[44] Mark Prydderch. *CBC3.1 User Manual*. Science and Technology Facilities Council. Sept. 19, 2017. URL: http://cern.ch/go/8qmQ.

[45] Mark Raymond, Mark Prydderch, Michelle Key-Charriere, Lawrence Jones, and Stephen Bell. *CBC3 Status*. Presented during the CMS Tracker Week. Mar. 10, 2017. URL: http://cern.ch/go/7nSW (visited on Aug. 25, 2019).

[46] David Braga. "Development of the Readout Electronics for the High Luminosity Upgrade of the CMS Outer Strip Tracker". PhD thesis. Imperial College London, June 2016. URL: http://hdl.handle.net/10044/1/33725 (visited on Aug. 20, 2019).

[47] Mark Raymond. *CBC2 test results and plans*. Presented duringCMS Tracker Week. May 2013. URL: http://cern.ch/go/8bgl (visited on Oct. 16, 2018).

[48] Jean-Pierre Adloff. *Fundamentals of radiochemistry*. Milton: CRC Press, 2018. ISBN: 9781315893099. URL: https://cds.cern.ch/record/2309218.

[49] A.G. Wright. *The Photomultiplier Handbook*. 1st edition. Oxford University Press, Aug. 2017. ISBN: 9780199565092. DOI: 10.1093/oso/9780199565092.001.0001.

[50] Mercedes Minano Moya. *Pixel module production and qualification for the Phase 1 Upgrade of CMS*. Technical report CMS-CR-2014-388. Geneva: CERN, Nov. 2014. URL: https://cds.cern.ch/record/1970449.

[51] Albert Thompson, David Attwood, Eric Gullikson, et al. *X-ray Data Booklet*. LBNL/PUB-490 Rev. 3. Oct. 2009. URL: http://cxro.lbl.gov//PDF/X-Ray-Data-Booklet.pdf.

[52] J. H. Hubbell and S. M. Seltzer. *X-ray Mass Attenuation Coefficients*. NIST Standard Reference Database 126. July 2004. URL: http://cern.ch/go/HRH6.

[53] Marius Preuten. *Module number 2 Noise update*. Presented during CMS Tracker Upgrade Systemtest meeting. Feb. 2017. URL: http://cern.ch/go/X6Sn.

[54] M. Miñano Moya. "Pixel module production and qualification for the phase-1 upgrade of CMS". In: *Journal of Instrumentation* 10.01 (Jan. 2015), pages C01045–C01045. DOI: 10.1088/1748-0221/10/01/c01045. URL: https://doi.org/10.1088%2F1748-0221%2F10%2F01%2Fc01045.

[55] K Grotz. *The weak interaction in nuclear, particle and astrophysics*. Milton: CRC Press, 2018. URL: https://cds.cern.ch/record/2309194.

[56] Giovanni Zevi Della Porta, Sarah Seif El Nasr-Storey, Nikkie Deelen, and Stefano Mersi. *CBC3 simulator*. Presented during System tests meeting of the CMS Phase-2 upgrade. Mar. 2018. URL: http://cern.ch/go/W9CL.

[57] Georg Auzinger, Nikkie Deelen, Suchandra Dutta, et al. *Beam Test Performance of a 2S-CBC3 Prototype Module: FNAL Test Beam Report*. Feb. 2018. URL: http://cern.ch/go/7hXG.

[58] Jeremy Andrea, Georg Auzinger, R. Bhattacharya, et al. "Performance of Prototype Silicon Detectors for the Outer Tracker for the Phase-2 Upgrade of CMS". Submitted for publication. 2018.

[59] Jan Dreyling-Eschweiler and Paul Schütze. "The DESY II Test Beam Facility". In: *Nuclear Instruments and Methods in Physics Research Section A: Accelarators, Spectrometers, Detectors and Assiciated Equipment* AIDA-2020-POSTER-2019-016 (Feb. 5, 2018). URL: http://cds.cern.ch/record/2673006.

[60] Hendrik Jansen, Simon Spannagel, Jörg Behr, et al. "Performance of the EUDET-type beam telescopes". In: *EPJ Techniques and Instrumentation* 3.1 (Oct. 4, 2016), page 7. ISSN: 2195-7045. DOI: 10.1140/epjti/s40485-016-0033-2. URL: https://doi.org/10.1140/epjti/s40485-016-0033-2.

[61] I. Rubinskiy. "An EUDET/AIDA Pixel Beam Telescope for Detector Development". In: *Phys. Procedia* 37.AIDA-CONF-2015-035 (June 9, 2011), pages 923–931. DOI: 10.1016/j.phpro.2012.02.434. URL: https://cds.cern.ch/record/2000287.

[62] Bosch Rexroth. *Aluminum Strut Profiles*. Overview of Bosch profiles. URL: http://cern.ch/go/lsM7 (visited on Apr. 4, 2019).

[63] R. Morrison. *Grounding and Shielding Techniques*. 4th edition. John Wiley & Sons, 1998.

[64] KeyShot . *3D Redering Software*. 2019. URL: https://www.keyshot.com/ (visited on Sept. 2, 2019).

[65] Physik Instrumente (PI) GmbH & Co. KG. *M-060, M-061, M-062 Precision Rotation Stage*. Design specifications. Jan. 18, 2018. URL: http://cern.ch/go/Sg6K (visited on Jan. 20, 2019).

[66] Physik Instrumente (PI) GmbH & Co. KG. *C-863 Mercury Servo Controller*. Design specifications. July 17, 2019. URL: http://cern.ch/go/9nlJ (visited on Aug. 21, 2019).

[67] Standa Ltd. *8MT295 Long-Travel Motorized Linear Stage*. Design specifications. 2018. URL: http://cern.ch/go/tZJ9 (visited on Aug. 21, 2019).

[68] Standa Ltd. *8SMC5.USB - Stepper & DC Motor Controller*. Design specifications. 2018. URL: http://cern.ch/go/jrz6 (visited on Aug. 21, 2019).

[69] The DOW Chemical Company. *SYLGARD™186 Silicone Elastomer*. Design specifications. 2017. URL: http://cern.ch/go/J6HR (visited on Aug. 21, 2019).

[70] Andreas Kornmayer. "Studies on the response behaviour of pixel detector prototypes at high collision rates for the CMS experiment". PhD thesis. Karlsruher Institut für Technologie, Dec. 4, 2015.

[71] Newport Corporation. *X95 Structural Optical Rails and Carriers*. Design specifications. URL: http://cern.ch/go/8thG (visited on Apr. 2019).

[72] Eljen Technology. *General Purpose EJ-200, EJ-204, EJ-208, EJ-212*. Design specifications. 2016. URL: http://cern.ch/go/tf6D.

[73] Hamamatsu Photonics K.K. *Photosensor Modules H11900/H11901 Series*. Design specifications. July 2016. URL: http://cern.ch/go/V8z7 (visited on Aug. 21, 2019).

[74] Jennifer Ngadiuba. *Testing and Integration of the Service Cylinders for the CMS Phase 1 pixel detector*. Technical report CMS-CR-2016-357. Geneva: CERN, Nov. 10, 2016. URL: http://cds.cern.ch/record/2233045 (visited on Aug. 21, 2019).

[75] Adafruit. *Adafruit FT232H Breakout Board*. Design specifications. URL: http://cern.ch/go/JF8Z (visited on Apr. 1, 2019).

[76] Eoptolink Technology Inc. Ltd. *EOLS-1312-X Series*. Design specifications. Dec. 18, 2018. URL: http://cern.ch/go/Rq6W (visited on Apr. 5, 2019).

[77] Molex LLC. *Molex 0.30mm Pitch Premo-Flex Etched Copper Polyimide Jumper*. Design specifications. May 8, 2019. URL: http://cern.ch/go/S8h6 (visited on Apr. 19, 2019).

[78] Samtec. *Power Mate Cable Assembly*. Design specifications. URL: http://cern.ch/go/Kqt9 (visited on Apr. 22, 2019).

[79] CMS Collaboration. *Pixel Online Software*. URL: https://gitlab.cern.ch/cmspops/pos (visited on Aug. 21, 2019).

[80] CMS Collaboration. *POSoftware Installation*. URL: http://cern.ch/go/zrV9 (visited on Aug. 21, 2019).

[81] The CMS Collaboration. *XDAQ: CMS Online Software*. Apr. 5, 2019. URL: http://cern.ch/go/9TLW (visited on Aug. 21, 2019).

[82] Allesandro di Mattia. *I^2C development for the Pixel telescope*. Presention during the CMS Tracker Week. Nov. 7, 2018. URL: http://cern.ch/go/KrT6.

[83] Hugo Furtado. "Delay25 an ASIC for timing adjustment in LHC". In: (2005). DOI: 10.5170/CERN-2005-011.148. URL: http://cds.cern.ch/record/920425.

[84] Paulo Rodrigues Simoes Moreira and Arianna Marchioro. "QPLL : a Quartz Crystal Based PLL for Jitter Filtering Applications in LHC". In: 2003.

[85] P Moreira, A Marchioro, and P Placidi. *CMS Tracker PLL Reference Manual*. Technical report. Geneva: CERN, 2000. URL: http://cds.cern.ch/record/1069705.

[86] Peter Trüb. "CMS pixel module qualification and Monte-Carlo study of $H \to \tau^+\tau^- \to l^+l^-ET$". PhD thesis. Eindgenössische Technische Hochschule Zürich, 2008. DOI: https://doi.org/10.3929/ethz-a-005725061.

[87] Michael Stückelberger. "Threshold Calibration of the CMS Pixel Detector". PhD thesis. Eidgenössische Technische Hochschule Zürich, Feb. 2009.

[88] Simon Spannagel. *CMS Pixel Detector Upgrade and Top Quark Pole Mass Determination*. Springer Theses, Jan. 2017. ISBN: 978-3-319-58879-7. DOI: 10.1007/978-3-319-58880-3.

[89] PSI. *pixel Xpert analysis and readout*. URL: https://github.com/psi46/pxar/tree/master (visited on Aug. 21, 2019).

[90] CMS Collaboration. *PXAR - Pixel eXpert Analysis Readout*. URL: http://cern.ch/go/8fC7 (visited on Aug. 21, 2019).

[91] Anders Ryd, Steve Stroiney, Souvik Das, Karl Ecklund, and Josh Tompson. *CMS Pixel Online Software and Calibrations*. Jan. 2009. URL: http://cern.ch/go/CLx9 (visited on Oct. 16, 2018).

[92] Jiri Kvasnicka. *DESY Table*. Sept. 21, 2018. URL: http://cern.ch/go/Wd7R (visited on Aug. 19, 2019).

[93] Jeroen Hegeman, Andreas Kornmayer, Matthew Kilpatrick, and Lea Michaela Caminada. *Pixel Debug tools*. Git repository. Dec. 5, 2017. URL: https://gitlab.cern.ch/cmspops/pixel_debug_tools/ (visited on Aug. 22, 2019).

[94] Sarah Freed and Matthew Kilpatrick. *FED Tester Errors*. Presented during 2018 Pixel DAQ Workshop. July 26, 2018. URL: http://cern.ch/go/m9mp (visited on Aug. 21, 2019).

[95] T. F. Coleman and Y. Li. "An Interior, Trust Region Algoritm for Nonlinear Minimization Subject to Bounds". In: *SIAM Journal for Optimazation* 6.2 (1996), pages 418–445.

Appendices

A. Telescope modules and their connections

It is important for the readout of the telescope to know which connections belong to which modules. This is communicated to the hardware through the so-called `nametraslation` file that is read upon issuing the configuration of the system. All these connections are summarized in Table A.1. The module ID is physically written on each module and is therefore used to identify them. This is also the ID number with which they can be retrieved from the Phase-1 production database. The module connectors on the MBs are also labeled. Those labels are given in the second column of the table. The hub address is a binary hardware address in the form of five wire-bonds one top of the HDI of a module. Each wire-bond connects two microscopic pads together. An in-tact wire-bond represents a bit that is set to one, and upon breaking a bond the bit is set to zero. Next in the table are the fiber number and the FED channels which are related to each other. The fiber number can be retrieved by looking at the fiber color or label. The FED channels are derived from the fiber number by multiplying it by 2. In CMSSW a module is recognized by its Detector ID (DetID) that is based on its physical location in the setup. The DetID is given in the table as well. The telescope module map is given in Figure A.1 as a reminder.

Table A.1.
A summary of all the connections from the FED to each module in the telescope.

Module ID	**MB connector**	**Hub address**	**Fiber number**	**FED channels**	**CMSSW DetID**
M3164	224	15	20	39 and 40	353 375 236
M3173	214	23	17	33 and 34	353 376 260
M3023	223	26	18	35 and 36	353 113 092
M3239	213	27	15	29 and 30	353 114 116
M3226	222	28	13	25 and 26	352 850 948
M3265	212	29	24	47 and 48	352 851 972
M3192	221	30	23	45 and 46	352 588 804
M3204	211	31	22	43 and 44	352 589 828
M3124	211	15	8	15 and 16	344 201 220
M3090	221	23	5	9 and 10	344 200 196
M3175	212	26	6	11 and 12	344 463 364
M3082	222	27	3	5 and 6	344 462 540
M3057	213	28	1	1 and 2	344 725 508
M3009	223	29	12	23 and 24	344 724 484
M3074	214	30	11	21 and 22	344 987 652
M3027	224	31	10	19 and 20	344 986 628

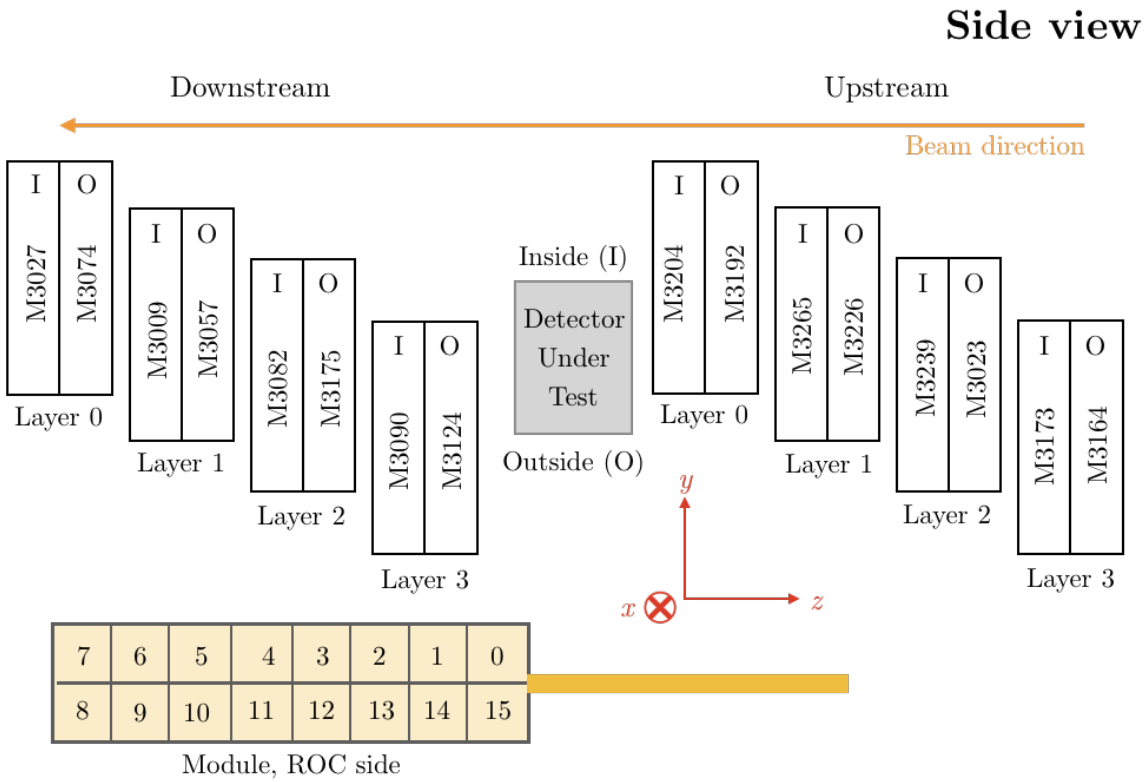

Figure A.1. *A map with the locations of each module as it was installed in the telescope. The red coordinate system shows the CMSSW coordinates. The arrow at the top of the image specifies the beam direction.*

B. Hit Position Correlation between Telescope Modules in Different Layers of the new Telescope

In this appendix, hit correlation plots from run 100 333 are given that were not previously presented in Chapter 3. As modules M3057 and M3175 were not physically connected to the telescope, there are no correlation plots of those modules here. This appendix does not enclose plots that concern two modules in the same layer, as there is no correlation between them. As a reference, Table B.1 gives an overview of the physical positions of the telescope modules.

Table B.1.
An overview of all the physical module positions of each detector in the CHROMIE telescope.

Module ID	Upstream or downstream	Inside or outside	Layer
M3164	Upstream	Outside	3
M3173	Upstream	Inside	3
M3023	Upstream	Outside	2
M3239	Upstream	Inside	2
M3226	Upstream	Outside	1
M3265	Upstream	Inside	1
M3192	Upstream	Outside	0
M3204	Upstream	Inside	0
M3124	Downstream	Outside	3
M3090	Downstream	Inside	3
M3175	Downstream	Outside	2
M3082	Downstream	Inside	2
M3057	Downstream	Outside	1
M3009	Downstream	Inside	1
M3074	Downstream	Outside	0
M3027	Downstream	Inside	0

Modules M3124 and M3192 have noisy pixels that were not masked in the readout (see Section 3.6.6). Consequently, Figures B.4 and B.6 have a high correlation count for the horizontal bins associated to the noisy pixels.

Due to the beam position during run 100 333, the Inside modules were hit more often than the Outside modules. As a result, the z-scale of the plots with Outside modules was made ten times smaller than the z-scale of the Inside module plots.

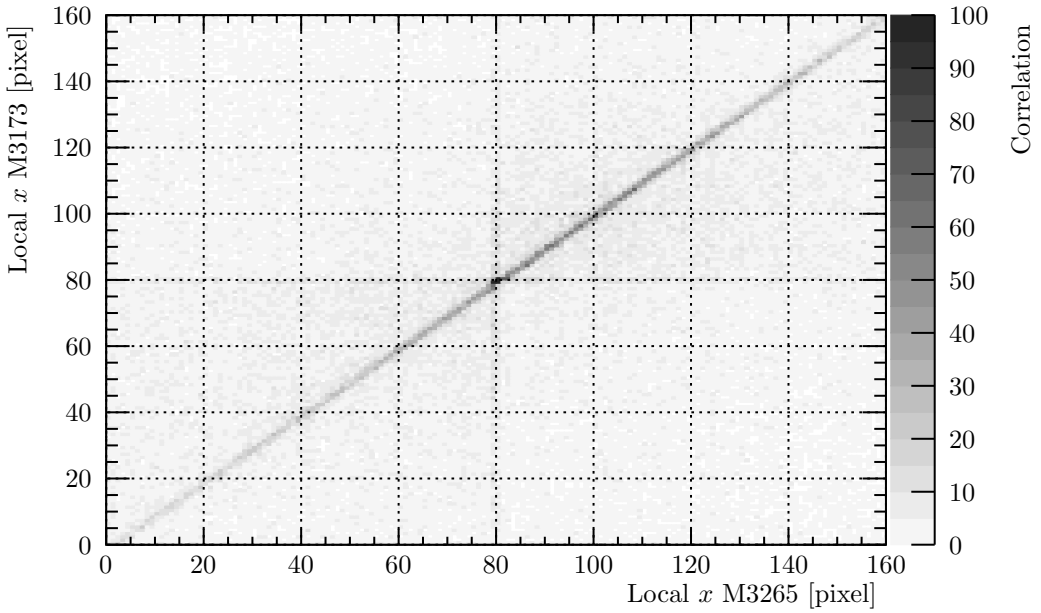

(a) *Local x.*

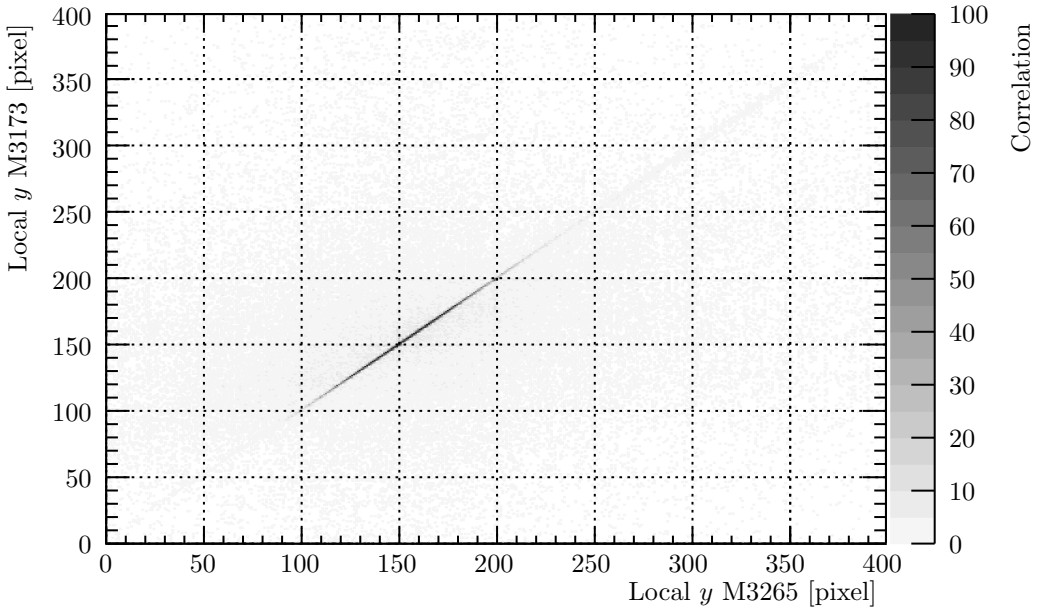

(b) *Local y.*

Figure B.1. *Hit correlation between module M3265 and M3173, both in Upstream Layer 3.*

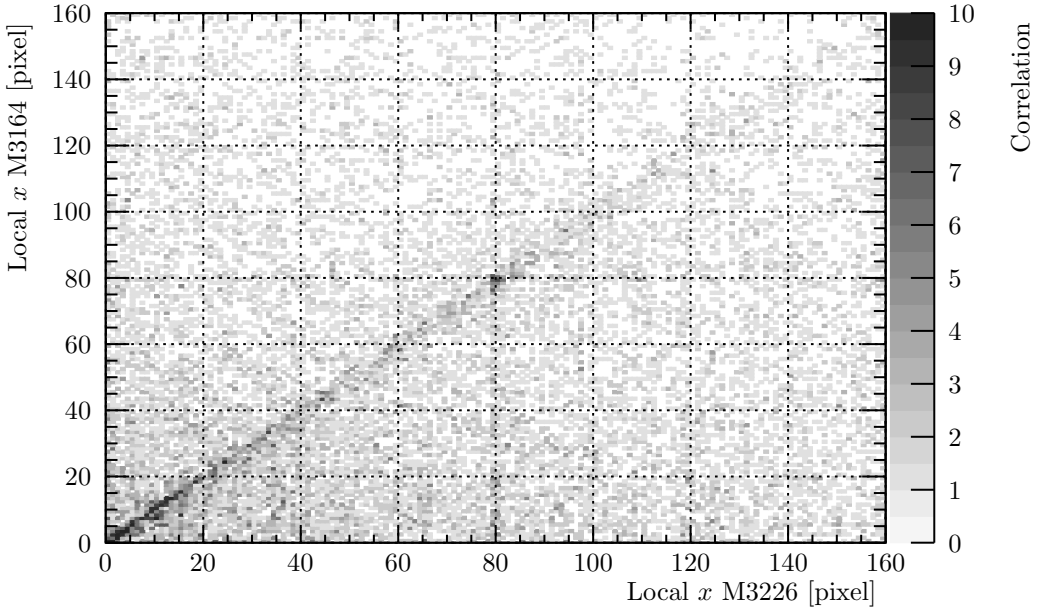

(a) *Local x.*

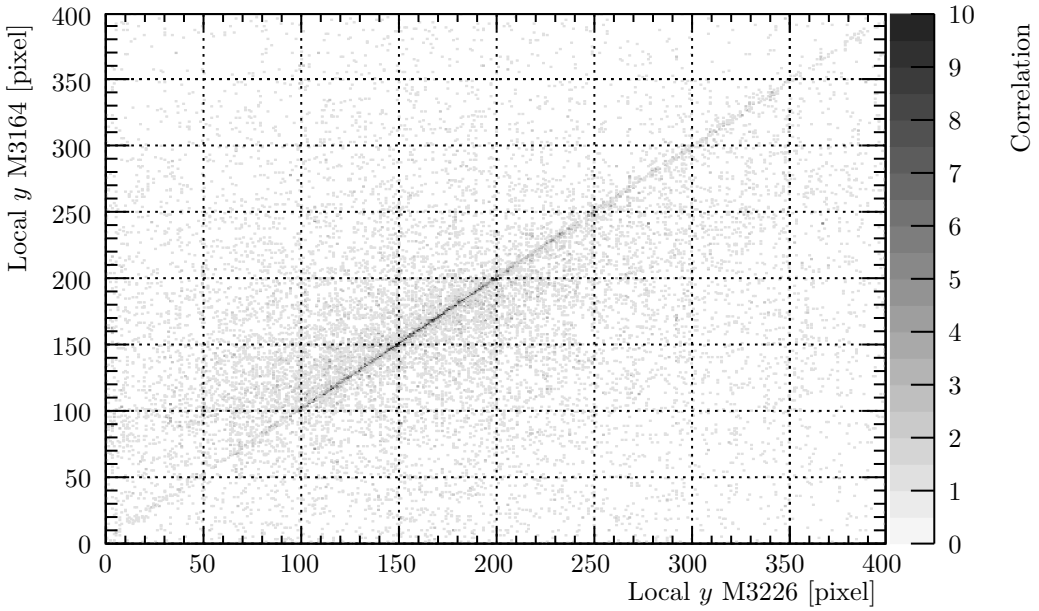

(b) *Local y.*

Figure B.2. *Hit correlation between module M3226 and M3164, both in Upstream Layer 3.*

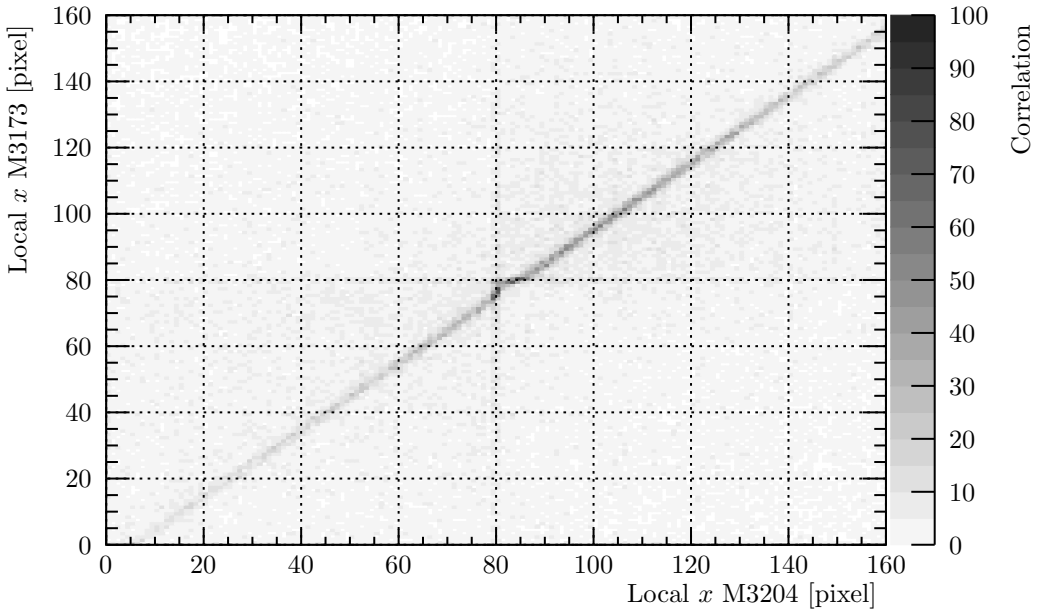

(a) *Local x.*

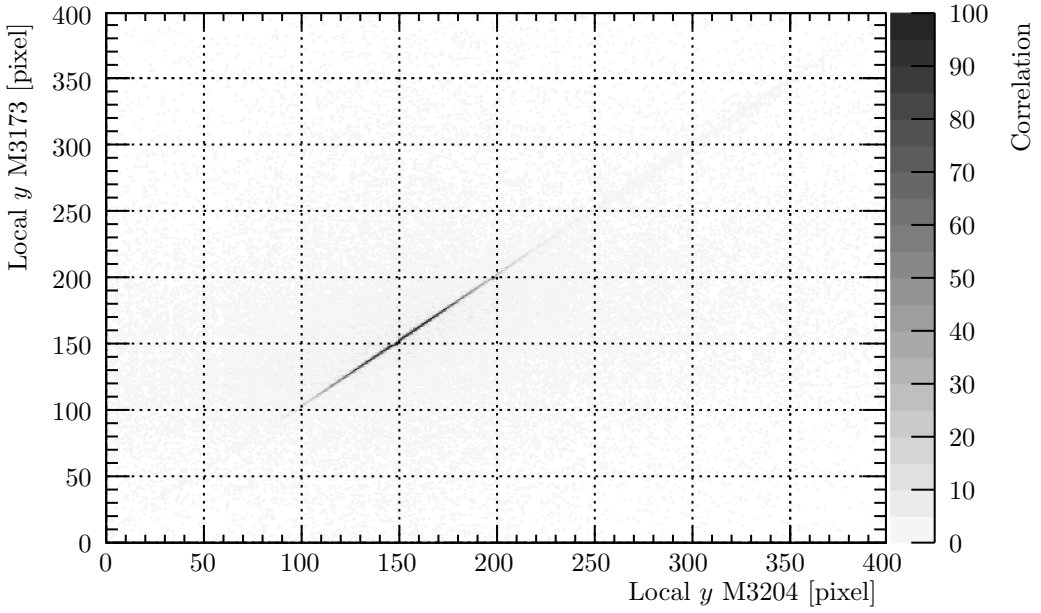

(b) *Local y.*

Figure B.3. *Hit correlation between module M3204 and M3173, both in Upstream Layer 3. This data is from run 100333.*

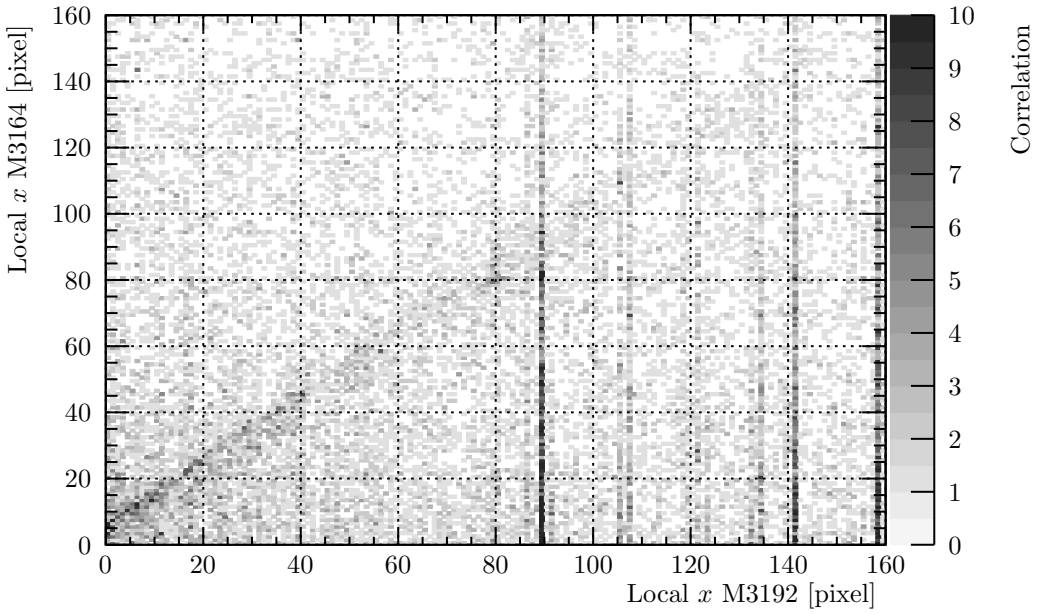

(a) *Local x.*

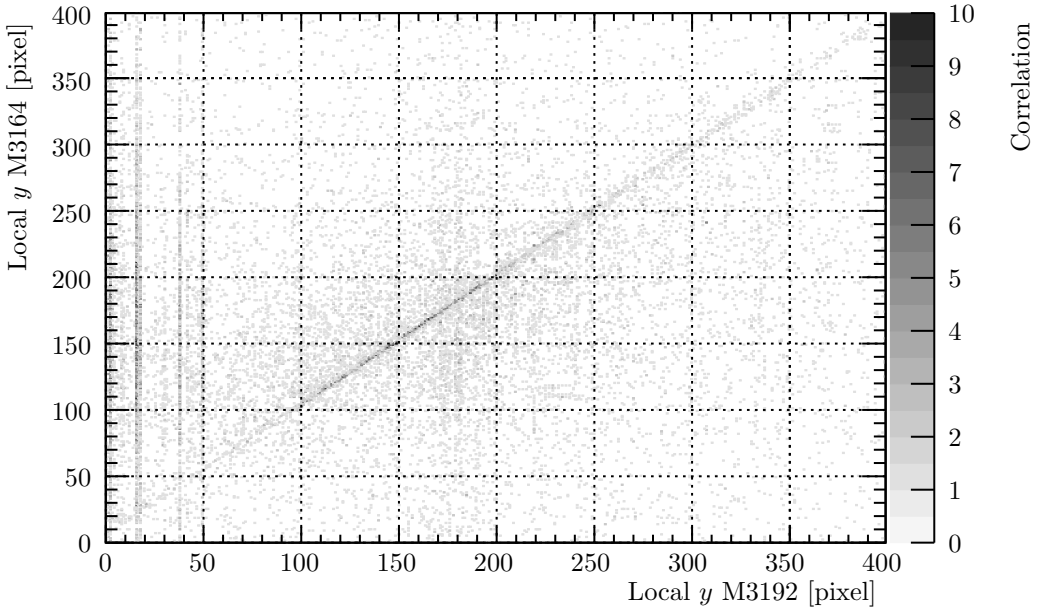

(b) *Local y.*

Figure B.4. *Hit correlation between module M3192 and M3164, both in Upstream Layer 3. This data is from run 100333.*

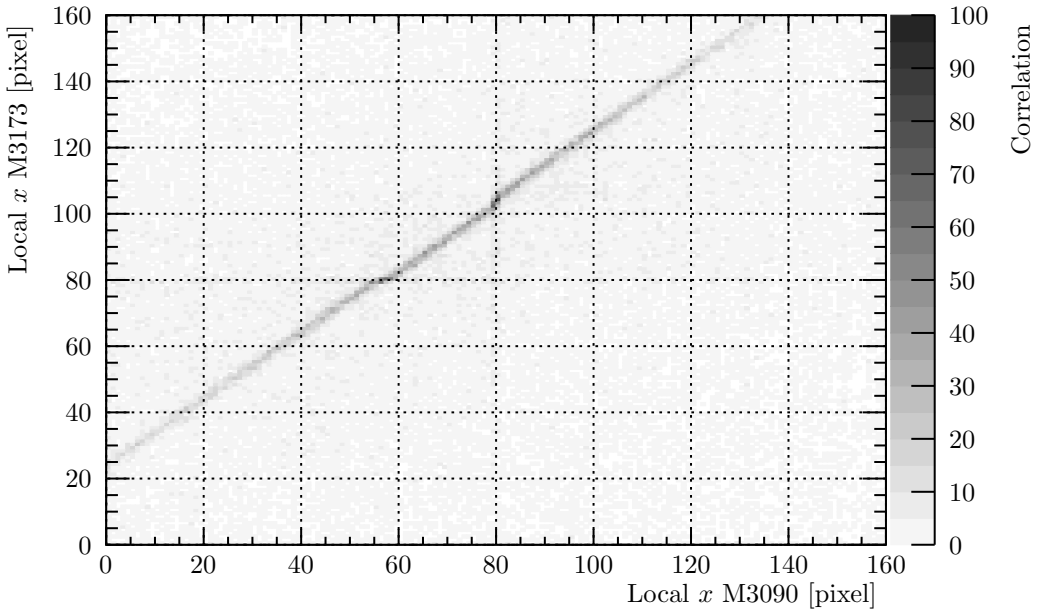

(a) *Local x.*

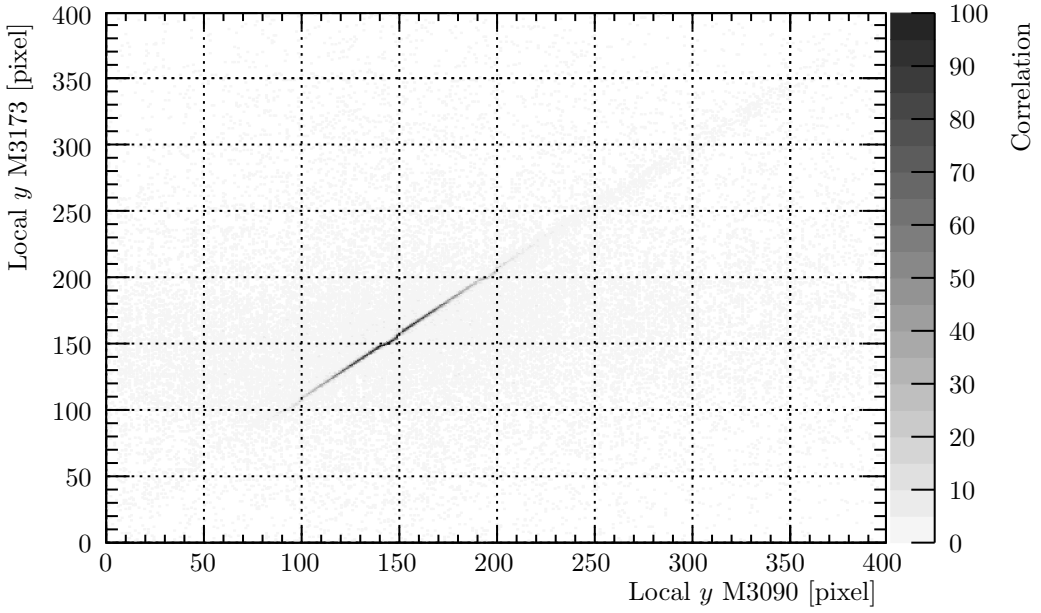

(b) *Local y.*

Figure B.5. *Hit correlation between module M3090 and M3173, both in Upstream Layer 3. This data is from run 100333.*

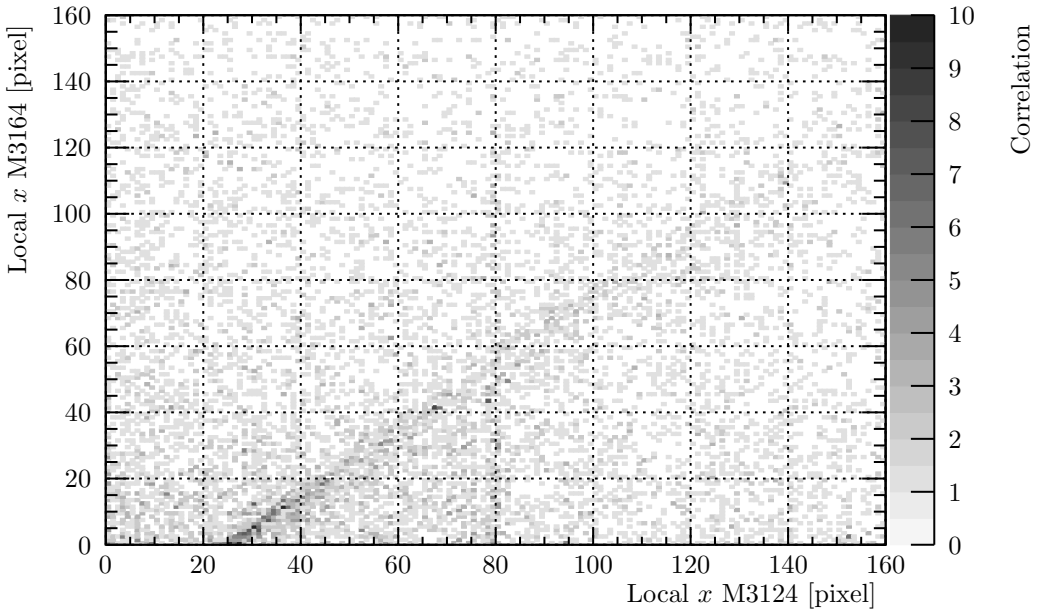

(a) *Local x.*

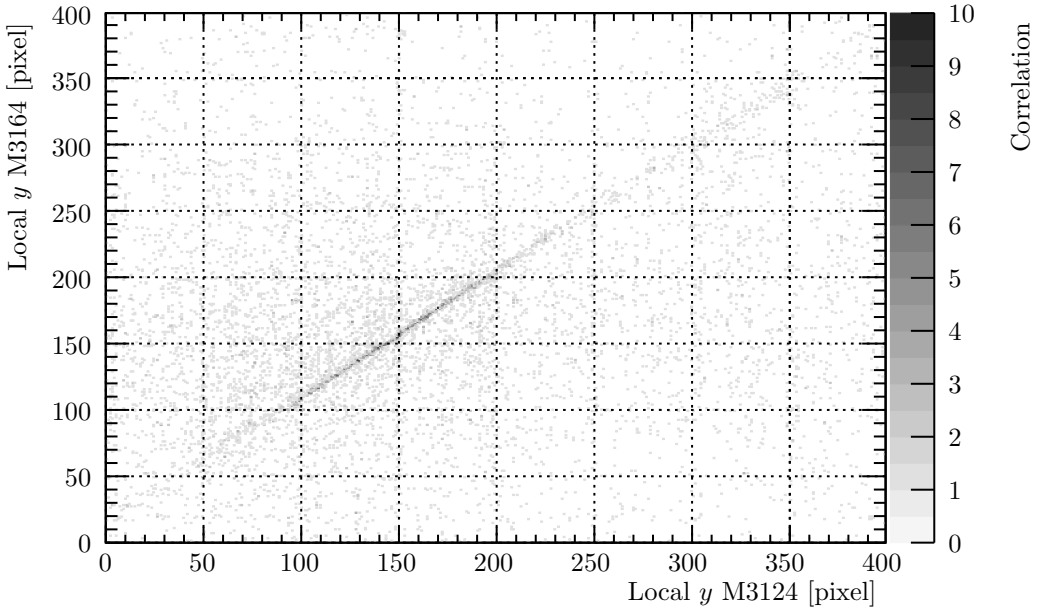

(b) *Local y.*

Figure B.6. *Hit correlation between module M3124 and M3164, both in Upstream Layer 3. This data is from run 100333.*

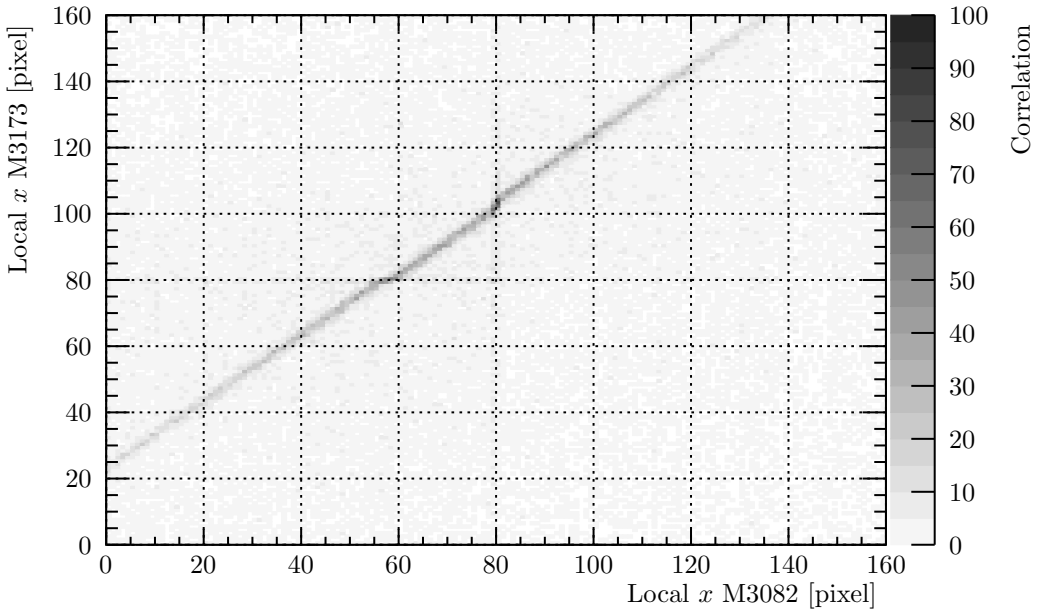

(a) *Local x.*

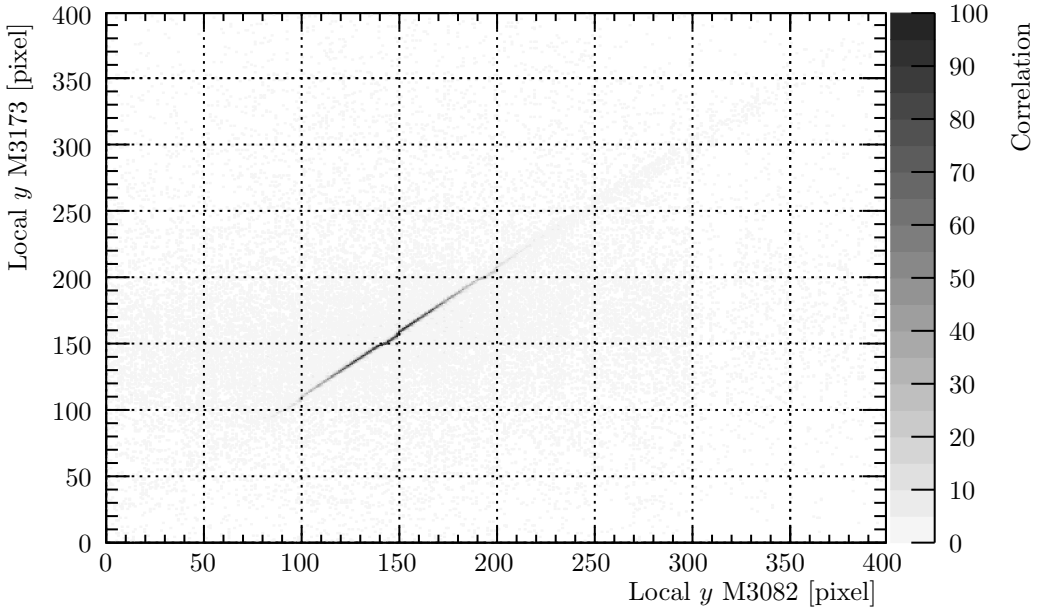

(b) *Local y.*

Figure B.7. *Hit correlation between module M3082 and M3173, both in Upstream Layer 3. This data is from run 100333.*

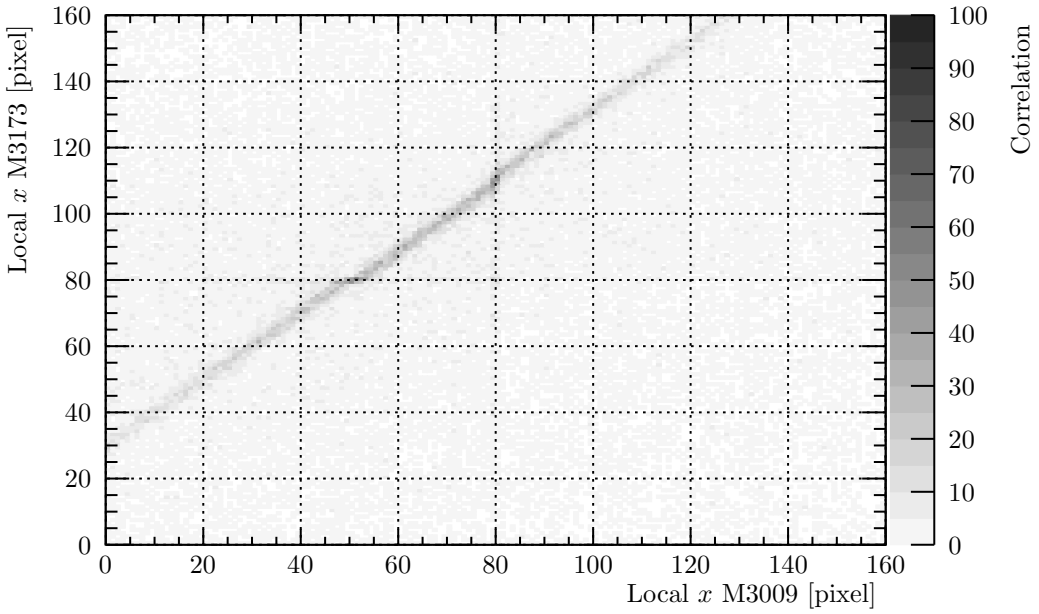

(a) *Local x.*

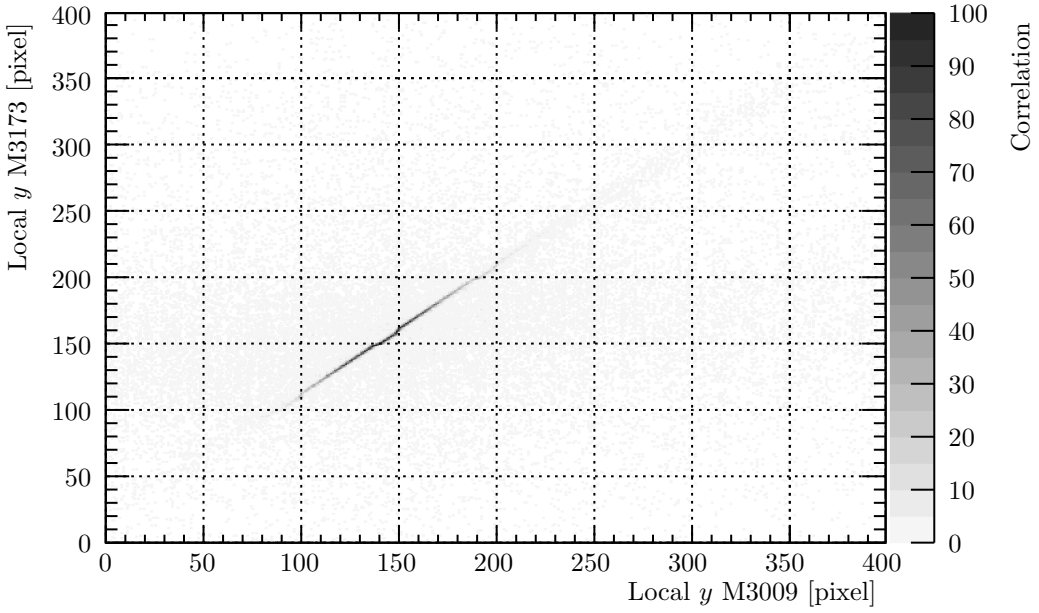

(b) *Local y.*

Figure B.8. *Hit correlation between module M3009 and M3173, both in Upstream Layer 3. This data is from run 100333.*

C. The Single Point Resolution of Individual Modules in the new Telescope

This appendix gives an overview of the single point resolution in global x and global y respectively, of all the modules in the CHROMIE telescope. These are computed based on the unbiased residual distributions of all clusters in that module, that have a cluster size of 2 pixels in x and y respectively.

For each unbiased residual graph, a fit is performed that is the sum of two Gaussian distributions. One of these Gaussians has a small sigma, which is defined as the resolution. The other Gaussian has a larger sigma that gives a measure of the background that was measured by that module.

As a reference, the unbiased residual distributions of the clusters with cluster size 1 in the given direction, as well as the fits to those distributions, are also drawn. The resolution is chosen to be computed with the cluster size 2 distributions, because the cluster position of those clusters is more accurate due to the charge sharing between the pixels.

These residuals plots were made with telescope data from run 100 321, 100 322 and 100 323. They were taken within 45 min of each other, and because of the beam position, the Inside modules were mostly hit. Therefore, it was only possible to aligned those modules with these runs. After alignment, the tracking efficiency for these three runs was 78 %, see Section 3.7.2.

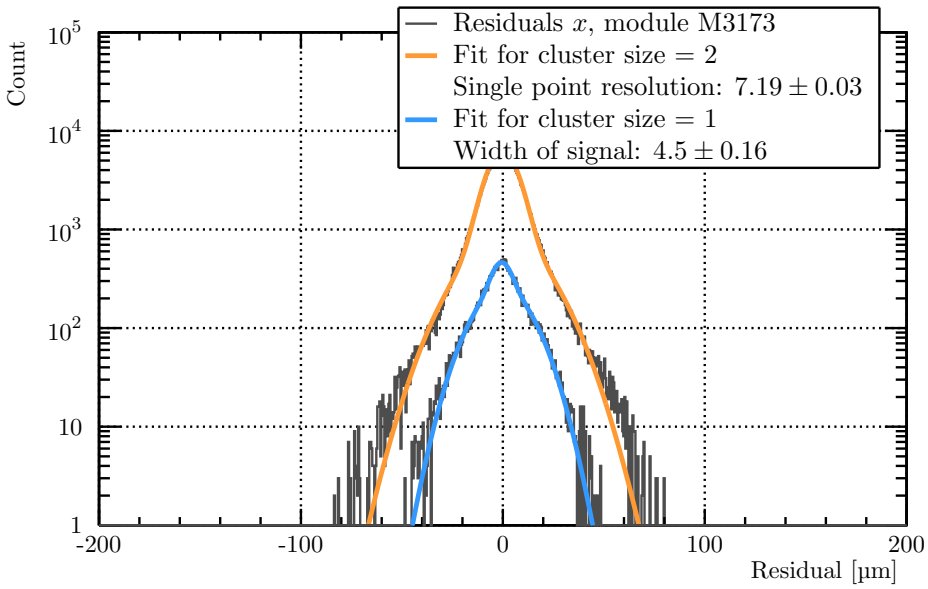

(a) *Global x.*

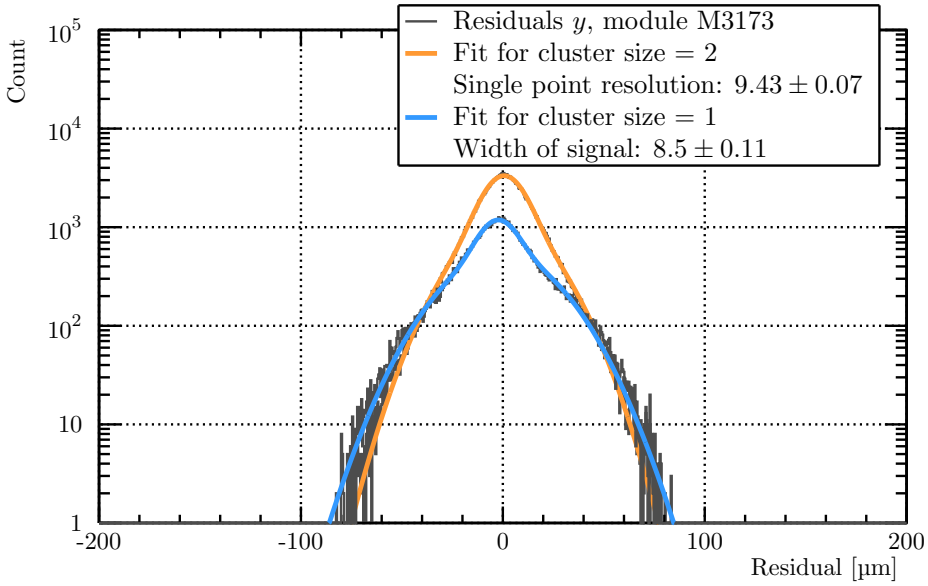

(b) *Global y.*

Figure C.1. *Fits to the unbiased residuals, for cluster size 1 (blue) and 2 (orange), between the cluster position on module M3173 and the track, interpolated on the detector plane. The data is shown in grey, and the resolution for the two different fits are given in the legend.*

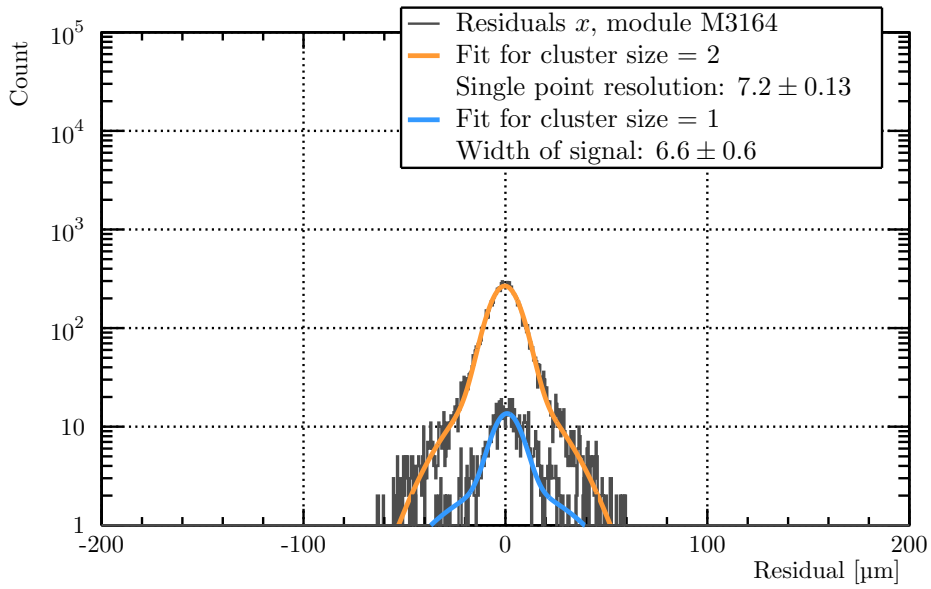

(a) *Global x.*

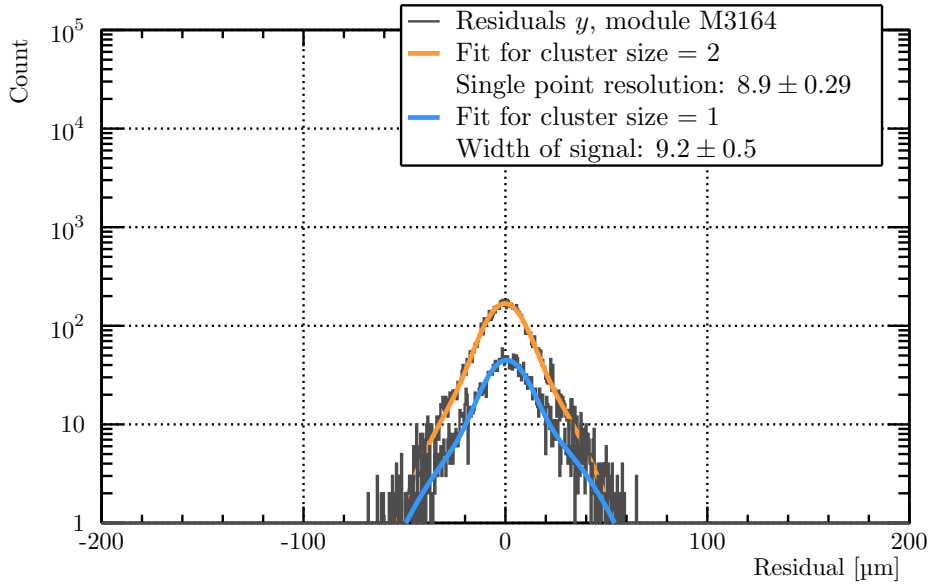

(b) *Global y.*

Figure C.2. *Fits to the unbiased residuals, for cluster size 1 (blue) and 2 (orange), between the cluster position on module M3164 and the track, interpolated on the detector plane. The data is shown in grey, and the resolution for the two different fits are given in the legend.*

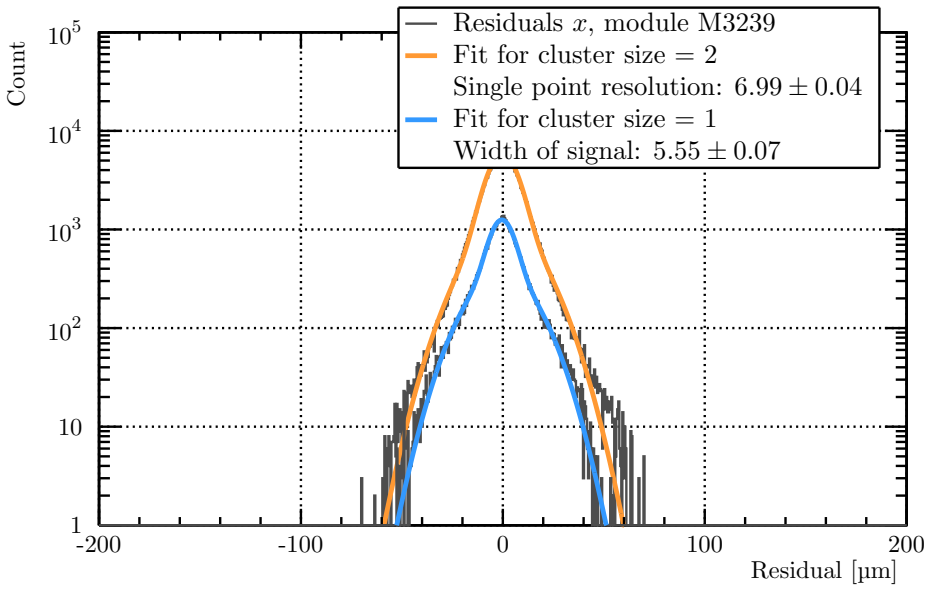

(a) *Global x.*

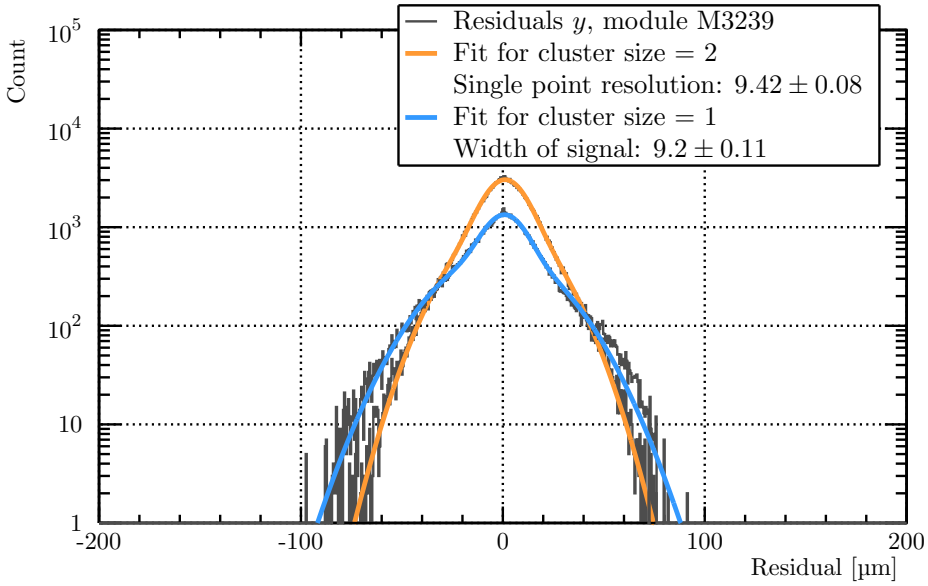

(b) *Global y.*

Figure C.3. *Fits to the unbiased residuals, for cluster size 1 (blue) and 2 (orange), between the cluster position on module M3239 and the track, interpolated on the detector plane. The data is shown in grey, and the resolution for the two different fits are given in the legend.*

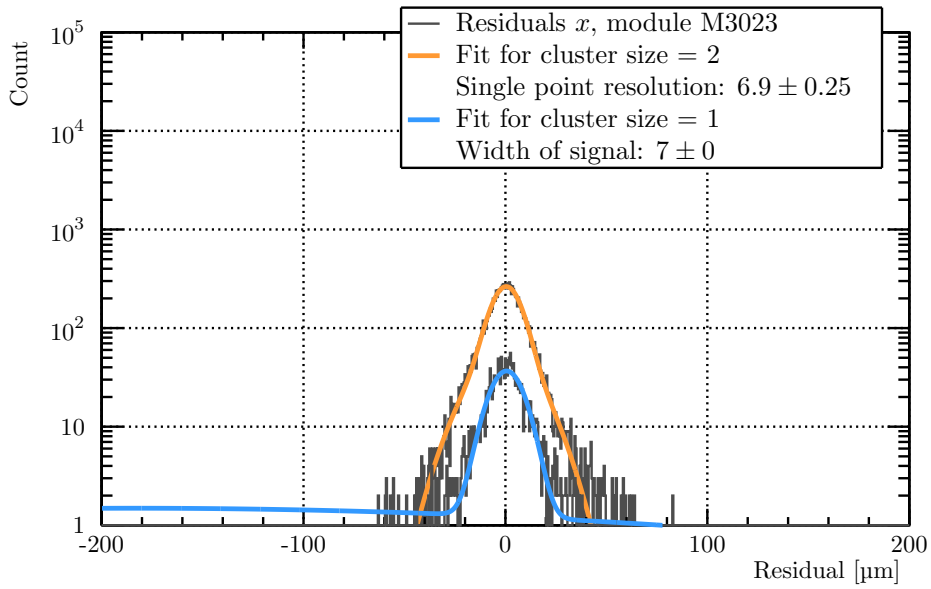

(a) *Global x.*

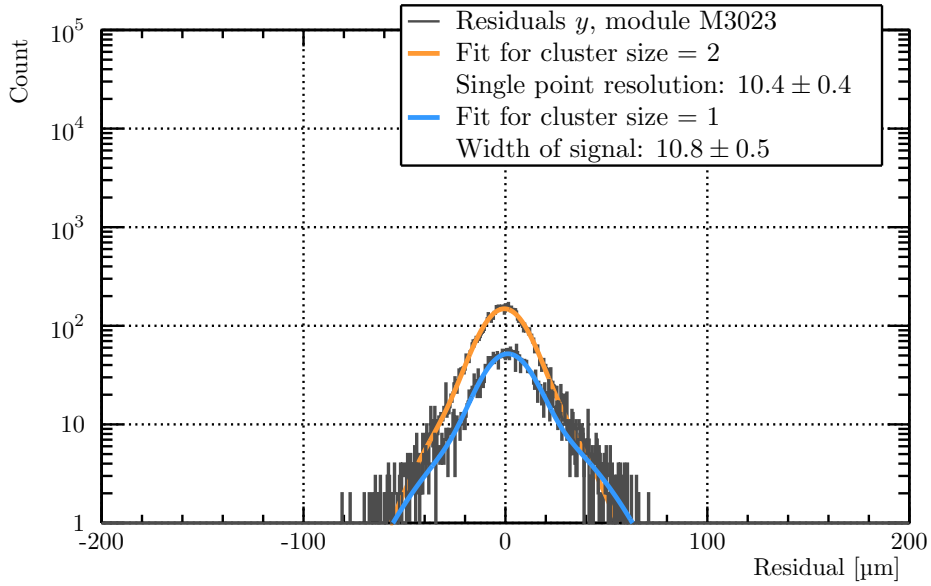

(b) *Global y.*

Figure C.4. *Fits to the unbiased residuals, for cluster size 1 (blue) and 2 (orange), between the cluster position on module M3023 and the track, interpolated on the detector plane. The data is shown in grey, and the resolution for the two different fits are given in the legend.*

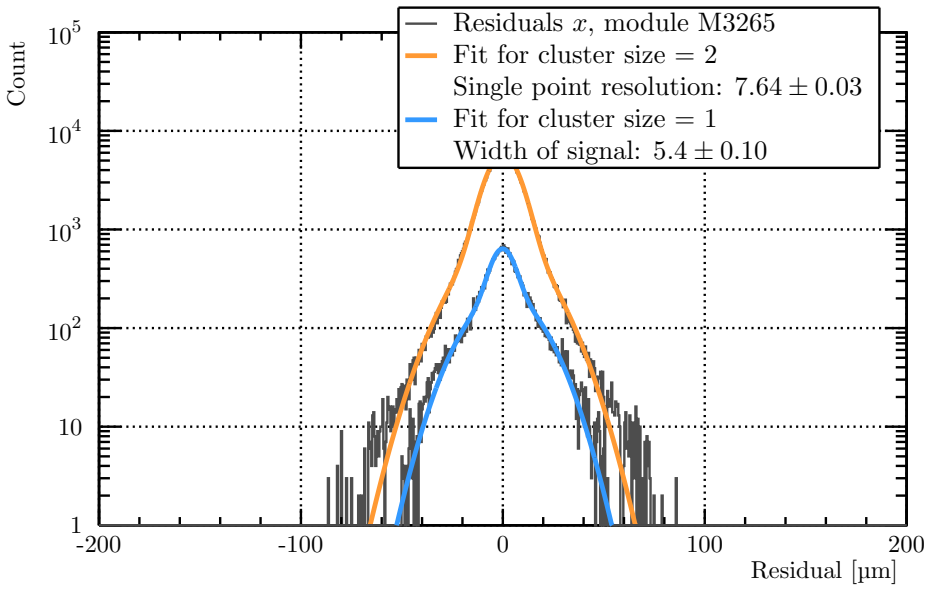

(a) *Global x.*

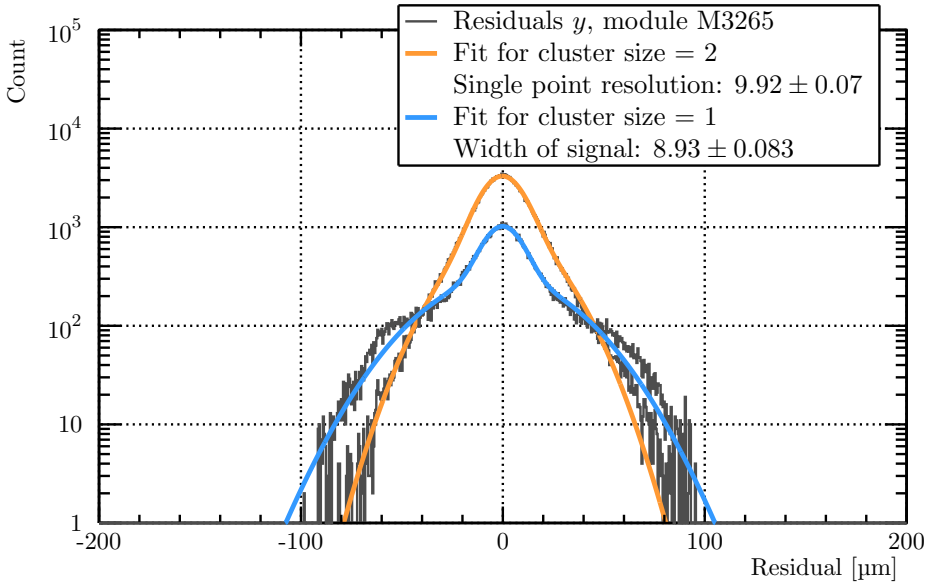

(b) *Global y.*

Figure C.5. *Fits to the unbiased residuals, for cluster size 1 (blue) and 2 (orange), between the cluster position on module M3265 and the track, interpolated on the detector plane. The data is shown in grey, and the resolution for the two different fits are given in the legend.*

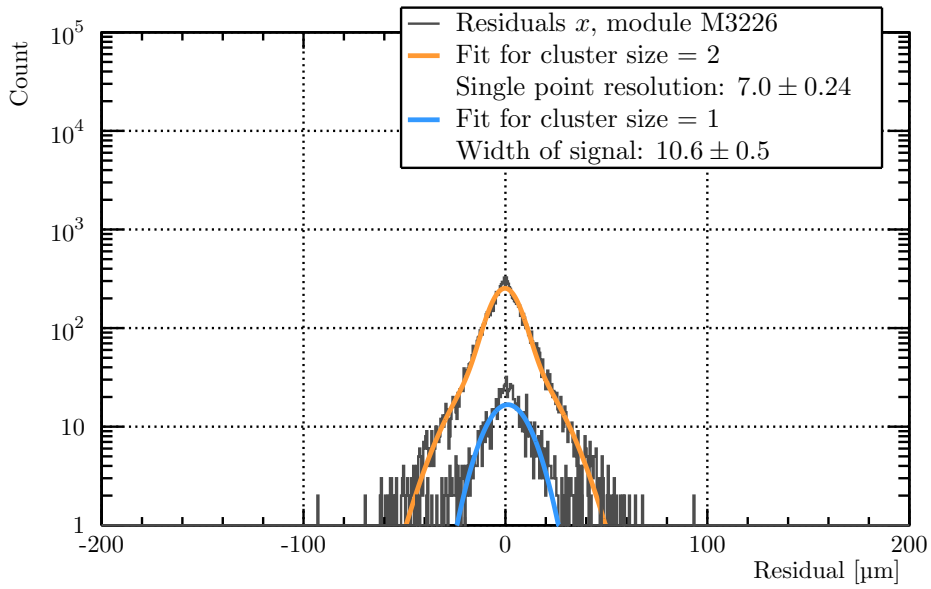

(a) *Global x.*

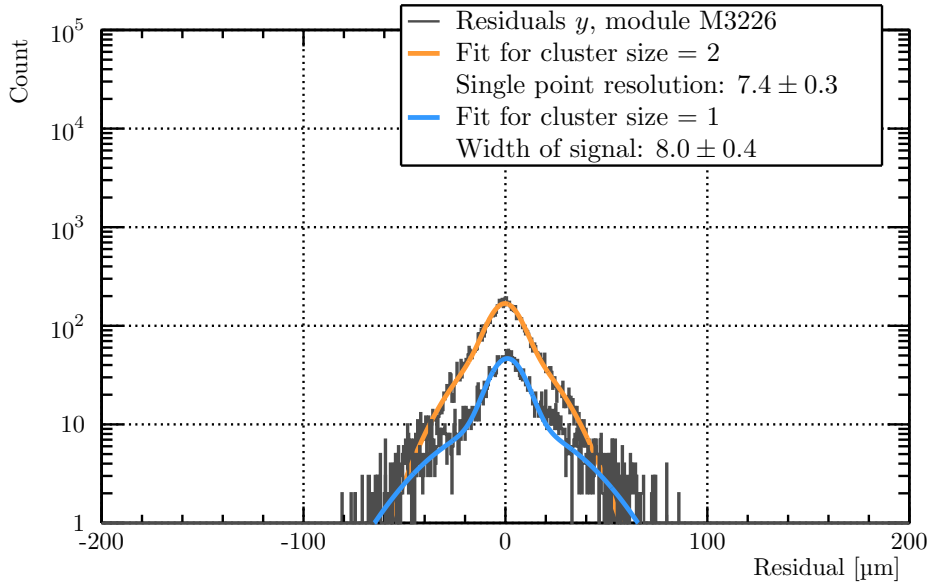

(b) *Global y.*

Figure C.6. *Fits to the unbiased residuals, for cluster size 1 (blue) and 2 (orange), between the cluster position on module M3226 and the track, interpolated on the detector plane. The data is shown in grey, and the resolution for the two different fits are given in the legend.*

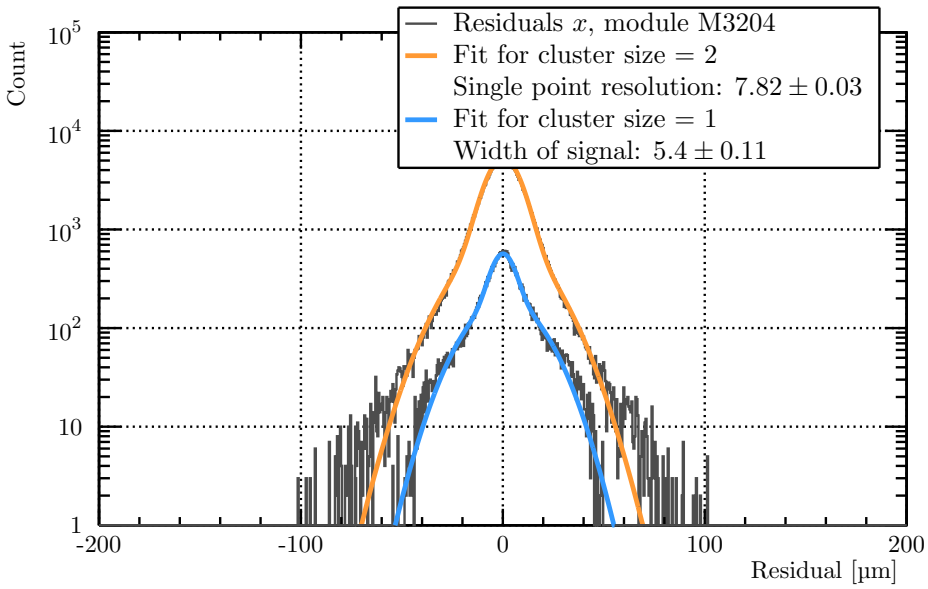

(a) *Global x.*

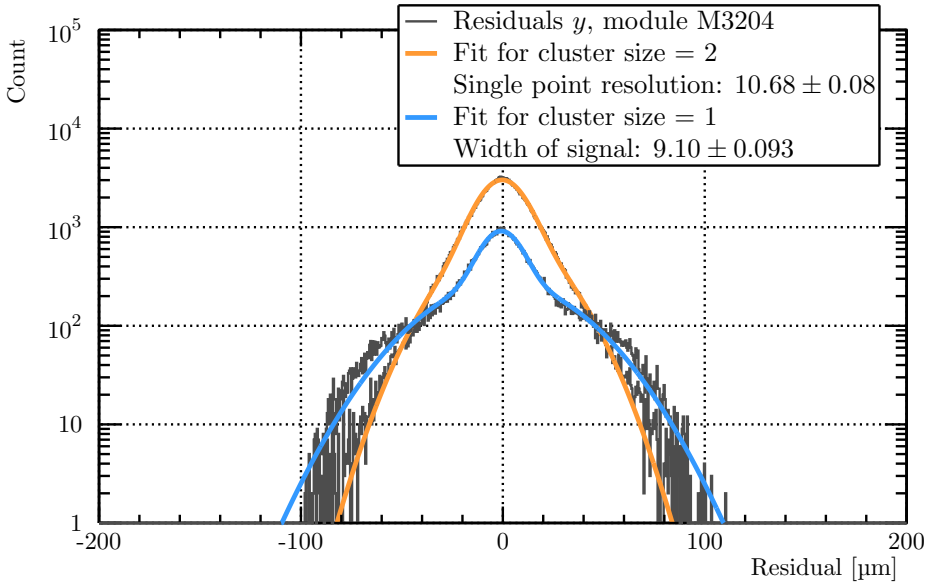

(b) *Global y.*

Figure C.7. *Fits to the unbiased residuals, for cluster size 1 (blue) and 2 (orange), between the cluster position on module M3204 and the track, interpolated on the detector plane. The data is shown in grey, and the resolution for the two different fits are given in the legend.*

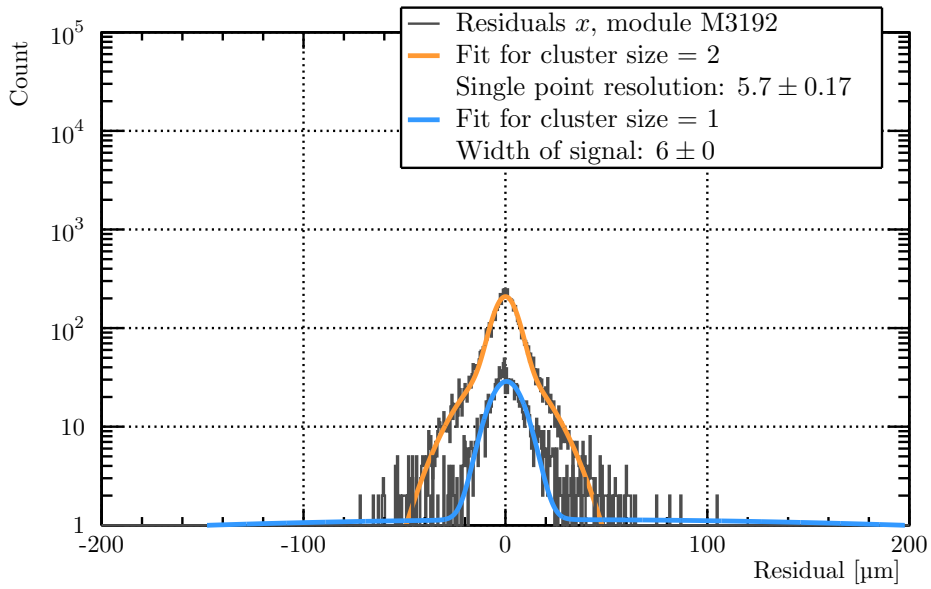

(a) *Global x.*

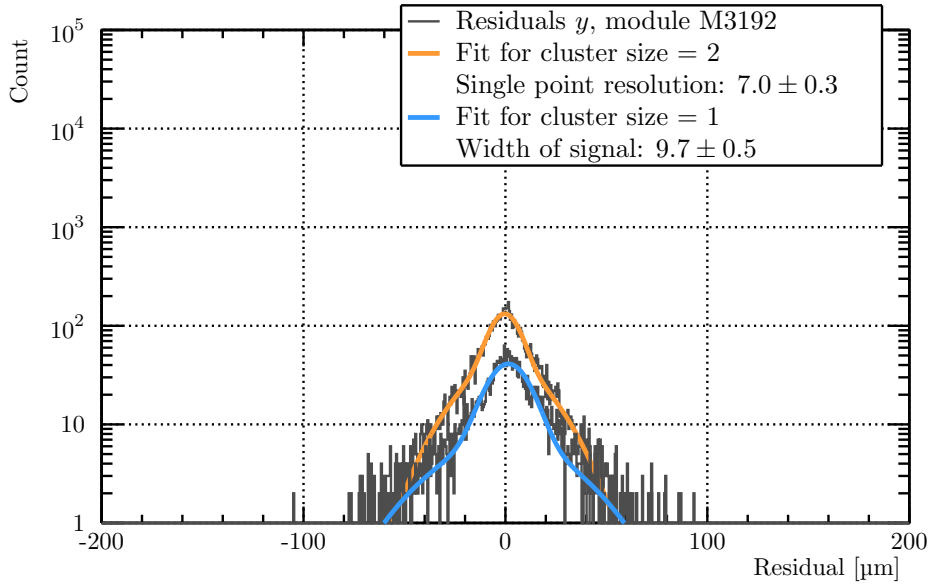

(b) *Global y.*

Figure C.8. *Fits to the unbiased residuals, for cluster size 1 (blue) and 2 (orange), between the cluster position on module M3192 and the track, interpolated on the detector plane. The data is shown in grey, and the resolution for the two different fits are given in the legend.*

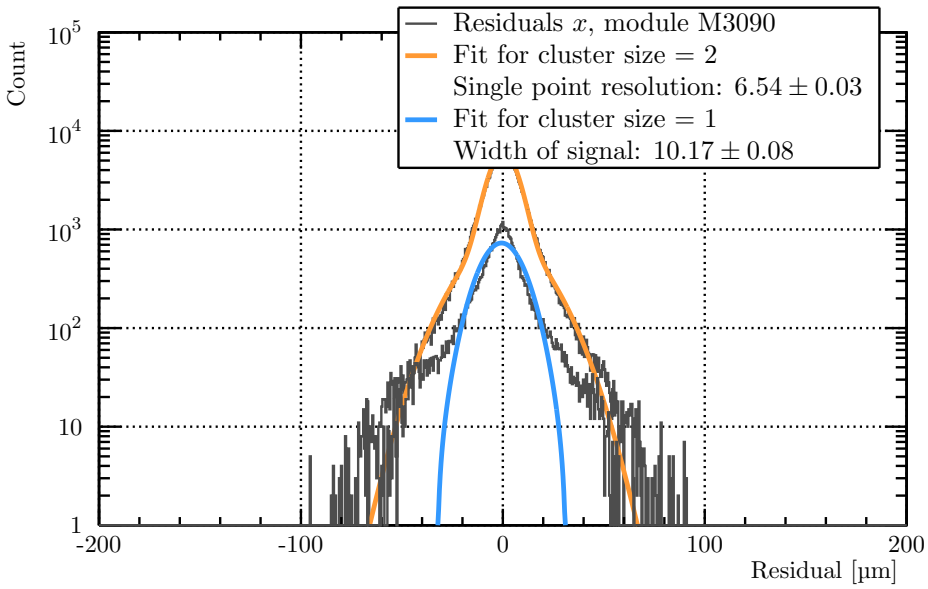

(a) *Global x.*

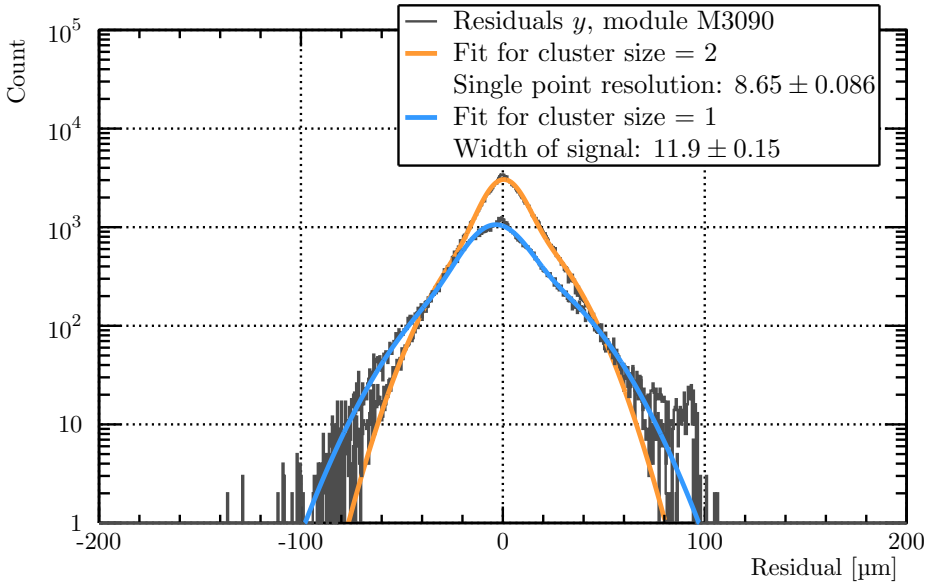

(b) *Global y.*

Figure C.9. *Fits to the unbiased residuals, for cluster size 1 (blue) and 2 (orange), between the cluster position on module M3090 and the track, interpolated on the detector plane. The data is shown in grey, and the resolution for the two different fits are given in the legend.*

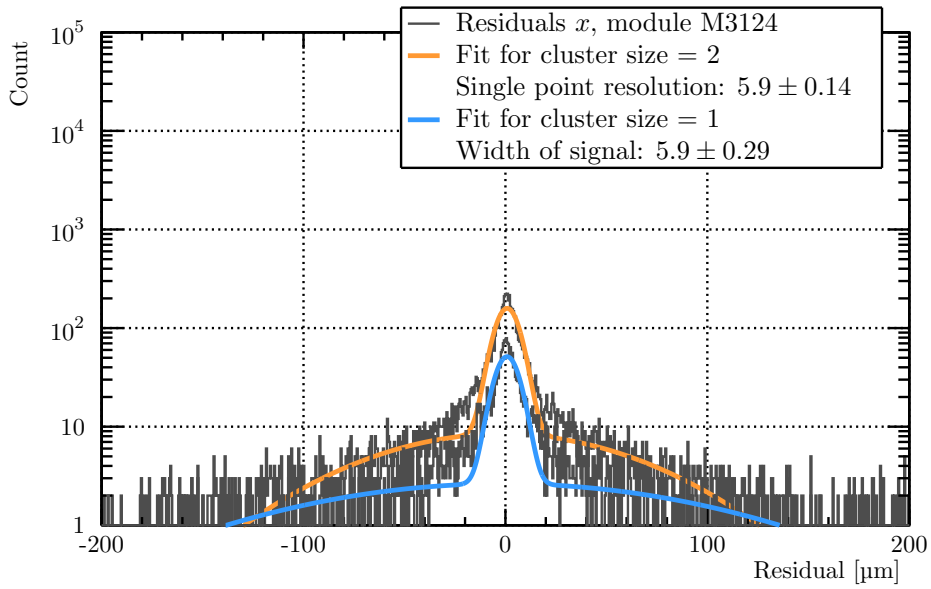

(a) *Global x.*

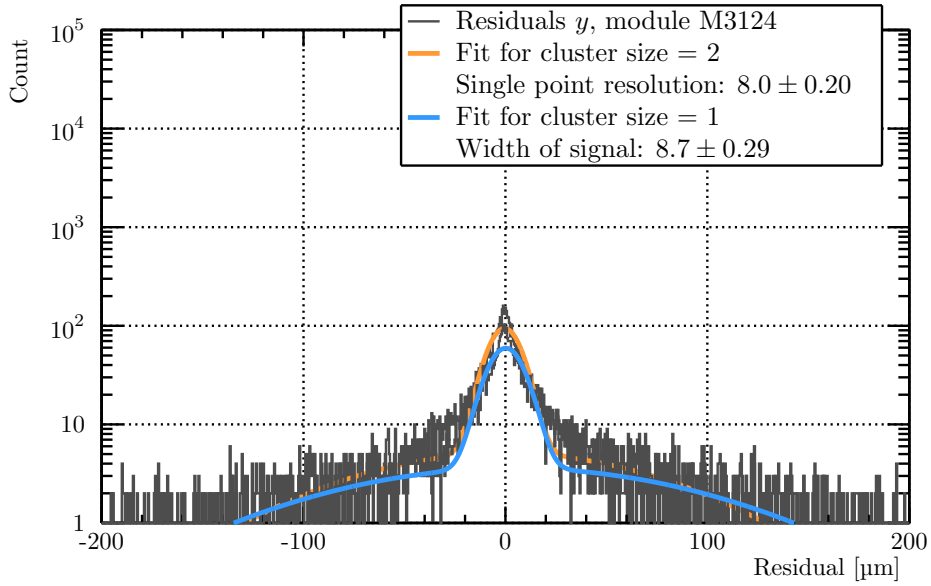

(b) *Global y.*

Figure C.10. *Fits to the unbiased residuals, for cluster size 1 (blue) and 2 (orange), between the cluster position on module M3124 and the track, interpolated on the detector plane. The data is shown in grey, and the resolution for the two different fits are given in the legend.*

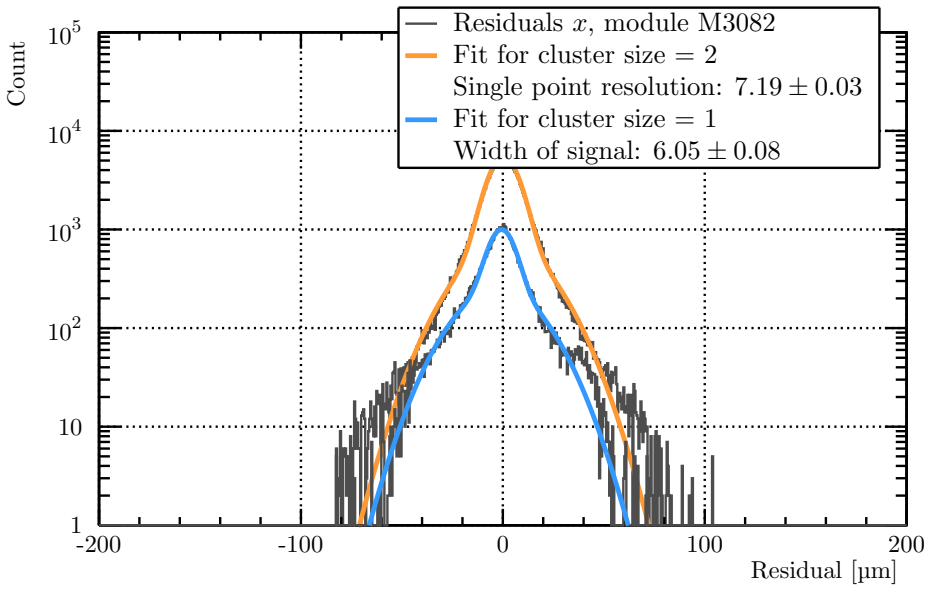

(a) *Global x.*

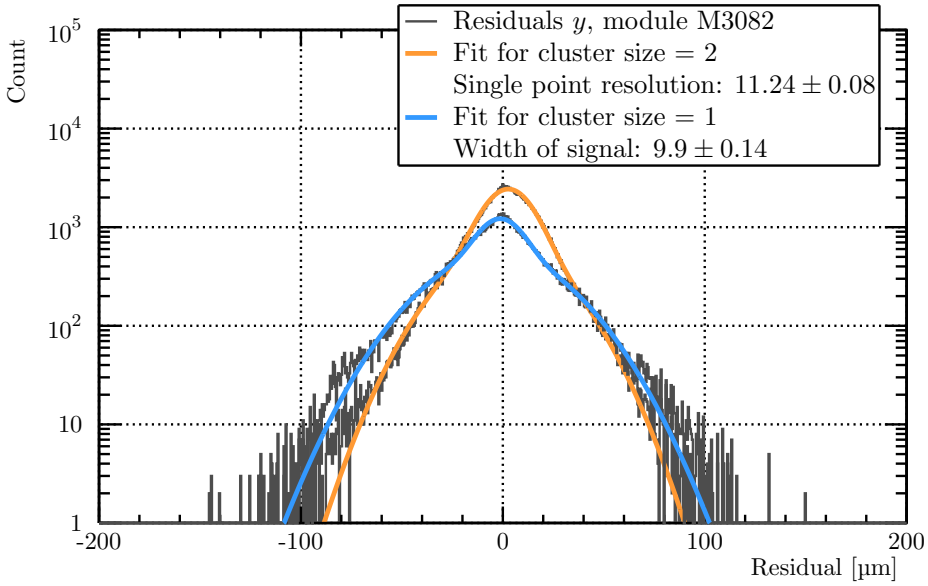

(b) *Global y.*

Figure C.11. *Fits to the unbiased residuals, for cluster size 1 (blue) and 2 (orange), between the cluster position on module M3082 and the track, interpolated on the detector plane. The data is shown in grey, and the resolution for the two different fits are given in the legend.*

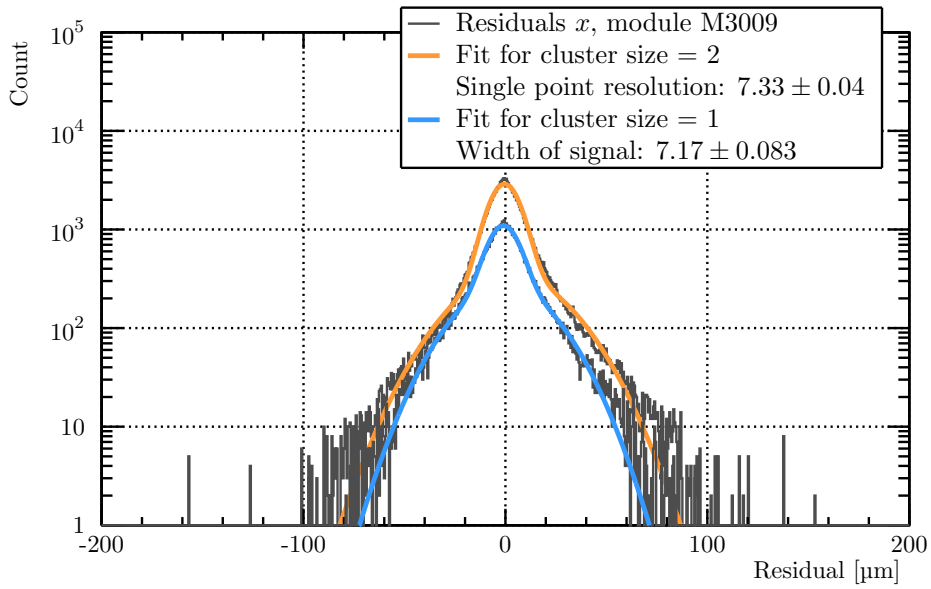

(a) *Global x.*

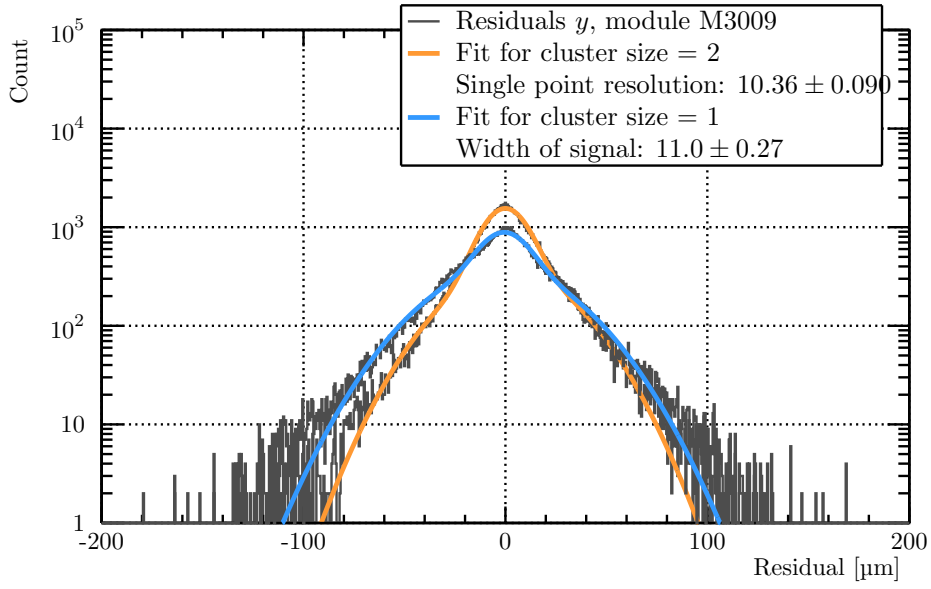

(b) *Global y.*

Figure C.12. *Fits to the unbiased residuals, for cluster size 1 (blue) and 2 (orange), between the cluster position on module M3009 and the track, interpolated on the detector plane. The data is shown in grey, and the resolution for the two different fits are given in the legend.*

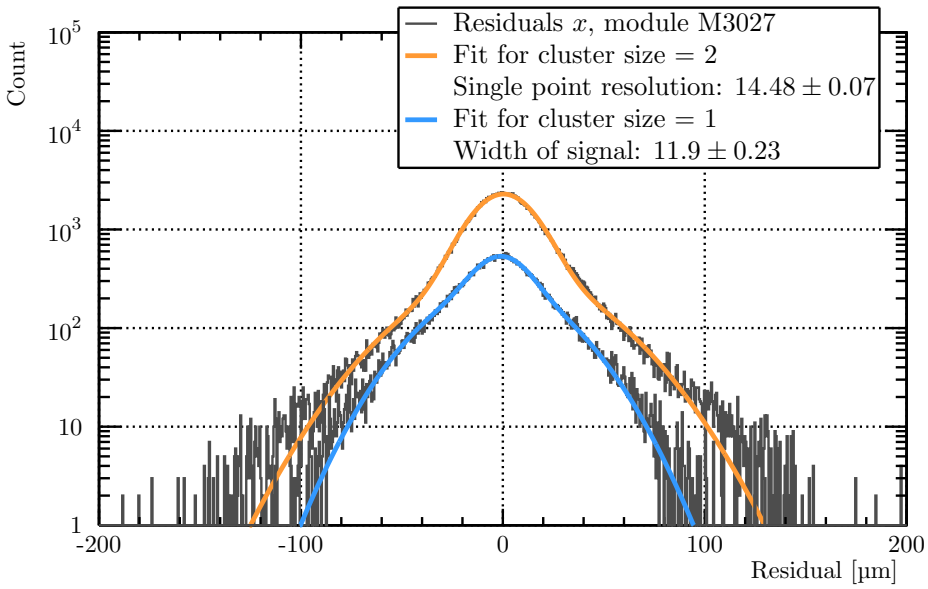

(a) *Global x.*

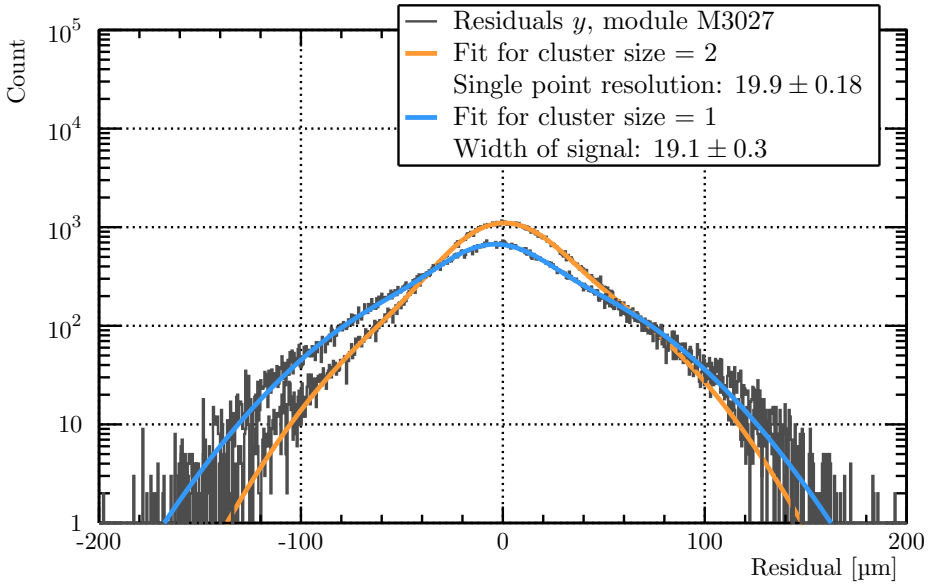

(b) *Global y.*

Figure C.13. *Fits to the unbiased residuals, for cluster size 1 (blue) and 2 (orange), between the cluster position on module M3027 and the track, interpolated on the detector plane. The data is shown in grey, and the resolution for the two different fits are given in the legend.*

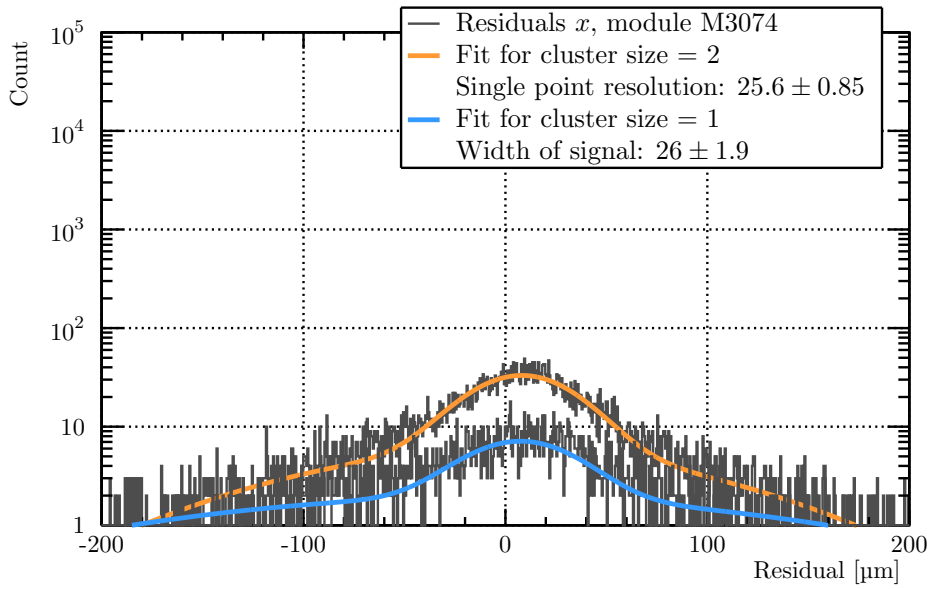

(a) *Global x.*

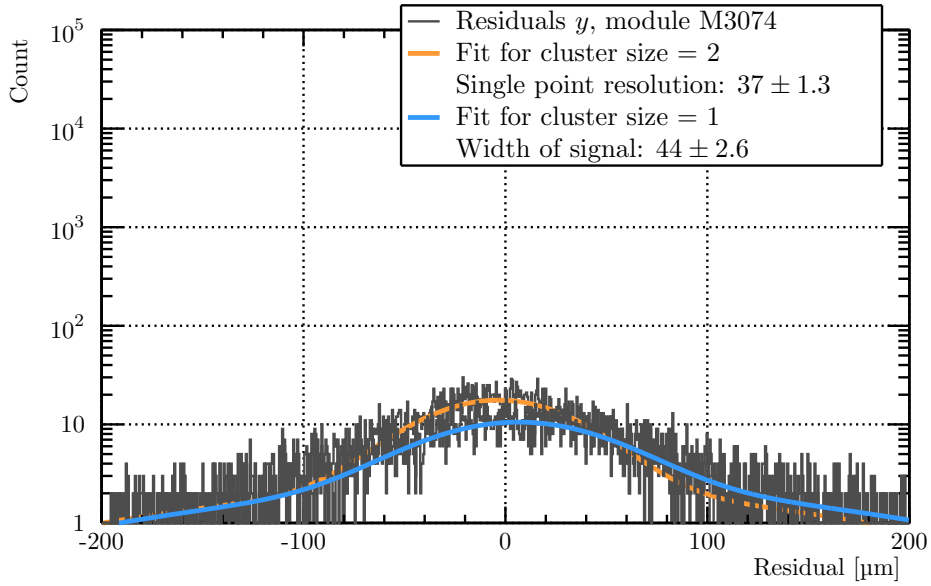

(b) *Global y.*

Figure C.14. *Fits to the unbiased residuals, for cluster size 1 (blue) and 2 (orange), between the cluster position on module M3074 and the track, interpolated on the detector plane. The data is shown in grey, and the resolution for the two different fits are given in the legend.*

D. Results of a Mini Beam Test with a Phase-2 Inner Tracker Module inside the new Telescope

After the pilot beam test with a CBC3 mini module, it was confirmed that the telescope was ready for use in beam tests with CMS Phase-2 Tracker Upgrade modules. Therefore it was immediately used for a short beam test with an RD53A module, which is a prototype CMS Phase-2 Inner Tracker module, in the H6A area of the SPS beam line as well. An image of the module after installation in the telescope is given in Figure D.1. In the photograph, the blue module in the center has an hourglass stuck on it with kapton tape, to protect the sensor and the ROC.

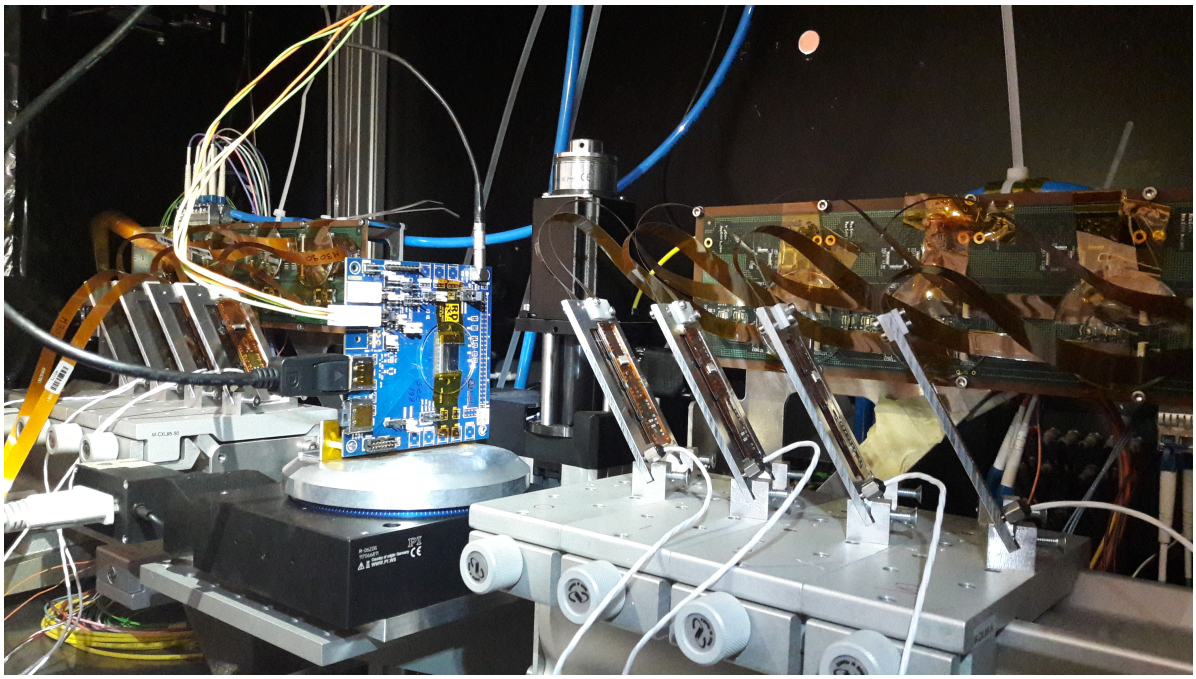

Figure D.1. *A photograph of the RD53A module installed in the telescope.*

D.1. Installation of the RD53A in the telescope

The RD53A DUT was installed on the mounting piece of telescope's rotational stage, with the same L-shape adapter piece that was used for the CBC3 mini module (Section 3.8.1). The low-voltage power, high-voltage bias and readout cables all left the telescope box via the same window in the telescope ceiling, that was used for the CBC3 DUT cables during the pilot beam test.

Outside the telescope box, a Xilinx Kintex-7 FPGA KC705 board was placed on a table for the RD53A readout. A CERN FMC was used for receiving triggers and clock on the FPGA

board. Since the KC705 is not a µTCA form factor board, it could not receive the triggers directly from the AMC13. Therefore the NIM trigger logic was altered to send out two trigger signals at the same time; one to the AMC13 and one to the KC705 directly.

Data was taken with the RD53A module and the telescope simultaneously in the following manner. First the telescope would be configured to prepare it for data taking. To ensure that the first trigger send to the telescope, was also the first trigger send to the DUT, the spill structure of the SPS beam line was taken advantage of. In between two consecutive spills, the RD53A would be configured after which the triggering to the telescope was started with the AMC13 software. Once the next spill would arrive, the triggers were simultaneously send to both the DUT and telescope readout. There was no veto signal coming from the RD53A module or it's readout, nor any other way of monitoring whether the DUT was synchronized to the telescope readout. Therefore it was expected that the DUT would loose sync with the telescope every now and then, but this can be compensated for in the offline analysis.

D.2. Preliminary results from the RD53A mini beam test

In this section all results shown are from run number 100 454. The cluster density per event in the telescope, during this runs of the mini beam test with the RD53A module is shown in Figure D.2. The beam was centered on one side of the telescope planes. The shadow of the scintillators on the modules is visible here as well.

For each trigger that the firmware of the DUT receives it sends out 32 consecutive triggers to the module. Instead of having a trigger latency setting, the data from all the 32 triggers is send back to the firmware. As a result of the trigger latency, only a few of those triggers will actually have hits in them.

This trigger latency is seen in Figure D.3. It shows the DUT's trigger ID which is in the range of 0 to 31, versus the number of hits in each trigger ID. In the case of run 100 454, most of the hits are in trigger number 21, and less than 10 % in the two trigger IDs before and after number 21. This means that module was correctly configured and the triggers from the telescope NIM logic were being received correctly.

With the use of the linear actuators of the telescope, the DUT was positioned as much as possible in the center of the H6, SPS beam. Figures D.4a and D.4b show the beam profile as measured by the RD53A module. The DUT has three different readout chips, all bump-bonded to the same small silicon sensor. During this mini beam test, only the middle readout chip was used during data taking, the other two were disabled. As a consequence, there are only hits observed in the columns and rows connected to the ROC in the center. In Figure D.4b it can be seen that all rows were illuminated during the run. But because of the beam's position on the module and scintillators, the center of the beam is close to the edge of the module with the high row numbers. The sharp edge between row number 180 and 192 is caused by the scintillators not fully covering the module. The particles measured in those rows are most likely off-time beam particles.

From the timing histogram (Figure D.3) and the beam profile measured by the RD53A module it is concluded that the DUT was able to measure the beam particles correctly. The last results in this chapter, show that the telescope is able to provide reference tracks for Phase-2 Inner Tracker as well. It is shown by plotting the hit-position correlation between the global cluster position of telescope module M3226, and the respective row and column numbers of the RD53A module. This is shown in Figure D.5. The first plot shows the correlation in global x direction, and the second plot is for the correlation in the global y direction. For the telescope module the global position is given in centimeter and the hit position of the DUT is given in pixels.

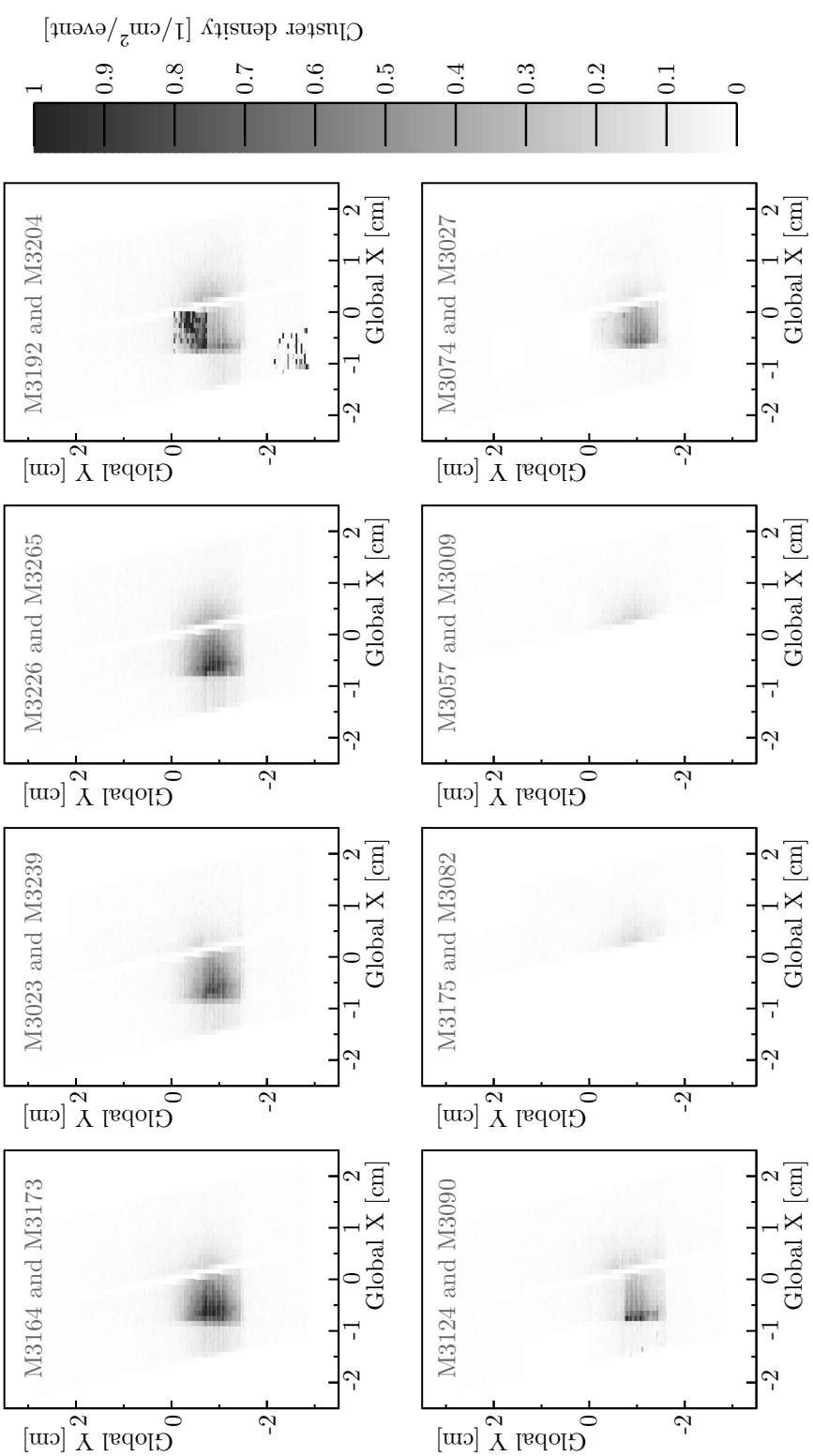

Figure D.2. *The cluster density in the telescope, measured during run* 100 454*, of the mini beam test with the RD53A module.*

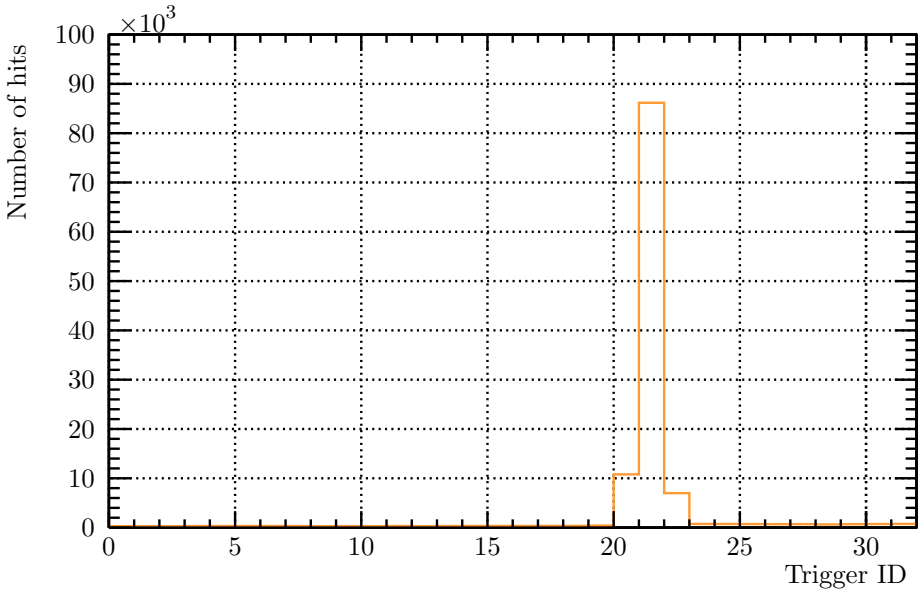

Figure D.3. *Trigger ID versus the number of hits measured by the RD53A module during run* 100 454.

The DUT lost synchronicity with the telescope about 15 times during this run. This was compensated for in the offline analysis by fitting a line for the correlation plot, and then computing the difference from this line for each event. If this difference is larger than 5 % for 10 successive triggers, it is marked as out of sync and from that trigger number on the telescope events are compared to the DUT events of one trigger number earlier.

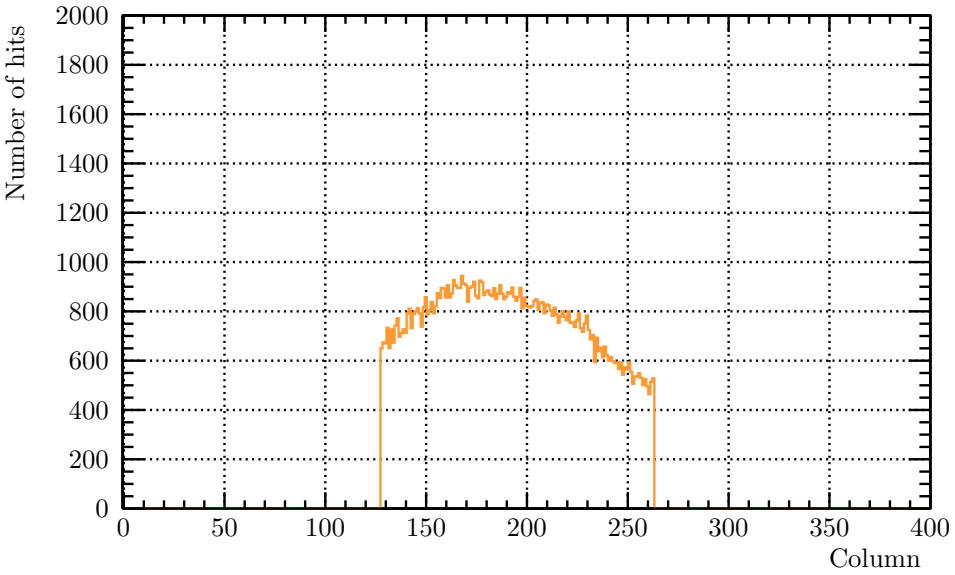

(a) *Local x.*

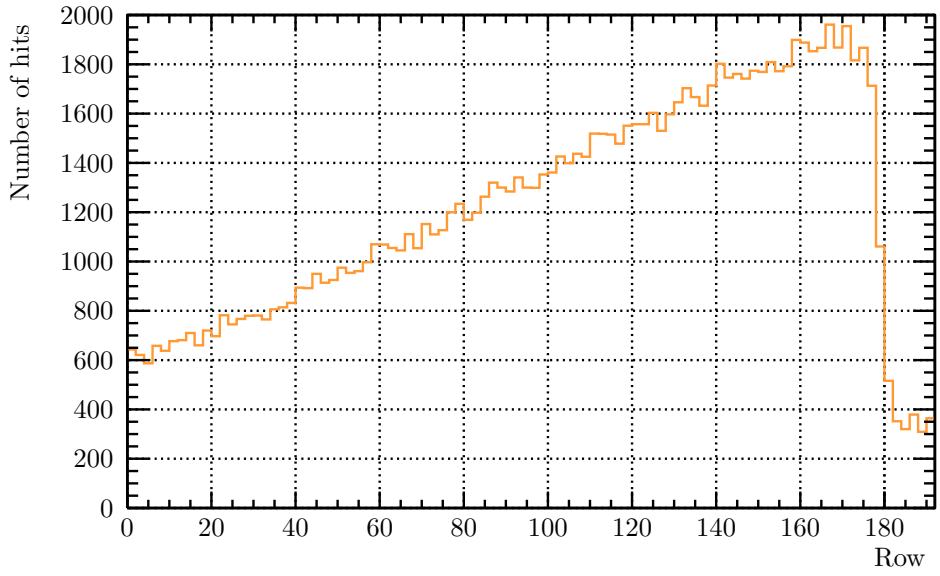

(b) *Local y.*

Figure D.4. *Beam profiles in the global x and y direction respectively, measured by the RD53A module during run* 100 454.

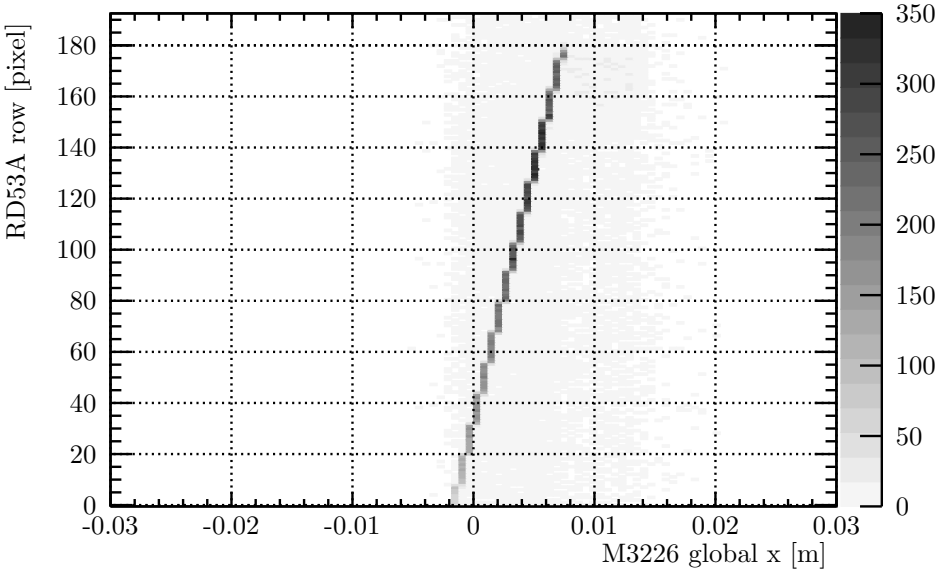

(a) *Global x.*

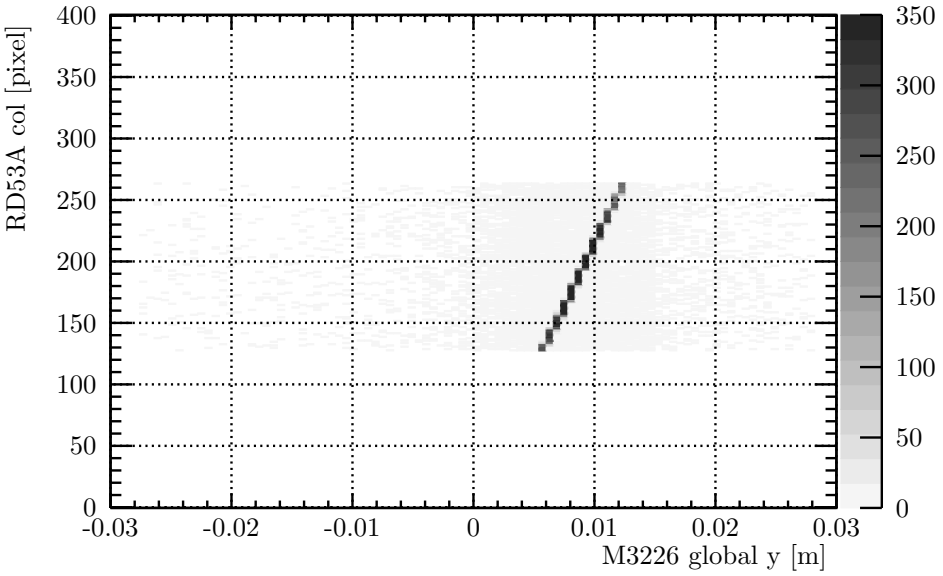

(b) *Global y.*

Figure D.5. *Hit correlation between telescope module M3226 and the RD53A DUT, in the global x and y direction respectively, measured by the RD53A module during run* 100 454.